INVESTIGATIONS ON $AgInO_2$ AND PbS: PREPARATION, CHARACTERIZATION AND GAS SENSING BEHAVIOR OF THICK AND THIN FILMS

by

T. V. BEATRICEVEENA

Enrolment No: CHEM02201504003

Indira Gandhi Centre for Atomic Research
Kalpakkam

A thesis submitted to the
board of studies in Chemical Sciences
in partial fulfillment of requirements
for the Degree of

DOCTOR OF PHILOSOPHY
of
HOMI BHABHA NATIONAL INSTITUTE

January 2021

Homi Bhabha National Institute

Recommendations of the Viva Voce Committee

As members of the Viva Voce Committee, we certify that we have read the dissertation prepared by **T. V. Beatriceveena** entitled **"Investigations on $AgInO_2$ and PbS: Preparation, Characterization and Gas Sensing Behavior of Thick and Thin Films"** and recommend that it may be accepted as fulfilling the thesis requirement for the award of Degree of Doctor of Philosophy.

JPhilip 15.04.21

Chairman – Prof. John Philip **Date:**

Guide / Convener – Prof. K. I. Gnanasekar **Date:** 15/4/2021

Gnanasekar

Examiner – Prof. Karuna Kar Nanda **Date:15.04.2021**

KKNanda

Member 1- Prof. V. Jayaraman **Date:** 15.04.2021.

V. Jayaraman

Member 2- Prof. T. R. Ravindran **Date:**

T R Ravindran 15/4/2021

Member 3- Prof. V. Sudarsan , HBNI-BARC **Date:15.04.2021**

Sudarsan. V

Final approval and acceptance of this thesis is contingent upon the candidate's submission of the final copies of the thesis to HBNI.

I/We hereby certify that I/we have read this thesis prepared under my/our direction and recommend that it may be accepted as fulfilling the thesis requirement.

Date: 15/4/2021

Place: Kalpakkam

Gnanasekar

Dr. K. I. Gnanasekar
(Guide / Convener)

STATEMENT BY AUTHOR

This dissertation has been submitted in partial fulfillment of requirements for an advanced degree at Homi Bhabha National Institute (HBNI) and is deposited in the Library to be made available to borrowers under rules of the HBNI.

Brief quotations from this dissertation are allowable without special permission, provided that accurate acknowledgement of source is made. Requests for permission for extended quotation from or reproduction of this manuscript in whole or in part may be granted by the Competent Authority of HBNI when in his or her judgment the proposed use of the material is in the interests of scholarship. In all other instances, however, permission must be obtained from the author.

Beatrice Veena T.V.

T. V. Beatriceveena

DECLARATION

I, hereby declare that the investigation presented in the thesis entitled **"Investigations on $AgInO_2$ and PbS: Preparation, Characterization and Gas Sensing Behavior of Thick and Thin Films"** submitted to **Homi Bhabha National Institute (HBNI)**, Mumbai, India for the award of **Doctor of Philosophy in Chemical Sciences** is the record of work has been carried out by me under the guidance of **Dr. K. I. Gnanasekar**. The work is original and has not been submitted earlier as a whole or in part for a degree/diploma at this or any other Institution/University.

Beatrice

T. V. Beatriceveena

LIST OF PUBLICATIONS

Publications in Refereed Journal

a. Published

1. **T. V. Beatriceveena,** A. Sree Rama Murthy, E. Prabhu & K. I. Gnanasekar, Wide range hydrogen sensing behavior of a silver delafossite: Performance towards long term stability, repeatability and selectivity, **International Journal of Hydrogen Energy,** 46 (2021) pp 2824 – 2834.
2. **T. V. Beatriceveena,** A. Sree Rama Murthy, S. Murugesan, E. Prabhu & K. I. Gnanasekar, A Factorial Design Approach for Hydrothermal Synthesis of Phase Pure $AgInO_2$ – A Parametric Optimization Study, ***Angewandte Chemie*** **International Edition,** 59 (2020) pp 2241 –2245.
3. **T. V. Beatriceveena,** E. Prabhu, V. Jayaraman, & K. I. Gnanasekar, X-ray photoelectron and Hall studies on nanostructured thin films of PbS grown by pulsed laser deposition, **Materials Letters,** 238 (2019) pp 324 – 327.
4. **T. V. Beatriceveena,** E. Prabhu, A. Sree Rama Murthy, V. Jayaraman, & K.I. Gnanasekar, Highly selective PbS thin film based ammonia sensor for inert ambient: in-situ Hall and Photoelectron studies, **Applied Surface Science,** 456 (2018) pp 430 – 436.

b. Under preparation

1. **T. V. Beatriceveena,** E. Prabhu & K. I. Gnanasekar, High Pressure Delafossite $AgInO_2$ stabilized as thin films at 0.7 mbar in-situ oxygen pressure using PLD and its performance towards hydrogen sensing (Manuscript under progress).

2. **T. V. Beatriceveena,** E. Prabhu & K. I. Gnanasekar, PLD made thin films of $AgInO_2$ based gas sensor for inert ambient: in-situ Hall, Photoelectron studies and principle component analysis (Manuscript under progress).

Other Publications

a. Co-authored and publications not part of the thesis

1. A. Nancy Anna Anasthasiya, Gurpreet Kaur, **T.V. Beatriceveena**, V. Jayaraman, K. I. Gnanasekar, Understanding of ammonia detection of PbS in inert ambient: Experimental and computational approach, **Applied Surface Science,** 495 (2019) pp 143605.
2. **T.V. Beatriceveena**, E. Prabhu, A. Sree Rama Murthy, K. I. Gnanasekar and V. Jayaraman, Selective sensing behaviour of 1D β-Ag_2MoO_4 nanorods towards ammonia (Manuscript under progress).

b. Conference / Symposium Publications

1. **T. V. Beatriceveena,** E. Prabhu, V. Jayaraman, & K. I. Gnanasekar, Laser Ablated Thin Films of PbS for NH_3 Sensing Under Inert Ambient, **SMC Bulletin, Vol 10(2), 2019**

Conference Presentations

1. **T.V. Beatriceveena**, E. Prabhu, V. Jayaraman & K. I. Gnanasekar, Selective sensing behaviour of β-Ag_2MoO_4 nanorods towards ammonia, *6th Nano Today Conference (Nano Today – 2019),* Lisbon, Portugal (Poster).
2. **T.V. Beatriceveena**, E. Prabhu, V. Jayaraman & K. I. Gnanasekar, Laser Ablated Thin Films of PbS for NH_3 Sensing Under Inert Ambient, DAE-BRNS, *7th Interdisciplinary Symposium on Materials Chemistry (ISMC-2018),* BARC, Mumbai (Best Poster Award).

3. **T.V. Beatriceveena** & K. I. Gnanasekar, In-situ Hall studies on PbS thin films, Homi Bhabha National Institute, *Research Scholars Meet on Material Science and Engineering of Nuclear Materials (RSM-MSENM- 2018)*, IGCAR, Kalpakkam (Poster).

4. **T.V. Beatriceveena**, E. Prabhu, A. Sree Rama Murthy, K.I. Gnanasekar and V. Jayaraman, Low temperature synthesis of β-Ag_2MoO_4 its electrical conductivity and gas sensing properties towards gases, *International Conference on Electrochemical Science and Technology (ICONEST 2017),* IISc., Bengaluru (Poster).

Beatrice Veena T.V.

T. V. Beatriceveena

DEDICATED

TO

MY FAMILY

ACKNOWLEDGEMENTS

I thank God Almighty for the guidance, protection, blessings and for all the blessings in my life.

First and foremost, I would like to express my sincere gratitude to my thesis advisor Dr. K. I. Gnanasekar, Head, Novel Chemical Sensors Section (NCSS), Indira Gandhi Centre for Atomic Research (IGCAR) for his continuous support, patience, encouragement, enthusiasm and immense knowledge. His intellectual ideas, guidance and writing skills helped me in the successful completion of my research work and preparation of the thesis.

I thank my present and previous doctoral committee members Dr. John Philip, Dr. V. Jayaraman, Dr. T. R. Ravindran, Dr. V. Sudarsan (HBNI-BARC) and Dr. B. K. Panigrahi for their encouragement, insightful comments and suggestions during the course of my research work.

I express my sincere gratitude and indebtedness to Dr. A. K. Bhaduri, Director, IGCAR, Dr. N. Sivaraman, Group Director, Materials Chemistry and Metal Fuel Cycle Group (MC&MFCG) and former Dean-Chemical Sciences, Dr. V. Jayaraman, Associate Director, MC&MFCG and Dr. C. V. S. Brahmananda Rao, Dean-Chemical Sciences for their constant encouragement and support.

I extend my heartfelt gratitude to Dr. E. Prabhu and Dr. A. Sree Rama Murthy for their continuous help and technical support in teaching me the experimental techniques, handling of instruments, designing and execution of experiments, interpretation of data and for enriching my ideas.

I thank my section members Mr. K. H. Mahendran, Dr. K. Chandran, Dr. P. C. Clinsha, Mr. Nair Afijith Ravindranath, Mr. I. Lakshmigandhan, Mr. Ravindra Babu, Mr. Jose Joseph, Dr. Nancy Anna Anasthasiya, Miss. Lisa John, Miss. Jeena (late), Mr. P.

Madhurai and Mrs. Lavanya for their timely help, useful technical discussions, suggestions and moral support.

I thank Dr. Ramanathaswamy Pandian, Dr. Pavan K. Narayanam, Dr. S. Balakrishnan, Dr. Sajal Ghosh, Dr. Arup Dasgupta, Mr. Dwarapudi Bola Sankar, Mr. Mahima Kumar, Mr. K. Ramaswamy and Miss. Jakathamani for helping me in doing various experimental studies.

I express my deepest gratitude to my parents Mr. T. Vincent and Mrs. P. D. Josephine, husband Dr. K. Sambasiva Rao, grandmother Mrs. T. Kanikamary, uncle Mr. T. Selvaraj, aunts Sr. T. Annie and Sr. T. Lilly Josephine and other family members for their support, love and affection which brings hope in my life and helped me to accomplish my goals.

Apart from the intellectual support, an emotional support is always needed to conquer the hardships. For this, I would like to thank Dr. E. Jayanthi, Dr. Prema, Miss. Shirley Auxilia, Miss. Akshaya Devi, Miss. Sneha, Mr. A. Praveen, 2015 batch mates and fellow enclavians for their warm friendship.

I take an opportunity to thank the technical and non-technical members of MC&MFCG and IGCAR for their support.

Apart from all the people mentioned in this acknowledgment, there are many others who have helped me in various ways during the course of this thesis work. My sincere thanks to all those I might have forgotten to mention. This thesis would not have been possible without the support of many people who contributed and extended their valuable co-operation in the completion of the research work.

Beatrice Veena T.V

T. V. Beatriceveena

CONTENTS

Title **Page No.**

INVESTIGATIONS ON $AgInO_2$ AND PbS: PREPARATION, CHARACTERIZATION AND GAS SENSING BEHAVIOR OF THICK AND THIN FILMS

by

T. V. BEATRICEVEENA

Enrolment No: CHEM02201504003

Indira Gandhi Centre for Atomic Research

Kalpakkam

A thesis submitted to the
board of studies in Chemical Sciences
in partial fulfillment of requirements
for the Degree of

DOCTOR OF PHILOSOPHY

of

HOMI BHABHA NATIONAL INSTITUTE

January 2021

Homi Bhabha National Institute

Recommendations of the Viva Voce Committee

As members of the Viva Voce Committee, we certify that we have read the dissertation prepared by **T. V. Beatriceveena** entitled **"Investigations on $AgInO_2$ and PbS: Preparation, Characterization and Gas Sensing Behavior of Thick and Thin Films"** and recommend that it may be accepted as fulfilling the thesis requirement for the award of Degree of Doctor of Philosophy.

15.04.21

Chairman – Prof. John Philip **Date:**

Guide / Convener – Prof. K. I. Gnanasekar **Date:** 15/4/2021

Gnanasekar

Examiner – Prof. Karuna Kar Nanda **Date:15.04.2021**

KUNanda

Member 1- Prof. V. Jayaraman **Date:** 15.04.2021.

V. Jayaraman

Member 2- Prof. T. R. Ravindran **Date:**

T R Ravindran 15/4/2021

Member 3- Prof. V. Sudarsan , HBNI-BARC **Date:15.04.2021**

Sudarsan. V

Final approval and acceptance of this thesis is contingent upon the candidate's submission of the final copies of the thesis to HBNI.

I/We hereby certify that I/we have read this thesis prepared under my/our direction and recommend that it may be accepted as fulfilling the thesis requirement.

Gnanasekar

Date: 15/4/2021

Place: Kalpakkam

Dr. K. I. Gnanasekar
(Guide / Convener)

STATEMENT BY AUTHOR

This dissertation has been submitted in partial fulfillment of requirements for an advanced degree at Homi Bhabha National Institute (HBNI) and is deposited in the Library to be made available to borrowers under rules of the HBNI.

Brief quotations from this dissertation are allowable without special permission, provided that accurate acknowledgement of source is made. Requests for permission for extended quotation from or reproduction of this manuscript in whole or in part may be granted by the Competent Authority of HBNI when in his or her judgment the proposed use of the material is in the interests of scholarship. In all other instances, however, permission must be obtained from the author.

Beatrice Veena T.V.

T. V. Beatriceveena

DECLARATION

I, hereby declare that the investigation presented in the thesis entitled **"Investigations on $AgInO_2$ and PbS: Preparation, Characterization and Gas Sensing Behavior of Thick and Thin Films"** submitted to **Homi Bhabha National Institute (HBNI)**, Mumbai, India for the award of **Doctor of Philosophy in Chemical Sciences** is the record of work has been carried out by me under the guidance of **Dr. K. I. Gnanasekar**. The work is original and has not been submitted earlier as a whole or in part for a degree/diploma at this or any other Institution/University.

Beatrice V G.V.

T. V. Beatriceveena

LIST OF PUBLICATIONS

Publications in Refereed Journal

a. Published

1. **T. V. Beatriceveena,** A. Sree Rama Murthy, E. Prabhu & K. I. Gnanasekar, Wide range hydrogen sensing behavior of a silver delafossite: Performance towards long term stability, repeatability and selectivity, **International Journal of Hydrogen Energy,** 46 (2021) pp 2824 – 2834.
2. **T. V. Beatriceveena,** A. Sree Rama Murthy, S. Murugesan, E. Prabhu & K. I. Gnanasekar, A Factorial Design Approach for Hydrothermal Synthesis of Phase Pure $AgInO_2$ – A Parametric Optimization Study, ***Angewandte Chemie*** **International Edition,** 59 (2020) pp 2241 –2245.
3. **T. V. Beatriceveena,** E. Prabhu, V. Jayaraman, & K. I. Gnanasekar, X-ray photoelectron and Hall studies on nanostructured thin films of PbS grown by pulsed laser deposition, **Materials Letters,** 238 (2019) pp 324 – 327.
4. **T. V. Beatriceveena,** E. Prabhu, A. Sree Rama Murthy, V. Jayaraman, & K.I. Gnanasekar, Highly selective PbS thin film based ammonia sensor for inert ambient: in-situ Hall and Photoelectron studies, **Applied Surface Science,** 456 (2018) pp 430 – 436.

b. Under preparation

1. **T. V. Beatriceveena,** E. Prabhu & K. I. Gnanasekar, High Pressure Delafossite $AgInO_2$ stabilized as thin films at 0.7 mbar in-situ oxygen pressure using PLD and its performance towards hydrogen sensing (Manuscript under progress).

2. **T. V. Beatriceveena,** E. Prabhu & K. I. Gnanasekar, PLD made thin films of $AgInO_2$ based gas sensor for inert ambient: in-situ Hall, Photoelectron studies and principle component analysis (Manuscript under progress).

Other Publications

a. Co-authored and publications not part of the thesis

1. A. Nancy Anna Anasthasiya, Gurpreet Kaur, **T.V. Beatriceveena**, V. Jayaraman, K. I. Gnanasekar, Understanding of ammonia detection of PbS in inert ambient: Experimental and computational approach, **Applied Surface Science,** 495 (2019) pp 143605.
2. **T.V. Beatriceveena**, E. Prabhu, A. Sree Rama Murthy, K. I. Gnanasekar and V. Jayaraman, Selective sensing behaviour of 1D β-Ag_2MoO_4 nanorods towards ammonia (Manuscript under progress).

b. Conference / Symposium Publications

1. **T. V. Beatriceveena,** E. Prabhu, V. Jayaraman, & K. I. Gnanasekar, Laser Ablated Thin Films of PbS for NH_3 Sensing Under Inert Ambient, **SMC Bulletin, Vol 10(2), 2019**

Conference Presentations

1. **T.V. Beatriceveena**, E. Prabhu, V. Jayaraman & K. I. Gnanasekar, Selective sensing behaviour of β-Ag_2MoO_4 nanorods towards ammonia, *6th Nano Today Conference (Nano Today – 2019)*, Lisbon, Portugal (Poster).

2. **T.V. Beatriceveena**, E. Prabhu, V. Jayaraman & K. I. Gnanasekar, Laser Ablated Thin Films of PbS for NH_3 Sensing Under Inert Ambient, DAE-BRNS, *7th Interdisciplinary Symposium on Materials Chemistry (ISMC-2018)*, BARC, Mumbai (Best Poster Award).

3. **T.V. Beatriceveena** & K. I. Gnanasekar, In-situ Hall studies on PbS thin films, Homi Bhabha National Institute, *Research Scholars Meet on Material Science and Engineering of Nuclear Materials (RSM-MSENM- 2018)*, IGCAR, Kalpakkam (Poster).

4. **T.V. Beatriceveena**, E. Prabhu, A. Sree Rama Murthy, K.I. Gnanasekar and V. Jayaraman, Low temperature synthesis of β-Ag_2MoO_4 its electrical conductivity and gas sensing properties towards gases, *International Conference on Electrochemical Science and Technology (ICONEST 2017),* IISc., Bengaluru (Poster).

Beatrice V. T.V.

T. V. Beatriceveena

DEDICATED

TO

MY FAMILY

ACKNOWLEDGEMENTS

I thank God Almighty for the guidance, protection, blessings and for all the blessings in my life.

First and foremost, I would like to express my sincere gratitude to my thesis advisor Dr. K. I. Gnanasekar, Head, Novel Chemical Sensors Section (NCSS), Indira Gandhi Centre for Atomic Research (IGCAR) for his continuous support, patience, encouragement, enthusiasm and immense knowledge. His intellectual ideas, guidance and writing skills helped me in the successful completion of my research work and preparation of the thesis.

I thank my present and previous doctoral committee members Dr. John Philip, Dr. V. Jayaraman, Dr. T. R. Ravindran, Dr. V. Sudarsan (HBNI-BARC) and Dr. B. K. Panigrahi for their encouragement, insightful comments and suggestions during the course of my research work.

I express my sincere gratitude and indebtedness to Dr. A. K. Bhaduri, Director, IGCAR, Dr. N. Sivaraman, Group Director, Materials Chemistry and Metal Fuel Cycle Group (MC&MFCG) and former Dean-Chemical Sciences, Dr. V. Jayaraman, Associate Director, MC&MFCG and Dr. C. V. S. Brahmananda Rao, Dean-Chemical Sciences for their constant encouragement and support.

I extend my heartfelt gratitude to Dr. E. Prabhu and Dr. A. Sree Rama Murthy for their continuous help and technical support in teaching me the experimental techniques, handling of instruments, designing and execution of experiments, interpretation of data and for enriching my ideas.

I thank my section members Mr. K. H. Mahendran, Dr. K. Chandran, Dr. P. C. Clinsha, Mr. Nair Afijith Ravindranath, Mr. I. Lakshmigandhan, Mr. Ravindra Babu, Mr. Jose Joseph, Dr. Nancy Anna Anasthasiya, Miss. Lisa John, Miss. Jeena (late), Mr. P.

Madhurai and Mrs. Lavanya for their timely help, useful technical discussions, suggestions and moral support.

I thank Dr. Ramanathaswamy Pandian, Dr. Pavan K. Narayanam, Dr. S. Balakrishnan, Dr. Sajal Ghosh, Dr. Arup Dasgupta, Mr. Dwarapudi Bola Sankar, Mr. Mahima Kumar, Mr. K. Ramaswamy and Miss. Jakathamani for helping me in doing various experimental studies.

I express my deepest gratitude to my parents Mr. T. Vincent and Mrs. P. D. Josephine, husband Dr. K. Sambasiva Rao, grandmother Mrs. T. Kanikamary, uncle Mr. T. Selvaraj, aunts Sr. T. Annie and Sr. T. Lilly Josephine and other family members for their support, love and affection which brings hope in my life and helped me to accomplish my goals.

Apart from the intellectual support, an emotional support is always needed to conquer the hardships. For this, I would like to thank Dr. E. Jayanthi, Dr. Prema, Miss. Shirley Auxilia, Miss. Akshaya Devi, Miss. Sneha, Mr. A. Praveen, 2015 batch mates and fellow enclavians for their warm friendship.

I take an opportunity to thank the technical and non-technical members of MC&MFCG and IGCAR for their support.

Apart from all the people mentioned in this acknowledgment, there are many others who have helped me in various ways during the course of this thesis work. My sincere thanks to all those I might have forgotten to mention. This thesis would not have been possible without the support of many people who contributed and extended their valuable co-operation in the completion of the research work.

Beatrice Veena T.V

T. V. Beatriceveena

CONTENTS

Title **Page No.**

PREFACE

With the increasing consumption of fossil fuels and rapid growth of industrialization, emission of various hazardous gases has also increased dramatically in recent times. H_2S, NH_3, CO, NO and NO_2 are some of the pollutants having a threshold limit value (TLV) of 20, 25, 25, 20 and 3 vppm respectively and will affect the health adversely for an increase in their levels beyond the specified values. In addition, some of the gases like H_2, H_2S and NH_3 can form explosive mixtures with oxygen in the air and lead to undesirable consequences. Many countries have toughened the legislation towards the reduction of emission of pollutants and encouraged the development of chemical sensors for accurate measurement of toxic gases for use in the process streams, automobile industry, security sector, medical diagnostics and environmental monitoring. Although the development of robust, miniaturized, low-cost and low power devices for environmental monitoring is given the priority, their reliability to operate in harsh industrial ambients is also stressed. Sensors that operate on electrochemical, optical, thermal and chemiresistive principles have been reported to be useful for this purpose. Among them, semiconducting oxides (SMOs) based chemiresistive gas sensors are very attractive due to their ease of fabrication, simple operation, low power consumption and amenable for miniaturization. The first commercial gas sensor device was developed in the 1960s using metal oxide as the sensing layer. Since then, search for new materials with improved features, methodologies to configure them as nanostructured thick/thin films and development of technology for miniaturization for low power operation is being pursued across the globe to achieve higher sensitivity, selectivity, speed (response and recovery times), and stability, namely the “4s”. With the emergence of nanoscience and nanotechnology, a race to exploit the advantages of this field to develop sensing devices with improved performance is also seen from the number of publications in the last couple of decades.

A variety of materials that include metal oxides/sulphides/halides, organic semiconductors and carbon nanostructures have been demonstrated to be gas sensors. The response towards a particular analyte gas depends on the nature of semi-conductivity (p-type/n-type), the chemistry of the analyte (oxidizing/reducing) and the type of chemical interaction taking place on the surface. The primary requirement of the sensor is that it must be highly sensitive, selective, having quick response and recovery times and should not suffer baseline drifts with respect to changes in humidity levels. To achieve high sensitivity, the probability of interaction of the analyte with the semiconductor surface has to be maximized and nanomaterials with the high specific surface area are the right choices offering large changes in conductivity even for trace levels of analyte gas. To have a short response and retrace times, configurations having large surface-to-volume ratio are preferred to avoid the slower diffusion-controlled reactions. One of the major concerns of the SMO gas sensors is their cross-sensitivity to other gases which constrain their reliability. Choice of suitable dopants and additives was shown to promote the specific catalytic reaction in addition to the operating temperature for achieving selectivity. Surface modification, hybrid or composite nanostructures and photo-illumination have also been reported to improve the performance of the devices. However, the effect of humidity on long term performance, baseline drifts and frequent calibrations are some of the challenges which still remain unresolved driving the search for advanced materials. This thesis outlines some of the issues specific to certain industrial processes requiring rugged and reliable devices that operate under harsh and humid ambient.

The first part of the thesis (Chapter 3 to 5) deals with the development of wide range hydrogen sensors that operate under harsh industrial environments. Nuclear fuel reprocessing industry requires a rugged and reliable device for detecting hydrogen (generated from radiolysis) from trace to percentage levels under highly humid conditions in the presence of NO_x, a highly toxic and corrosive gas. Most of the sensing materials fail to operate under highly reactive NO_x ambient resulting in gradual degradation in performance of the sensor. Thus, the choice of new materials that withstand NO_x environment is highly constrained by limited options. Sensors for this specific application are either very expensive or not available forcing us to look out for new materials. Most of the commercial hydrogen sensors have a narrow working range with relatively a short life in harsh ambient enforcing frequent calibrations due to continuous baseline drifts and therefore, they cannot be employed. Although the search for new semiconducting binary oxides is currently in progress, the scope of expanding the search domain to include ternary and quaternary oxides is also considered. Based on broad empirical guidelines, wide bandgap transparent conducting (TCOs) delafossites drew our attention to check their suitability as many of them fulfil the empirical guidelines. Predicted to be promising materials for various applications, the initial drive failed to sustain the enthusiasm across the globe largely due to the obstacles faced during their synthesis in pure form as most of them are synthesized at high pressures. The semiconductor that forms under high hydrothermal pressures will be the natural choice to begin our investigation as it is expected to be resistant to any moisture/steam attack. Incidentally $AgInO_2$, semiconducting delafossite reported to stabilize at a hydrothermal pressure of about 10 bar at 210 ^oC is attractive. However, this compound does not form in a pure phase. After addressing the issues related to its synthesis, a modified hydrothermal route is employed to stabilize the impurity-free phase pure nanoplates of $AgInO_2$. The nanoplates of $AgInO_2$ are then configured as thick films using a screen printing technique and investigated for hydrogen sensing at different humidity levels.

The second part of the thesis (Chapter 6) is focused on the development of ammonia sensor for inert ambient to track the moisture leaks which generates ammonia due to hydrolysis of uranium nitrides stored in fuel storage facilities. Sensors based on semiconductor oxides cannot be deployed for inert streams as they require oxygen for operation. This prompted us to shift our focus on non-oxide based semiconductors and PbS, a p-type semiconducting chalcogenide, drew our attention. The Lewis acidic character of PbS is particularly attractive for adsorption of ammonia and its valence band made up of Pb 5d/6p makes it suitable for interaction.

To summarize, the thesis is focused on optimization of process parameters of the hydrothermal method for the high-pressure stable $AgInO_2$, investigation on gas sensors studies on $AgInO_2$ thick films, optimization of thin-film deposition parameters of pulsed KrF (248 nm) laser method for deposition of high-quality thin films of $AgInO_2$. For the development of ammonia sensor for operations in inert streams, deposition parameters of PLD have been optimized for the growth of nanostructured thin films of PbS and its ammonia sensing properties are presented.

LIST OF FIGURES

LIST OF TABLES

LIST OF ABBREVIATIONS

v	$AgInO_2$	Silver Indium Oxide
v	PbS	Lead Sulphide
v	TLV	Threshold limit value
v	LEL	Lower explosive limit
v	UEL	Upper explosive limit
v	ppm	Parts per million
v	SMO	Semiconducting metal oxides
v	TCOs	Transparent conducting oxides
v	GB	Grain boundary
v	D	Grain size
v	L	Depletion layer
v	X	Neck size
v	E_a	Activation energy
v	k	Rate constant
v	PLD	Pulsed laser deposition
v	XPS	X-ray photoelectron spectroscopy
v	IDEs	Inter-digitated electrodes
v	DC	Direct current
v	AC	Alternating current
v	PXRD	Powder X-ray diffraction
v	GI-XRD	Grazing incidence X-ray diffraction
v	FE-SEM	Field Emission Scanning Electron Microscope
v	HR-TEM	High Resolution Transmission Electron Microscope
v	SAED	Selected area electron diffraction
v	EDX	Energy Dispersive X-ray spectroscopy
v	AFM	Atomic force microscopy
v	UV-Vis	Ultraviolet-Visible
v	TG - DTA	Thermo gravimetric - Differential thermal analysis
v	SS	Stainless steel
v	CF flange	ConFlat flange
v	2D	Two dimensional

v	f.u.	Formula unit
v	SOCP	Spin-orbit coupling parameter
v	at %	Atom percent
v	R	Resistance
v	R_a	Resistance in presence of air
v	R_g	Resistance in presence of analyte gas
v	ρ	Resistivity
v	σ	Conductivity
v	μ	Mobility
v	n	Electron carrier concentration
v	p	Hole carrier concentration
v	FWHM	Full width half maxima

ABSTRACT OF THESIS

With the increasing consumption of fossil fuels and rapid growth of industrialization, emission of various hazardous gases have also increased dramatically in recent times. H_2S, NH_3, CO, NO and NO_2 are some of the pollutants having a threshold limit value (TLV) of 20, 25, 25, 20 and 3 vppm respectively and will affect the health adversely for an increase in their levels beyond the specified values. In addition, some of the gases like H_2, H_2S and NH_3 can form explosive mixtures with oxygen in the air and lead to undesirable consequences. Although the development of robust, miniaturized, low-cost and low power devices for environmental monitoring is given the priority, their reliability to operate in harsh industrial ambients is also stressed. Among the various methods, semiconducting metal oxides (SMOs) based chemiresistive gas sensors are very attractive due to their ease of fabrication, simple operation, low power consumption, amenable for miniaturization and ease of formation of arrays. Literature shows a variety of materials that include metal oxides/sulphides/halides, organic semiconductors and carbon nanostructures have been tested for different gases. The primary requirement of the sensor is that it must be highly sensitive, selective, having quick response and recovery times and should not suffer baseline drifts with respect to changes in humidity levels. One of the major concerns of the SMO gas sensors is their cross-sensitivity to other gases which constrain their reliability. The effect of humidity on long term performance, baseline drifts and frequent calibrations are some of the challenges which still remain unresolved driving the search for advanced materials. This thesis outlines some of the issues specific to certain industrial processes requiring rugged and reliable devices that operate under harsh and humid ambient.

First part of the thesis (Chapter 3 to 5) deals with the development of wide range hydrogen sensors that operate under harsh industrial environments. Nuclear fuel reprocessing industry requires a rugged and reliable device for detecting hydrogen generated from radiolysis from trace to percentage levels under highly humid conditions in the presence of highly toxic and corrosive NO_x. Most of the commercial hydrogen sensors have a narrow working range with relatively a short life in harsh ambient enforcing frequent calibrations due to continuous baseline drifts and therefore, they cannot be employed. Based on broad empirical guidelines, wide bandgap transparent conducting (TCOs) delafossites drew our attention to check their suitability and among them $AgInO_2$ is chosen. However, its formation

is highly sensitivite to hydrothermal pressures and is always reported to be contaminated with impurities. After addressing the issues related to its synthesis, a modified hydrothermal route is employed to stabilize the impurity-free phase pure nanoplates of $AgInO_2$ by applying a factorial design approach. The combined effect of 180 ˚C & 4 M KOH with no dwell time dependency between 24 h and 60 h are found to be the favoured conditions for hydrothermal sysntheis to get phase pure $AgInO_2$. The nanoplates of $AgInO_2$ are configured as thick films using a screen printing technique and investigated for hydrogen sensing at different humidity levels. Thick film sensors of $AgInO_2$ respond to hydrogen over a wide concentration range from 1 ppm to 10000 ppm with good repeatability and baseline stability. The low cross-sensitivity to a wide range of other analytes which make them a potentially wide range H_2 sensor. XPS results showed a decrease in the peak area of chemisorbed oxygen (O_x^-) after exposure to H_2 indicating its consumption and confirms their participation during sensing. Granular thin films of randomly oriented rhombohedral $AgInO_2$ were successfully deposited at 200 ˚C under the in-situ pressure of 0.7 mbar oxygen which otherwise requires high pressures and temperatures. The growth conditions of Ag_2O are adopted for stabilization of $AgInO_2$. Thin films exhibited columnar growth with a column width of ~20 nm and thickness of ~175 nm. A significant reduction in response and recovery times is observed for thin film configuration as compared to that of thick films of $AgInO_2$. In-situ Hall studies show that both resistivity and carrier concentration were strongly attenuated in the presence of even trace levels of hydrogen.

The second part of the thesis (Chapter 6) is focused on the development of ammonia sensor for inert ambient to track the moisture leaks which generates ammonia during hydrolysis of uranium nitrides in fuel storage facilities. Sensors based on semiconductor oxides cannot be deployed for inert streams as they require oxygen for operation. Thin films of PbS, a chalcogenide semiconductor is chosen and is deposited by pulsed laser deposition. Deposition is carried out in the presence of inert gas to suppress oxygen outgassing which oxidizes the film. Films were highly selective and sensitive to NH_3 with a typical response and recovery times of about 26 s and 125 s respectively for 500 ppm of NH_3 at 473 K. In-situ Hall studies show that both carrier concentration and mobility are altered significantly in the presence of trace levels of ammonia (100 ppm). Adsorption of NH_3 does not alter the oxidation states of Pb and S, but the binding energy value of 398.1 eV for N 1s level shows dissociative adsorption of NH_3 involving $–NH_x$ species at 473 K.

CHAPTER 7

Conclusions and Future Directions

This chapter brings out the outcomes arrived from chapters 3, 4, 5 and 6 based on the systematic investigations and the scope for the future work plan.

7.1. Conclusions

The performance of a wide range hydrogen sensor using $AgInO_2$ that operates in the presence of trace levels of NO_x and hydrocarbons under harsh and humid ambient is demonstrated. The challenges posed by humidity on long term performance and baseline drifts enforcing frequent calibrations of other semiconducting metal oxides are considered in the material choice. Similarly, the performance of a NH_3 sensor using thin film of PbS for operations in inert ambients is also demonstrated. Both the sensors are developed based on the specific requirement for the nuclear industry for which the sensors have to be specific, rugged and reliable. The cross-selectivity issue of SMOs is also addressed by exploiting the relative changes in rate constants of the interfering gases by the choice of the operating temperature. The experimental findings obtained during the studies are described in detail in chapters 3 – 6 of the thesis and are summarized below.

7.1.1. Hydrothermal synthesis of phase pure silver indium oxide ($AgInO_2$) – A parametric optimization using factorial design approach

$AgInO_2$, being a high pressure stabilized material not amenable to conventional synthetic routes, is prepared for the first time by a modified hydrothermal route from $AgNO_3$ and Indium nitrate which yielded hexagonal nanoplates of phase pure $AgInO_2$. The importance of factorial design approach to identify the desirable conditions for successful synthesis of phase pure product is highlighted. The combined effect of a temperature of 180 ˚C and the concentration of 4 M KOH with no significant effect on dwell time (24 h - 60 h) is the favoured condition to get phase pure compound. Rietveld and HRTEM analysis show that $AgInO_2$ exhibits rhombohedral crystal structure and no detectable impurities. XPS survey scan confirms the absence of K^+ ions. The selected area high resolution scans confirm that the oxidation states of Ag, In and oxygen are respectively +1, +3 and -2. Impedance spectroscoy studies show that an activation energy of 0.24 eV/f.u is obtained for electrical conduction. We emphasize the application of factorial design approach be extended to synthesize other high pressure stable delafossite/compounds if the issues related to their synthesis are carefully analysed.

7.1.2. Thick film of $AgInO_2$: Response towards wide range of hydrogen, repeatability, selectivity and long term performance

H_2 sensing behavior and the long term performance of thick films of $AgInO_2$ composed of hexagonal nanoplates are presented. Configured in the form of thick film using a screen printing technique, $AgInO_2$ responds to hydrogen from 1 ppm to 10000 ppm with good repeatability and baseline stability which makes it a potentially wide range H_2 sensor. The material exhibits a high degree of selectivity and repeatability without any significant drift in the baseline over a period of 6 months under high humid conditions. Analysis of XPS results after exposure to hydrogen showed a decrease in relative fraction of O_x^- chemisorbed species with no significant change in the patterns of Ag & In. Only the phase pure $AgInO_2$ exhibits high selectivity towards H_2 whereas the $AgInO_2$ with trace levels of metallic (Ag) or oxide (In_2O_3) impurities loses the sensitivity and selectivity. The performance of $AgInO_2$ in different humidity levels reveals its potential for applications in harsh conditions, ideally suitable for environmental monitoring also.

7.1.3. Thin films of $AgInO_2$: Optimization of deposition parameters, characterization and hydrogen sensing studies

Stabilization of the high pressure $AgInO_2$ as thin films is attempted after analyzing the factors that demand the use of high pressures. Pulsed laser deposition technique demonstrated to successfully grown thin films of meta-stable phases is chosen as it meets some of the requirement conditions. Decomposition of Ag_2O to elemental Ag identified to be the key issue is addressed by tuning the PLD parameters to stabilize Ag^+ ions. Experimental conditions which favour the stabilization of Ag^+ ions were worked out and thin films were deposited under these conditions. Granular thin films of randomly oriented rhombohedral $AgInO_2$ were successfully deposited at 200 ˚C under high (0.7 mbar) in-situ oxygen pressure as against 0.1 mbar commonly used to grow oxide thin films. Thin films exhibited columnar growth and each column has an average width of ~ 20 nm and length extending up to thickness of the film which is about ~175 nm in this present case. Gas sensing studies carried out on thin films show that they were highly selective and sensitive to H_2 and respond from 1 ppm to 10000 ppm just as thick films. But the performance of thin films sensors were superior to that of thick films in terms of quicker response and recovery times. Hall measurements showed n-type behaviour with a room temperature carrier concentration of 1.1×10^{16} cm^{-3}. In-situ Hall studies show that both resistivity and carrier concentration are strongly attenuated in the presence of even trace levels of hydrogen. This result opens up stabilization of other delafossite members forming at high pressures directly in thin films and provides opportunities to investigate their properties in thin films.

7.1.4. Highly selective PbS thin film based ammonia sensor for inert ambient: In-situ Hall and photoelectron studies

As the semiconducting metals oxides need air for operation, a non oxide based semiconductor is chosen for inert ambient. Among the various metal sulphides, PbS having reasonable chemical stability and exhibiting selective interaction with NH_3, a lewis base is therefore chosen. Our attempts to deposit thin films at 10^{-6} mbar, the highest vaccum achievable in the present deposition chamber, yielded only PbO films. To reduce the probability of residual outgassing oxygen strking the surface of the growing film, deposition was carried out at higher in-situ pressures of argon. Granular thin films of p-type semiconducting PbS (Cubic) with predominantly a-axis oriented grains having an average thickness of about 140 nm were realized at 553 K under the in-situ argon pressure of 1×10^{-1} mbar. We have also demonstrated the use of PLD for depositing thin films of PbS for the first time. Films were highly selective and sensitive to NH_3 with a typical response and recovery times of about 26 s and 125 s respectively for 500 ppm of NH_3 at 473 K. In-situ Hall studies show that both carrier concentration and mobility are altered significantly in the presence of trace levels of ammonia (100 ppm). Adsorption of NH_3 does not alter the oxidation states of Pb and S but causes a shift of 0.2 eV towards the lower binding energy side. A binding energy value of 398.1 eV for N 1s level shows dissociative adsorption of NH_3 involving –NH_x species at 473 K. Laser deposited thin films of PbS were highly promising for sensing trace levels of NH_3 in the inert ambient (Ar) and potentially useful for monitoring NH_3 released during the hydrolysis of uranium nitrides stored in an inert atmosphere.

7.2. Scope for future plans

The future directions of the present investigations are listed below:

- Application of Factorial design approach for hydrothermal synthesis to be extended to other members of high pressure stabilized compounds.
- Deposition of other members of high pressure stabilized delafossites/compounds as thin films by suitably addressing the issues and investigating their physicochemical properties
- Development of miniaturized low power consuming thin film based devices made of $AgInO_2$ and PbS
- Interference of humidity effect (10 % to 90 %) towards long term repeatability of $AgInO_2$
- Electronic band structure calculations using Density Functional Theory (DFT) for $AgInO_2$ interaction with hydrogen

- Realization of p-n junctions made of thin films of transparent conducting $AgInO_2$ (n-type oxide) – $AgCoO_2$ (p-type oxide) using pulsed laser deposition and exploring their structural, electrical and gas sensing properties
- Development of array based sensors for quantitative estimation of gases from a mixture using principal component analysis (PCA) and pattern recognition systems.

PREFACE

With the increasing consumption of fossil fuels and rapid growth of industrialization, emission of various hazardous gases has also increased dramatically in recent times. H_2S, NH_3, CO, NO and NO_2 are some of the pollutants having a threshold limit value (TLV) of 20, 25, 25, 20 and 3 vppm respectively and will affect the health adversely for an increase in their levels beyond the specified values. In addition, some of the gases like H_2, H_2S and NH_3 can form explosive mixtures with oxygen in the air and lead to undesirable consequences. Many countries have toughened the legislation towards the reduction of emission of pollutants and encouraged the development of chemical sensors for accurate measurement of toxic gases for use in the process streams, automobile industry, security sector, medical diagnostics and environmental monitoring. Although the development of robust, miniaturized, low-cost and low power devices for environmental monitoring is given the priority, their reliability to operate in harsh industrial ambients is also stressed. Sensors that operate on electrochemical, optical, thermal and chemiresistive principles have been reported to be useful for this purpose. Among them, semiconducting oxides (SMOs) based chemiresistive gas sensors are very attractive due to their ease of fabrication, simple operation, low power consumption and amenable for miniaturization. The first commercial gas sensor device was developed in the 1960s using metal oxide as the sensing layer. Since then, search for new materials with improved features, methodologies to configure them as nanostructured thick/thin films and development of technology for miniaturization for low power operation is being pursued across the globe to achieve higher sensitivity, selectivity, speed (response and recovery times), and stability, namely the “4s”. With the emergence of nanoscience and nanotechnology, a race to exploit the advantages of this field to develop sensing devices with improved performance is also seen from the number of publications in the last couple of decades.

A variety of materials that include metal oxides/sulphides/halides, organic semiconductors and carbon nanostructures have been demonstrated to be gas sensors. The response towards a particular analyte gas depends on the nature of semi-conductivity (p-type/n-type), the chemistry of the analyte (oxidizing/reducing) and the type of chemical interaction taking place on the surface. The primary requirement of the sensor is that it must be highly sensitive, selective, having quick response and recovery times and should not suffer baseline drifts with respect to changes in humidity levels. To achieve high sensitivity, the probability of interaction of the analyte with the semiconductor surface has to be maximized and nanomaterials with the high specific surface area are the right choices offering large changes in conductivity even for trace levels of analyte gas. To have a short response and retrace times, configurations having large surface-to-volume ratio are preferred to avoid the slower diffusion-controlled reactions. One of the major concerns of the SMO gas sensors is their cross-sensitivity to other gases which constrain their reliability. Choice of suitable dopants and additives was shown to promote the specific catalytic reaction in addition to the operating temperature for achieving selectivity. Surface modification, hybrid or composite nanostructures and photo-illumination have also been reported to improve the performance of the devices. However, the effect of humidity on long term performance, baseline drifts and frequent calibrations are some of the challenges which still remain unresolved driving the search for advanced materials. This thesis outlines some of the issues specific to certain industrial processes requiring rugged and reliable devices that operate under harsh and humid ambient.

The first part of the thesis (Chapter 3 to 5) deals with the development of wide range hydrogen sensors that operate under harsh industrial environments. Nuclear fuel reprocessing industry requires a rugged and reliable device for detecting hydrogen (generated from radiolysis) from trace to percentage levels under highly humid conditions in the presence of NO_x, a highly toxic and corrosive gas. Most of the sensing materials fail to operate under highly reactive NO_x ambient resulting in gradual degradation in performance of the sensor. Thus, the choice of new materials that withstand NO_x environment is highly constrained by limited options. Sensors for this specific application are either very expensive or not available forcing us to look out for new materials. Most of the commercial hydrogen sensors have a narrow working range with relatively a short life in harsh ambient enforcing frequent calibrations due to continuous baseline drifts and therefore, they cannot be employed. Although the search for new semiconducting binary oxides is currently in progress, the scope of expanding the search domain to include ternary and quaternary oxides is also considered. Based on broad empirical guidelines, wide bandgap transparent conducting (TCOs) delafossites drew our attention to check their suitability as many of them fulfil the empirical guidelines. Predicted to be promising materials for various applications, the initial drive failed to sustain the enthusiasm across the globe largely due to the obstacles faced during their synthesis in pure form as most of them are synthesized at high pressures. The semiconductor that forms under high hydrothermal pressures will be the natural choice to begin our investigation as it is expected to be resistant to any moisture/steam attack. Incidentally $AgInO_2$, semiconducting delafossite reported to stabilize at a hydrothermal pressure of about 10 bar at 210 ^{o}C is attractive. However, this compound does not form in a pure phase. After addressing the issues related to its synthesis, a modified hydrothermal route is employed to stabilize the impurity-free phase pure nanoplates of $AgInO_2$. The nanoplates of $AgInO_2$ are then configured as thick films using a screen printing technique and investigated for hydrogen sensing at different humidity levels.

The second part of the thesis (Chapter 6) is focused on the development of ammonia sensor for inert ambient to track the moisture leaks which generates ammonia due to hydrolysis of uranium nitrides stored in fuel storage facilities. Sensors based on semiconductor oxides cannot be deployed for inert streams as they require oxygen for operation. This prompted us to shift our focus on non-oxide based semiconductors and PbS, a p-type semiconducting chalcogenide, drew our attention. The Lewis acidic character of PbS is particularly attractive for adsorption of ammonia and its valence band made up of Pb 5d/6p makes it suitable for interaction.

To summarize, the thesis is focused on optimization of process parameters of the hydrothermal method for the high-pressure stable $AgInO_2$, investigation on gas sensors studies on $AgInO_2$ thick films, optimization of thin-film deposition parameters of pulsed KrF (248 nm) laser method for deposition of high-quality thin films of $AgInO_2$. For the development of ammonia sensor for operations in inert streams, deposition parameters of PLD have been optimized for the growth of nanostructured thin films of PbS and its ammonia sensing properties are presented.

CHAPTER 1

Introduction to Chemical Sensors

A brief description about chemical sensors and their classification are presented in this chapter. An overview of chemiresistive gas sensors using semiconductor metal oxide/sulphides is also included. Relavance of nanoparticles of metal oxide/sulphides in sensing action and the principle of detection are reviewed. The scope and methodology of the present thesis is presented at the end of this chapter.

1.1. Chemical sensors

Chemical sensing technology stands as a notable area of research and development covering physical, chemical, material, biological sciences along with electrical and electronics engineering. Rapid growth of industrialization has driven the society to face the broad spectrum of gaseous pollutants having profound toxic effects. The urgent need for the development of state-of-the-art chemical sensors for accurate measurement of toxic gases in the process streams, automobile industry, environmental monitoring, the security sector and medical diagnostics has been realized over the last decade owing to the growing public awareness of the hazards associated with many airborne chemicals in the ambient [1-3]. Various countries had toughened the legislation towards the reduction of emission of pollutants and encouraged the development of new measuring concepts. Recent survey of 'Global Industry Analysts Inc.', reports that the estimated global gas sensor market in the year 2020 is likely to be around US$ 960 Million and is projected to reach a revised estimate of US$1.4 Billion by 2027, growing at a compound annual growth rate (CAGR) of 5.6 % over the period 2020-2027 [4].

Fast industrial growth demands the development of low-cost, miniaturized, reliable and robust sensors for various toxic gases for environmental monitoring and for process control in industries. The major hazardous gases in air are nitrogen oxides (NO_x), carbon monoxide (CO), carbon dioxide (CO_2), chlorine (Cl_2), hydrogen chloride (HCl), fluorine (F_2), hydrogen sulphide (H_2S), phosgene ($COCl_2$), ammonia (NH_3), sulfur dioxide (SO_2) and hydrocarbons. Each of these pollutants have different threshold limit values (TLV)[1][5]

---

[1] The concentration in air to which the workers can be exposed daily without an adverse effect (i.e. the threshold between safe and dangerous concentrations). The values were established and are revised annually by the ACGIH and are time-weighted concentrations (TWA) for a 7 h or 8 h workday and 40-h workweek and thus are related to chronic effects.

represented in parts per million (ppm). Monitoring of these gases are of major concern to ensure the safety. Some of these gases have a specific odor so that human nose discerns even if they are present in trace levels. Some of the flammable gases like H_2, propane, butane, etc. are odourless and their leak can cause explosions. In such cases, continuous monitoring of these flammable and environmental pollutants below their explosive / TLV limits is required to reduce their impacts. Acceptable concentration levels (i.e. TLVs and explosive limits (LEL [6] & UEL [6])) regulated by Occupational Safety and Health Administration (OSHA), U.S. Environmental Protection Agency Acute Exposure Guideline Levels (AEGL) and American Conference of Governmental Industrial Hygienists (ACGIH) for some of the gases/vapors are given in Table 1.1 [7-9].

Various methods have been reported to be used to assess the concentration of the analyte gas. They include mass spectrometry, gas chromatography, infrared spectroscopy, chemiluminescence detectors, UV-Visible spectrophotometry and others. Among them, the spectroscopy based methods make use of direct analysis of the spectrum qualitative and quantitative estimation of the analytes present. However, all these techniques are bulky, expensive and sophisticated requiring periodic calibrations. They are more appropriate for the off-line mode of detection and not suitable for continuous on-line monitoring. Therefore, miniaturized, robust and lower power consuming devices are preferred for continuous online monitoring of the analytes at trace levels and thus the development of chemical sensors based on different principles is given the priority.

Table 1.1. Regulated concentration levels of some of the gases/vapors given by different organizations

S.No.	Gases/Vapors	TLV (vppm)	LEL[2] (v %)	UEL[3] (v %)
1	Ammonia	25	15	28
2	Nitric oxide	25	-	-
3	Nitrogen dioxide	0.2	-	-
4	Carbon monoxide	50	12.5	74
5	Carbon dioxide	5000	-	-
6	Formaldehyde	0.75	7	73
7	Hydrazine	0.1	2.9	98
8	Hydrogen	-	4	75
9	Gasoline	300	1.2	7.1
10	Methane	-	5	17
11	Butane	-	1.8	8.4
12	Propane	-	2.1	9.5

1.2. Definition, classifications, advantages and disadvantages of chemical sensors

“A chemical sensor is a device that transforms chemical information, ranging from the concentration of a specific sample component to total composition analysis into an analytically useful signal”. The chemical information may originate from a chemical

---

[2] Lower explosive limit (LEL): The minimum concentration of gas/vapor in air (% by volume at room temperature) below which propagation of a flame does not occur in the presence of an ignition source.

[3] Upper explosive limit (UEL): The maximum concentration of flammable gas/vapor in air (% by volume at room temperature) above which propagation of flame does not occur on contact with a source of ignition.

reaction of the analyte or from a physical property of the system investigated [10]. Modern chemical sensors comprise of two functional units: 1) a receptor and 2) a transducer as illustrated in Figure 1.1 [11]. The receptor transforms the chemical information into a form of energy and the transducer transforms the energy-carrying the chemical information about the sample into a useful analytical signal [10, 11]. The receptor part of chemical sensors may be based on different principles: 1) physical, where no chemical reaction takes place, 2) chemical, in which the analyte participates in a chemical reaction and 3) biochemical, in which a biochemical process becomes the source of energy [10].

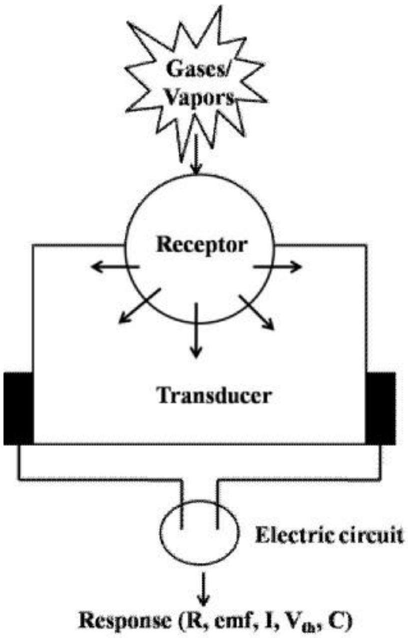

Figure 1.1. Gas sensor composed of a receptor and a transducer [11]. R = resistance, emf = electromotive force, I = current, V_{th} = threshold voltage (FET), C = capacitance.

Chemical sensor technologies based on electrochemical, optical, electrical, mass-selective and thermometric principles have been demonstrated [2, 10, 12]. The IUPAC classification of chemical sensors based on the operating principle is listed in Table 1.2 [10]. Among them, chemiresistive gas sensors using semiconducting metal oxides (SMOs) are the most attractive due to the ease of fabrication, low power consumption, simple operation, low production cost and amenable for miniaturization for the development of arrays [1, 13, 14].

The specifications of an ideal gas sensor are high sensitivity, reasonable selectivity, measurable signal output at specified gas concentration, fast response and recovery times, consistency and reproducibility, unaffected by the fluctuations in temperature and humidity, resistant to contamination and poisoning, low energy consumption and suitable for continuous operations [2, 11, 15]. However, sensing devices fulfilling all the requirements are not available in the sensor market today in spite of the advances made over the decades. Moreover, each type of sensor has its own advantages and disadvantages. Therefore, a review of the merits and demerits of each technique is necessary for deciding the right technology for the intended application. Table 1.2 provides the information on different types of chemical sensors commonly employed [2, 16, 17].

Table 1.2. Classification of chemical sensors based on the operating principle, their advantages and disadvantages

S. No.	**Classification of chemical sensor**	**Operating principle**	**Advantages**	**Disadvantages**
1	Electrochemical	Changes in potential, current, capacitance.	Ambient temperature of operation, sensitive to a wide range of gases and VOCs with very low concentrations.	Bulky, limited temperature range of operation, limited sensitivity to low molecular weight gases, not suitable for combustible gases.
2	Optical	Changes in absorbance, emission, reflectance, scattering of light.	Operates in the absence of oxygen, immune to electromagnetic interference, wide monitoring area, multi-parameter detection capabilities,	Ambient light interference, complexity of the detection system, expensive optics and electrical components.

			suitable for inaccessible area.	
3	Electrical	Changes in conductivity of metal oxides/organic semiconductors, electric permittivity, electrolytic conductivity.	Small size, easy to integrate into measurement circuitry, fast response and recovery time, high sensitivity.	Poisoning with sulfur gas, sensitive to humidity, poor precision, cross-sensitivity.
4	Mass-selective	Changes in the mass, propagation velocity, frequency, amplitude.	High sensitivity, fast response, diverse sensing materials, small size.	Relatively poor signal to noise performance, complex circuitry, unsatisfactory reproducibility, mass resolution.
5	Thermometric	Measurement of heat changes accompanying the specific chemical interaction.	High sensitivity, fast response, robustness in a hazardous environment.	Sensitive to humidity, complex supporting software and instrument, short lifetime, sensitive only to oxygen and VOCs.

1.3. Desirable characteristics and interpretation of sensor signal

Independent of the transduction function of the technology utilized for gas sensing applications, all sensors should exhibit a sharp change in some fundamental properties that make them useful for practical applications. A typical response pattern of chemiresistive sensor towards a reducing gas is illustrated in Figure 1.2.

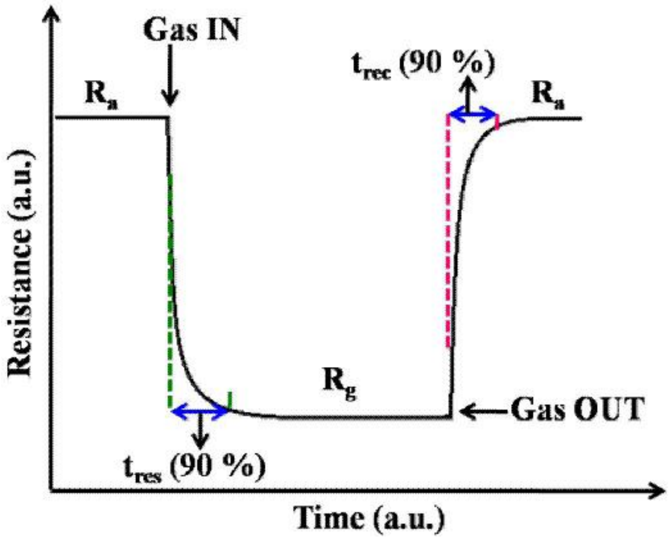

Figure 1.2. The typical response pattern of chemiresistive sensor towards a reducing gas

The performance of a gas sensor can be evaluated by considering several parameters [18, 19] and most important are listed below:

1. Response (R): Change in signal per unit concentration of the analyte, i.e. the slope of a calibration graph (called sensitivity). It can be represented in two ways as shown in Equations 1.1 and 1.2:

$$\textbf{Response (\%)} = \left(\frac{|R_a - R_g|}{R_a}\right) \times 100 = \frac{\Delta R}{R} \times 100 \tag{1.1}$$

$$\textbf{Response} = \left(\frac{R_a}{R_g}\right) \tag{1.2}$$

where “R_a & R_g” are the resistance of the receptor material in air and the presence of an analyte respectively. Response defined by Equation 1.1 is employed whenever the ‘ΔR’ of the sensor is high. When ‘ΔR’ exhibited by the sensor is low, the response defined by Equation 1.2 is used.

2. Selectivity: An expression of whether a sensor responds selectively to a group of analytes or specifically to a single analyte. The selectivity of a material to a particular analyte among other analytes is defined as:

$$\textbf{Selectivity} = \frac{\textbf{Sensitivity towards the desired analyte}}{\textbf{Sensitivity of the sensor towards the interfering analyte}} \qquad \textbf{(1.3)}$$

3. Response time (t_{res}): Time required to respond from zero concentration to a specified concentration in the step-like pattern. It is specified as the relative change in the signal to a set value. For example, the value of t_{90} represents the time necessary to reach 90 percent of the full-scale output shown in Figure 1.2.

4. Recovery time (t_{rec}): Time interval over which the sensor signal retraces to 90 percent of the baseline value in clean air after exposure to the full-scale concentration of the gas (Figure 1.2).

5. Detection and quantification limit: Lowest concentration which can be detected and quantified by the sensor under specified operating conditions. The limit of detection (LOD) is defined as the smallest amount of concentartion of analyte in the sample that can be reliably distinguished from zero and calculated using the following formula [20]:

$$\textbf{Limit of detection (LOD)} = 3\left(\frac{\textbf{rms}_{\textbf{noise}}}{\textbf{slope}}\right) \qquad \textbf{(1.4)}$$

The limit of quantification (LOQ) is defined as the lowest amount of analyte in a sample, which can be quantitatively determined with suitable precision and accuracy and is given by the formula [20]:

$$\textbf{Limit of quantification (LOQ)} = 10\left(\frac{\textbf{rms}_{\textbf{noise}}}{\textbf{slope}}\right) \qquad \textbf{(1.5)}$$

where rms_{noise} is the sensor noise, which can be calculated using the variation in the gas response at baseline using the root mean square deviation and slope is the slope value of the linear curve-fitting of gas response (R) versus gas concentration (ppm).

6. Linearity: The relative deviation of an experimentally determined calibration graph from an ideal straight line. Usually, values for linearity are specified for a definite concentration range.

7. Resolution: The lowest concentration difference which can be distinguished when the composition is varied.

8. Stability: Performance of the device for a specified interval of time without any drifts in the baseline due to changes in the ambient conditions across the day.

9. Dynamic range: The concentration range between the lower and upper limits of detection.

10. Hysteresis: The maximum difference in output when the value is sunjected to a systematic increase and decrease in analyte concentration. It is given as a percentage of full-scale output.

11. Life cycle: The length of time over which the sensor will operate. The maximum storage time (shelf life) must be distinguished from the maximum operating life. The latter can be specified either for continuous operation or repeated on-off cycles.

1.4. Requirement of chemical sensors in the nuclear industry

For nuclear industry (nuclear reactors, spent fuel reprocessing plants, spent fuel storage areas, etc.), sensors are essential to ensure the safe running of the reactors and plants. The structural components of the reactor produce different types of corrosion products with time due to the high heat energy produced during the fission process. Even though the reactor is designed and constructed with structural materials which have undergone stringent quality control tests, structural material failures can lead to accidents. To avoid these types of accidents, different types of sensors are being used for continuous monitoring to detect any coolant leaks or steam leaks in FBRs at their inception [21-23]. Lists of analytes that require monitoring at different nuclear areas are given in Table 1.3.

Table 1.3. Lists of analytes required monitoring at different nuclear areas

Nuclear industry	Monitoring area	Analyte of interest
Waste management	Spent fuel storage area	Hydrogen
Pressurized heavy water reactor (PHWR)	Integrity of pressure tube	Hydrogen, Iodine
Fast breeder reactor (FBR)	Steam leak	Hydrogen in argon
Fuel reprocessing plant	Off gas vault area	NO, NO_2, H_2, hydrazine, ammonia
Heavy water production plant	Storage and plant ambience	H_2, NH_3, and H_2S
Waste management	Acid killing	Formaldehyde (HCHO)
Fast breeder reactor (FBR)	Coolant (sodium) purity	Oxygen and carbon
Fuel storage facilities	Fuel storage area	Ammonia in argon
Fuel reprocessing plant	Pyro-reprocessing area	Cl_2, Cadmium vapours

Thesis outlines some of these issues listed above. Reliable devices for detecting hydrogen from trace to percentage levels at harsh industrial ambient under highly humid conditions for specific applications in the nuclear industries are very expensive and are not available. Most of the commercial chemical sensors have a narrow working range with a relatively short life span for operations in harsh ambient and exhibit continuous baseline drifts under humid conditions enforcing frequent calibrations. To be specific, in nuclear fuel reprocessing industry, H_2 has to be monitored in the presence of NO_x, highly corrosive gas and in high humidity and both of which can potentially interfere with the H_2 sensing process. Similarly, development of the ammonia sensor for inert ambient to track the hydrolysis of uranium nitrides in low levels of moisture by monitoring the ammonia release.

1.5. Mechanism of gas detection

The gas sensing mechanism of semiconducting metal oxides are of two types. The first one deals with the involvement of chemisorbed oxygen on their surface whereas the second deals with the involvement of lattice oxide ions. In the former case, the analyte gas interacts directly with the chemisorbed oxygen whereas in the latter case, the analyte gas interacts with the lattice oxygen causing changes in oxygen non-stoichiometry. Based on the conduction type, the metal oxide/sulphide semiconductors can be divided into n- and p-type, which exhibited different sensing behaviors to the same detecting gas. The sensing mechanism based on n-type semiconducting metal-oxide is described below.

1.5.1. Chemisorbed oxygen mediated gas sensing

Metal oxides used for gas sensing are wide-bandgap semiconductors exhibiting non-stoichiometry in oxygen (eg. $SnO_{2-\delta}$, $In_2O_{3-\delta}$, etc.) which in turn introduces the donor levels near the conduction band [24]. The n-type property shown by these oxides is due to the existence of oxygen vacancies $(V_O^{\bullet\bullet})$ which in turn introduce electrons in the donor levels. Abrupt termination of atomic periodicity leaves unsatisfied valence states of metal ions on the surface. Upon exposure to an oxygen containing environment, oxygen first physisorbs on the oxide surface and then chemisorbs. Different forms of oxygen species viz., O_2^-, O^- and O^{2-} are known to exist on the surface and the relative fraction of the each of the species is determined by the temperature of the surface. One or more of species participate in the sensing action [2, 25, 26]. O_2^- is the majority of the species in the temperature range of 50 ˚C to 200 ˚C. Similarly, O^- is the major fraction in the temperature range of 200 ˚C to 400 ˚C [2, 25, 26]. At temperatures above 400 ˚C, O^{2-} ion dominates [25]. The surface adsorbed oxygen on an n-type oxide acts as a surface trap for electrons from the bulk and becomes charged adsorbates which in turn lead to a decrease in conductivity. Since these electrons come from ionized donors via the conduction band, the charge (electron) carrier concentration of the semiconductor is reduced. In the case of p-type oxides, the adsorbed oxygen abstracts electrons from the valence band resulting in an increase of the charge (hole) carrier concentration and conductivity.

When the surface coverage of the adsorbed species increases, more and more electrons of the bulk will be transferred to the surface and get trapped by the surface adsorbed species. This constitutes a space charge layer near the surface at equilibrium with an electric field operating across the layer which resists the transfer of the electrons from the bulk to the surface. When the grains are interconnected, a potential barrier V_s develops across the grain boundaries as shown in Figure 1.3 (a) [27]. A change in charge carrier concentrations of the metal oxide was observed which is reflected in conductivity during sensing (Figure 1.3 (b)).

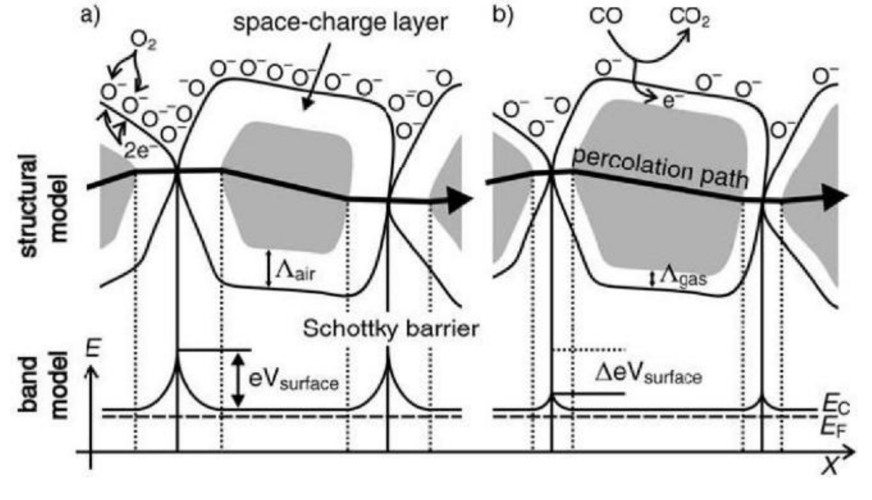

Figure 1.3. Structural and band models for the intergranular percolation path of an electron in n-type SMOs **(a)** in clean air and **(b)** air containing CO [27].

In case of an n-type oxide, the width of the charge depleted region or the space charge region of the grain is given by:

$$\mathbf{L_D = \sqrt{\frac{\varepsilon k_B T}{e^2 n}}} \qquad \textbf{(1.4)}$$

where L_D, k_B, $\mathcal{E}$, T, e and n are Debye length, Boltzmann constant, permittivity of the material, temperature, the charge of an electron and charge carrier concentration of the material respectively. The charge carriers must overcome a surface potential barrier V_s, called the Schottky barrier to cross the boundary between the grains. An equation relating the conductance (G) and the Schottky barrier (V_s) at temperature (T) is given by:

$$\mathbf{G = G_o exp\left(\frac{-eV_s}{k_B T}\right)} \qquad \textbf{(1.5)}$$

where G_o is the proportionality constant. During the gas sensing, the analyte reacts with some of the chemisorbed oxide ions resulting in the release of surface trapped carriers which in turn reduces the potential barrier across the grains in accordance with Equation 1.5 which is reflected in conductivity [27].

For a chemical reaction to occur, not only thermodynamics but also the kinetics of the process play an important role. The sequences of steps that occur during the sensing action of SMOs are presented as follows:

(i) Physisorption of oxygen on vacant active sites [S( )] on the surface:

$$\mathbf{S(\,) + O_2(gas) \xrightarrow{k_1} S(O_2) + \Delta H_1} \qquad \textbf{(1.6)}$$

Here, ΔH_1 is the enthalpy of physisorption of oxygen which is an exothermic process. For oxygen adsorption to occur, the heat of physisorption should be greater than the thermal energy (> k_BT). The surface coverage of the adsorbed species is governed by the activation energy of adsorption and the temperature.

(ii) Electron capture by the physisorbed oxygen:

Being highly electronegative, physisorbed oxygen captures the electron from the conduction band of the oxide and converts to chemisorbed oxygen ion:

$$\mathbf{S(O_2) + e^-(CB) \xrightarrow{k_2} S(O_2^-) + \Delta H_2} \qquad \mathbf{(1.7)}$$

where ΔH_2 is the enthalpy of chemisorption of oxygen on the surface. Depending on the temperature, three different species of oxygen ion are observed as seen in the section 1.5.1. This step causes the buildup of a space charge region on the surface leading to the development of potential barrier across the grains which is seen by a decrease in conductivity (for n-type SMOs) due to the depletion of carrier concentration as discussed in Figure 1.3 (a).

(iii) Adsorption of reactant gas:

When the surface of the semiconductor metal oxide is exposed to a reducing analyte (R), adsorption of the analyte accompanied by a enthalpy change takes place as shown below:

$$\mathbf{S(\,) + R\,(gas) \xrightarrow{k_3} S(R) + \Delta H_3} \qquad \mathbf{(1.8)}$$

where ΔH_3 is the enthalpy of physisorption. For adsorption of R to be significant, the conditions $k_3 >> k_1$ and $\Delta H_3 \geq k_BT$ have to be satisfied.

(iv) Sensing reaction suggested to takes place between adsorbed reactant gas (R) and the chemisorbed oxygen ion as shown below:

$$\mathbf{S(O_2^-) + S(R) + \Delta H_4 \xrightarrow{k_4} S(B) + e^-(CB)} \qquad \mathbf{(1.9)}$$

This surface reaction produces the product B and releases the trapped electron back to the conduction band which inturn reduces the potential barrier across the grains as shown in Figure 1.3 (b). Here, ΔH_4 is the enthalpy change associated with the reaction. This is manifested in increase in the electrical conductivity of the sensor.

(v) Finally desorption of the product is given by the following reaction:

$$\mathbf{S(B) + \Delta H_5 \xrightarrow{k_5} S(\;)} \qquad \mathbf{(1.10)}$$

where ΔH_5 is the heat of desorption. This process restores the active site S( ) for repeating the adsorption cycle. The kinetics of desorption of the product from the surface paves the way for the regeneration of the sensor and brings the sensor back to its initial baseline.

1.5.2. Lattice oxygen mediated gas sensing

In this mechanism, oxygen from the ambient is in equilibrium with the oxide ion vacancies and gets converted to lattice oxide ions through the uptake of electrons from the bulk. These surface lattice oxide ions directly react with the reducing gas (R) resulting in the release of electrons back into the conduction band. This changes the conductivity thereby generating more oxide ion vacancies [27]. Various steps involved in the mechanism of gas sensing is given below:

$$\mathbf{V_O^{\times} \rightarrow V_O^{\bullet} + e^-} \qquad \mathbf{(1.11)}$$

$$\mathbf{2V_O^{\bullet} + O_2(gas) + 2e^- \rightarrow 2O_O^{\times}} \qquad \mathbf{(1.12)}$$

$$\mathbf{R + O_O^{\times} \rightarrow RO + V_O^{\times}} \qquad \mathbf{(1.13)}$$

Thus, the oxide ion defects controlling the conductivity of the metal oxide is exploited for gas sensing.

1.6. Strategies for improving gas sensing performance

Several factors that contribute to the sensing performance of SMO-based gas sensors need to be carefully balanced to realize the best performance. Some of them are surface area, surface catalytic activity, grain size, width of the charge depletion layer, intergranular coupling, grain boundary barrier potential, adsorption/desorption kinetics, role of crystallographic surface (lattice planes), operating temperatures, porosity, charge carrier concentration and band gap of sensing materials. This section will briefly outline the role of these factors in gas sensing.

1.6.1. Effect of morphology

The role of morphological features like grain size, porosity and geometric effects (exposed high energy crystal facets) towards gas sensing is outlined.

1.6.1.1. Grain size and intergranular coupling

Gas sensing being the surface phenomenon, the surface area of the sensing material plays a key role. Two different structures offer high specific surface area. They are grains with high degree of porousity and materials composed of nanocrystalline grains. The former is not preferred owing to diffusion controlled gas kinetics affecting the retrace adversely. Although, the second configuration geometry is preferred, issues like intergranular coupling should be addressed for efficient charge transfer across grains. The advent of nanoscience not only introduced a remarkable revolution in this field thereby offering large specific surface area, but also brought in electron confinement effects critically affecting the electrical conductivity of nanostructured thin films. A semi-quantitative model proposed by Rothschild et al. brings out the importance of grain size (D) and the width of the depletion layer (L) [28]. He considered three different situations wherein grain boundary (GB), neck and grain controlling the overall conductivity of the specimen. Case I with D>>2L, most of the crystallite volume remains unaffected by the interaction of the analyte with the surface due to low surface area to volume ratio (Figure 1.4 (a)). Relatively a less fraction of charge carriers of the bulk participate in sensing action and the contribution of the bulk carriers to overall conductivity remains high which leaves the changes in conductivity during sensing are largely due to inter-granular coupling or grain boundaries. Thus, for large grains (D>>2L) the gas sensing mechanism is controlled by the GB barriers and the sensitivity is independent of grain size (D) [28, 29].

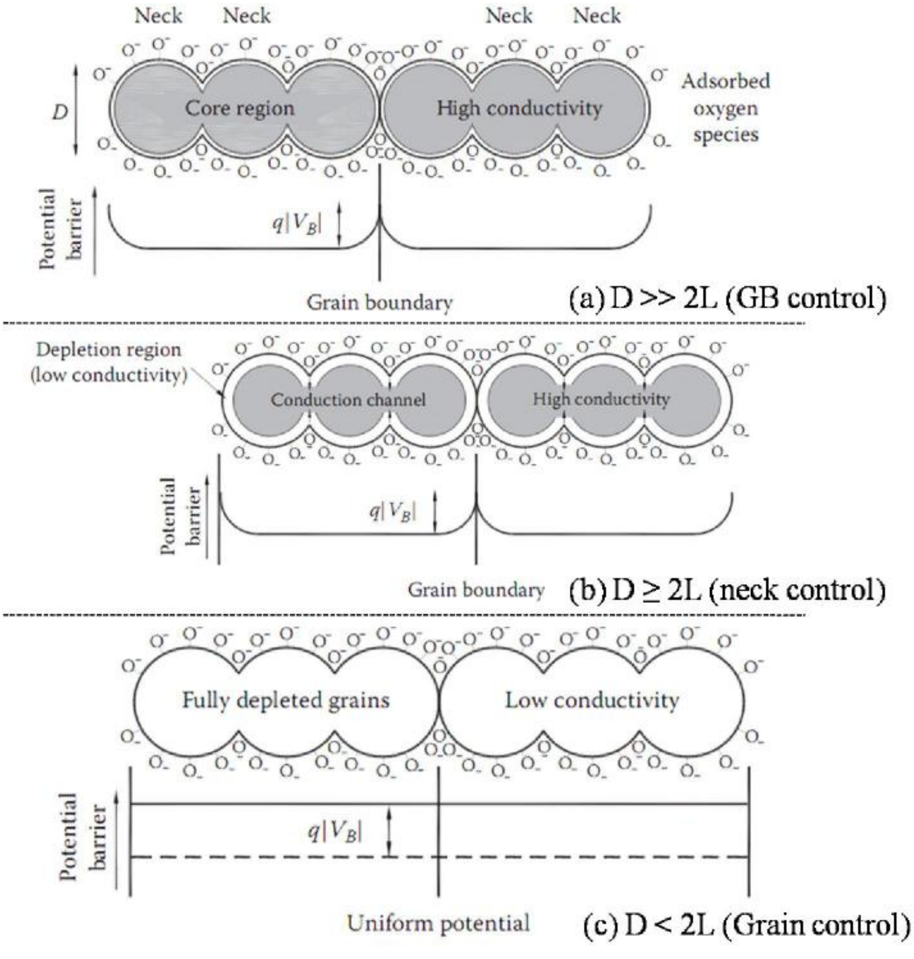

Figure 1.4. Schematic model showing the effect of crystallite size on the sensitivity of metal oxide gas sensors: **(a)** D >> 2L (grain-boundary controlled); **(b)** D ≥ 2L (neck controlled) and **(c)** D < 2L (grain controlled) [28].

In case II with D ≥ 2L, the grain size is decreased and made comparable to that of the width of the depletion layer and the latter begins to dominate forming a constricted channel for conduction as shown in Figure 1.4 (b). In this case, the conductivity depends not only on the height of the potential barrier but also on the cross-sectional area (called neck size “X”) of those channels [28, 29].

In case III with D < 2L, the grains are completely depleted of charge carriers as the depletion region extends throughout the grain as depicted in Figure 1.4 (c). Also, the conduction channels between the grains do not exist. In this case, the conductivity is grain controlled. In the presence of a specific analyte, a large modulation in the number of carriers occurs leading to high sensitivity [28, 29].

1.6.1.2. Pore size

The pore size and its distribution across the sensing material decide the utility factor of the sensor which is concerned with the effects of diffusion of the targeted analyte through the pores as well as the out-diffusion of gaseous products formed during sensing. Gas diffusion process affects the sensing properties like sensitivity, response and recovery times. Gas diffusion through a porous material consists of surface diffusion, Knudsen diffusion and molecular diffusion and their diffusion constants increase with increase in pore size [30, 31]. A high degree of gas permeability for quick diffusion of gas molecules is desirable for good response [32]. If the pore size is controlled, large molecules can be filtered allowing the smaller molecules to diffuse through the film and in such cases, the selectivity can be achieved by tuning the pore size of the material [33]. Selectivity can further be enhanced by the choice of the crystallographic facets, a phenomenon known as geometric effects.

1.6.1.3. Geometric effects

Geometric effects exploit the role of certain crystallographic planes of the lattice for promoting the specific chemical interaction of the analytes and the sensor performance. Crystallographic facets with lower packing density usually have higher energy which can facilitate surface reactivity. Crystal facets having higher surface energy and more defect sites widely exploited in the field of catalysis [34-38] is also expected to contribute to gas sensing [39-44]. Their major impact will be on gas adsorption and electron transport. High coverage of gas adsorption is mainly due to a high density of dangling bonds and unsaturated oxygen coordination [39]. The kinetics of charge transfer between the gas and high-energy crystal facet is favoured in certain planes which can significantly influence the response.

1.6.2. Effect of incorporation of dopants and additives

Various additives have been used to promote the specific catalytic chemical interaction and their choice depends on the specific analyte. A catalyst enhances the reaction rate thereby lowering the activation energy of the reaction as shown in Figure 1.5 [45]. These catalysts are either dispersed on the surface of the sensing material or incorporated into the lattice (doped). Metal oxides and sulphides impregnated with noble metals such as platinum, palladium, gold and silver have been shown to exhibit improved performance [46-53]. The superior gas sensing performance is attributed to the reduction in adsorption activation energy [51, 53], re-distribution of charge carriers forming Schottky barriers which prevent the recombination of electron-hole pairs, known as electronic sensitization [48, 52] and through spillover effect known as chemical sensitization wherein the analyte gas dissociatively adsorbs on the noble metal cluster producing active atomic species. These species then migrate to the surface of the sensor and interacts with the surface adsorbed gases [46, 47, 50].

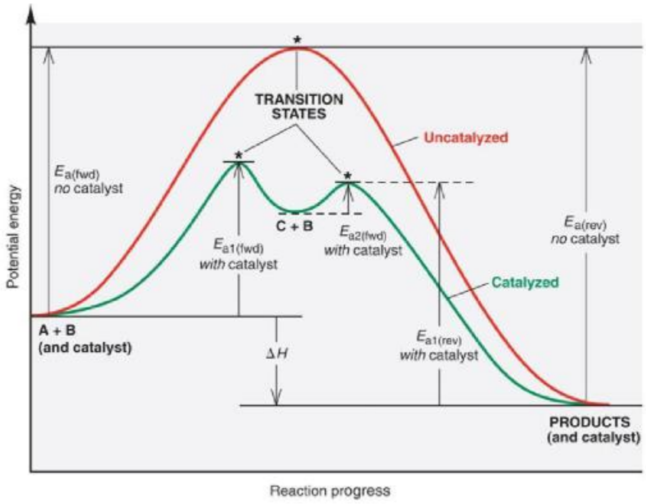

Figure 1.5. Reaction energy diagram for a catalyzed and un-catalyzed process [45]

In many cases, doping with other oxides of metals (e.g. Al, Ga, In, Sb, Bi, Cr, Fe, Ni, Cu, Zn, etc.) have also been shown to improve the gas sensitivity [54-60]. Incorporation of these metal cations into the lattice of metal oxide is reported to alter the width of the depletion layer [61]. In some cases, size, porosity and specific surface area of the sensing material are also affected by doping [55, 57].

1.6.3. Effect of heterojunctions

Hetero-junctions of two or more SMO materials have also been reported to yield improved performance [61-64]. Heterojunctions can be roughly divided into p–n junctions, n–n junctions and p–p junctions, depending on the SMOs that are combined with each other.Variations in electron depletion layers, and band structure of the heterojunctions have significantly improved the response. To maintain the balance in the system, the movement of electrons or holes occurs, so the amount of change in the electrical signal is amplified [61, 63].

1.6.4. Effect of temperature

Gas sensing being a chemical reaction, the rate of the reaction can be controlled by temperature. The effect of temperature on rate constant (k) is closely related to the activation energy (E_a) of a reaction, an energy threshold that the colliding molecules must exceed to react. Collision energy and collision frequency change with temperature. The effect of temperature on collision frequency is minor whereas its effect on collision energy is major. At a given temperature, the fraction "*f*" of collisions with energy equal to or greater than E_a is given by:

$$f = \exp\left(\frac{-E_a}{RT}\right) \tag{1.16}$$

where T is the temperature and R is the universal gas constant. This equation shows that an increase in T increases the fraction of collisions"*f*" as depicted in Figure 1.6 [45].

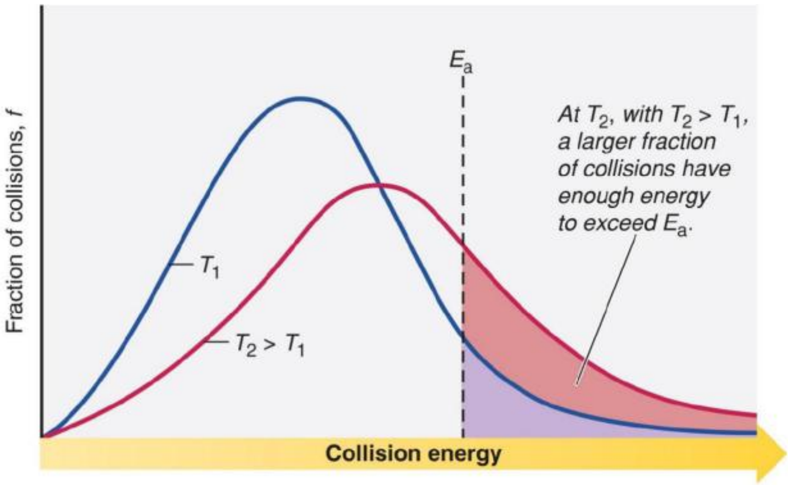

Figure 1.6. The effect of temperature on the distribution of collision energies [45]

Just as other chemical reactions, gas sensing reactions are also influenced by the operating temperature. In a typical case, the sensitivity increases gradually with an increase in temperature and reaches a maximum value at a specific temperature and thereafter it falls as seen from Figure 1.7. At low operating temperatures, the rates of the reactions between the chemisorbed oxygen / lattice oxide ions and the adsorbed analytes are slow which is reflected by a poor response which increases with the increase in temperature. Generally, selectivity towards the specific analyte depends on the activation energy of the sensing reaction. The choice of temperature to discriminate the analytes is very useful in achieving the selectivity in addition to catalysts and additives if other interfering gases have different activation energies [61, 65, 66]. The same way, with an increase in temperature, the desorption rate of the products formed on the surface also increases leading to a quick restoration of the sensor [67]. At the same time, surface coverage of the adsorbed is significantly reduced at higher temperatures which triggers the desorption of the adsorbed species. This reduces the sensitivity at high temperatures. While reactivity and adsorption processes can have a large impact on sensor performance, it is the synergistic relationship between the surface and conduction processes that ultimately control the response [61]. The shape, size, structures, dopants and additives are the important parameters to be considered during material selection.

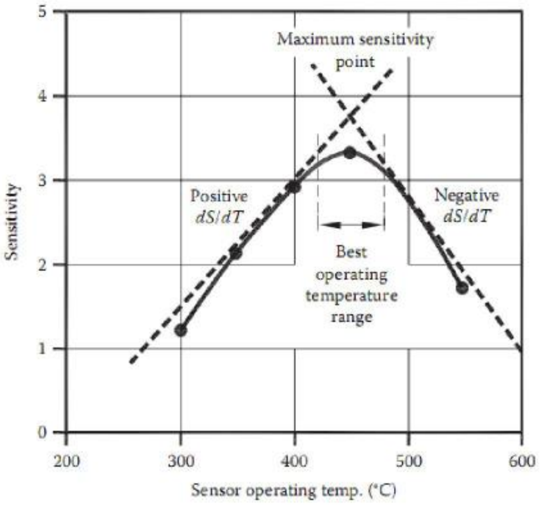

Figure 1.7. Response of SnO_2 sensor towards 100 ppm of CH_4 in dry air as a function of operating temperature

1.6.5. Effect of film thickness

At present three configurations are adopted in the gas sensor development which includes porous bodies composed of nanocrystals, thick films preferably composed of nanocrystalline grains and nanostructured thin films [68]. For porous structures and thick film sensors, process parameters have greater control over thickness by virtue of controlling the size of the grains. However, for porous structures and thick films composed of nanocrystalline grains with a size comparable of electron correlation distances, quantum effects will dominate. In case of thin films with average grain size greater than the electron correlation distances,both the grain size and thickness directly affect the response patterns. Gas diffusions across the film during sensing and recovery are thickness controlled [69]. Thinner films minimizes the effect of diffusion-controlled processes as the sensing reaction is enforced on the surface which favours relatively short response and retrace times [30]. In addition, as the thin films configured directly to map the surface reaction in terms of the surface conductivity, it produces high response even for trace levels of analytes as the bulk contribution to conductivity is minimized. Moreover, thick films prepared from the nanocrystalline powders have to be heat treated at elevated temperatures for necessary adhesion during which grain growth occurs. This problem is circumvented by depositing nanostructured thin films directly under in-situ conditions well above the highest operating temperature of the sensor [69].

1.7. Literature review and selection of materials for gas sensing

1.7.1. Literature review on semiconducting oxides and sulphides based gas sensor

The first report on semiconductor – gas interactions was reported in the 1930s by L. J. Edgar on CuS thin films [70] which was investigated in detail by Dowden [71] and Weisz [72] in 1950s. The voltage modulation observed on semiconductor caused by the adsorbed gas was termed as an electro-adsorptive effect by Wolkeinstein [73]. In 1953, Brattain, et al. observed that the resistance of germanium (Ge) changes with the changes in the surrounding ambient [74]. Subsequently, Heiland found that the electrical conductivity of zinc oxide (ZnO) was sensitive to the variations in the surrounding atmosphere in 1954 [75]. Later, in 1962, Seiyama, et al. showed that when ZnO heated up to 300 ˚C, exhibited sharp changes in resistance even for the trace levels of certain gases present in air [26]. In 1967, Shaver demonstrated that the addition of noble metal (Au, Ag, Pd, etc.) improves the gas sensing properties of semiconducting metal oxides [76]. It was in 1970s, the world's first chemiresistive commercial gas sensor based on SnO_2 was developed by Taguchi [77]. Since then, a race to work with different semiconducting metal oxides began and eventually became a thrust area of research. Large number of binary metal oxides such as SnO_2, In_2O_3, MoO_3, ZnO, TiO_2, CuO, NiO, Cr_2O_3, etc., has been surveyed by a number of research groups across the globe for different gases and the gas sensing properties have been documented. Recently, the choice of materials was extended to include ternary and quaternary compounds such as perovskites (ABO_3), delafossites (ABO_2), spinels (AB_2O_4), pyrochlores ($A_2B_2O_7$), heterometallates ($A_nXM_{12}O_{40}$, n = 3-4, X = P, Si or As, M = W or Mo), etc. Development of chemical sensors array along with multi-variable data management tools such as pattern recognition, artificial neural networks, etc. have gained significance in recent times. However, in spite of the advances in SMO, challenges still remain for using them for any specific application.

1.7.2. Selection of materials for the intended applications

The growing concern about the rise in gaseous pollutants in domestic and industrial environments became a driving force to search for new materials with high specificity. Conventional semiconducting oxide based sensors lack specificity towards a particular analyte and their baseline drift in highly humid conditions. Even though the choice of materials for gas sensing applications is enormous, applications demand stringent conditions on material selection. A sensor should have high sensitivity in the desired operating range, high selectivity, quick response and fast recovery characteristics with a high degree of repeatability. It should not have baseline drifts with time in the presence of humidity or other interfering gases. Therefore, material selection plays a vital role in the development of the gas sensors.

Adsorption capability, physical properties, catalytic activity, thermodynamic stability, crystallographic structure, chemical compatibility of the sensing material, the kinetics of interaction and geometrical configuration are some of the general properties which determine the choice of material. In addition to the above, factors like bandgap and type of carriers, also have their impact on the sensor's performance. Even though large number of materials fulfil many of the above-listed criteria, only a few are promising candidates. For practical applications, the sensor should possess long term stability in the working ambient with high degree of reversibility of interaction with the analyte at the chosen working temperature. Effect of humidity on long term performance, baseline drifts, frequent calibrations, decrease in active sites due to poisoning, structural and phase transformations during the period of operation are some of the challenges driving the search for advanced materials. This thesis outlines some of the issues specific to certain industrial processes requiring rugged and reliable sensors that operate under harsh, humid and inert ambient.

1.7.2.1. Silver indium oxide ($AgInO_2$)

Nuclear fuel reprocessing industry requires rugged and reliable devices that can operate in radioactive ambient for detecting hydrogen generated from radiolysis of H_2O. Concentration of hydrogen released during the process may vary from ppm to percentage levels and needs to be monitored under highly humid conditions in the presence of highly toxic and corrosive NO_x gas as well as hydrocarbons. Most of the sensing materials fail to operate in the presence of even trace levels of highly reactive NO_x ambient which causes gradual degradation in the performance of the sensor. Thus, the choice of new materials that withstand NO_x environment is highly constrained by limited options. Sensors for this specific application are either very expensive or not available forcing us to look out for new materials resistant to NO_x attack. Most of the commercial chemical hydrogen sensors have a narrow working range with relatively a short life for this type of harsh ambient enforcing frequent calibrations due to continuous baseline drifts and therefore, they cannot be employed. Although the search for mixed semiconducting binary oxides is currently in progress, the scope of expanding the search domain to include ternary and quaternary semiconducting oxides is also considered. Based on broad empirical guidelines, wide bandgap transparent conducting (TCOs) delafossites drew our attention to check their suitability as many of them fulfil the empirical guidelines [78-82]. Predicted to be promising materials for various technological applications, the initial drive failed to sustain the enthusiasm across the globe is largely attributed to the obstacles faced during their synthesis in pure form as most of them form at high pressures. For continuous operations under highly humid ambient, semiconductors that form under high hydrothermal pressures will be the natural choice to begin our investigation as they are expected to be resistant to any moisture/steam attack. Incidentally $AgInO_2$, semiconducting delafossite reported to stabilize at a hydrothermal pressure becomes our natural choice [78, 83].

$AgInO_2$ is an n-type semiconducting oxide [84] belongs to delafossite family represented by the general formula ABO_2 (A = Cu, Ag, Pt, Pd etc., B = Al, In, Fe, Ga etc.). The layered delafossite ($A^{+1}B^{+3}O_2$) structure consists of monovalent A-site cations and trivalent B-site cations. This structure consists of linearly co-ordinated A-cations linking the BO_2 layers along c-axis. The BO_2 layers consist of BO_6 octahedra, sharing edges as shown in Figure 1.8. Furthermore, each oxygen is coordinated by four cations (one A^+ and three B^{3+}) in a pseudo-tetrahedral arrangement. Depending on the stacking of layers (close-packed A cations and BO_6 octahedra), two polytypes are possible [85]. The 3R-polytype consists of "AaBbCcAaBbCc" stacking along the c-axis and has rhombohedral symmetry with the space group $R\bar{3}m$, whereas the 2H-polytype consists of an alternate "AaBbAaBb" stacking sequence in the $P6_3/mmc$ space group. The presence of BO_2 layers in the delafossite structure is especially important for the design of n-type conductivity. In the BO_2 layer, B-cations occupy octahedral sites and the octahedra share edges. Consequently, the distance between two neighboring B-cations in the same layer is short and there are no intervening oxygen atoms on the line connecting the two cations. Combination of appropriate A and B cations in this structure determines whether the delafossite phase is a p-type or n-type semiconductor. The fascinating structure features exhibited by this new class of delafossite compounds and the choice of combination of A and B site cations make them potentially rich with properties useful for applications in transparent electrodes, pn-junction, solar cells, photocatalysts and light-emitting devices [86, 87].

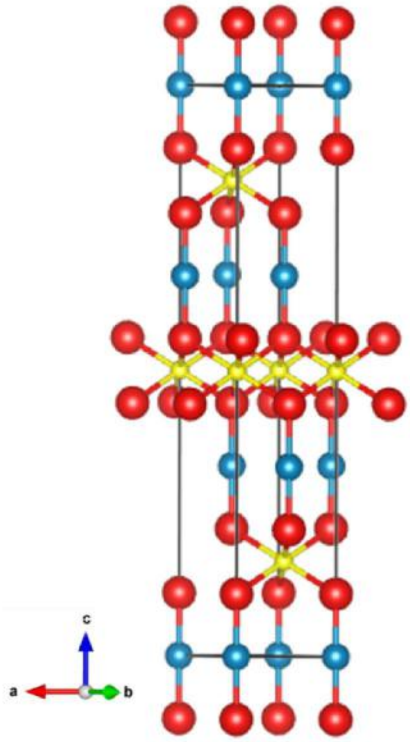

Figure 1.8. Crystal structure of $AgInO_2$ rhombohedral symmetry (blue, yellow & red balls indicate Ag, In & O respectively)

$AgInO_2$ has been reported to stabilize under high pressure (3000 atm) and temperature (500 ˚C – 700 ˚C) for 24 h [88] which was further refined by Jansen et al. to 2000 atm and 580 ˚C for 96 h [86]. Claims of pure phase employing ion-exchange reactions with KNO_3 as an oxidizing flux with 50 % excess $AgNO_3$ followed by a post-synthesis removal of excess nitrates using water were made but the reproducibility of the latter results by other laboratories has not yet been successful as trace amount of metallic Ag was always present [89]. In 2003, Shahriari and co-workers adopted a single-step hydrothermal route under 10 atm and claimed a significant improvement to the purity of $AgInO_2$ but the final product still had metallic Ag impurity [90]. These reports along with their findings indicate that the phase pure $AgInO_2$ is always elusive. A recent publication in 2019 on silver delafossites by Zwiener et al. mentioned the limited solubility of starting materials that resulted in secondary phases [91]. Thereafter, no reports are available on the synthesis of $AgInO_2$ which almost concludes that the presence of trace amounts of metallic silver in the product is inevitable and prevents the evaluation of the physical properties of pure $AgInO_2$ with reasonable accuracy.

First part of the thesis (Chapter 3 to 5) addresses the issues related to its synthesis and based on the chemistry of the reactants, a modified hydrothermal route is employed to stabilize the impurity-free phase pure $AgInO_2$ for the first time. The nanoplates of $AgInO_2$ are then configured as thick films using screen printing method and thin films using PLD and investigated for hydrogen sensing at different humidity levels for the first time.

1.7.2.2. Lead sulphide (PbS)

The second part of the thesis (Chapter 6) is focused on the development of ammonia sensor for operations in inert ambient to track the moisture leaks as the hydrolysis of uranium nitrides stored in fuel storage facilities generates ammonia [92]. Sensors based on semiconductor oxides cannot be deployed for inert streams as they require oxygen for operation. This prompted us to shift our focus on non-oxide based semiconductors. Hardly few non-oxide materials have been investigated for gas sensing. In this context, PbS, a p-type semiconducting chalcogenide, drew our attention. Not only its Lewis acidic character is attractive for adsorption of ammonia, a lewis base but also having valence band of PbS made up of Pb 5d/6p making it suitable for interaction.

Lead sulfide (PbS), a semiconducting chalcogenide, is of great importance from both fundamental as well as technological applications point of view due to the size-tunable direct bandgap [93-95]. The quantum confinement in nanosized structure causes a shift in the absorption wavelength from infrared to the visible region [96] which envisages a variety of electronic and optoelectronic applications. PbS is an extremely promising material for infrared detection [97, 98], photovoltaics & solar cells [99, 100], light-emitting devices [101] and sensing [102]. The crystal structure of PbS (Figure 1.9) corresponds to a cubic system with the space group of $Fm\bar{3}m$. The basis of a PbS unit cell contains eight atoms: four Pb atoms in positions 4(a) with the coordinates (0 0 0), (½ ½ 0), (½ 0 ½), and (0 ½ ½) and four S atoms in positions 4(b) with the coordinates (½ ½ ½), (0 0 ½), (0 ½ 0), and (½ 0 0); The lattice constant 'a' of the PbS is 0.5940 nm and the radii of Pb^{2+} and S^{2-} ions are 0.121 and 0.184 nm, respectively.

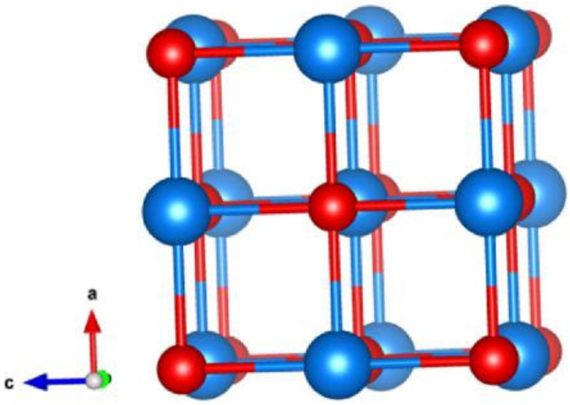

Figure 1.9. Crystal structure of PbS Cubic system (red & blue balls indicate Pb & S respectively)

In this work, the ammonia sensing characteristics of PLD made thin films of PbS in inert ambient is addressed for the first time along with its sensing mechanism to track the hydrolysis of uranium nitrides in low levels of moisture.

Among the various methods reported for deposition of thin films, electrochemical deposition, chemical vapor deposition (CVD), Atomic layer deposition (ALD) and successive ionic layer adsorption and reaction (SILAR) are the leading techniques and each one has its merits and demerits. CVD and ALD films are fairly uniform but these techniques use hazardous, toxic and corrosive precursor gases. While sulphide based films produced by electrochemical deposition and SILAR methods contain oxide impurities with poor adhesion. Further, the aforementioned methods require post-annealing at high temperature which not only degrades the quality but also increases the interfacial interactions.

Laser ablation is an appropriate method in the synthesis of functional materials with controlled composition, morphology and grain size. These are the parameters which the gas detection sensitivity of semiconducting materials depend. Pulsed laser deposition (PLD) has been demonstrated as a thin film deposition method due to its non-equilibrium, stoichiometrically maintained depositions of multi-component materials that can be difficult to fabricate using other deposition techniques. The energy source (laser) is outside the vacuum chamber which, in contrast to vacuum-installed devices, provides a much greater degree of flexibility in materials use, geometrical arrangements and offers larger play in in-situ pressures up to 1 mbar. Due to higher energetic laser-ablated species, it also offers high-quality films even at lower temperatures. Moreover, the implementation of lower growth temperatures avoids the introduction of additional residual thermal strain occurs between the film and substrate. The extreme non-equilibrium prevails during the growth of film under pulsed plume with high kinetic energies and deposition at high partial pressures of the background gas makes it ideal to explore the deposition of oxide and non-oxide compounds.

1.8. Objectives and scope of the thesis

The objectives of the present work are intended to develop a rugged and reliable wide range hydrogen sensor that operates in the presence of trace levels of NOx and hydrocarbons under harsh and humid ambient and NH_3 sensors for operations in inert ambient. The thesis is focused on optimization of process parameters of the hydrothermal method for the high-pressure stable $AgInO_2$, investigation on gas sensor studies on thick films of $AgInO_2$, optimization of deposition parameters of PLD (KrF: λ = 248 nm) for producing high-quality thin films of $AgInO_2$ and investigations on its gas sensing performance. For the development of ammonia sensor for operations in inert streams, PbS is chosen and the deposition parameters of PLD have been optimized for the growth of nanostructured thin films of PbS.

The ammonia sensing properties of PbS thin films are presented. The scope of the thesis includes:

1. Hydrothermal synthesis of phase pure silver indium oxide ($AgInO_2$) – A parametric optimization using a factorial design approach
2. Wide range hydrogen sensing behavior of thick films of $AgInO_2$: Performance towards long term stability, repeatability and selectivity and the mechanism of sensing probed by XPS
3. Deposition of thin films of $AgInO_2$ using PLD, its sensing characteristics towards H_2, NO_x, LPG (hydrocarbons), CH_4, HCHO & NH_3 and mechanism of sensing probed by in-situ Hall studies
4. Highly selective PbS thin film based ammonia sensor for inert ambient. Mechanism of gas sensing probed by in-situ Hall studies and XPS studies.

CHAPTER 2

Materials and Experimental Methods

This chapter provides an overview of preparation methods adopted for the synthesis of materials selected for investigation. As the sensors are configured as thick or thin films, screen printing technique for prepration of thick films and pulsed laser deposition (PLD) technique for growth of thin films are discussed. This chapter elaborates the principles of various characterization techniques employed for structural, morphological, chemical, optical and electrical investigation. This chapter also discusses the experimental facilities developed for carrying out gas sensing studies.

2.1. Materials investigated

Table 2.1 presents the list of materials taken up for investigation of gas sensing properties. The details of the starting precursor materials, their purity, methods employed for the synthesis are included.

Table 2.1. Summary of materials investigated in this thesis, precursors with corresponding suppliers, synthesis methods and associated chapter number within which the material has been investigated

S.No.	Material	Precursors and suppliers with purity	Synthesis method	Chapter No.
1	$AgInO_2$	Silver nitrate ($AgNO_3$, 99.9%, Loba-Chemie) and Indium metal (In, 99.99%, Alfa Aesar)	Hydrothermal synthesis	3, 4 & 5
2	PbS	Thiourea ($SC(NH_2)_2$, 99.5%, Merck) and lead acetate ($Pb(CH_3COO)_2$, 99.9%, Merck)	Co-precipitation method	6

2.2. Preparation techniques

2.2.1. Synthesis of nanomaterials

Large number of synthetic routes are available to prepare nanomaterials in the form of powders, tubes, rods, wires, thin films, etc. They can be divided into three groups namely physical methods, chemical methods and bio-assisted methods and among these, chemical methods are widely used for the preparation of nanocrystalline powders [103, 104]. Chemical methods offer the possibility of low to high temperatures for synthesis, high degree of homogeneity, preparation of large quantities, controlled size and shape and so on. The commonly adopted chemical routes include co-precipitation, sol-gel, micro-emulsion, hydrothermal, combustion synthesis, polyol synthesis, sonochemical synthesis, microwave-assisted synthesis, etc. [103]. The present thesis brings out the importance of hydrothermal method for $AgInO_2$ and co-precipitation method for PbS for the synthesis of nanomaterials.

2.2.1.1. Hydrothermal synthesis

The term “hydrothermal” was first used by a British Geologist, Sir Roderick Murchison (1792-1871) to describe the action of water at elevated temperature and pressure leading to the changes in the earth’s crust resulting in the formation of various minerals [103, 105-108]. In this technique, the chemical precursors dissolved in water/organic solvents are placed in a specially designed stainless steel vessel called an “autoclave” to withstand high temperatures (100 ˚C – 1000 ˚C) and pressures (1 MPa - 100 MPa). The hydrothermal reaction which takes place among the complex-ions yields the product [103, 106, 107].

The main requirement is that the minimum solubility of the constituents in water/solvents should be in the range of 2 % - 5% [108] and to promote that the pH of the medium will be suitably changed by the addition of appropriate base or acid. These substances are known as “mineralizers”. In terms of reaction temperature, hydrothermal synthesis can be classified into subcritical and supercritical reactions. Hydrothermal synthesis taking place in the temperature range of 100 ˚C - 250 ˚C are termed as subcritical reactions whereas the synthesis taking place beyond 250 ˚C up to 1000 ˚C and at 0.3 GPa are termed as supercritical reactions [107]. The pressure and temperature of the water during hydrothermal conditions depend on the volume fraction of water as shown in Figure 2.1. For an effective hydrothermal experiment, the degree of fill is usually between 50 % and 80% [108].

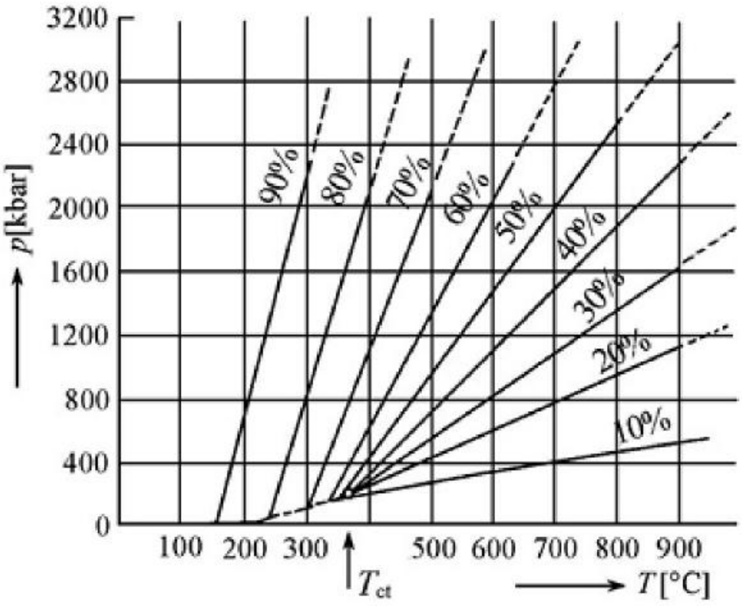

Figure 2.1. Pressure and temperature correlation of water concerning the degree of fill of the sealed hydrothermal reactor **[108]**.

The schematic diagram of the home built hydrothermal vessel is shown in Figure 2.2. The design contains a stainless steel autoclave provided with a Teflon liner which can withstand a temperature of ~ 250 ˚C. $AgInO_2$ is prepared by this method. A detailed synthesis procedure is given in Chapter 3.

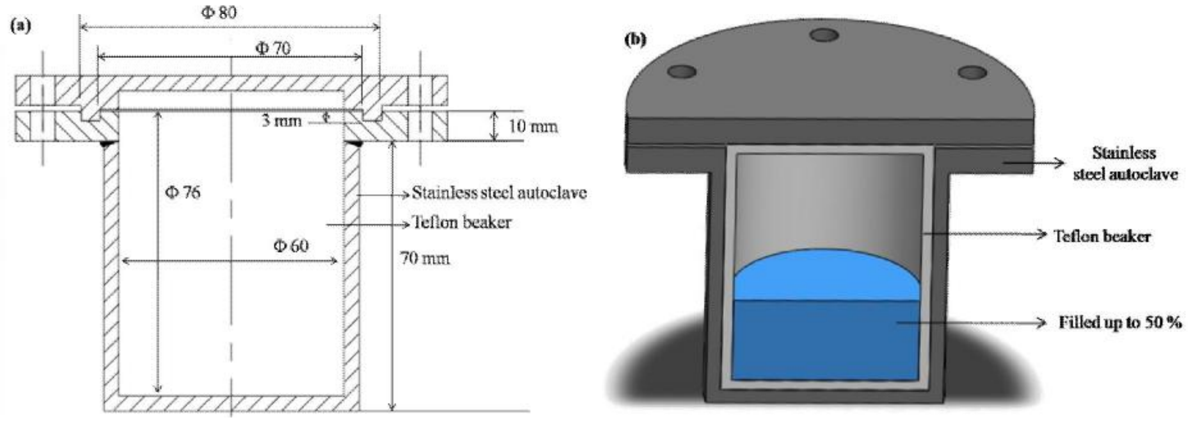

Figure 2.2. (a) Schematic of home built hydrothermal vessel and **(b)** its cross-sectional view

2.2.1.2. Co-precipitation method

In Co-precipitation method, the metal cations taken in the form of soluble salts (e.g. nitrates, acetates) are simultaneously precipitated from a common medium as hydroxides or carbonates or oxalates or citrates. The salts having comparable solubility products are co-precipitated [109]. In some cases, oxides or carbonates of the relevant metals are digested with an acid and then the precipitating reagent is added to the solution. The precipitate obtained is subsequently heated to the desired temperature to produce the final product [110]. To obtain the final product with required properties, the concentration of the solution, pH, temperature and stirring speed of the mixture is varied during the synthesis [103, 109, 111, 112]. In the present study, the co-precipitation method was adopted for the synthesis of lead sulphide (PbS). A detailed synthesis procedure is given in Chapter 6.

2.2.2. Thick film preparation methods

Thick films for gas sensing were prepared by screen printing technique in which specially formulated pastes made of fine powders are printed on the ceramic substrate in a definite pattern and sequence through the use of a finely-woven screen [113-116]. The typical range of thicknesses for thick film layers is 0.1 µm – 100 µm. Other methods used for producing thick films include spin coating, slurry paste method and flexible plastic sheet precursors [114-116].

The basic components of the screen printing process adopted for preparing thick films are illustrated in Figure 2.3. A typical thick film screen consists of a finely woven mesh of nylon or polyester, mounted under tension on a metal or wooden frame. The mesh is coated with an ultra-violet (UV) light sensitive emulsion onto which the pattern can be formed. The property of emulsion film gets modified on exposure to UV light. The finished stencil has open mesh areas through which the desired pattern can be printed. The substrate is held in place by vacuum during printing. The position of the screen is adjusted to ensure good contact between consecutive layers. The paste is applied to the upper surface of the screen and the squeegee, a flexible blade transfers the ink through the open areas of the screen mesh generating the required pattern on the substrate. This layer on the substrate is oven dried and then subjected to a firing process to remove the binders. Finally, the thick films are sintered at a desired temperature to provide the necessary adhesion.

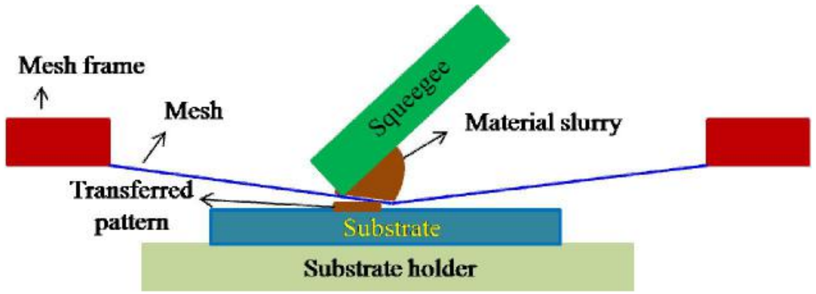

Figure 2.3. The basic components of the screen printing process **[113]**.

In the present studies, polycrystalline alumina substrates with the dimensions of 12.5 mm×12.5 mm×0.5 mm (length × width × thickness) were used. Prior to coating, gold interdigitated electrodes (IDEs) were screen printed on one side of the substrate for providing electrical contact for the sensor film. The distance between the fingers of the IDEs is about 0.7 mm and the width of the individual fingers is around 0.3 mm. Serpentine type platinum heaters were printed on the rear side of the substrate using Dek J 1202 (Kyoritsu Mfg. Co. Ltd., Japan) using a nylon screen with the mesh size of ~ 200 μm. The length of the platinum heater is about 80 mm with the room temperature resistance ranges from 18 Ω to 25 Ω. Schematic of the sensor having heater and electrode patterns deposited on Al_2O_3 substrate are shown in Figure 2.4.

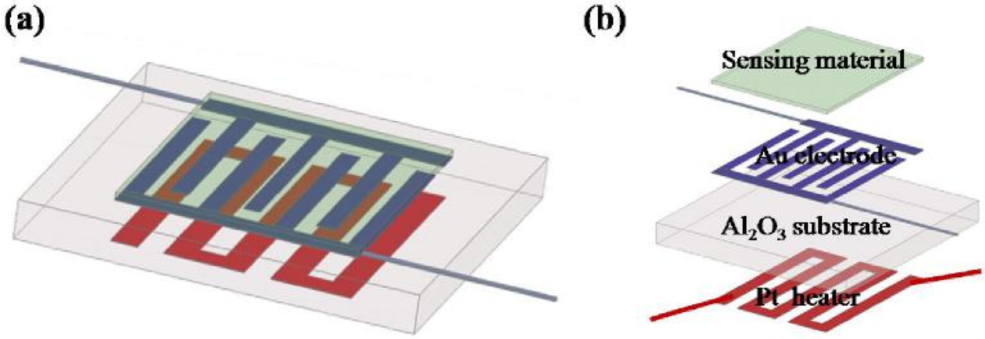

Figure 2.4. (a) Schematic of serpentine platinum heater pattern on the bottom side and the gold inter-digitated electrode on the top side of Al_2O_3 substrate with the sensing material over IDE and **(b)** split-up view of the sensor

The following sequence is followed for preparation of thick film sensors. First, the serpentine type platinum heaters were printed which were fired at higher temperatures. The interdigitated gold electrodes were screen printed next. Finally, $AgInO_2$ paste prepared by mixing finely ground powder with poly-ethylene glycol (2 vol %) and thick films were screen printed on polycrystalline alumina substrates. The details of the inks used for printing the heaters, IDE and thick film and their thermal treatment procedure are given in Table 2.2. The thickness of the films ranges between 20 µm – 50 µm. Figure 2.5 shows the photographs of different patterns of nylon screens, screen printed IDEs, platinum heaters and thick films on Al_2O_3 substrate respectively.

Table 2.2. Screen printing paste / inks used for heaters and electrodes, thick film binder and their respective thermal treatment conditions

S. No.	Paste / Ink – Manufacturer – Model No.	Thermal treatment conditions
1	Platinum – ESL Electroscience– 5544	Drying at 100 ˚C for 30 mins followed by annealing at 900 ˚C for 3 h at a heating rate of 5 ˚C/min
2	Gold – Heraeus – C 5007	Drying at 100 ˚C for 30 mins followed by annealing at 800 ˚C for 30 mins at a heating rate of 5 ˚C/min
3	Thick film binder (poly-ethylene glycol, 2 vol%)	Drying at 100 ˚C for 30 mins followed by annealing at 400 ˚C for 24 h at a heating rate of 1 ˚C/min

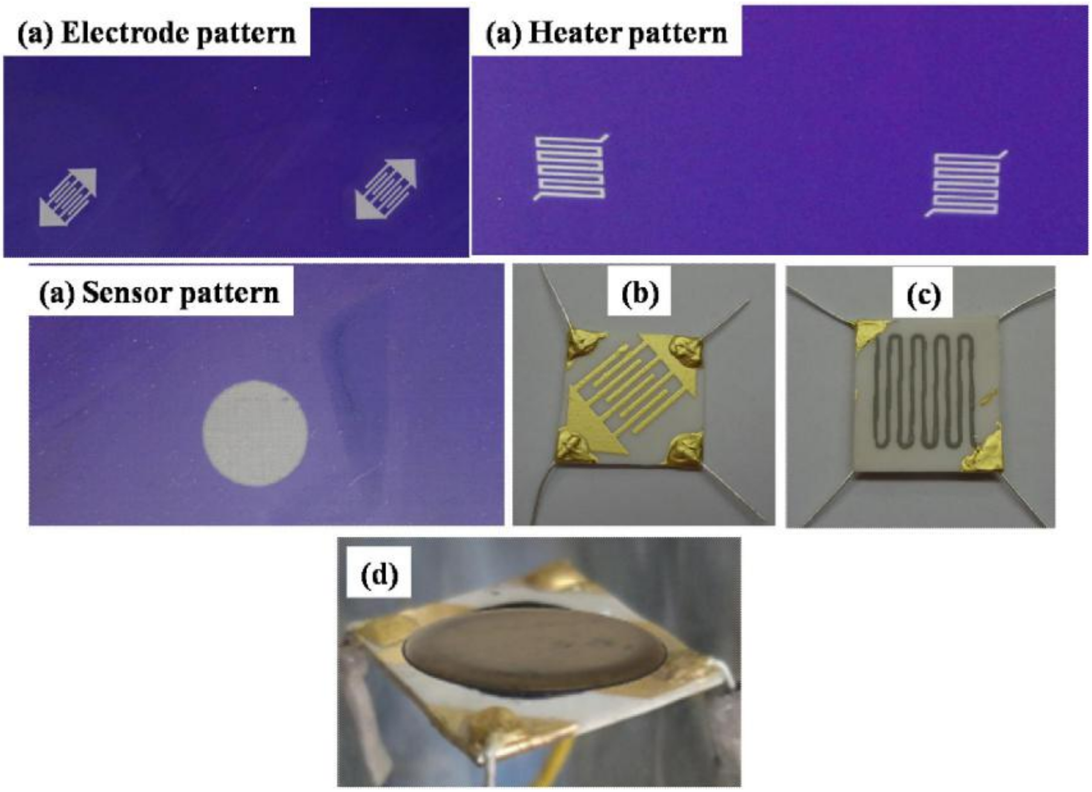

Figure 2.5. Photographs of **(a)** different patterns of nylon screens, **(b)** screen printed IDE, **(c)** platinum heater & **(d)** thick film on Al_2O_3 substrate

2.2.3. Thin film deposition methods

Thin film deposition techniques may broadly be classified as wet and dry methods. Sensing films made by wet methods like spin coating, drop-casting, Langmuir-Blodgett, successive ionic layer adsorption and reaction (SILAR), etc. have particulate or porous morphology in addition to poor adhesion and hence require high temperature treatments. Although particulate or porousmorphologies are favourable for high sensor response, reproducibility of wet-film morphology is poor because of crack formation during the evaporation of the binders and solvents at high temperatures [117]. The necessary or ideal conditions for the crack free stongly adherent nanostructured sensor grade thin films of multicomponent oxides requires(i) an arrangement to make the constituents of the films to arrive the substrate at precise relative abundance (stoichiometry) (ii) supply of necessary thermal energy required to those ions/atoms for in-situ growth and (iii) the ability to deposit the ions/atoms in high partial pressures of background gas in-order to suppress the escape of highly volatile components. Although the conditions mentioned may appear to be simple, they are not met by most of the physical methods. Remarkably, they are present in pulsed laser deposition (PLD) that sets this method unique. The kinetic energy of the ablated species varies from 1 – 100 eV by the choice of the laser wavelength, pulse duration and pulse energy which can directly be converted to thermal energy upon arrival at the substrate heated to a suitable temperature. As the laser source is located outside the deposition chamber, the pressure inside during the growth can be increased to higher values allowing the deposition to take place at higher pressures. Moreover, this technique offers to test the idea of hybrid structures by the use of multitarget carrousel so that multilayers and superlattices can be sequentially deposited without breaking the vacuum. Some of the dry methods include physical vapor deposition (PVD), chemical vapor deposition (CVD), electrochemical deposition, sputtering, atomic layer deposition (ALD), molecular beam epitaxy (MBE), etc.

The present thesis is focused on the use of pulsed laser deposition (PLD) technique in the preparation of thin films of multicomponent oxides offers in-situ growth at high partial pressures with ease. This method also offers greater control over the grain size, thickness, composition, adhesion and stoichiometry of the multi-component materials [118].

In 1986, J.T. Cheung, et al. reported the use of PLD to deposit high-quality, epitaxial semiconductor films for the first time [119]. An intense laser pulse is allowed to passes through an optical window of a vacuum chamber and is focused onto a solid surface (the target) wherein it is absorbed. Above a certain power density, significant material removal occurs in the form of a luminous plume. The threshold power density needed to produce such a plume depends on the target material, its density, laser wavelength and pulse duration. It is typically of the order of 10–500 MW cm^{-2} for ablation using ultraviolet (UV) excimer laser pulses of 10 to 30 ns duration. Material from the plume is allowed to re-condense on a substrate where film growth occurs. A schematic of the PLD deposition process is shown in Figure 2.6.

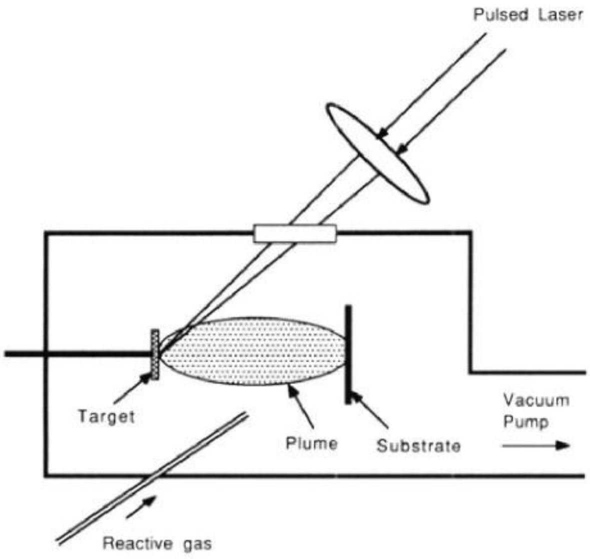

Figure 2.6. A schematic of the PLD deposition process

The interaction of short-pulse laser with the target material is extremely complex and can be viewed to constitute severage stages as shown in Figure 2.7. Optical irradiation of the target causes surface heating. When laser radiation is absorbed in the surface region of a target, the electromagnetic energy is immediately converted into electronic excitation in the form of plasmons and unbound electron. The electric-field amplitude (E) of an electromagnetic wave is given by:

$$\mathbf{E} = \sqrt{\left(\frac{\mathbf{2\Phi}}{\mathbf{cn\varepsilon_0}}\right)} \tag{2.1}$$

where Φ is the power density, ε_0 is the permittivity of free space, c is the velocity of light, and n is the refractive index. Taking the refractive index of 2 for the material and the power density of 2×10^8 $\mathrm{Wcm^{-2}}$, the calculated electric field strength of 2×10^5 $\mathrm{Vcm^{-1}}$ is sufficient to cause dielectric breakdown in many materials. The threshold electric-field strength for dielectric breakdown is proportional to the square root of the power density, which in turn is proportional to the laser fluence and inversely proportional to the laser pulse duration 'τ' [118, 120, 121].

The excited electrons transfer their energy to the lattice within few picoseconds resulting in heating the surface to a depth of 1/α, where 'α' is the optical absorption coefficient of the material. The thermal diffusion length for a material, l_{ther} is given by:

$$l_{\mathrm{ther}} = 2\sqrt{\mathrm{D}\tau} \tag{2.2}$$

where D is the thermal diffusivity and τ is the pulse duration. If thermal diffusivity 'D' is smaller than 1/α, then the heated depth will be 1/α and is independent of the pulse duration. The plasma plume produced under these conditions should have the same stoichiometry as the target. If the target surface is heated by absorbing the light from a continuous-wave laser source, then this would allow a significant amount of the incident power to be conducted into the bulk of the target in accordance with Equation 2.2. This leads to melting and evaporation of the surface making it essentially a thermal evaporation process. The difference between the melting points and vapor pressures of the target constituents would cause them to evaporate at different rates so that the composition of the evaporated material would change with time producing non-stoichiometric films from that of the target [118, 120, 121].

For congruent evaporation, the heat transport across the depth after absorption of the radiation must be minimized and the fractional distillation of the target constituents must be suppressed. This is achieved by the use of extremely short pulse width giving rise to high laser power density after focused to a small spot on the target. Continued interaction of the radiation with the evaporated material results in dissociation of the molecular species or aggregates and their desorption from the target. Photoionization of the evaporated material by nonresonant multiphoton processes leads to the formationof plasma above the surface. Once formed, the plasma absorbs the laser radiation by inelastic free electron scattering (or inverse bremsstrahlung) which results in further heating of the plasma.Theabsorption coefficient of the plasma (a) is given by:

$$\boldsymbol{\alpha = 3.69\times 10^{8}\left(\frac{Z^{3}n_{i}^{2}}{T^{0.5}v^{3}}[1-\exp(-hv/kT)]\right)} \tag{2.3}$$

where Z is the average charge, ‘n_i’ is the plasma density and ‘v’ is the laser frequency. The density of singly charged ions ‘n_i’ in cm^{-3} is given by the Saha equation:

$$\boldsymbol{n_{i} = (2.4\times 10^{15}T^{3/2}n_{n}[\exp(-U_{i}/kT)])^{1/2}} \tag{2.4}$$

where T is the gas temperature in K, ‘n_n’ is the density of neutrals in cm^{-3} and U_i is the first ionization potential of the gas atoms (eV). Once generated, the plasma moves away from the target leading to a decrease in electron density. In this way, the behavior of plasma self-regulates the laser-target interaction [118, 120, 121].

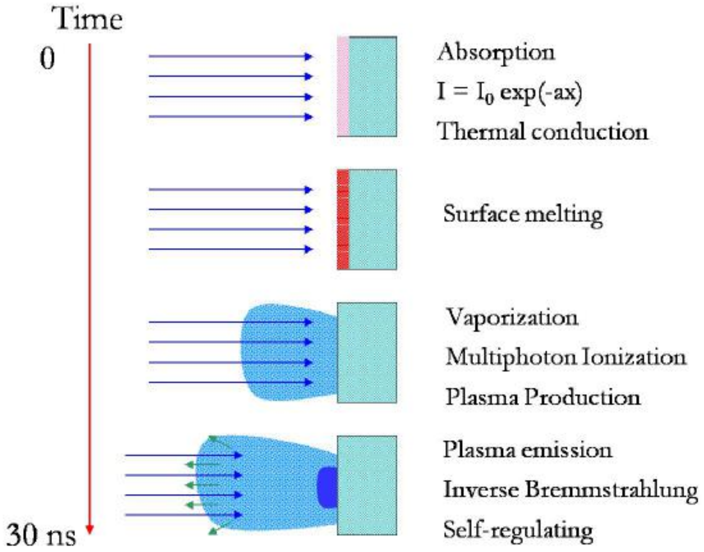

Figure 2.7. Schematic representation of the laser target interactions **[120]**

In the present work, thin films were deposited using an excimer laser (KrF; λ = 248 nm, M/s Lumonics, Canada) having the pulse width of 30 ns operating at 20 Hz. The laser from the source is allowed to pass through an optical window of a SS vacuum chamber and is focused on the surface of the target. Using a gate valve mounted between the vacuum chamber and the turbo-molecular pump and by maintaining a constant flow of oxygen/argon into the chamber using a needle valve, oxygen/argon pressure inside the chamber is varied. The target is rastered using a DC motor to avoid laser drilling the target. The plasma generated from the target is allowed to fall on the substrate which is heated to adesired temperature using a heater facility. Thin films of $AgInO_2$ and PbS were deposited by PLD on polycrystalline alumina, quartz, (012) $LaAlO_3$ and (001) Al_2O_3 substrates.

2.3. Characterization techniques

2.3.1. X-ray diffraction (XRD)

X-ray diffraction is a widely used characterization tool for phase identification of samples. When X-rays having wavelengths ranging from 0.1 to 100 Å (10^{-10} m) propagate through a substance, they can be diffracted, scattered or absorbed (ionization or photoelectric effect). Analysis of the diffracted X-rays provides the information on the nature of the crystallographic structure. X-ray beam will interact with the electrons of the atoms in the crystal lattice, generating oscillations with the same frequency of the electric field component of the electromagnetic wave. This causes radiation of X-rays of the same wavelength emitted in all directions which undergo constructive or destructive interferences producing wavefronts that are in phase [122-124]. The necessary conditions for in-phase diffraction by the parallel atomic planes can be expressed using Bragg's equation:

$$\mathbf{n\lambda = 2d\sin\theta} \tag{2.5}$$

This law states that an integer value of the wavelength is related to the distance between the parallel atomic planes (d) and the angle of the diffracted beam (θ).

Powder X-ray diffraction (PXRD) generally employs the conventional θ - 2θ (Bragg-Brentano) "reflection" geometry, in which the incidence angle equals the angle of the diffracted beam from the sample surface (Figure 2.8 (a)). This configuration ensures an intense sharp diffracted pattern from any particular set of crystalline planes if the diffracted is collimated using Soller slit located in front of the rotating detector [123, 124]. X-rays with large angles of incidence will penetrate few to several hundred micrometres inside the material under investigation and the depth of penetration depends on "radiation" density. If the sample thickness is less than the depth of penetration, then the intensity of the diffracted beam from the sample will not only be less but also will be masked by the diffraction peaks of the substrate.

To overcome this limitation, geometry is modified to provide ‘asymmetric’ diffraction, which allows access to small depth in the sample by varying the angle of incidence. In this mode called glancing incidence, the incident angle is reduced to few degrees so that the X-rays pass through the film to a longer distance producing relatively intense diffraction peaks of the film. Schematic of glancing incidence X-ray diffraction is shown in Figure 2.8 (b). Unlike conventional powder diffraction geometry, which observes planes parallel to the surface of the sample, in the case of glancing incidence XRD, crystal planes inclined with respect to the surface of the sample are observed; who’s normal is the bisector of the angle formed by the incident and the diffracted beam [122].

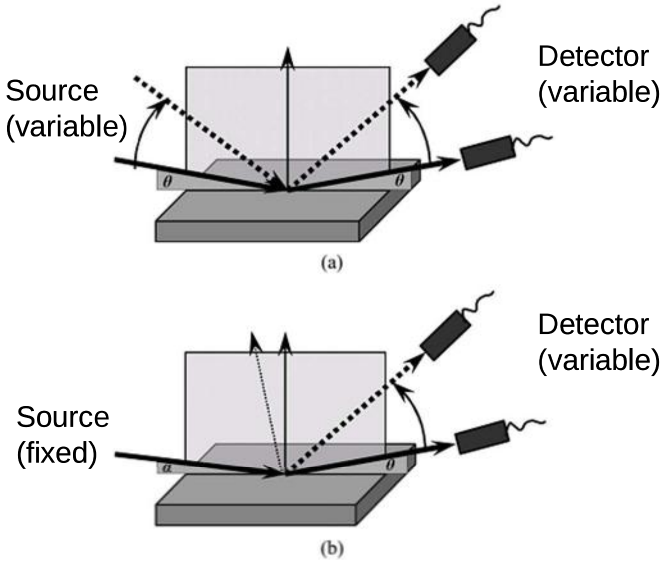

Figure 2.8. Schematic diagrams indicate **(a)** powder and **(b)** grazing incidence XRD configuration

In the present thesis, powder X-ray diffraction patterns of $AgInO_2$ and PbS were recorded using GNR Explorer, Italy. The diffraction data were collected by operating the X-ray gun at 40 kV and 30 mA with Cu K_α radiation of 1.5418 Å for 2θ range from 10 to 80 degrees at a step size of 0.02 ° with an integration time of 2 s at each step.

2.3.2. Electron microscopy

Electron microscopes use signals arising from the interaction of an electron beam with the sample to obtain information about the structure, morphology and composition. Ernst Ruska (1906-1988), a German engineer and academic professor built the first electron microscope in 1931. There are two basic models of the electron microscopes: Scanning electron microscopes (SEM) and Transmission electron microscopes (TEM).

2.3.2.1. Scanning Electron Microscopes (SEM)

In SEM, the secondary electrons produced by the specimen due to the irradiation of primary radiation are collected and mapped based on their kinetic energy to generate an image that contains morphological features of the specimen. The electrons produced by the electron gun are guided and focused by the magnetic lenses on the specimen. Thermionic or field emission electron emission is used in electron guns. The focused beam of electrons is then scanned across the surface in a raster fashion. The energy dispersion of secondary electrons is used to produce the two-dimensional (2D) image. In the present thesis, field emission scanning electron microscope (FE-SEM) (Zeiss SUPRA 55, Germany) was used to record the morphologies of the powder and thin film of $AgInO_2$ and PbS.

2.3.2.2. Transmission Electron Microscopes (TEM)

TEM is useful for determining size, shape and crystal structure of the material. The selected area electron diffraction (SAED) helps in resolving the structures of the materials and HRTEM is useful for the determination of lattice planes. The major components of TEM include the illumination system, the objective lens/stage and the imaging system.

The very first requirement of TEM is that the specimens have to be very thin. The electron beam from the source is made coherent using a condenser lens and is allowed to strike the specimen. Depending on the thickness and electron transparency of the specimen, the transmitted beam from the specimen is focused on the phosphor screen or charge-coupled device (CCD) camera by the objective lens to produce the image.

In the present thesis, High-Resolution Transmission Electron Microscope (HR-TEM, FEI TECNAI G2-20 TWIN) with LaB_6 filament is used to record the morphology, crystallographic patterns, identify the impurity phases in $AgInO_2$. Prior to TEM measurements, the samples were dispersed in isopropyl alcohol and a drop of the solution was cast on copper-coated TEM grids. The film formed on the TEM grids was allowed to dry for 10 minutes following to remove the excess solvent.

2.3.3. Energy Dispersive X-ray spectroscopy (EDX)

EDX is used to determine the elemental composition of a material. When electrons from incident beam interact with atoms on the surface, secondary electrons from inner shells of the atoms are ejected out. Electrons from outer shells will drop into the vacant levels of the inner shells resulting in the emission of characteristic X – rays of the atom. Hence, by measuring the relative intensity of the characteristic X – rays of the elements, information about the elemental composition of the sample can be obtained if the instrument is already calibrated. Since the penetration depth of the electron beam is about few angstroms, the characteristic X – rays are from the surface atoms and hence it is a useful tool for investigating thin films.

2.3.4. Atomic Force Microscopy (AFM)

Atomic Force Microscopy gives granular features of the films, size and uniformity along with the surface roughness [125, 126]. A micro-cantilever tip often made of silicon oxynitride with a thin coating of gold for better reflection of light is allowed to scan along the surface of the sample. A laser beam is allowed to fall on the tip of the micro-cantilever while probing the topography of the sample surface. The laser deflected by the cantilever is collected by the position sensitive photodiodes (PSD) and sent to the detector for analyzing. The process of characterization can be either in contact or non – contact or semi-contact mode with the sample surface. The non – contact mode is more useful since the tip of cantilever doesn't touch the sample surface and hence doesn't deform the surface. The force of interaction between the tip of the cantilever and the sample atoms is given by Equation 2.6.

$$\mathbf{f} = \frac{\mathbf{1}}{\mathbf{2\pi}}\sqrt{\left(\frac{\mathbf{k}}{\boldsymbol{\mu}}\right)} \qquad \mathbf{(2.6)}$$

where 'f' is the resonance frequency, 'k' is the force constant and 'μ' is the reduced mass which is given by $\left(\mu = \frac{(m_1 \, x \, m_2)}{(m_1 + m_2)}\right)$. Here, m_1 and m_2 are the masses of atoms in the sample and the cantilever tip respectively. The resonance frequency of the micro-cantilever is generally kept constant by varying the amplitude of its vibrations [125, 126]. This interaction is controlled by a feedback loop connected to the cantilever. In the present thesis, surface topography and roughness of $AgInO_2$ and PbS thin films were analyzed using Atomic Force Microscope (Solver Pro of M/s NT – MDT, Russia).

2.3.5. X-ray Photoelectron Spectroscopy (XPS)

X-ray photoelectron spectroscopy (XPS) is a surface-sensitive technique used for the analysis of energy distribution of electrons ejected from solids by irradiation of X-rays. The ejected electrons contain information regarding the oxidation state and atomic composition of the solids being investigated. The photoelectrons escape from the surface atomic layers up to a depth of (~ 10 nm) and provide the information of the surface and hence this technique is ideally suitable for probing thin films.

In the photoemission process, kinetic energy of the electron ejected from the core level is measured after absorption of a photon of known energy (hυ) (Figure 2.9 (a)). The spectral peaks generated by the emission of photoelectrons are named according to the orbital (l = 0, 1, 2, 3... denoted as s, p, d, f...) and spin (s = ±1/2) quantum numbers of the core levels from which they emanate. The total momentum of the photoelectrons ($J = l \pm s$) is included in the nomenclature of a measured XPS spectral peak [127-131].

In the photoelectron spectrum, electrons in the 's' orbital will appear as a singlet whereas the electrons in the other orbitals (i.e. p, d, f…) will appear as doublets due to spin-orbit coupling. The binding energy of the lower 'J' component is higher than that of the other. The energy separation between the components increases with increase in atomic number. A shift in the binding energy can occur due to the oxidation state of the ion. The shift due to the groups coordinating the ion is called chemical shift. The overall shift in BE values caused by the surface charging of the insulating samples is corrected either by the electron flood gun to neutralize the positive surface charges or by the use of reference standards such as carbon or gold [128-131].

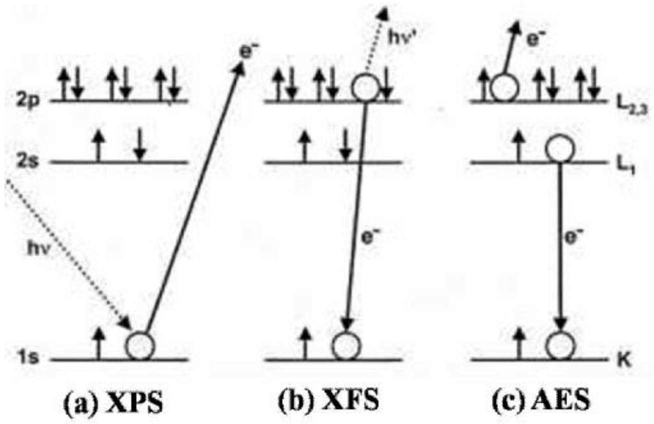

Figure 2.9. Photoemission process for XPS along with secondary emission processes **[132]**

Photoionization is accompanied by two secondary emissions (Figure 2.9 (b & c)) involving either a photon emission causing X-ray fluorescence or ejection of a valence level electron, called an Auger electron whose kinetic energy is independent of the photon energy. The Auger effect dominates for use of low energy (~ 1 kV) incident X-rays while fluorescence dominates at high energies (~ 10 keV). Since conventional XP spectrometers utilize relatively a low photon energy (i.e. Mg K_α = 1253.6 eV; Al K_α = 1486.6 eV), contributions from fluorescence in the XPS spectra are relatively less compared to auger transitions [127, 131].

In the present thesis, X-ray photoelectron spectra of the samples were recorded using XPS system of M/s SPECS, Germany. The XPS system is provided with a special reaction chamber which can be evacuated to 10^{-8} mbar after (Figure 2.10) heating the specimen to the desired temperature (up to 600 ˚C) in flowing air/analyte using IR lamp and a transfer mechanism to introduce the specimen to the analysis chamber without breaking the vacuum. Vacuum level inside the analysis chamber was maintained around 10^{-10} mbar throughout the measurements. Monochromatic Al K_α (1486.6 eV) radiation was used for excitation at a constant power of 400 W. The hemispherical Phoibos 150 mm analyser equipped with 1D – delay line detector was operated in Fixed Analyser Transmission (FAT) mode with a constant pass energy of 10 eV throughout the measurements. The spectrometer work function was adjusted to Au $4f_{7/2}$ peak centred for metallic gold located at a binding energy of 84.0 eV using electron gun operated at 1 eV with an emission current of 2.3 µA for charge correction of the specimen. Survey scans were recorded with an energy step of 1 eV in the energy range 1000 to - 1 eV, whereas selected regions were recorded with an energy step of 0.05 eV and dwell time of 0.1 s/step. All the selected region recordings were averaged out for 5 scans. Shirley background subtraction procedure was adopted using CasaXPS (version: 2.3.16Dev52). The deconvolution/peak fitting was carried out using XPS PeakFit (version 4).

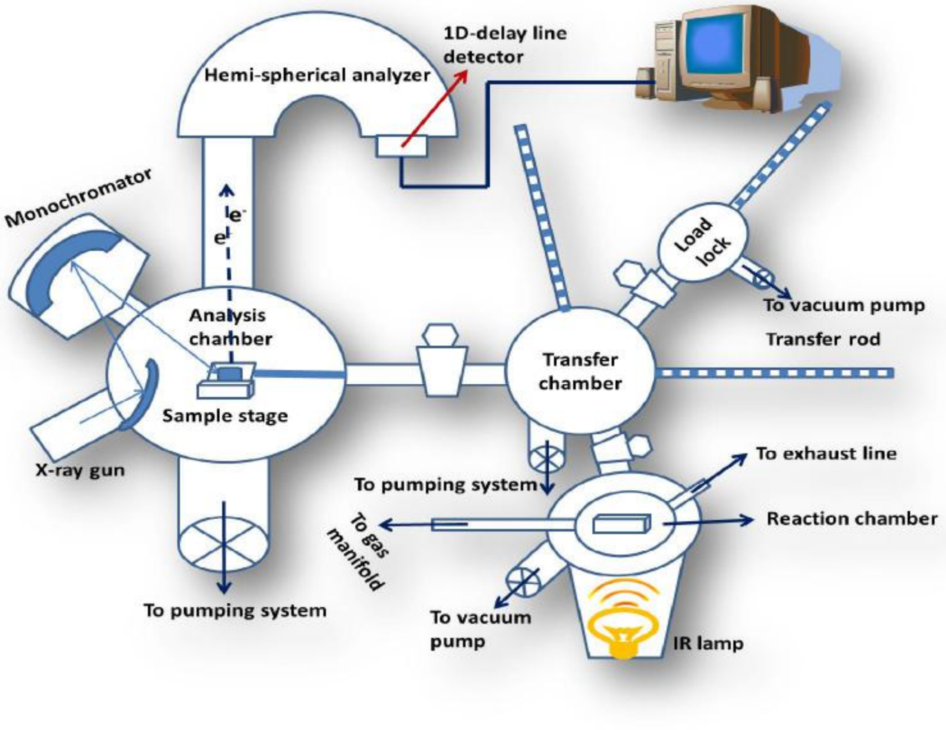

Figure 2.10. Schematic of XPS system

2.3.6. UV-Visible Spectrophotometry

Absorption spectra of the specimen were recorded by Ultraviolet-Visible (UV-Vis) spectrophotometer to measure the band gaps of semiconducting materials under investigation.

The relative change in intensity of the radiation of wavelength λ absorbed by a material is given by Beer-Lambert's law:

$$\mathbf{I = I_0 exp(-\alpha t)} \qquad \mathbf{(2.7)}$$

where I_0 and I are incident and transmitted light, α and t are the absorption coefficient and path length respectively. A semiconductor exhibits absorption for photons with energies greater than the bandgap. As a result, there is a sharp increase in the absorption at energies close to the bandgap that manifests itself as an absorption edge in the UV-Vis absorbance spectrum. The optical bandgap (E_g) was calculated using the Tauc relation given in Equation 2.8:

$$\mathbf{(\alpha h\upsilon)^n = A(h\upsilon - E_g)} \qquad \mathbf{(2.8)}$$

where α is the absorption coefficient (cm^{-1}), $h\upsilon$ is the incident photon energy (eV), A is a constant and n is 2 for direct bandgap semiconductor and ½ for indirect bandgap semiconductor. From the plot of $(\alpha h\upsilon)^n$ versus photon energy ($h\upsilon$), the bandgap of the material is determined.

In the present thesis, the absorbance or transmittance spectra of $AgInO_2$ and PbS were recorded in the range of 200 to 800 nm using Avantes fiber optic spectrophotometer (M/s AvaSpe-3648-USB2, Netherland). From the absorbance or transmittance data, the bandgap of the materials was obtained using Tauc relation.

2.3.7. Thermo Gravimetric - Differential Thermal Analysis (TG-DTA)

The thermal analysis brings out the thermal history of the specimen when subjected to programmed heat treatment. Thermogravimetric analysis (TG) measures mass changes in a material associated with decomposition, oxidation, reduction or any other chemical changes as a function of temperature under a controlled atmosphere. In differential thermal analysis

(DTA) where the temperature of a sample is compared with that of inert reference material during a programmed heating/cooling, heat changes accompanied by the thermal events such as melting, decomposition or structural changes in the material are investigated. The temperature of the sample will lag behind that of the reference and a minimum during an endothermic event whereas an opposite effect will be observed for an exothermic event taking place in the material. The area under the endotherm is related to the enthalpy of the thermal event, ΔH [109, 133, 134]. In the present thesis, the TG-DTA measurements of $AgInO_2$ and PbS were carried out using STA 449-F3, Jupiter Model (Netzsch, Germany) in a dynamic air / argon flow of 5 mL/min in the temperature interval of 30 ˚C to 750˚C to analyze its thermal stability.

2.3.8. Adiabatic bomb calorimeter

The chemical change associated with either liberation or absorption of heat causing temperature changes. These heat-changes in thermochemical processes are measured directly using calorimeters. Chemical reactions are quite often carried out at constant pressure and hence the heat changes are a direct measure of the enthalpy change of the reaction. Enthalpy is a state function and it is convenient to measure the changes in enthalpy from an initial state (H_i) to final state (H_f) given as $\Delta H = H_f - H_i$.

Calorimeters are widely used for the measurement of heat of formation, heat of reaction, heat of solution and heat of mixing, etc. A calorimeter, in general, consists of a reaction vessel known as the calorimeter proper in which the thermal events occur with a shield or a jacket, which may be kept at a constant or varying temperature. In the present studies, an adiabatic bomb calorimeter (PHI-TEC 1 of M/s HEL, UK) used to probe the heat changes associated with the chemical reactions at high pressures and temperatures is employed to measure the in-situ changes in pressure at 150˚C, 180˚C and 210˚C during hydrothermal synthesis. The term adiabatic refers to the prevention of heat exchange between the measuring system (calorimeter) and the surroundings. If $T_c = T_s$ and heat (q) varies, the calorimeter is termed as an adiabatic calorimeter. Here, T_c is the temperature of the calorimeter and T_s isthe temperature of the surrounding / thermostat. This condition ensures that there is no exchange of heat between the calorimeter and the surroundings. As maintaining $T_c = T_s$ can be done only if the heat is released slowly and the adiabatic calorimeter can give precise data on slow processes. Since heat capacity is a function which varies slowly varying with temperature, adiabatic calorimeters are used for the direct measurement of molar heat capacities [135].

In this present thesis, an adiabatic bomb calorimeter having a bomb cell of volume 10 mL containing half the volume of reactant mixture[1] was subjected to identical synthesis conditions and the changes in pressure inside the cell is continuously monitored by the pressure transducer at different temperatures (150˚C, 180˚C and 210˚C) for 24 h in independent experiments.

2.3.9. Electrical Measurements

2.3.9.1. Two-probe measurement

The two probe technique sources a current to the device under test and measures the voltage. The measurement of total resistance (R_T) of the sample between the two probes is given in Equation 2.9. The schematic of the two probe arrangement is shown in Figure 2.11.

$$\mathbf{R_T = \frac{V}{I} = 2R_p + 2R_c + 2R_{sp} + R_s} \qquad \textbf{(2.9)}$$

where R_p is the probe resistance, R_c is the contact resistance at each metal/sample contact, R_{sp} is the spreading resistance under each probe and R_s is the sample resistance. The contact

---

[1] The aspect ratio of volume of autoclave to the reactant mixture is maintained.

resistance arises from the mechanical metal probe contacting the semiconductor. The spreading resistance accounts for the resistance encountered by the current when it flows from the small metal probe into the semiconductor and from the semiconductor to the probe. The polarization of charges and/or ions at the respective electrodes will occur during DC measurements. The two probe technique is suitable only to those materials whose resistances are above kΩ. Due to the limitations in the two-probe method, the four-probe resistance method was implemented for low resistance measurements. In the present thesis, the two-probe resistance measurements were carried out for $AgInO_2$ and PbS thick and thin films using Agilent Data Acquisition Switch Unit (34970A), Malaysia.

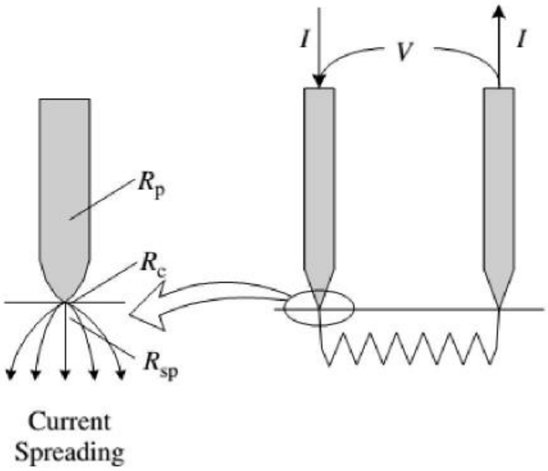

Figure 2.11. Two – probe measurement showing the probe resistance R_p, the contact resistance R_c and the spreading resistance R_{sp} **[136]**

2.3.9.2. Four-probe measurement

Four-probe resistance method involves bringing four equally spaced probes in contact with a material of unknown resistance as shown schematically in Figure 2.12. The two outer probes (1, 4) are used for sourcing current and the two inner probes (2, 3) are used for measuring the resulting voltage drop across the surface of the sample [136]. Here S_1, S_2 and S_3 are the distances between the probes. High impedance voltmeter draws little current;therefore, the voltage drops across the probe, spreading and contact resistance are very small and negligible. The four-probe resistivity of the sample is calculated using Equation 2.10.

$$\rho = F(s,t)\frac{\Delta V}{I} \tag{2.10}$$

where ‘ΔV’ is the measured differential voltage and ‘I’ is the applied current. Here ‘F’ is the correction factor, ‘s’ is the distance between the probes and ‘t’ is the sample thickness. Since the measurements are made on finite areas, correction factors have to be incorporated based on the sample geometry. Other considerations that need to be considered for accurate four-probe measurements are the spacing of the probes and temperature effects. This limitation was modified by van der Pauw method [137, 138].

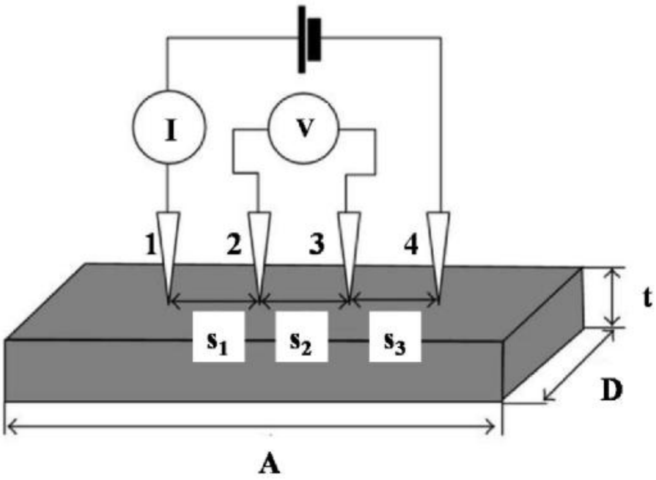

Figure 2.12. Schematic of collinear four-probe showing current and voltage flow measurement

2.3.9.3. Four probe measurement of resistivity using van der Pauw technique

The van der Pauw holds for a flat sample of arbitrary shape (Figure 2.13) and would be applicable if the following conditions are obeyed:

1. The contacts are at the circumference of the sample.
2. The contacts are sufficiently small.
3. The sample is homogenous in thickness.
4. The surface of the sample is singly connected, i.e., the sample does not have isolated holes.

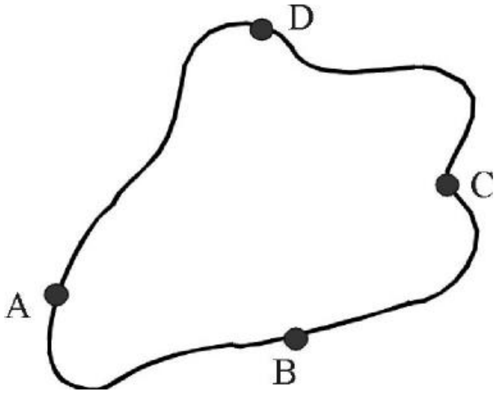

Figure 2.13. Schematic of a typical sample of arbitrary shape with four small contacts to measure specific resistivity by van der Pauw and Hall measurements **[138]**

A flat sample of conducting material of arbitrary shape with successive contacts A, B, C and D fixed on arbitrary places along the circumference is considered such that the resistance $R_{AB,\,CD}$ defined as the potential difference $V_D - V_C$ between the contacts D and C per unit current passing through the contacts A and B. Similarly we define the resistance $R_{BC,\,DA}$ and the following relationship would be valid (Equation 2.11):

$$\mathbf{e^{\left(-\frac{\pi d}{\rho} R_{AB,CD}\right)} + e^{\left(-\frac{\pi d}{\rho} R_{BC,DA}\right)} = 1} \qquad \textbf{(2.11)}$$

where ‘ρ’ is the specific resistance of the material and ‘d’ is the thickness of the sample. $R_{AB,\,CD}$ is obtained by applying a current (I) through contact 1 and 2 and measuring the voltage (V_{43}) across 4 and 3 as shown in Figure 2.14 (a). Similarly $R_{BC,\,DA}$ is obtained by allowing the current I through contact 2 and 3 and measuring the voltage (V_{14}) across 1 and 4 (Figure 2.14 (b)). R_A and R_B are calculated using the following Equation 2.12:

$$\mathbf{R_A = \frac{V_{43}}{I_{12}} \text{ and } R_B = \frac{V_{14}}{I_{23}}} \qquad \textbf{(2.12)}$$

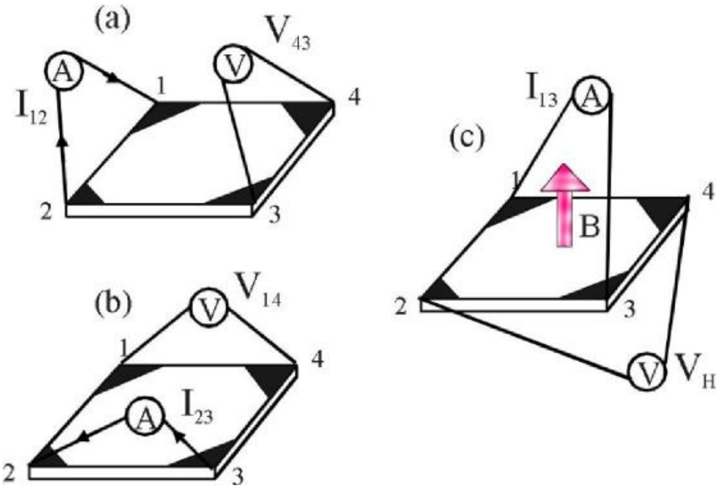

Figure 2.14. Schematic of a van der Pauw configuration used in the determination of the two characteristic resistances R_A and R_B **[137]**

From Equation 2.12, ‘ρ’ can be represented as in Equation 2.13:

$$\boldsymbol{\rho = \frac{\pi d}{\ln 2}\left(\frac{(R_{AB,CD} + R_{BC,DA})}{2}\right) f \left(\frac{R_{AB,CD}}{R_{BC,DA}}\right)} \qquad \textbf{(2.13)}$$

where ‘f’ is the geometric factor. The geometric factor becomes unity for a perfect square shape.

2.3.9.4. Carrier concentration measurement using the Hall technique

The objective of the Hall measurement in the van der Pauw technique is to determine the changes in sheet carrier (electrons or holes) concentration ‘n or p’ of the thin film by measuring the Hall voltage V_H. As the van der Pauw method is applicable for thin film geometries and the sensors are configured as a thin film, this method is ideal to track the changes in carrier concentration and mobility during sensing and becomes useful for understanding the mechanism. When a conductor is placed in a magnetic field and a current is allowed to flow through it, an electric field with direction normal to both the current and magnetic field is produced in the material. This phenomenon, discovered by E.T. Hall in 1879 is known as Hall Effect [136]. The schematics of Hall effect measurement is shown in Figure 2.15.

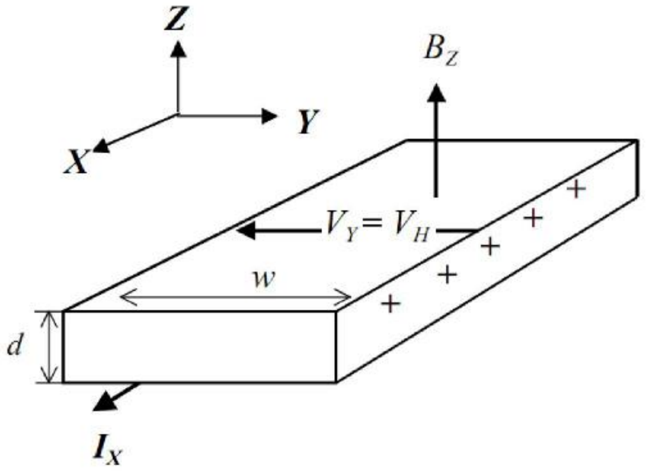

Figure 2.15. Schematics of Hall effect measurement for a semi-conducting material

For thin specimen having a uniform thickness, Hall effect is performed by van der Pauw method. A thin strip (thickness ‘d’) of the material to be studied is placed in a magnetic field B oriented at right angles to the strip. A current I is arranged to flow through the strip in the x-direction. The charge carriers experience a Lorentz force in presence of the magnetic field is given by

$$\mathbf{F_L = -e(v_x B_z)} \tag{2.14}$$

This force pushes electrons in y-direction leaving net +ve charge on one face, as shown in Figure 2.15 and produces the Hall voltage (V_H). If the carriers are electrons (-e), the voltmeter would read a negative potential difference. Alternately, should the carriers be holes (+e), a positive voltage would be measured.

In the steady-state, a force due to the electric field ($F_E = e \times E_y$) will balance the Lorentz force (F_L), so that

$$eE_y = -B_z e v_x \tag{2.15}$$

From I = nAve, the current density J is given as

$$J_x = \frac{I_x}{A} = nev_x \tag{2.16}$$

The subscripts on J, I and v give their directions. Since J = σE, where σ is the conductivity. Therefore,

$$J_x = \frac{I_x}{A} = \sigma E_x = nev_x \tag{2.17}$$

Rearranging these we find that

$$E_y = -\frac{B_z J_x}{ne} = -\frac{B_z E_x \sigma}{ne} \tag{2.18}$$

wherein the Hall coefficient is defined as:

$$R_H = -\frac{E_y}{B_z J_x} \tag{2.19}$$

Note that,

$$E_y = \frac{V_y}{w} = \frac{V_H}{w} \tag{2.20}$$

where ‘w’ is the width of the specimen in meter. So, if the current (I) and magnetic field (B) is known, measurement of the Hall voltage V_H gives us the electron concentration ‘n’:

$$\mathbf{n = -\frac{B_z J_x}{E_y e} = -\frac{w B_z I_x}{A V_H e}} \qquad \mathbf{(2.21)}$$

where ‘A’ is the cross-sectional area of the specimen. Since, A = w × d, Equation 2.21 can be rearranged as:

$$\mathbf{n = -\frac{B_z I_x}{d V_H e}} \qquad \mathbf{(2.22)}$$

giving carrier concentration ‘n’ in terms of magnetic induction B, current I, Hall voltage V_H and electronic charge ‘e’.

To measure the Hall voltage V_H, a current I is forced through the opposing pair of contacts 1 and 3 and the Hall voltage V_H (i.e. V_{24}) is measured across the remaining pair of the contacts 2 and 4 of the sample geometry shown in Figure 2.14 (c). Once the Hall voltage V_H is acquired; the sheet carrier electron density ‘n’ can be calculated using Equation 2.22. From the measured four-probe resistivity (ρ) using van der Pauw method and charge carrier density (n) calculated from Hall voltage, carrier mobility (μ) in the sample can be calculated using the Equation 2.23:

$$\boldsymbol{\mu = \frac{1}{\rho}\left(\frac{1}{ne}\right)} \qquad \mathbf{(2.23)}$$

2.4. Home-built facilities

2.4.1. Gas sensing facility for thick and thin film samples

A glass chamber of volume 55 mL provided with a gas injection port, air inlet and outlet is used for testing thick or thin film specimen in static mode. Figure 2.16 shows the photograph of the sensor set-up.

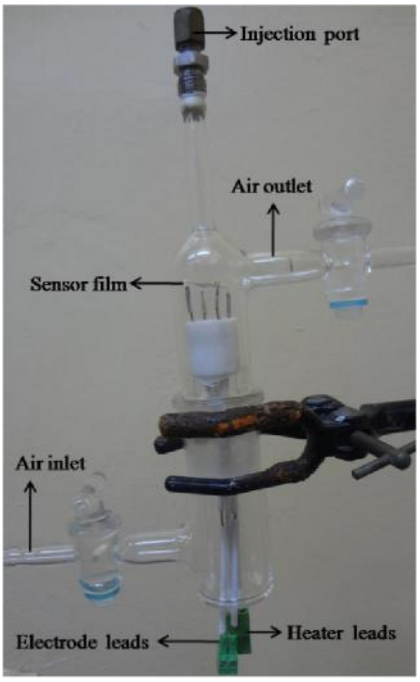

Figure 2.16. Photograph of a test chamber for gas interaction studies using thick or thin film in static mode of injections

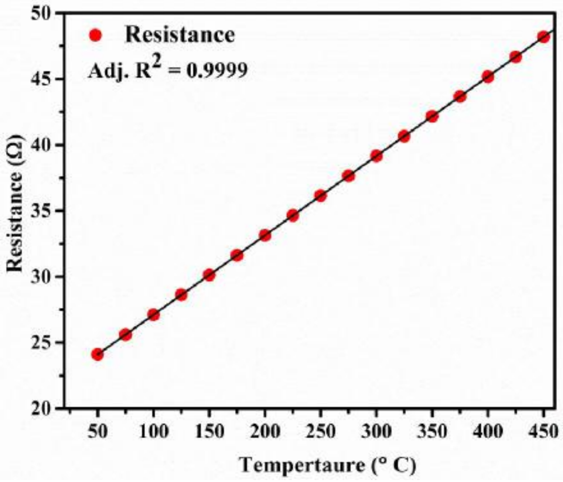

Figure 2.17. A typical plot showing the variations in platinum heater resistance with temperature. This calibration fit is used for setting the operating temperature of the $AgInO_2$/ PbS sensors

The electrical leads of the heater were connected to the DC power source and the temperature of the heater was calibrated by positioning heater inside the temperature-controlled furnace (Eurotherm 2132). The furnace was heated to 500 ˚C at a heating rate of

1˚C/min. From the electrical leads attached to the platinum heater, its resistance was measured externally between 25 ˚C and 500 ˚C. The resistance versus temperature calibration plot was made and a typical plot is shown in Figure 2.17. To maintain a specific operating temperature for the sensor, the current through the platinum heater is varied by varying the DC voltage. The electrode leads were connected to the data logger acquisition switch unit (M/s Agilent 34970A) for measuring the resistance changes.

The baseline resistance of the thick or thin film samples was continuously measured at a set temperature using M/s Agilent data logger interfaced with a personal computer. A known volume of the analyte is injected into the sensor housed inside the glass chamber and the response in terms of change in resistance of the sensor is recorded. After attaining the equilibrium, the sensor is purged continuously with air till the sensor retraces back to its original baseline resistance. Based on the relative change in resistance, the response of the sensor is evaluated.

Figure 2.18 shows the test module made of stainless steel of 8 mL capacity provided with an inlet and outlet for gas flow to perform sensor studies under dynamic flow conditions. The concentration of the analytes was adjusted with the help of mass flow controllers (MFCs, M/s Alicat, USA) having different flow ranges (0 – 50 mL for NH_3, H_2 and NO_x; 0 – 100 mL for Argon) for different gases. Swagelok needle valves were used for introducing or by-passing the chosen analyte into the test chamber. Individual mass flow controllers were calibrated with the help of calibrated gas mixtures. For a given set value of the mass flow controller, the gas flow was measured using a home built soap-bubble apparatus (Figure 2.19). The average time taken for the soap bubble to traverse a given volume in a calibrated burette was measured and the flow rate of the calibrated gas was calculated.

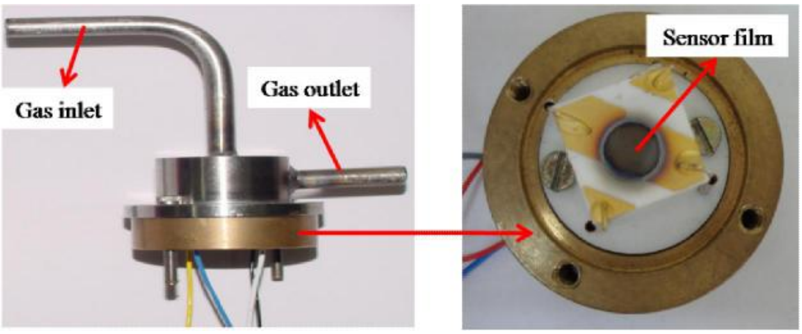

Figure 2.18. Photograph of thin film assembled in SS housing for dynamic gas interaction studies and top view of thin film deposited on Al_2O_3 substrate

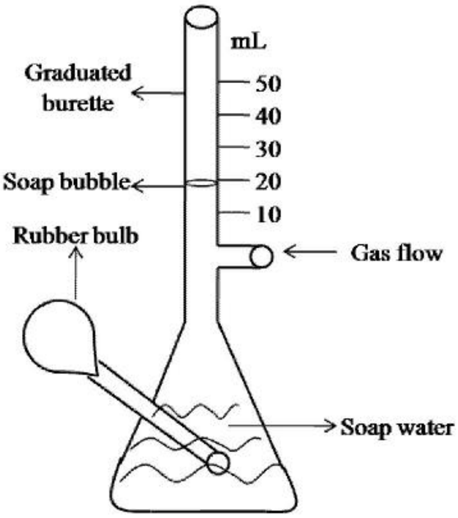

Figure 2.19. Home built soap-bubble apparatus for measuring the gas flow

In the present thesis, the gas sensing studies of $AgInO_2$ thick and thin films were carried out using the glass setup as shown in Figure 2.16. The gas sensing studies of PbS thin film was carried out in dynamic condition using the stainless steel facility as shown in Figure 2.18. The carrier gas (argon) was flushed continuously at a flow rate of 100 mL/min for testing the films.

2.4.2. Electrical conductivity measurement setup for AC Impedance technique

The temperature dependence conductivity of bulk specimen of AgInO$_2$ is measured by AC impedance studies to check the ionic/electronic conduction and the contribution of grain/grain boundary to the total conductivity.

A frequency response analyzer (Model SI 1255 of Solartron, M/s Schlumberger, UK) coupled with an electrochemical interface (Model SI 1286 of Solartron, M/s Schlumberger, UK) for the frequency range of 1 Hz - 1MHz in different ambient is used. The experimental cell for measuring the conductivity of the pellet specimen is shown in Figure 2.20. It consists of one end closed (~ 12.5 mm OD and 11 mm ID) quartz tube having a cut-out at the closed end. The sample pellet is sandwiched between two gold electrodes. The open end of the quartz tube was secured to stainless steel (SS) coupling through an O-ring sealed fitting. Two springs hanging from the (SS) coupling is used for connecting the quartz tube through hooks.

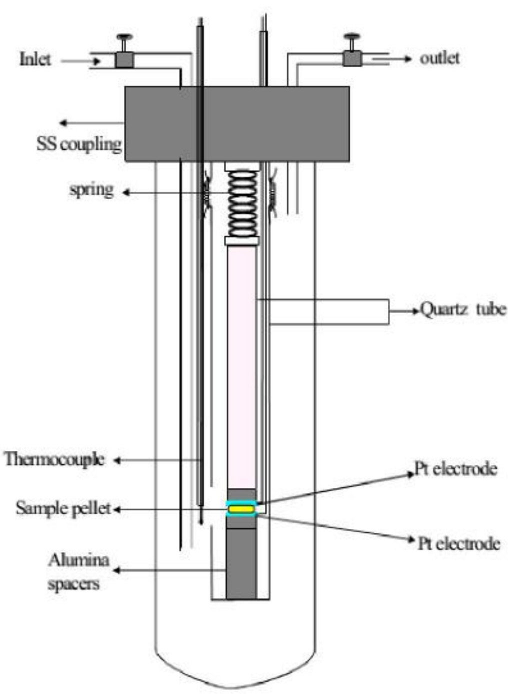

Figure 2.20. Schematics representation of the set up employed for electrical conductivity measurements using AC impedance method

With the help of springs, electrodes were pressed onto the sample. Platinum wires of 1 mm thickness attached to the platinum foils served as electrical leads and were taken through O-ring sealed feed-throughs after ensuring the electrical insulation. A stainless steel sheathed type K thermocouple was positioned close to the sample pellet. The SS coupling had tubes for gas inlet and outlets provided with needle valves. The whole set up was kept inside a furnace. The temperature of the sample was controlled to ± 1 ˚C at a chosen temperature using a PID controller. Impedance measurements for $AgInO_2$ pellet was carried out in the frequency range of 1 MHz and 1 Hz for the temperature range of 25 ˚C to 400 ˚C in air.

2.4.3. van der Pauw test facility

Four probe resistivity, carrier concentrations and mobility of thin film specimen were measured by Hall facility which operates on van der Pauw method. For this purpose a vacuum chamber made of SS provided with a necessary gas inlet, outlet and a sample holder mounted on the CF (ConFlat) flange provided with electrical feed-throughs are fabricated. The whole assembly is designed such that the chamber fits into the pole gap of 60 mm with a uniform magnetic field of 1T. The schematic diagram of the Hall measurement facility is shown in Figure 2.21. The SS chamber is fixed to the frame of the electromagnet and is provided with a tilt adjustment for the alignmentof the test specimen. The heater is designed such that there is no net magnetic field generated from the resistive heater.

The temperature of the sample is measured using a thermocouple mounted inside the chamber. The electromagnet is provided with a switching facility for automated reversal of the magnetic field. The magnetic field in the gap is measured using a Hall probe (Group 3, DTM – 150 Digital Teslameter, USA). Thermo EMFs generated by the longitudinal / transverse temperature gradients of the thin film also get super imposed on the Hall voltage which is eliminated by maintaining a uniform temperature with ± 2 ˚C variations and by reversing the current/voltage and magnetic field polarities. The photograph of an external view of the four-probe thin film facility used for measurements is shown in Figure 2.22.

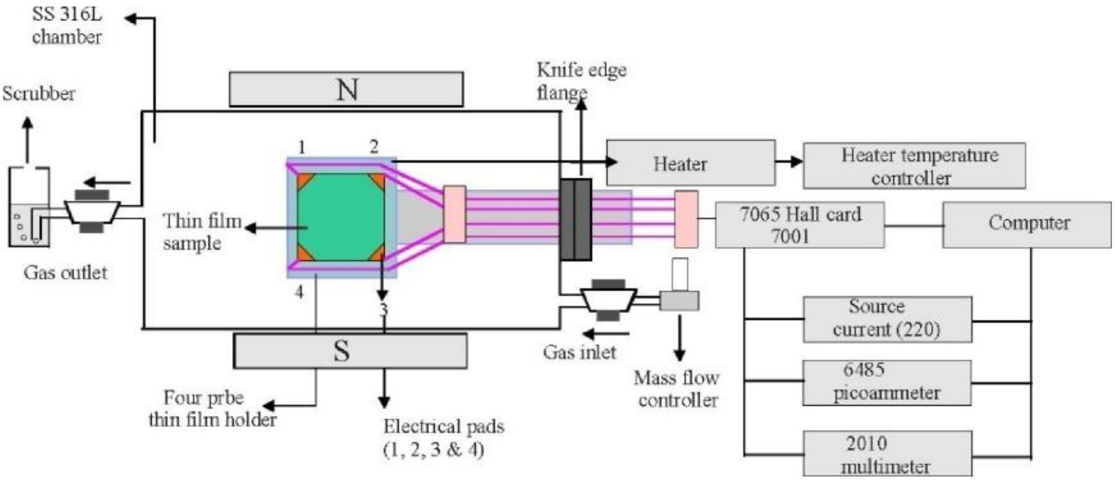

Figure 2.21. Schematic of Home built Hall measurement facility

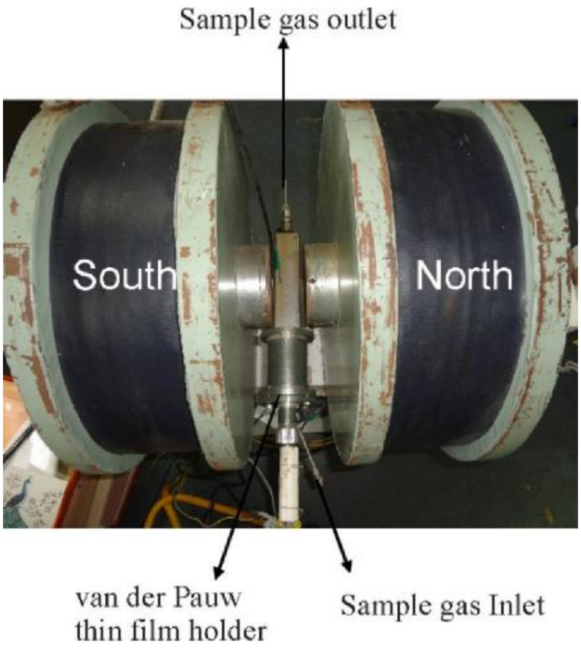

Figure 2.22. Photograph of four-probe van der Pauw thin film facility with an electromagnet for Hall measurement studies

A programmable current source (M/s Keithley Instruments, Model 220) is used for sourcing the current through any two of the four terminals and the voltage developed across the other two terminals is measured using a multimeter (M/s Keithley Instruments, Model

2010). A picoammeter (M/s Keithley Instruments, Model 6485) connected in series is used to measure the actual current passing through the thin film specimen. A Hall voltage card (M/s Keithley Instruments, Model 7065), which operates based on van der Pauw is used in the scanner (M/s Keithley Instruments, Model 7001) for switching the currents and voltage terminals through the software program. All these instruments are integrated and interfaced with a personal computer using a GPIB card. To avoid the voltage signal arising from the deviation from orthogonality of the magnetic field and current directions, the polarities of the current and magnetic fields were reversed and the measurements were taken again.

The four-probe resistivity, carrier concentrations and charge carrier mobility of PbS (in argon and NH_3 in argon) and $AgInO_2$ (in air and air containing H_2) thin films were measured using van der Pauw and Hall measurement facility at different temperatures (25 ˚C to 400 ˚C).

CHAPTER 3

Hydrothermal synthesis of phase pure silver indium oxide ($AgInO_2$) – A parametric optimization using factorial design approach

---

This chapter deals with the formation of hexagonal nanoplates of $AgInO_2$ mainly dominated by (00l) facets with no metallic Ag impurity, reported using a facile hydrothermal route at 180 ˚C using KOH as mineralizer by adopting a factorial design approach. Rietveld analysis of the powder XRD pattern and SAED confirms the rhombohedral system of $AgInO_2$. FE-SEM image shows a uniform hexagonal plate-like morphology with an average width of about 300 nm and thickness of 70 nm. XPS and EDX analysis confirm K^+ ion free $AgInO_2$. Temperature-dependent AC impedance measurements revealed an activation energy of 0.24 eV/f.u. Further, TG-DTA studies found that the compound is stable in air up to 595 ˚C.

3.1. Introduction

The birth of first delafossite, a copper and iron oxide mineral came to light in 1873 by Friedel [139] and its crystal structure was confirmed by Pabst in 1946 [140]. A comprehensive study on delafossite compounds represented by the general formula ABO_2 (A = Cu, Ag, Pt, Pd etc., B = Al, In, Fe, Ga etc.) was reported in 1971 by Shannon et al. [88, 141] and their crystallographic structures investigated in detail by Jansen et al. in 1987 [86]. After the discovery of p-type conductivity reported in 1997 in $CuAlO_2$ [81], the quest for examining the physical properties of other members of this family began.

The beauty exhibited by this new class of delafossite compounds lays in their layered two-dimensional (2D) crystal structure (low dimensionality) makes them widely studied for various applications [86, 87]. Such kind of low dimensional materials plays a vital role in thermoelectric energy conversions, an important technology for utilizing clean energy [84, 142]. Furthermore, in the field of semiconductor photocatalysis, the commonly used photocatalysts (TiO_2) absorbs only small amount of solar energy (UV light), which restricts its practical use in the visible region [143, 144]. However, the effort made by various researchers in finding the highly active visible-light-driven photocatalyst in view of the efficient utilization of solar energy resulted in the effective use of delafossite compounds as photocatalysts. The structural features adopted by them are related to the effective charge carrier separations and mobility that are advantageous to the photocatalytic activity [145, 146]. In addition to these, the discovery of p-type conductivity and transparency in delafossite type $CuAlO_2$ thin films established a new benchmark in transparent electronics due to their wide band gap (2.7 eV - 4.6 eV) resulting in the development of basic building block of transparent electrodes, pn-junction, solar cells, flat panel displays, semiconductor lasers and light-emitting devices [78, 147, 148].

Despite their promise for applications in various fields as transparent conductors, the interest failed to generate wider attention across the globe as evidenced by the number of publications and the primary reason for this is attributed to their poor amenability to synthesize in pure form. $AgInO_2$, an n-type semiconductor having high optical transparency has been reported to have stabilized under high pressure (3000 atm) and temperature (500 ˚C – 700 ˚C) for 24 h [88] which was further refined by Jansen et al. to 2000 atm and 580 ˚C for 96 h [86]. Claims of pure phase employing ion-exchange reactions with KNO_3 as an oxidizing flux with 50 % excess $AgNO_3$ followed by a post-synthesis removal of excess nitrates by water were made but the reproducibility of the latter results by other laboratories has not yet been successful as a trace amount of metallic Ag are always present [89]. Hydrothermal work reported by Croft et al. and Shannon et al. requires 50 % excess Ag_2O and increased basic conditions, followed by post-synthesis leaching with nitric acid to get phase pure product [88, 149]. Although post-synthesis leaching with nitric acid has offered some reduction of metallic silver, significant dissolution of the delafossite phase was also observed. In 2003, Shahriari and co-workers adopted a single-step hydrothermal route under 10 atm and claimed a significant improvement to the purity of $AgInO_2$ but the final product still had metallic Ag impurity [90] and followed by Dong et al. [145] report in 2009 indicates the phase pure $AgInO_2$ was always elusive. Recent publication on silver delafossites by Zwiener et al. mentioned limited solubility of starting materials that resulted in secondary phases [91]. Thereafter, no reports are available on the synthesis of $AgInO_2$ which almost concludes that the presence of trace amounts of metallic silver in the product is inevitable and prevents the evaluation of the physical properties of pure $AgInO_2$ with reasonable accuracy.

In this context, we report here the formation of phase pure $AgInO_2$ by hydrothermal method using $AgNO_3$ and Indium nitrate as starting precursors for the first time by conceiving the factorial design approach to identify the desirable conditions for the synthesis of phase pure product. The salient outcomes of the experimental results were presented in detail.

3.2. Experimental Details

3.2.1. Hydrothermal synthesis of $AgInO_2$

In a typical synthesis process, stoichiometric amounts of $AgNO_3$ and Indium were dissolved in 5 mL each of water and 16 M HNO_3 separately. The solutions were transferred to a Teflon-lined stainless steel autoclave of 100 mL capacity and the solution was stirred for 30 minutes by adding KOH and finally make-up to 50 mL. The vessel was sealed and the reaction was carried out by heating the autoclave to the desired temperature. After the dwell time, the autoclave was cooled to room temperature naturally and the resultant was washed several times with deionized water, ethanol and acetone and then dried in air. The details of alternate methods used for preparing $AgInO_2$ are discussed in Appendix 1.

For hydrothermal synthesis, three preparative conditions viz., temperature, dwell time[1] and concentration of KOH with mixed levels are considered to optimize the formation of phase pure $AgInO_2$ using factorial design approach. The detailed description on methodology of factorial analysis is presented in Appendix 2. Keeping in view the reported temperature window, KOH concentration and dwell time for formation of $AgInO_2$, experiments are performed at three different temperatures (150˚C, 180˚C and 210˚C) and two different levels of KOH concentration (4 M & 6 M) and dwell time (24 h & 60 h). The mixed-level design is shown in Table 3.1. The coded values of actual experimental conditions considered for the two design matrices are given in Table 3.2.

---

[1] Dwell time refers to the holding time at the reaction temperature

Table 3.1. Mixed level design for the synthesis of $AgInO_2$

Run No.	Temperature (°C)	Concentration of KOH (M)	Dwell time (h)
1	150	4.0	24
2	150	4.0	60
3	150	6.0	24
4	150	6.0	60
5	180	4.0	24
6	180	4.0	60
7	180	6.0	24
8	180	6.0	60
9	210	4.0	24
10	210	4.0	60
11	210	6.0	24
12	210	6.0	60

Table 3.2. Coded values of actual experimental conditions considered for the two design matrices

	Block I		Block II	
Experimental condition/coded value	-1	+1	-1	+1
Temperature (˚C)	150	180	180	210
Concentration of KOH (M)	4	6	4	6
Dwell time (h)	24	60	24	60

3.2.2. Characterization of $AgInO_2$

An adiabatic bomb calorimeter primarily used to probe the heat changes associated with the chemical reactions at high pressures and temperatures is employed to measure the in-situ changes in pressure at 150˚C, 180˚C and 210˚C during hydrothermal synthesis. A bomb cell of volume 10 mL containing half the volume of reactant mixture[2] was subjected to identical synthesis conditions and the changes in pressure inside the cell is continuously monitored at different temperatures for 24 h in independent experiments.

The X-ray diffraction (XRD) data were collected by operating the X-ray gun at 40 kV and 30 mA with Cu K_α radiation of 1.5418 Å for 2θ range from 10 to 80 degrees at a step size of 0.02 ° with an integration time of 2 s at each step. Patterns were indexed and the known phases were identified by comparing them with the standard ICDD powder diffraction files. The XRD patterns were subjected to Rietveld analysis [150] using the General Structure Analysis System (GSAS) [151] program with the EXPGU [152] graphical user interface software to study the structural refinement and also to quantify the impurity phases. The initial structural model of $AgInO_2$ phase was chosen as rhombohedral crystal system with $R\bar{3}m$ space group (Space group No. 166) with silver atom at Wyckoff 3a site (0.0, 0.0, 0.0), indium atom at Wyckoff 3b site (0.0, 0.0, 0.5), and oxygen atom at 6c site (0.0, 0.0, z). The initial model of In_2O_3 phase was chosen as a cubic crystal system with $Ia\bar{3}$ space group (Space group No. 206) containing two Indium atoms at Wyckoff 8b, 24d site positions and O atoms at Wyckoff 48e site positions. Similarly, Ag phase was considered as a cubic system with a space group of $Fm\bar{3}m$ (Space group No. 225) containing silver atom at Wyckoff 4a sites. The quantitative phase analysis of powder mixtures was carried out from the refined scale factors as per the standard procedure reported in the GSAS [151]. The weight fractions (W_p) of each phase was calculated from the scale factors using the Equation 3.1:

$$\mathbf{W_p = \frac{S_p\, m_p}{\sum_{p=1}^{Np} S_p\, m_p}} \qquad \mathbf{(3.1)}$$

---

[2] The aspect ratio of volume of autoclave to the reactant mixture is maintained.

where S_p is the value of scale factor for the respective phase, and m_p is unit cell mass of the particular phase p of the N phases present in the sample. The background of the pattern was modeled with shifted Chebyschev function and the profile peaks were fitted as a linear combination of Gaussian / Cauchy Pseudo-Voigt model. Field emission scanning electron microscope and transmission electron microscope were used to inspect and record the morphology, the elemental composition, the crystal structure of single crystals, identify the impurity phases if any and the distribution of the latter. X-ray photoelectron spectroscopy measurements (XPS) were carried out to determine the valence states of Ag, In and any possible substitution of potassium for Ag. The bandgap was estimated from the UV-Visible absorption spectrum of $AgInO_2$ recorded in the wavelength range of 200 nm – 1000 nm. The TG-DTA measurements were carried out in a dynamic air flow of 5 mL/min in the temperature interval of 30 ˚C to 750˚C to analyze its thermal stability. The electrical conductivity of $AgInO_2$ was measured in air using impedance spectroscopy in the frequency range of 1 MHz to 10 Hz by a frequency response analyzer coupled with an electrochemical interface for the temperature interval from 160 ˚C to 400˚C and the data were analyzed using the Z-view2 (version 2.8d).

3.3. Results and Discussion

3.3.1. Factorial analysis

The preliminary X-ray analysis of the samples prepared at different experimental conditions (Table 3.1) revealed that runs corresponding to 5 and 6 yielded phase pure product. The factorial analysis performed by splitting the experimental runs into two blocks corresponding to two levels of each factor. Two design matrices (Tables 3.3 & 3.4) of two levels each were constructed by considering response as the fractional intensities of the highly oriented peaks[3] of the phases $AgInO_2$, Ag and In_2O_3, calculated from the X-ray diffraction patterns of the respective samples prepared under the conditions shown in Table 3.2. The -1 and +1 are coded values for low and high levels of the different experimental conditions viz., temperature, dwell time and concentration of KOH.

Table 3.3. Design matrix for the first block of experiments

Run No.	Intercept	Temperature (A)	Concentration of KOH (B)	Dwell time (C)	A×B	B×C	C×A	A×B×C	Response
1	1	-1	-1	-1	1	1	1	-1	91.11
2	1	-1	-1	1	1	-1	-1	1	97.07
3	1	-1	1	-1	-1	-1	1	1	96.99
4	1	-1	1	1	-1	1	-1	-1	98.01
5	1	1	-1	-1	-1	1	-1	1	100.00
6	1	1	-1	1	-1	-1	1	-1	100.00
7	1	1	1	-1	1	-1	-1	-1	97.48
8	1	1	1	1	1	1	1	1	97.82

Table 3.4. Design matrix for the second block of experiments

Run No.	Intercept	Temperature (A)	Concentration of KOH (B)	Dwell time (C)	A×B	B×C	C×A	A×B×C	Response
5	1	-1	-1	-1	1	1	1	-1	100.00
6	1	-1	-1	1	1	-1	-1	1	100.00
7	1	-1	1	-1	-1	-1	1	1	97.48
8	1	-1	1	1	-1	1	-1	-1	97.82
9	1	1	-1	-1	-1	1	-1	1	82.48
10	1	1	-1	1	-1	-1	1	-1	79.99
11	1	1	1	-1	1	-1	-1	-1	81.81
12	1	1	1	1	1	1	1	1	82.86

---

[3] $AgInO_2$ @ $2\theta = 28.343$, Ag @ $2\theta = 38.121$ and In_2O_3@ $2\theta = 30.586$

The main effects and interactions are calculated and shown in Table 3.5. The dwell time shows least significance in the first block of experiments. Even though temperature raise looks like a favourable factor, its interaction with the concentration of KOH has opposite effect to the same extent. The combined effect of temperature vs. concentration of KOH is shown in Figure 3.1, that indicate the temperature of 180 °C and 4 M KOH are the more suitable conditions for the formation of pure $AgInO_2$.

Table 3.5. Calculated effects and standard errors for the design matrices (Tables 3.3 & 3.4). Numbers in bold are of significance for consideration

	First block of experiments	**Second block of experiments**
Effect	**Estimate ± standard error**	**Estimate ± standard error**
Average	97.31 ± 2.77	90.31 ± 9.19
Main effects		
Temperature (A)	**3.03 ± 1.88**	**-17.04 ± 1.09**
Concentration of KOH (B)	0.53 ± 1.88	-0.63 ± 1.09
Dwell time (C)	1.83 ± 1.88	-0.27 ± 1.09
Two-factor interactions		
A×B	**-2.88 ± 1.32**	**1.73 ± 0.78**
B×C	-1.15 ±1.32	**0.97 ± 0.78**
C×A	-1.66 ±1.32	-0.44 ± 0.78
Three-factor interactions		
A×B×C	1.32	0.80

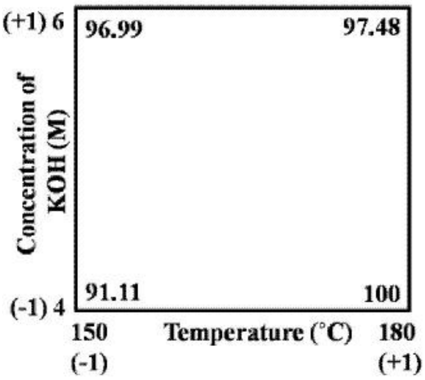

Figure 3.1. Temperature - concentration of KOH interaction for the first block of experiment. The numbers inside the corners are the average of the responses at respective levels.

Calculated effects for the second block of experiments where the temperature was raised from 180 °C to 210 °C by keeping other two factors at same levels as in the first block indicate that increase in temperature results in the composite mixture instead of pure phase. The high value of temperature effect dominates the positive contribution from interaction terms (A×B and B×C). Overall, the pure phase formation conditions derived from X-ray diffraction intensities suggest 180 °C and 4 M KOH as the best conditions with no dependence on dwell time (24 h to 60 h).

3.3.2. Structural, morphological and optical studies

The XRD pattern of $AgInO_2$ prepared at 180°C for 24 h using 4 M KOH (run 5) is in agreement with the Rhombhohedral $R\bar{3}m$ (166) system of $AgInO_2$. It is worth noting that the relative intensity of (006) to (012) facets (i.e, $I_{(006)}/I_{(012)}$ = 0.40, ICDD # 96-150-9398), is increased to 3.26 indicating texturing. The structural refinement and the quantitative estimation of phases were carried out by Rietveld analysis. Unit cell parameters, zero shift and oxygen positional parameter were refined along with background points. Isotropic temperature factors of Ag, In and O were refined in the consecutive refinement cycles. The Rietveld refined X-ray diffraction profile of $AgInO_2$ is shown in Figure 3.2. The refined unit cell parameters of $AgInO_2$ are a = 3.27668(10) Å and c = 18.8838(7) Å with the unit cell volume of 175.585(14) Å^3 suggests that the refined results are reliable. The atomic coordinates of $AgInO_2$ phase are given in Table 3.6 and the reliability factor of the profile fit as standard R_p, R_{wp} values are reported to be 0.0408 and 0.0570 respectively. The quantitative estimation indicates the presence of no secondary phases.

Table 3.6. Atomic coordinates obtained experimentally from the structural refinement for $AgInO_2$

Atom	x	y	z	Uiso
Ag	0.0	0.0	0.0	**0.0299(28)**
In	0.0	0.0	0.5	**0.0272(29)**
O	0.0	0.0	**0.1097(4)**	0.025

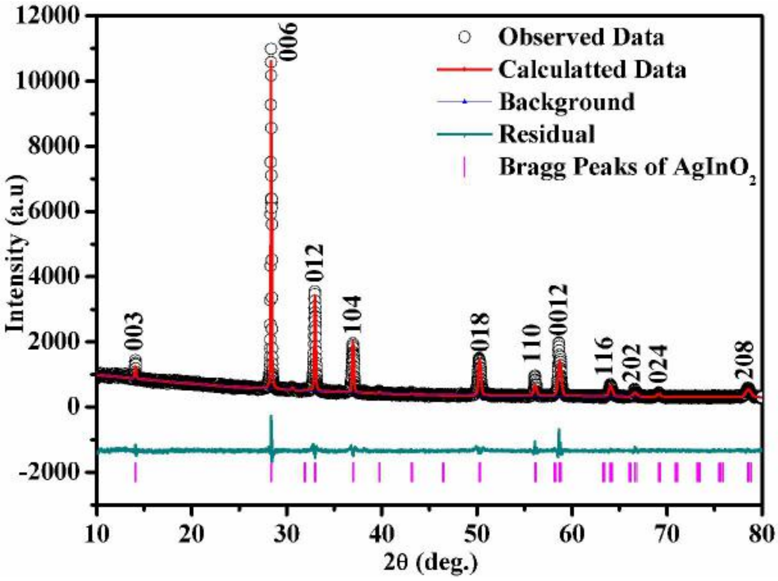

Figure 3.2. Rietveld refined powder XRD pattern of phase pure $AgInO_2$

Figure 3.3 (a) shows the panoramic FE-SEM image of $AgInO_2$ consists of hexagonal-shaped platelike morphology with an average diagonal width of ~ 300 nm. Figure 3.3 (b) shows the side view of the $AgInO_2$ crystal, from which the thickness can be determined to be

~ 70 nm. EDX analysis performed on the hexagon confirmed the atomic ratio of Ag to In is 0.98, close to the stoichiometric value and no evidence of potassium.

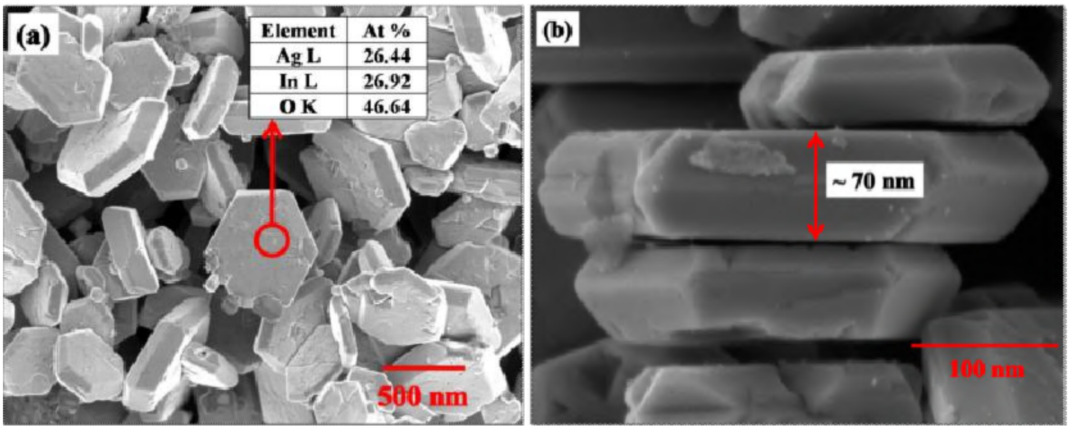

Figure 3.3. FE-SEM images of as-prepared phase pure $AgInO_2$ (run 5) **(a)** a panorama (inset corresponding EDX values) and **(b)** side view

The crystal system of $AgInO_2$ was further characterized by TEM, HRTEM and SAED. The analysis was carried out on a single grain of $AgInO_2$ and the as-obtained crystals have well-defined facets with a hexagonal plate-like shape (Figure 3.4 (a)). The SAED pattern (Figure 3.4 (b)) recorded on the surface of the hexagon shows diffraction spots along the [001] zone axis, indicating the single crystalline feature of $AgInO_2$ crystals with (1-20), (2-10), (110), and (300) atomic planes. This confirms that the faceted $AgInO_2$ single crystal has the dominantly exposed planes of (001), which is the only crystal plane normal to all the above-indexed crystal planes and the results are in agreement with that of XRD results. Figure 3.4 (c) shows a lattice resolved HRTEM image of an $AgInO_2$ crystal, in which the lattice can be determined to be the (006) crystal plane with a d spacing of 0.314 nm.

According to the 3D plate-like morphology of $AgInO_2$, the hexagonal faces correspond to (001) plane with (100), (-110) and (010) as edge facets. HRTEM image recorded over the edge showed the lattice fringes with the interplanar spacing of 0.16 nm corresponds to the (110) direction (Figure 3.5 (a)). The corresponding rhombus like SAED implies the presence of (012), (10-2), (1-1-4), (110) planes along the [-22-1] zone axis (Figure 3.5 (b)). Unlike earlier reported, no silver particles segregated at the surface of the $AgInO_2$ grain could be detected on the surface of the $AgInO_2$ [90]. The percentage fraction of the surface area of the dominantly exposed (001) facets to the total was estimated to be 52 % which is higher than the theoretical estimate of 2 % for isotropical specimen.

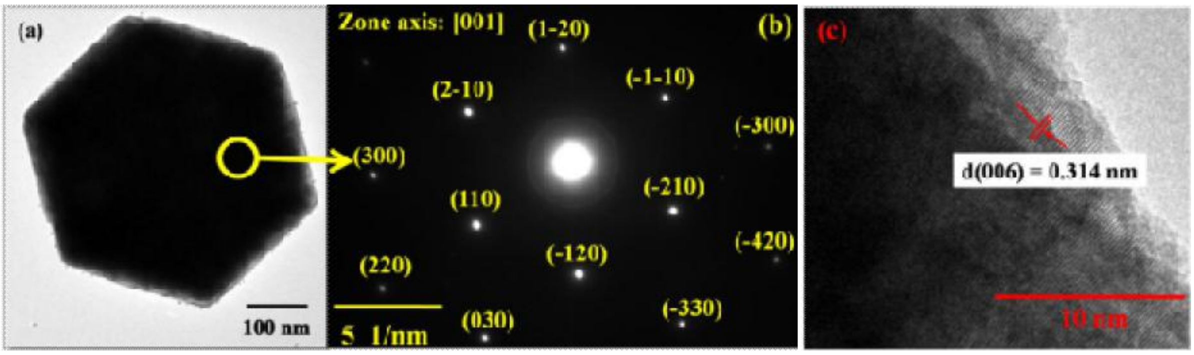

Figure 3.4. (a) High magnification TEM image of phase pure $AgInO_2$; **(b)** SAED pattern along the [001] zone axis and **(c)** high-resolution TEM recorded on the surface of the hexagon

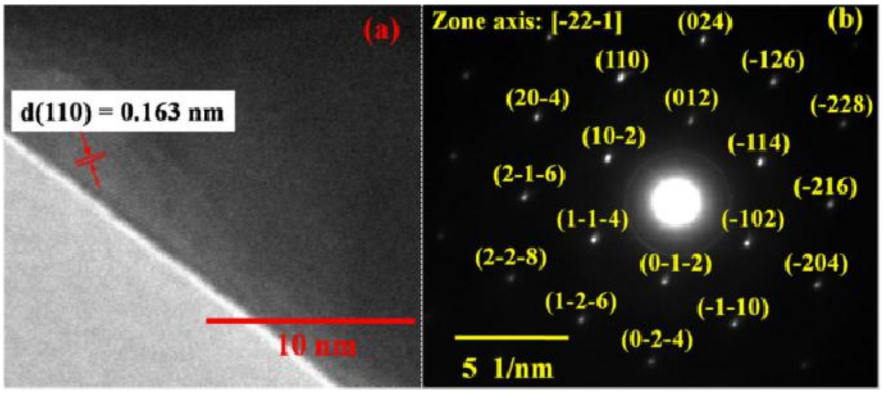

Figure 3.5. (a) High-resolution TEM recorded on the edges of the hexagon and **(b)** corresponding SAED pattern

XPS survey spectrum of $AgInO_2$ nanoplates shows the presence of only Ag, In, C and O (Figure 3.6 (a)). The selected area high-resolution spectrum of Ag 3d fitted with two components viz. $3d_{5/2}$ and $3d_{3/2}$ using the intensity ratio of 3:2. The fit data yielded the peak positions at 367.8 and 373.8 eV respectively with a spin-orbit coupling parameter (SOCP) of 6.0 eV (Figure 3.6(b)). Dong et al. and Tjeng et al. reported 367.6 eV and 373.6 eV with SOCP of 6 eV for the singly charged silver ion [145, 153]. Similarly, In 3d components were fitted with Gaussian curves for $3d_{5/2}$ and $3d_{3/2}$ using the intensity ratio of 3:2 resulted in peak positions at 444.4 eV and 452.0 eV respectively (Figure 3.6 (c)). The measured binding energies and SOCP value of 7.6 eV of In are in concurrent with the literature is indicative of its +3 oxidation state [145, 154]. The O 1s pattern shows three peaks viz., an intense peak at 529.7 eV corresponding to the lattice oxygen, a small peak at 531.5 eV attributed to the absorbed O_x^- species and a third weak peak at 533.5 eV ascribed to adsorbed moisture or hydroxyl groups (Figure 3.6 (d)) [145].

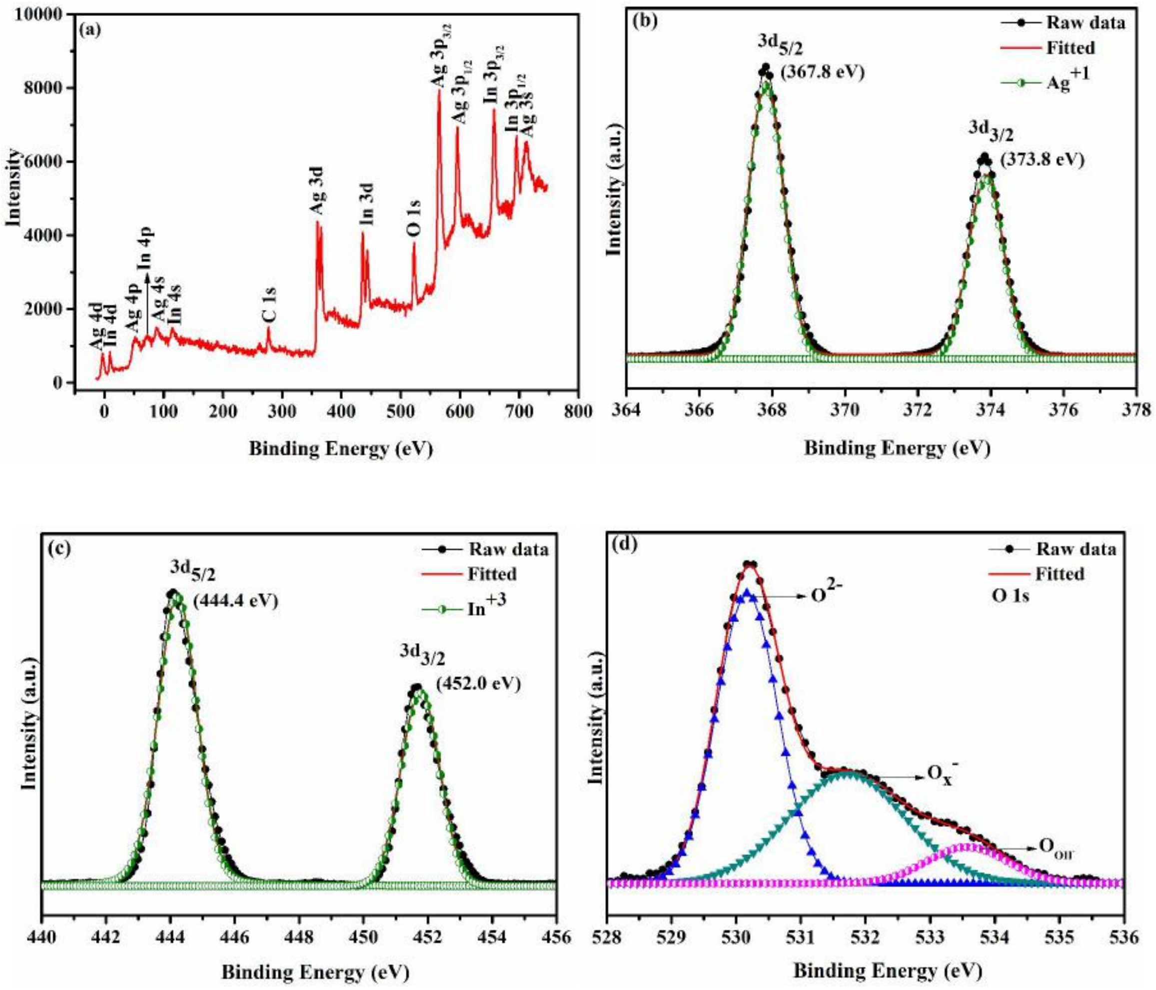

Figure 3.6. XPS spectra of $AgInO_2$ nanoplates **(a)** Survey, **(b)** Ag 3d, **(c)** In 3d & **(d)** O 1s

Based on the Tauc plot deduced from absorption spectra (inset of Figure 3.7), the optical bandgap (E_g) was estimated. $AgInO_2$ being an indirect semiconductor [91, 145, 146], the plot of $(\alpha h\upsilon)^{1/2}$ versus photon energy (hυ) (Figure 3.7) shows a straight line and the intercept to hυ axis after extrapolation gives rise to a bandgap of 2.50 eV which is in agreement with the literature data [91, 145, 146, 155].

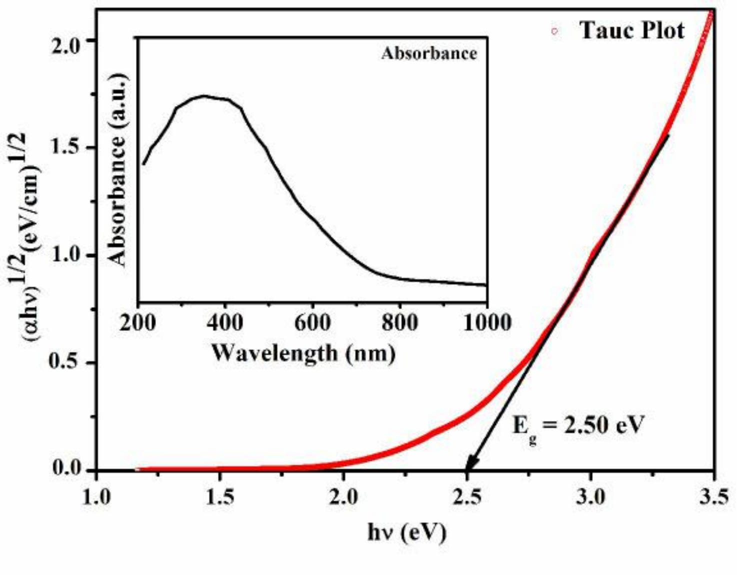

Figure 3.7. UV - Visible absorption spectrum (inset) with Tauc plot of $AgInO_2$

3.3.3. Thermal and electrical measurements

The TG-DTA pattern (Figure 3.8) shows a marginal weight loss of 0.3 % up to the temperature of 595 °C is possibly due to the oxygen non-stoichiometry of the compound. A noticeable weight loss of about ~ 3 % found in the temperature range of 595 °C – 680 °C accompanied by an endothermic peak indicates the decomposition of $AgInO_2$ into Ag and In_2O_3 [88] that is in agreement with the theoretical value.

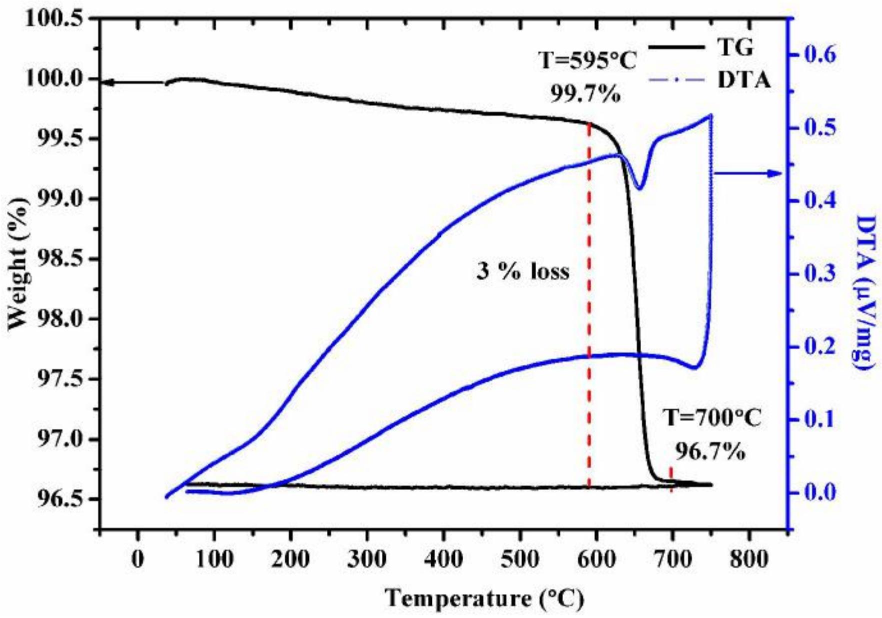

Figure 3.8. TG-DTA pattern of phase pure $AgInO_2$ hexagonal nanoplates

Figure 3.9 (a) shows the typical Nyquist plots of $AgInO_2$ recorded in the frequency region of 1 MHz to 10 Hz as a function of temperature in air ambient. The material exhibits a single semicircle throughout the temperature range of investigation (160 °C – 400 °C). The data was curve fitted using the equivalent circuit as shown in the inset of Figure 3.9 (a). From the real axis intercept, the resistance of the sample was calculated and the data is presented in Table 3.7. The systematic decrease in the resistance with increase in temperature indicating the semiconducting nature of the material. This resistance value agrees well with that of other silver delafossites reported by Shannon et al. [141]. The temperature dependence of conductivity (Figure 3.9 (b)) shows the Arrhenius behaviour with an activation energy of 0.24 eV/f.u which matches with that of earlier reports [84, 156].

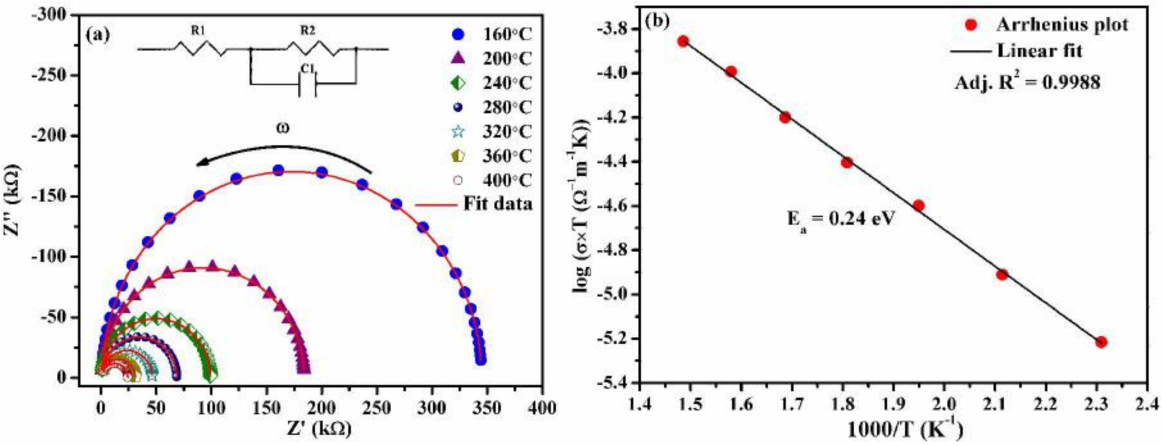

Figure 3.9. (a) Nyquist plot of $AgInO_2$ at different temperatures in air; Inset shows the equivalent circuit for fitting the impedance data and **(b)** log (σ×T) vs 1000/T of $AgInO_2$

Table 3.7. Calculated resistance and capacitance of $AgInO_2$ using Z-view2 program

S.No.	Temperature (˚C)	R1 (Ω)	C1 (pF)	R2 (kΩ)
1	400	564.9	80.2	23.7
2	360	627.4	79.0	30.5
3	320	654.6	78.5	45.9
4	280	664.9	78.5	67.9
5	240	682.9	78.4	98.4
6	200	692.9	78.9	183.8
7	160	745.1	78.6	343.7

3.3.4. Mechanism of phase pure formation of $AgInO_2$

In contrast to the results of $AgInO_2$ prepared at 4 M KOH and 180 °C, the samples processed at other conditions (Table 3.1) showed segregation of small grains of In_2O_3 and Ag along with the hexagonal $AgInO_2$ grains.

The sample processed at 180 °C with 6 M KOH showed segregation of small grains of In_2O_3 along with the hexagonal $AgInO_2$ platelike grains having an average width of about 800 nm and thickness less than 30 nm which correlates with that of factorial design. EDX analysis on grains marked in the image confirms the composition of the large hexagonal grain matching with that of $AgInO_2$ while the smaller grains are of In_2O_3 (Figure 3.10 (a & b)).

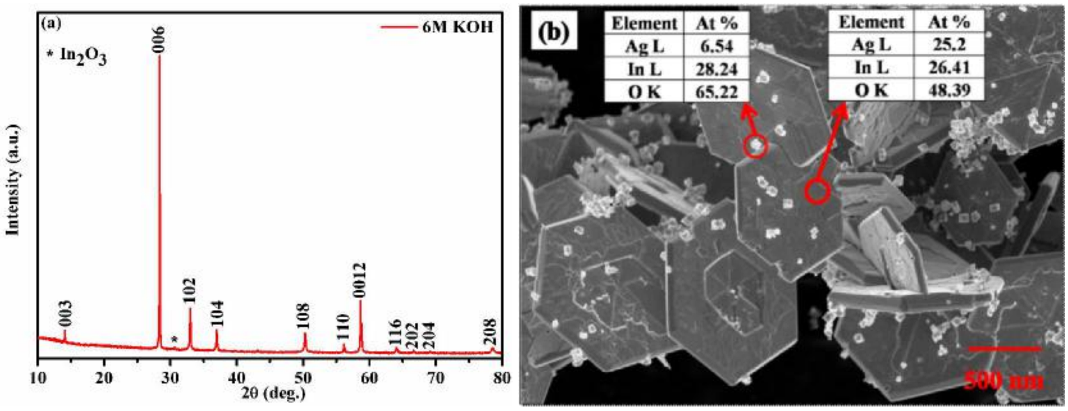

Figure 3.10. (a) Powder XRD pattern and **(b)** FE-SEM image of $AgInO_2$ prepared using 6M KOH at 180 °C for 24 h (run 7)

Having fixed the concentration of KOH to be 4 M, the processing temperature was varied from 150 °C to 210 °C in steps of 30 ˚C. Sample processed at 150 °C shows the evidence for the presence of In_2O_3 and Ag whereas the sample processed at 210 °C contains relatively large amounts of Ag and In_2O_3 as impurity phases in addition to $AgInO_2$ (Figure 3.11 (a) & (b)). FE-SEM images reveal smaller grains distributed on the regular hexagon of $AgInO_2$. Their EDX pattern recorded at two different locations as marked in their respective images reveal that the smaller grains are In_2O_3, whereas the larger hexagons were $AgInO_2$ (Figure 3.12 (a) & (b)). The processing duration (i.e. 24 h – 60 h) did not have any significant influence on the purity of the sample (Figure 3.13 & 3.14).

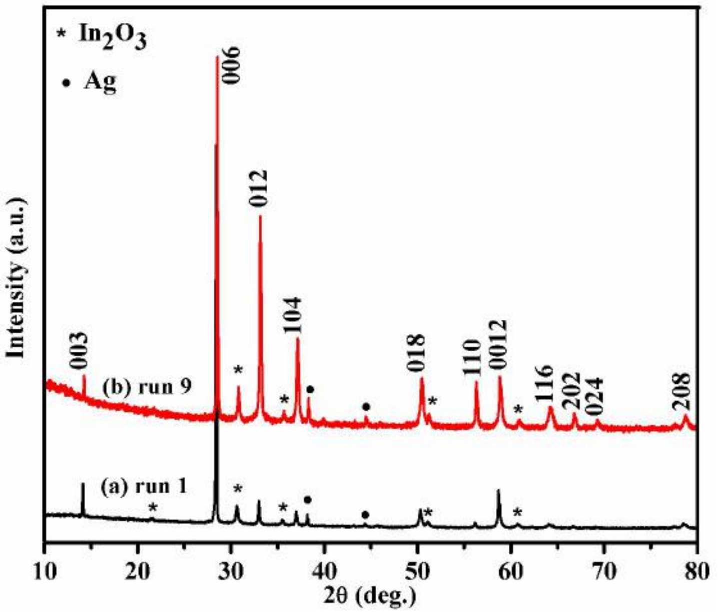

Figure 3.11. XRD patterns of samples obtained at **(a)** 150 °C (run 1) and **(b)** 210 °C (run 9) for 24 h with 4M KOH

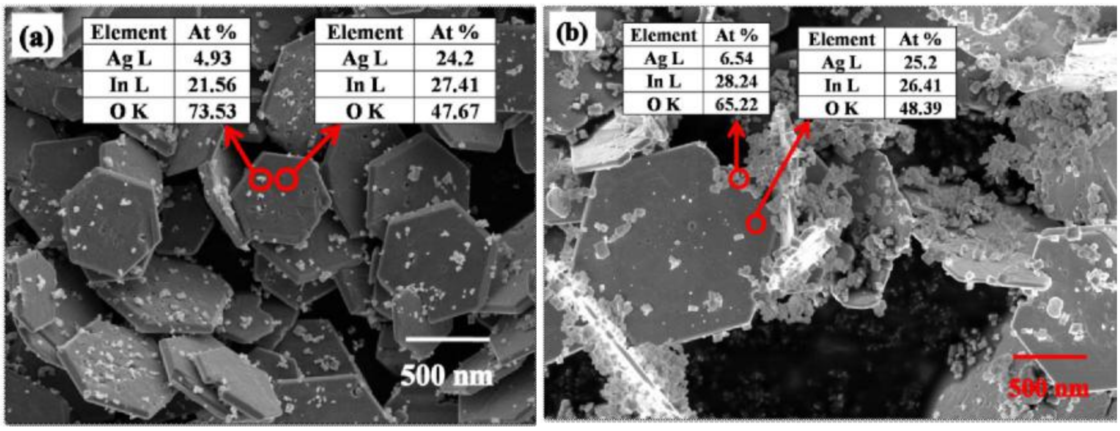

Element	At %
Ag L	4.93
In L	21.56
O K	73.53

Element	At %
Ag L	24.2
In L	27.41
O K	47.67

Element	At %
Ag L	6.54
In L	28.24
O K	65.22

Element	At %
Ag L	25.2
In L	26.41
O K	48.39

Figure 3.12. Panoramic FE-SEM images of samples obtained at **(a)** 150 °C (run 1) and **(b)** 210 °C (run 9) for 24 h with 4M KOH

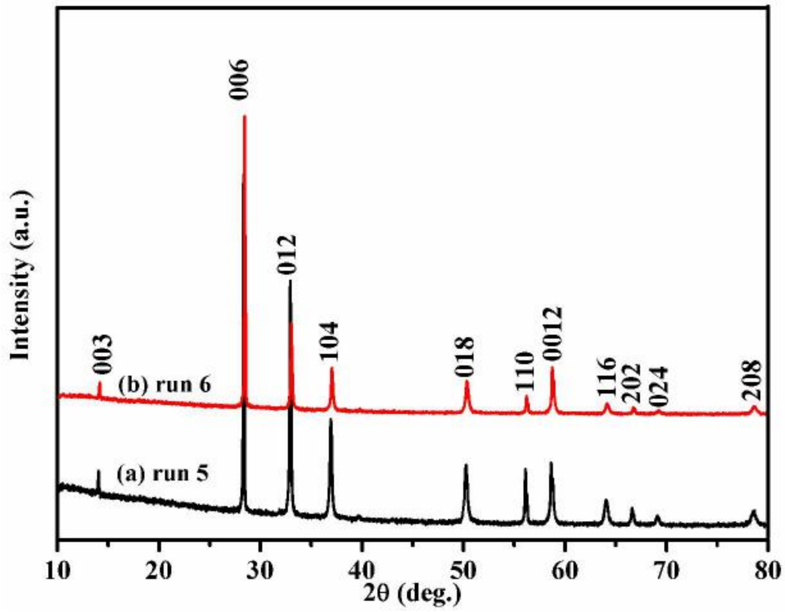

Figure 3.13. XRD patterns of samples obtained at **(a)** 24 h (run 5) & **(b)** 60 h (run 6) for 180 °C with 4M KOH

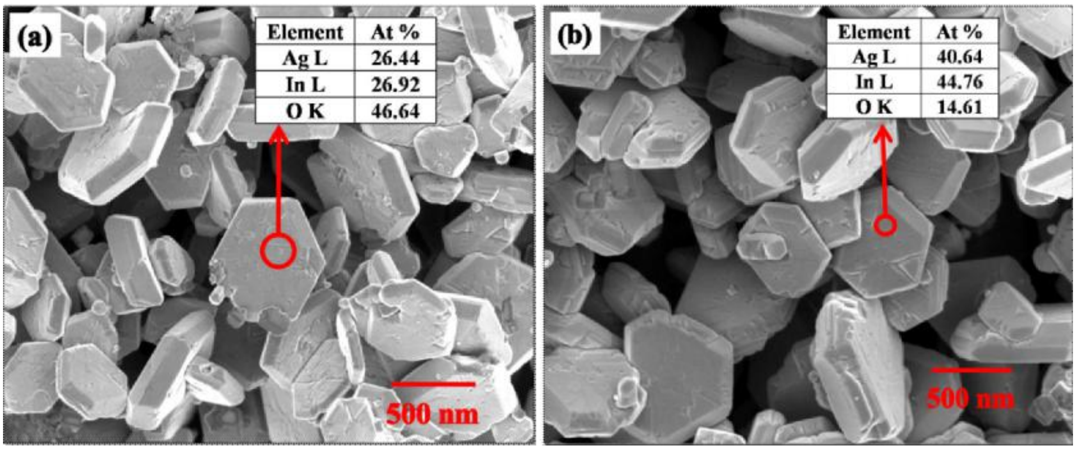

(a)

Element	At %
Ag L	26.44
In L	26.92
O K	46.64

(b)

Element	At %
Ag L	40.64
In L	44.76
O K	14.61

Figure 3.14. FE-SEM images of samples obtained at **(a)** 24 h (run 5) & **(b)** 60 h (run 6) for 180 °C with 4M KOH

The evolutionary stages of getting the phase pure $AgInO_2$ hexagonal nanoplates have to be understood by visualizing the growth mechanism. The preliminary step is to avoid or suppress the precipitation of metallic silver. This is anticipated by stabilizing the as-precipitated $Ag(OH)_2^-$ with Ag in +1 state that requires the presence of a large amount of hydroxyl ions in water to act as a common ion which necessitates the addition of a strong base. Although LiOH, NaOH & KOH are the candidates, the choice of KOH preferred to LiOH/NaOH stems due to the low probability of K^+ ion into the $AgInO_2$ structure [157]. Secondly, the solubility of both $Ag(OH)_2^-$ and $In(OH)_3$ in aqueous solution are necessary for the hydrothermal synthesis [108]. The Pourbaix diagrams for Ag - H_2O system over a wide range of temperature (25 °C − 300 °C) have shown that Ag^+ ion in alkaline conditions is stabilized by the formation of the aqueous soluble $Ag(OH)_2^-$ species [158]. The stability for this species becomes greater as the temperature increases and further, the alkaline solubility of Ag^+ ions in the aqueous solution is notably high ($10^{-2.5}$ mol/L) [87]. Similarly, $In(OH)_3$ has the maximum alkaline solubility of 6×10^{-2} mol/L [87, 88]. Moreover, it has been reported that the presence of KNO_3 in the solution suppresses the formation of Ag metal [89, 156]. Thirdly, both $Ag(OH)_2^-$ and $In(OH)_3$ have to be stabilized at processing temperatures of about 150 °C – 200 °C which is accomplished by the high vapour pressure of water in the hydrothermal reactor. The blank pressure inside the bomb calorimeter of volume 10 mL containing half the volume of water under the same conditions was measured to understand its effect during synthesis. The measured pressures were 4.8 atm, 9.2 atm and 18 atm at 150 ˚C, 180 ˚C and 210 ˚C respectively. By manipulation of temperature and pH, the reaction proceeds until all the starting materials are progressively dissolved in the solvent which then leads to the formation of pure $AgInO_2$. Although all the synthesis temperatures viz., 150 ˚C, 180 ˚C and 210 ˚C yielded $AgInO_2$, only the sample processed at 180 ˚C and 4 M KOH yielded the phase pure $AgInO_2$.

3.4 Conclusions

Hexagonal nanoplates of phase pure $AgInO_2$ was successfully prepared via hydrothermal route. In this synthesis, the combined effect of 180 ˚C & 4 M KOH with no dwell time dependency between 24 h and 60 h are the favoured conditions for phase purity. Rietveld, FE-SEM and HRTEM results revealed that the prepared $AgInO_2$ possessed a rhombohedral crystal structure with dominantly exposed *(00l)* facets and no detectable impurities. XPS confirms the absence of K^+ ions with Ag, In and oxygen to be +1, +3 and -2 respectively. The electrical conductivity shows that the activation energy for electrical conduction is 0.24 eV/f.u.

CHAPTER 4

Thick film of $AgInO_2$: Response towards wide range of hydrogen, repeatability, selectivity and long term performance

This chapter deals with wide range H_2 sensing behavior and the long term performance of thick films of $AgInO_2$ delafossite, composed of hexagonal nanoplates. Prepared material made in the form of a thick film using a screen printing technique. The material responds from 1 ppm to 10000 ppm of H_2 at the operating temperature of 360 ˚C at different humidity levels. The material exhibits a high degree of selectivity and repeatability without any significant drift in the baseline. Presence of trace levels of metallic (Ag) or oxide (In_2O_3) impurities degrades its sensitivity and selectivity towards hydrogen.

4.1. Introduction

Devices for detecting hydrogen from trace to percentage levels under highly humid conditions of the harsh industrial ambient are desirable for applications in the nuclear and other industries. Most of the commercial sensors have a specific working range with a relatively short life span and exhibit continuous baseline drifts under humid conditions. Rugged, reliable sensing devices with reasonable lifetimes and broad working range are preferred for nuclear reactors and fuel storage facilities to monitor hydrogen generated from radiolysis of water as most of the commercial chemical sensors with a limited working range do not work satisfactorily. For reprocessing industry, H_2 has to be monitored in the presence of NO_x, a corrosive gas which can enforce a chemical attack besides interfering with the H_2 sensing process. Although a commercial device with a single sensing element covering a broad working range of ppm to percentage levels is not available; the integrated module comprising an array of sensors each with specific range have also been reported.

In general, metal oxide gas sensors used for environmental monitoring, respond to other gases apart from the intended analyte, despite having the advantages of high sensitivity, low cost, simple design and fast response time [1, 159-161]. Dopants and additives to promote specific catalytic interaction along with the operating temperature to exploit the kinetics of the specific chemical interaction are used to improve the selectivity [160, 162-165]. However, the major drawback of such materials is the poisoning effect from hydroxyl groups formed during H_2 sensing and the prevailing humidity levels interfering with the long term performance causing drifts in the baseline. This enforces frequent calibrations and therefore these types of sensors are not desirable for the intended application. While the search for highly selective new semiconducting binary oxides is in progress, the scope of expanding the search domain to include ternary and quaternary oxides with better gas sensing characteristics is also considered. Based on certain empirical guidelines, some ternary oxides have also been screened for certain analyte gases. In this context, transparent conducting (TCOs) delafossites having wide bandgaps with scientific and technological importance for potential use in the field of light-emitting diodes, touch display panels, solar cells, flat panel displays, heaters, defrosters, energy-efficient windows, etc. are promising candidates for gas sensing investigation [78-82, 84, 147, 148]. Despite their promise for applications in the above-listed fields, the interest failed to generate the desired enthusiasm across the globe largely due to the obstacles faced during the synthesis in pure form as most of them require high pressures. In this context, $AgInO_2$, a semiconductor having a tunable bandgap from 1.35 to 2.26 eV [78] is reported to stabilize at a hydrothermal pressure of about 9 bar, drew our attention because of its exceptional stability at hydrothermal pressures. A few other delafossite compounds viz. $CuCrO_2$ [166], $CuAlO_2$ [167], $AgFeO_2$ [168] & $AgAlO_2$ [169] have been examined for ozone, ethanol and ammonia sensing which prompted us to look into $AgInO_2$ for the intended application under humid conditions and to the best of author’s knowledge, it's gas sensing properties are not reported till date.

In this contribution, hexagonal nanoplates of phase pure $AgInO_2$, prepared via a hydrothermal reaction, were configured as thick films using screen printing technique and their sensing characteristics for a wide range of H_2 under different humidity level is reported. The mechanism of sensing is probed through X-ray photoelectron studies.

4.2. Experimental Details

4.2.1. Thick film preparation

For gas sensing studies, firstly the as-synthesized powder of $AgInO_2$ (described in Chapter 3) and its composite ($AgInO_2$+Ag+In_2O_3) were mixed with 2 vol% polyethylene glycol to form a paste. The resulting paste was screen printed on an alumina substrate to form a sensing layer and the thick films were heated at 400 ˚C for 24 h at a heating rate of 1

˚C/min. The thick films were characterized using X-ray diffraction (XRD), FE-SEM and HR-TEM. The thickness of the thick films was measured using profilometer.

4.2.2. Gas sensing studies

The thick film of $AgInO_2$ was mounted in an in-house designed and fabricated sensor assembly of 75 mL capacity, with a provision for gas inlet and outlet as shown in Figure 2.16 (Chapter 2). The desired operating temperature of the sensor was maintained by adjusting the current through the Pt heater by a voltage source. The response to different analytes like H_2, NO_2, NH_3, CH_4, LPG and formaldehyde was measured at different operating temperature in the range of 200 ˚C to 400 ˚C at an interval of 40 ˚C. To optimize the temperature of operation, an adequate concentration of analyte gas was injected into the test chamber through an injection port and the transient changes in resistance in the presence of gas were continuously monitored using a data logger. The chamber was then purged with air through an air admittance valve so that the resistance of the sample retraces back to the original value. Gas sensing response for a given concentration of gas defined as

$$\mathbf{Response} = \left(\frac{\mathbf{R_a}}{\mathbf{R_g}}\right) \tag{4.1}$$

where R_a and R_g are the resistances of the $AgInO_2$ in air and the presence of an analyte respectively. After finding the suitable operating temperature, thick films of $AgInO_2$ was calibrated for highly sensitive gas for various concentrations. The short and long term repeatability of the $AgInO_2$ thick film sensor was tested by injection of known concentration of the selective analyte several times within a period of about 6 months. The sensors response for the relative humidity of 60 to 80 % was carried out. The baseline resistance value of the $AgInO_2$ thick film was recorded for 6 months at the optimum temperature of sensing.

4.2.3. X-ray photoelectron spectroscopic studies

X-ray photoelectron spectroscopy (XPS) was used to record the survey and selected area scans. A special reaction chamber attached to the XPS system for heating the thin film using an IR lamp to the desired temperature (360 ˚C) in flowing air/analyte. Photoelectron spectra of $AgInO_2$ specimen were recorded before exposure to hydrogen at room temperature. The same specimen was taken to the reaction chamber and was exposed to 1500 ppm of H_2 at 360 ˚C for about 10 minutes. The $AgInO_2$ specimen was cooled to room temperature under the same condition and the reaction chamber was evacuated. The $AgInO_2$ specimen exposed to H_2 was transported back to the analysis chamber without exposure to air ambient. The recorded spectra were corrected with respect to the C 1*s* (284.8 eV). A Shirley background subtraction procedure was adopted before processing the XPS data.

4.3. Results and Discussion

4.3.1. Structural and morphological studies

Chapter 3 described the preparation of phase pure $AgInO_2$ with detailed structural and morphological characterization for the first time using nitrate precursors under narrow pH conditions, which was otherwise elusive till date [83]. The screen-printed thick film of $AgInO_2$ was characterized using powder XRD, FE-SEM and HR-TEM with SAED pattern and the results are shown in Figure 4.1 & 4.2 respectively. All the diffraction peaks (Figure 4.1) are indexed in terms of the rhombohedral system of $AgInO_2$ [Space group: $R\bar{3}m$ (166), ICDD card no. 96-150-9398]. Analysis of the diffraction pattern indicated that the (006) peak of $AgInO_2$ was significantly stronger than the standard diffraction pattern. The degree of the crystal facet exposure was calculated by the relative texture coefficient (TC_{hkl}) of a certain crystal facet using the formula [170]:

$$\mathbf{TC_{006}} = \frac{\mathbf{I_{006}/I^{0}_{006}}}{\mathbf{I_{006}/I^{0}_{006} + I_{012}/I^{0}_{012}}} \tag{4.2}$$

where I_{hkl} is the measured intensity of the (hkl) facet and I°_{hkl} is the corresponding value of the standard XRD pattern. The evaluated value of TC_{006} of $AgInO_2$ is 0.75 which indicates that the structure of the sample exposes a larger portion of (006) facet.

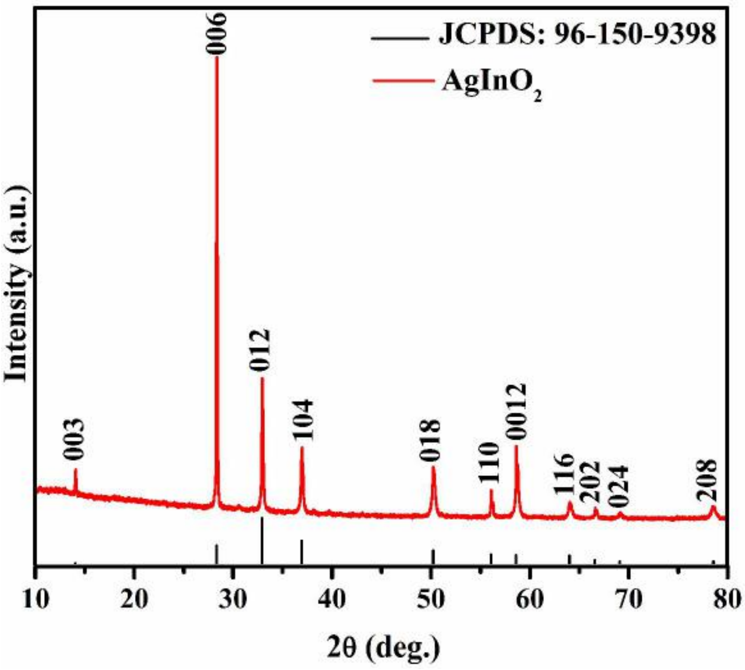

Figure 4.1. Powder XRD pattern of $AgInO_2$ thick film

FE-SEM image shows hexagonal platelike morphology with nearly uniform sized grains (Figure 4.2 (a)). The magnified view of a well defined hexagonal plate of $AgInO_2$ is shown in the inset of Figure 4.2 (a) reveals a diagonal width of ~ 300 nm. Further structural information was provided by HR-TEM and SAED pattern (Figure 4.2 (b)). The HR-TEM image recorded on the surface of the hexagon resulted in the d-spacing of 0.314 nm corresponds to the (006) plane of $AgInO_2$. The SAED pattern can be indexed to the (001) zone axis indicating the single-crystal nature of the material. The thickness of $AgInO_2$ thick film under investigation is ~ 21 μm.

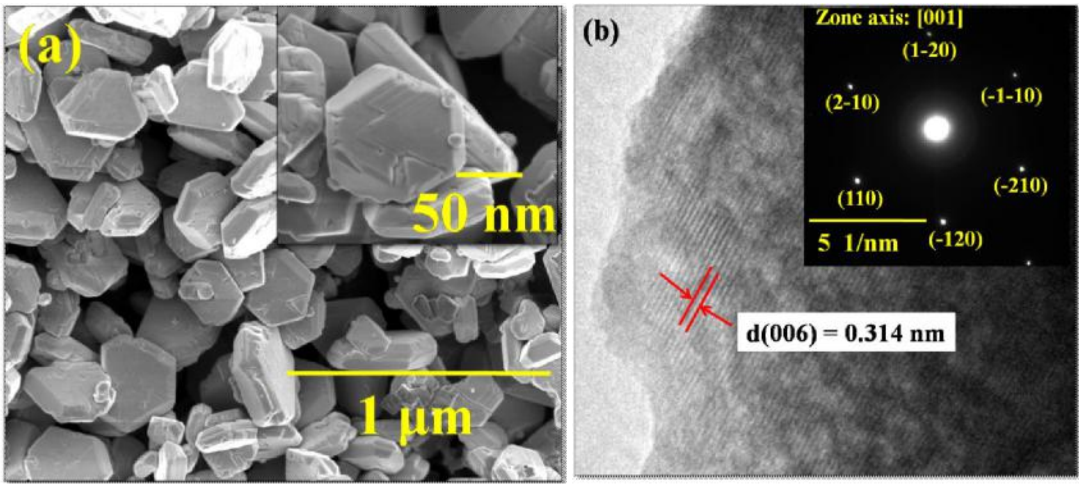

Figure 4.2. (a) FE-SEM and **(b)** HR-TEM with SAED pattern of $AgInO_2$

Similarly, thick films of $AgInO_2$ composite were characterized by XRD and FE-SEM with EDX and the results are given in Figure 4.3. The XRD pattern (Figure 4.3 (a)) shows the evidence for the presence of In_2O_3 [Space group: $Ia\bar{3}$ (206), ICDD card no. 06-0416] and Ag [Space group: $Fm\bar{3}m$ (225), ICDD card no. 89-3722] along with $AgInO_2$. The FE-SEM image (Figure 4.3 (b)) reveals smaller grains with an average size of about 80 nm distributed on the regular hexagon of $AgInO_2$. Their EDX pattern recorded at two different locations as marked in their respective images reveal that the smaller grains are In_2O_3, whereas the larger hexagons were $AgInO_2$.

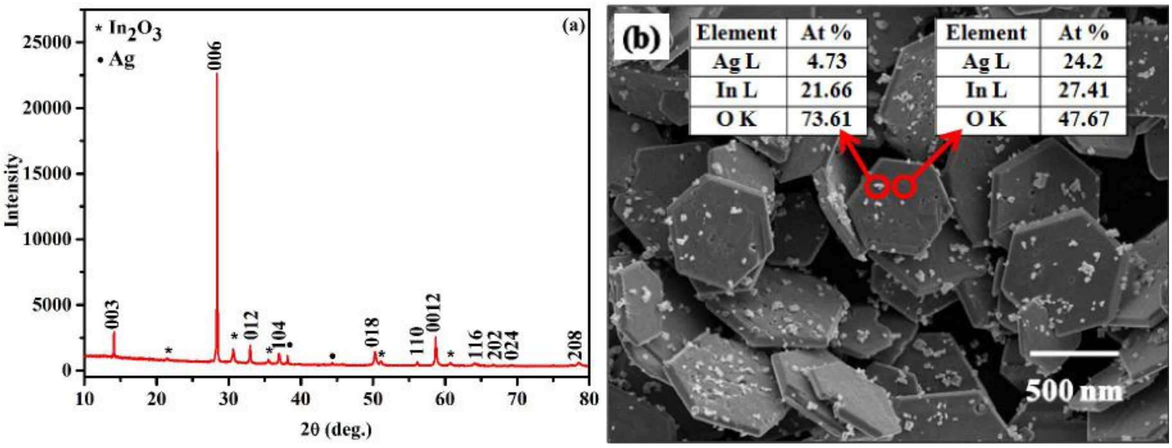

Element	At %
Ag L	4.73
In L	21.66
O K	73.61

Element	At %
Ag L	24.2
In L	27.41
O K	47.67

Figure 4.3. (a) Powder XRD pattern and **(b)** FE-SEM image of $AgInO_2$ composite

4.3.2. Gas sensing studies

The response of $AgInO_2$ nanoplates towards 100 ppm of H_2, LPG, NH_3, NO_2, CH_4, and HCHO (formaldehyde) analytes at different working temperatures was recorded to find the optimum temperature for each gas/vapour. The gases/vapours under study were chosen based on the potential interference towards H_2 for the intended application. The response (R_a/R_g) towards 100 ppm of H_2 increases with the increase of working temperature and reaches a maximum value of 6.5 at 360˚C (Figure 4.4), beyond which it decreases. On the other hand, the response towards petroleum gas increases with increase in temperature reaching a maximum value of 1.7 at 400˚C. The $AgInO_2$ thick film is found insensitive to NH_3, NO_2, CH_4 and HCHO in this temperature range from 200 ˚C to 400 ˚C, which makes this material highly selective to hydrogen at 360 ˚C. The variation of sensor resistance upon exposure to different analytes (100 ppm) at 360 ˚C is shown in Figure 4.5. As shown in Figure 4.5, the resistance of the thick film undergoes a sharp decrease upon exposure to H_2 and LPG gas and reaches its initial baseline resistance while equilibrating the surface with clean air shows an n-type semiconductor-like behaviour [84]. At this temperature, the response and recovery times for 100 ppm of H_2 are ~30s and ~120 s and these values are satisfactory; whereas for LPG a response time of 120 s with a lengthy recovery time of 70 mins was obtained. The selectivity coefficient of H_2 over LPG is 3.8 times higher, that indicate the better response of $AgInO_2$ towards H_2 (Figure 4.6 (a)).

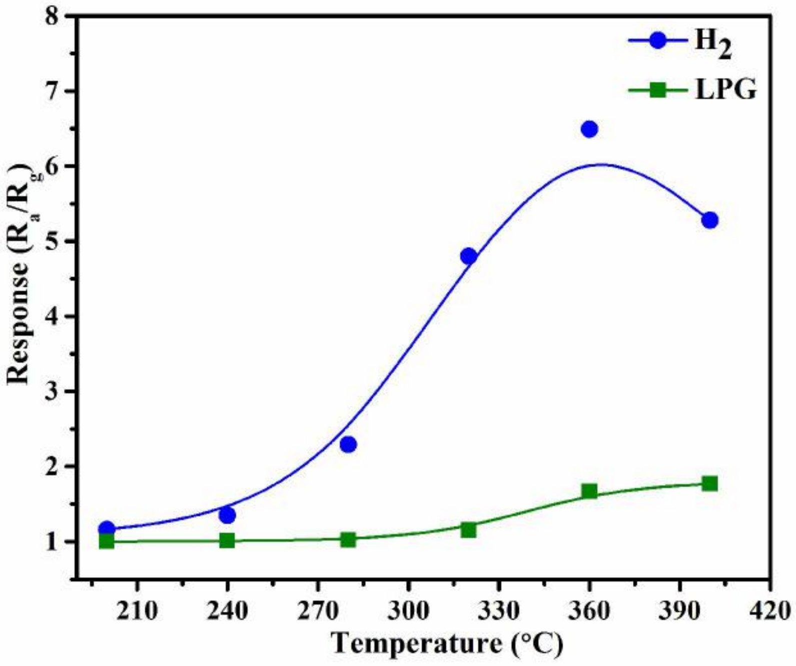

Figure 4.4. The response of $AgInO_2$ hexagonal nanoplates towards 100 ppm of H_2 & LPG at different temperatures

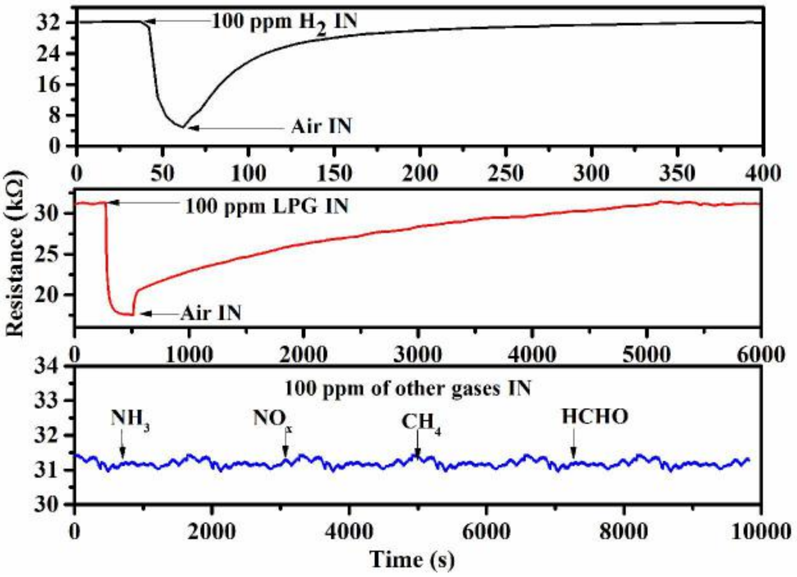

Figure 4.5. Variation of sensor resistance upon exposure to different analytes (100 ppm) at 360 ˚C

Further, the gas sensing studies were carried out similarly for the composite mixture of $AgInO_2$, In_2O_3 and Ag [171] to compare with that of the phase pure $AgInO_2$ and the results are shown in Figure 4.6 (b). It is observed that the composite mixture responds to all the analytes under study. The sensitivity towards hydrogen is 1.8 times less than that of pure $AgInO_2$. The comparisons of selectivity coefficients of 100 ppm of H_2 over other analytes for phase pure $AgInO_2$ and the composite mixture are presented in Table 4.1. This infers that phase pure hexagonal nanoplates of $AgInO_2$ are highly selective and sensitive towards hydrogen.

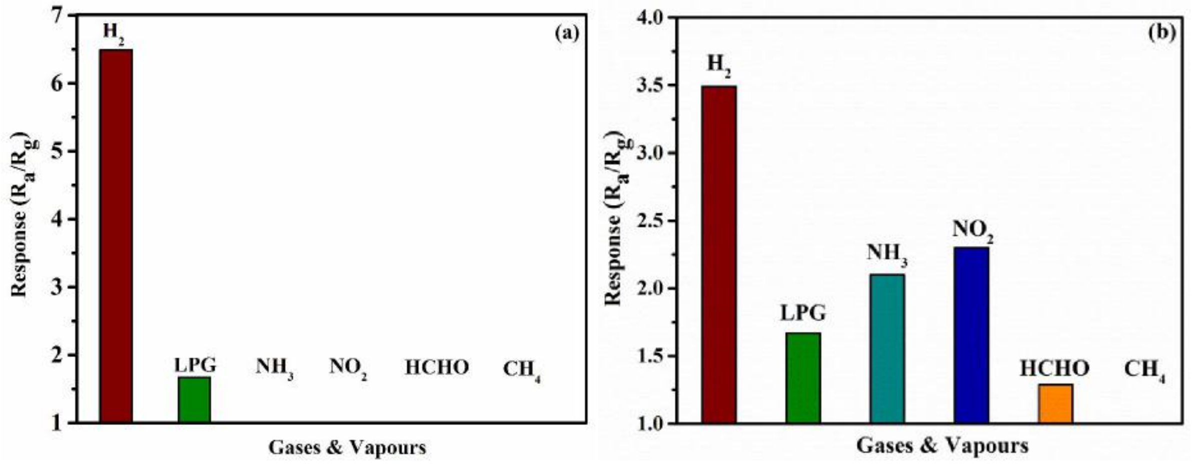

Figure 4.6. The responses for **(a)** phase pure $AgInO_2$ and **(b)** $AgInO_2$ composite towards 100 ppm of various gases/vapours at 360 ˚C

Table 4.1. Selectivity Coefficients of 100 ppm of H_2 over other analytes for pure $AgInO_2$ and its composite

	Selectivity Coefficients of H_2 over other gases	
Analyte	**Pure $AgInO_2$**	**Composite mixture**
LPG	3.8	2.1
NH_3	6.5	1.6
NO_2	6.5	1.5
CH_4	6.5	3.5
HCHO	6.5	2.7

The phase pure $AgInO_2$ nanoplates are tested for a wide dynamic range of H_2, from 1 ppm to 10000 ppm at 360˚C and the results are presented in Figure 4.7. The response found to be linear from 1 ppm to 1000 ppm with an Adj. R^2 of 0.9949 (inset of Figure 4.7); beyond which non-linear response is noticed. To the best of author’s knowledge, $AgInO_2$ is one of the unique material that can sense hydrogen in this wide concentration range (i.e.) (1 ppm to 10000 ppm) along with faster response and reasonable recovery times. The limit of detection (LOD) and limit of quantification (LOQ) for hydrogen gas was estimated to be 1 ppm and 10 ppm respectively.

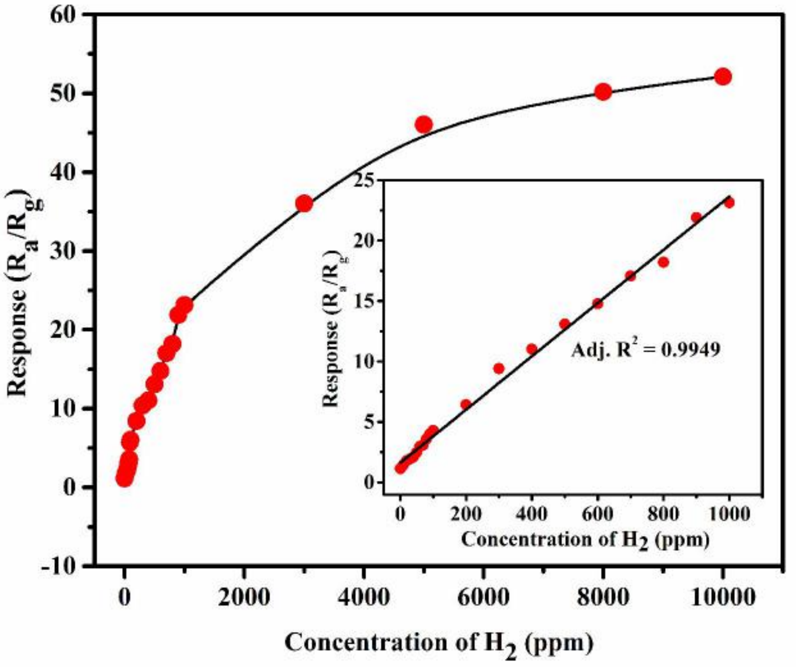

Figure 4.7. Calibration plot of $AgInO_2$ nanoplates towards different concentrations of H_2 at 360˚C (inset linear fit for 1 – 1000 ppm of H_2)

To confirm the repeatability and stability of the $AgInO_2$ nanoplates towards H_2, 10 consecutive injections were performed (Figure 4.8, bottom and left axes). The average response (R_a/R_g) was derived to be 2.6 and there was no significant change in the response pattern even after 10 repeatable exposures during a period of 4.5 h. The long-term repeatability tests were carried out for six months at an interval of 10 days towards 50 ppm of

H_2 at 360˚C and the results are displayed in Figure 4.8 (top and right axes). The responses are very similar showing an average value with a standard deviation of 2.64±0.005 for about 20 injections at regular intervals over a test period of 180 days. The repeatability tests were also performed for 5000 ppm and 5 ppm covering the high and low ranges of H_2 (Figure 4.9). The material shows good repeatability even at the elevated concentrations.

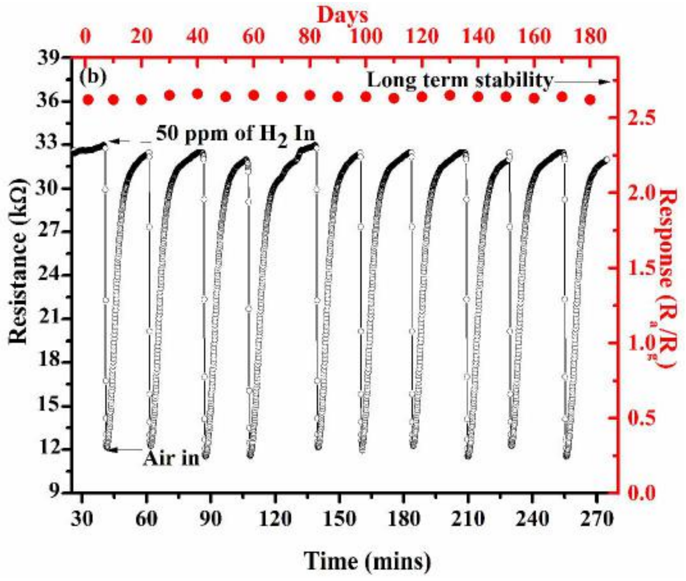

Figure 4.8. Repeatability and stability test data of $AgInO_2$ nanoplates towards 50 ppm of H_2 at 360˚C

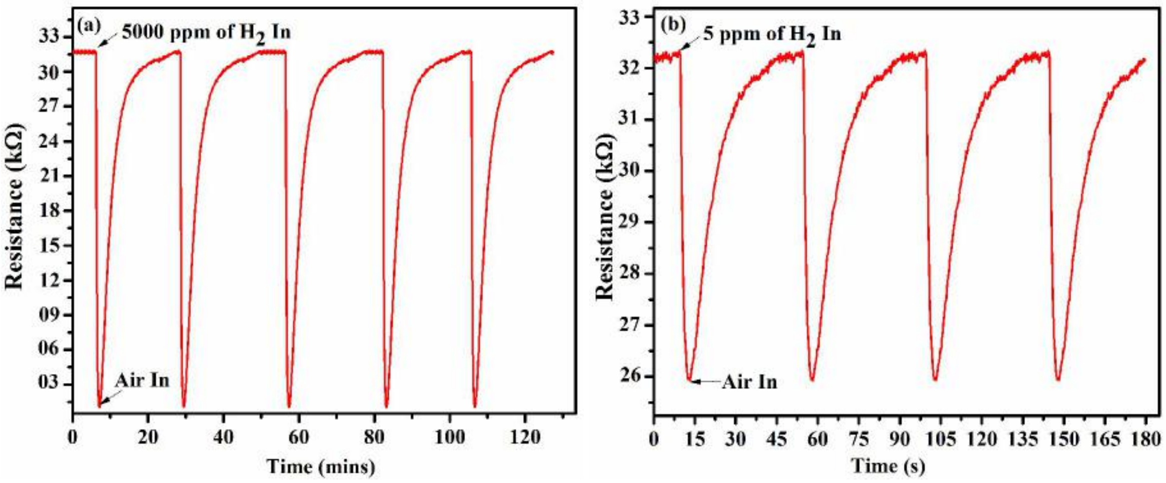

Figure 4.9. Repeatability test patterns of $AgInO_2$ towards **(a)** 5000 ppm and **(b)** 5 ppm of H_2 gas

The important aspect is its performance at a different relative humidity (RH). Figure 4.10 (a) demonstrates its response towards 100 ppm of H_2 at RH varied from 60 % - 80 %. No appreciable change in the sensing pattern is observed at these humidity levels. For any practical application, the baseline stability of the material needs to be assessed for a specified duration. Figure 4.10 (b) shows the baseline of $AgInO_2$ nanoplates monitored for six months at 360 ˚C. Figure displays the baseline resistance values averaged at a frequency of 10 days for a total duration of 180 days. The mean value of the baseline resistance of the sensor is worked out to be 34 kΩ with a standard deviation of 3 kΩ which is in the acceptable limit for the entire duration of the study indicating a good sign of baseline stability of the material. Brief performance comparison of $AgInO_2$ towards hydrogen (present work) with recently reported materials (since 2005) in the literature is presented in Table 4.2[1]. It is observed that the sensor based on $AgInO_2$ nanoplates exhibited a better gas sensing property towards hydrogen over a wide concentration range, fast response and reasonable recovery, better stability and repeatability and finally has satisfactory baseline stability. Therefore, the present material could be utilized as a sensor from ppm to % level detection of hydrogen.

---

[1] List is not complete, authors considered only limitedliterature based on thewell-studied wide range hydrogen sensing materials for first hand comparison.

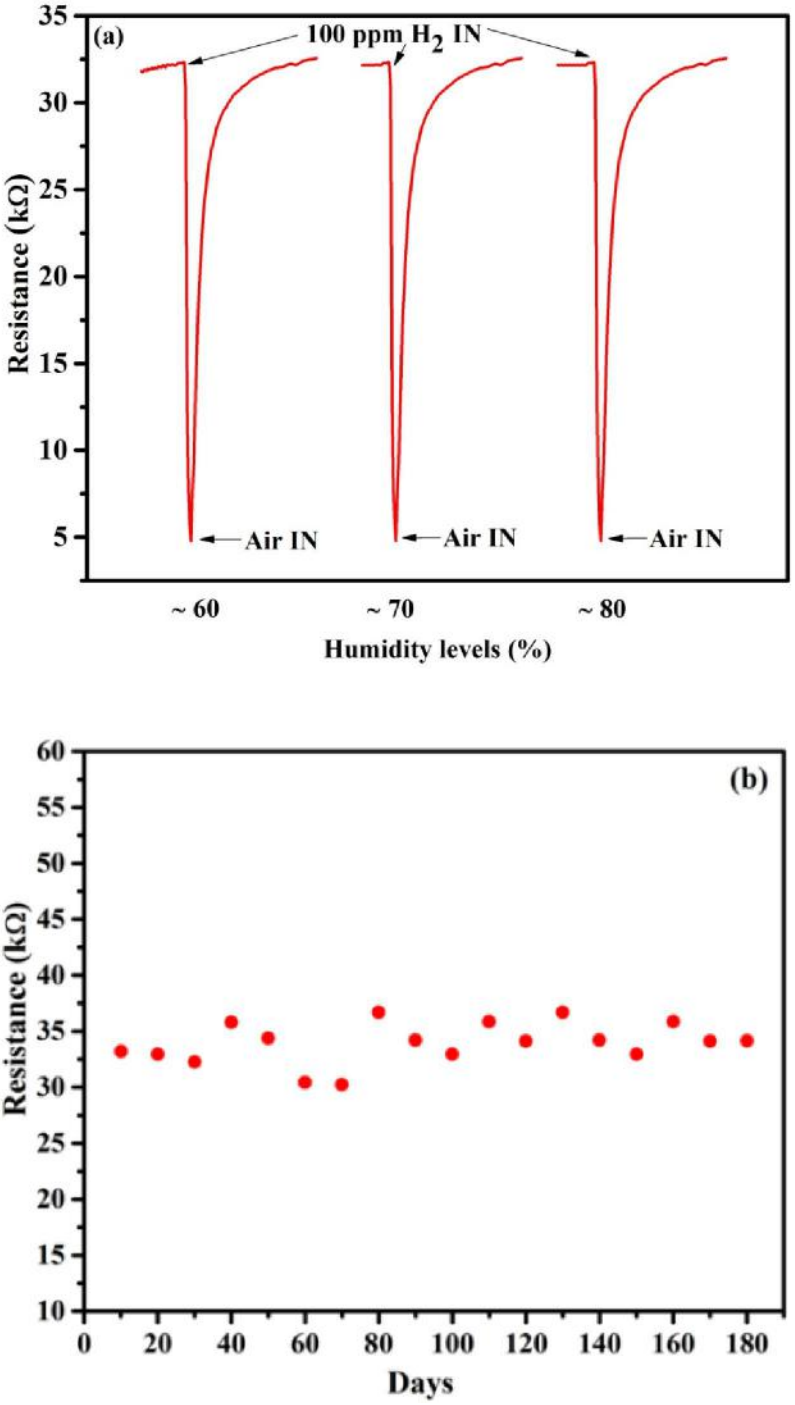

Figure 4.10. (a) Response patterns at different humidity levels and **(b)** baseline stability data of $AgInO_2$ nanoplates for six months at 360 ˚C

Table 4.2. Comparison of gas sensing performance of $AgInO_2$ based H_2 sensor with other SMO sensors

Materials	**Structures**	**Detection range (ppm)**	**Operating temperature (˚ C)**	**Sensitivity (R_a/R_g)**	**Response time (s)**	**Recovery time (s)**	**Cross selectivity**	**References**
Pd/SnO_2	nanofibers	20-1000	RT-340	1-36	4-13	3-9	CH_4, C_2H_2, CO, acetone, NH_3, ethanol, toluene	[172]
Co/SnO_2	nanofibers	100-35000	330	24 (100)	2	3	Not reported	[173]
$ZnSnO_3$	nanocubes	1-60	375	652 (50)	1	12	CO_2, CO, LPG, NH_3, ethanol	[174]
Ni/ZnO	nanoplates	5-10000	150	1.7 (10000)	-	-	CH_4, H_2S, CO_2	[175]
NiO	nanocrystals	1000−3000	175	10-60 %	67−134	117−788	Not reported	[176]
α-MoO_3	nanoflakes	600−10000	50−300	9-1	7−30	24−130	Not reported	[177]
In_2O_3	octahedra	1-20	200	12	-	-	Ethanol, CO, NO_2, H_2S	[178]
$CrNbO_4$	nanoparticles	500-4000	340	42	180	9000	NO_x, LPG, NH_3	[179]
$CuZnFe_2O_4$	nanofiber	100-20000	250	6 (500)	6-40	6-38	CO, CO_2, N_2	[180]
Pd/TiO_2	nanocomposite	4000-18000	RT	1.01-1.04	10-200	9-170	Not reported	[181]
Pd/WO_3	nanocomposite	50-2000	250	-	7-140	80-280	CO, CH_4	[182]
$AgInO_2$	**nanoplates**	**1-10000**	360	**1-52**	**10-60**	18-1110	**LPG**	**Present work**

4.3.3. Mechanism of sensing

Analysis of the gas sensing results of $AgInO_2$ gives a close resemblance to the gas sensing mechanism of the well-known n-type semiconducting materials like SnO_2, ZnO, WO_3, In_2O_3, etc. [178, 183-185], wherein the change in resistance is caused by the changes in surface coverage of the chemisorbed oxygen species [186]. Although the results indicate that the mechanism is nearly similar to that of the conventional semiconducting oxides, the participation of lattice oxygen of $AgInO_2$ needs to be probed to rule out its involvement during sensing. This requires a close look into the oxygen non-stoichiometry of $AgInO_2$ during sensing conditions. $AgInO_2$ was subjected to repeated heating and cooling cycles in air and argon and their thermograms were recorded (Figure 4.11). An initial weight loss of about 0.11 % is observed at 360 ˚C during first heating in air which upon cooling did not yield any weight gain. Subsequent heating run in air did not show any weight changes indicating that the oxygen non-stoichiometry is under equilibrium with air at this partial pressure. The initial weight loss may be due to desorption of surface adsorbed gases/moisture on $AgInO_2$. When the experiment is repeated in argon, a higher initial weight loss of 0.32 % is obtained which upon cooling did not show any weight gain. The subsequent heating run did not show any change in weight which indicates that the oxygen non-stoichiometry is in equilibrium with the oxygen partial pressure in argon and settles down at a lower value indicating the loss of lattice oxygen even in the absence of hydrogen.

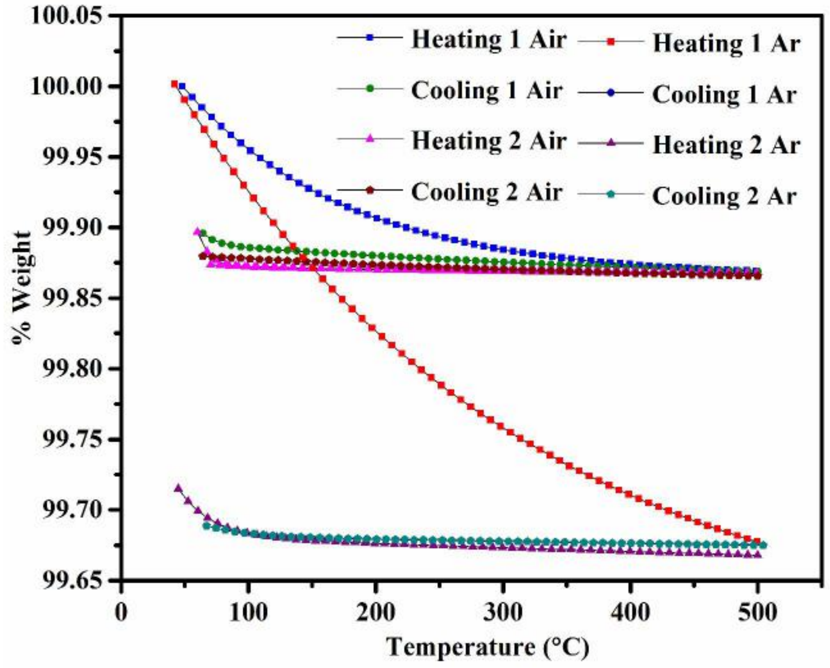

Figure 4.11. TG-DTA patterns of $AgInO_2$ in air and argon ambient

Upon exposure to H_2 at 360 ˚C, the optimized operating temperature for $AgInO_2$, both chemisorbed oxygen and lattice oxygen species may probably be expected to participate during sensing and their relative proportion varies with the concentration of H_2. For example, at low concentration of H_2, the participation of chemisorbed oxygen leads over the lattice oxygen whereas at percentage levels, the participation of lattice oxygen may be expected as the large fraction of chemisorbed oxygen is already consumed during the sensing action. To verify this, the XRD pattern and FE-SEM image of the sample after annealing the specimen in 4% hydrogen for one hour did not show any change indicating the structural integrity at this temperature even for such a large concentration (Figure 4.12).

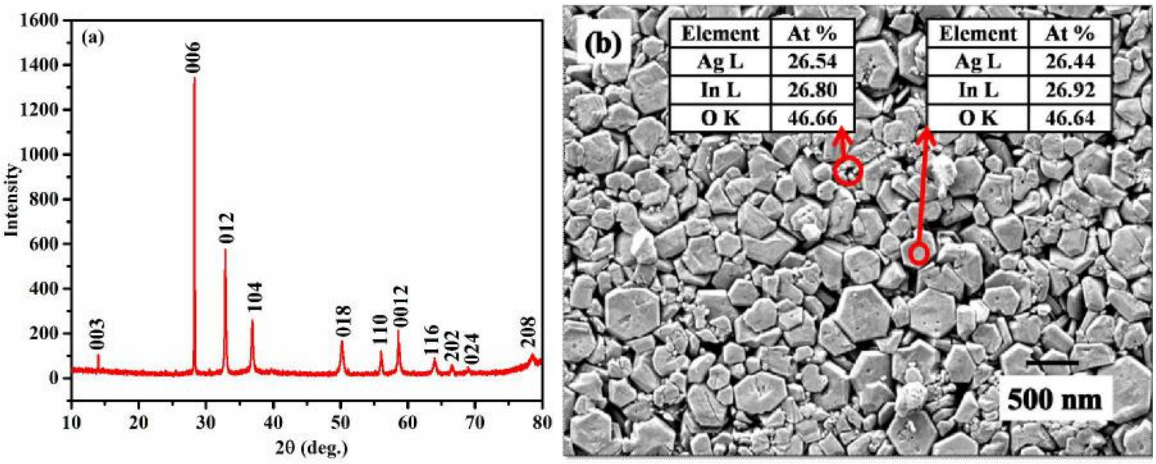

Element	At %
Ag L	26.54
In L	26.80
O K	46.66

Element	At %
Ag L	26.44
In L	26.92
O K	46.64

Figure 4.12. (a) XRD and **(b)** FE-SEM image of $AgInO_2$ exposed to 4% hydrogen

Based on these results, the mechanism of H_2 sensing of $AgInO_2$ can be divided into two regimes. At lower levels of H_2, active participation of chemisorbed oxygen is likely to occur just as observed for any conventional semiconductors wherein the relaxation in the width of the charge depletion layer is accounted for the changes in conductivity. At lower operating temperature (< 250 ˚C), O_2^- is the predominant oxygen specie whereas at higher operating temperatures (> 250°C), O^- and O^{2-} species are reported to be abundant [178, 183]. As the optimized operating temperature is 360 ˚C, the reduction reaction between O_x^- ions and H_2 takes place during H_2 sensing in accordance with the following Equation 4.3 which results in the release of trapped electrons back to the solid causing a decrease in resistance [187, 188].

$$\mathbf{O^-_{ad} + H_2 \xrightarrow{360^\circ C} H_2O + e^-(SMO)} \qquad \mathbf{(4.3)}$$

At higher concentration levels (percentage levels), probably the sensing action is likely to involve the participation of lattice oxygen. The relative weight change of about 0.32 % in argon with respect to air confirms the existence of oxygen non-stoichiometry in this compound. This loss of lattice oxygen can also cause the resistance to decrease as suggested by the following Equation 4.4:

$$O^{2-}_{lattice} + H_2 \xrightarrow{360^{\circ}C} H_2O + 2e^{-}(SMO) \qquad \textbf{(4.4)}$$

To further explore the sensing performance of $AgInO_2$ nanoplates towards hydrogen, the chemical state of each element in $AgInO_2$ were analyzed before and after exposure to 1500 ppm of H_2 at 360˚C by X-ray photoelectron spectroscopy.

The Shirley background-subtracted selected area high-resolution scan of Ag 3d and In 3d before and after exposure to H_2 is shown in Figure 4.13 & 4.14 respectively. The curve fitting was carried out using the intensity ratio of 3:2 corresponding to a spin-orbit coupling parameter (SOCP) of 6.0 eV. The peak positions of Ag-$3d_{5/2}$ and Ag-$3d_{3/2}$ peaks are found to be at 367.7 ± 0.1 eV and 373.7 ± 0.1 eV which are in good agreement with the reported data of singly charged silver ion of $AgInO_2$ phase (Figure 4.13) [145, 171, 189]. Similarly, curve fitting was carried out with an intensity ratio of 3:2 among the In 3d components yielded peak positions at 444.3 eV and 451.9 eV respectively. The measured binding energies and SOCP value of 7.6 eV of Indium can be well indexed to In^{3+} state (Figure 4.14). No significant differences were observed because of hydrogen exposure to the detection limit of XPS.

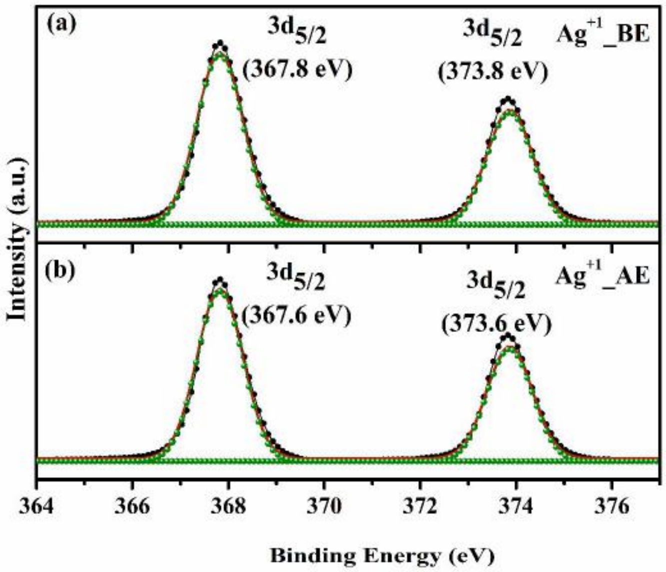

Figure 4.13. Ag 3d spectra of $AgInO_2$ nanoplates **(a)** before and **(b)** after exposure to H_2

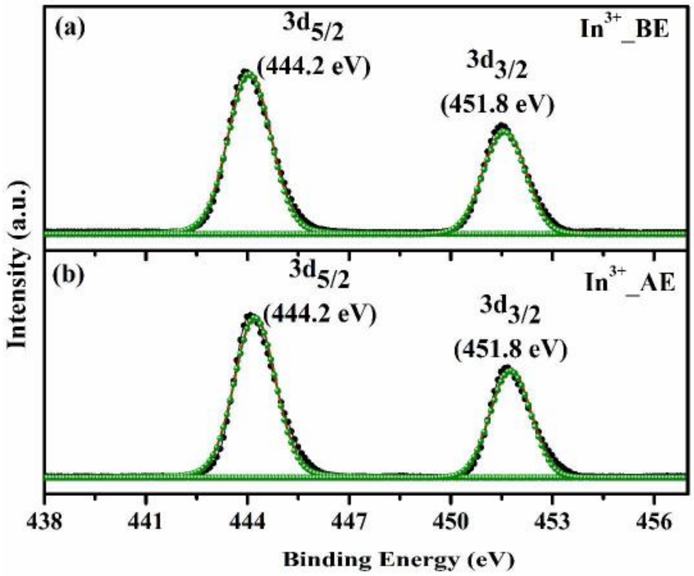

Figure 4.14. In 3d spectra of $AgInO_2$ nanoplates **(a)** before and **(b)** after exposure to H_2

The O 1s pattern of $AgInO_2$ nanoplates before exposure to H_2 is shown in Figure 4.15 (a) which can be fitted with three peaks accounting for different species. Based on the standard binding energy values, the intense peak at 529.6 eV corresponds to the lattice oxygen (O^{2-}) of $AgInO_2$. An intermediate peak at 531.0 eV is assigned to the chemisorbed O_x^- species [166]. A less intense peak at 532.9 eV is attributed to adsorbed hydroxyl groups (O_{OH}^-) [145, 166, 171]. Distinct changes in the O 1s pattern were observed after exposure to 1500 ppm of H_2 (Figure 4.15 (b)). The area under each peak was evaluated and the fraction of different oxygen species based on the relative area are deduced and the results are given in Table 4.3. The fraction of lattice oxygen, O^{2-} shows a marginal change after exposure to hydrogen whereas the fraction of O_x^- species shows a sharp decrease from 25.1 % to 18.6 %. In contrast, the fraction of O_{OH}^- species increases from 8.3 % to 12.6 % indicating the formation of hydroxyl groups. The relative ratio of O^{2-}: O_x^-: O_{OH}^- species after exposure to before exposure of hydrogen is 1.0001, 0.7203 and 1.4692 respectively. A decrease in the peak area of O_x^- is a clear indication of the consumption of O_x^- ions due to H_2 interaction.

This confirms the active role of chemisorbed oxygen during H_2 sensing and the loss of which results in a decrease in resistance as proposed for the lower levels of hydrogen.

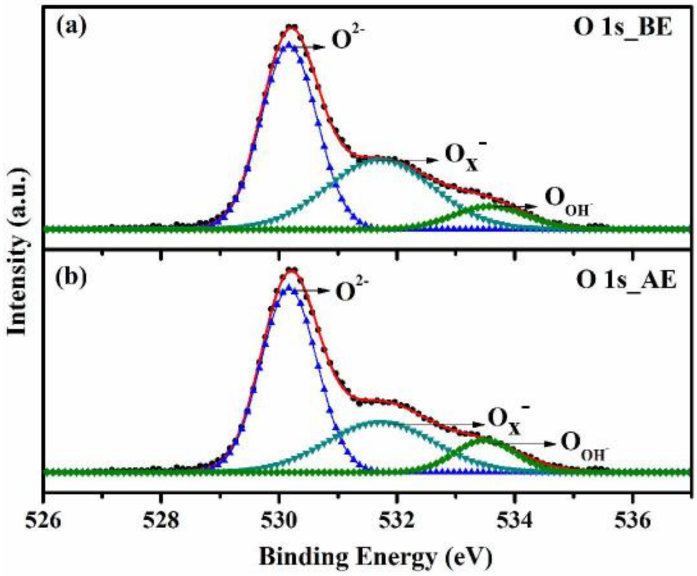

Figure 4.15. O 1s spectra of $AgInO_2$ nanoplates **(a)** before and **(b)** after exposure to H_2

Table 4.3. Relative area analysis of O 1s XPS spectra of $AgInO_2$ before and after exposure to hydrogen

	Lattice Oxygen (O^{2-})	**Oxygen vacancy (O_x^-)**	**Adsorbed hydroxyl groups (O_{OH}^-)**
Before exposure to hydrogen	66.5 %	**25.1 %**	**8.3 %**
After exposure to hydrogen	68.6 %	**18.6 %**	**12.6 %**

4.4. Conclusions

The gas sensing performance of rhombohedral $AgInO_2$ composed of hexagonal-shaped nanoplates of (006) facets are presented. The $AgInO_2$ nanoplates exhibit reasonable response towards hydrogen over a wide concentration range from 1 ppm to 10000 ppm with good repeatability and baseline stability which makes it a potentially wide range H_2 sensor.

Phase pure $AgInO_2$ is selective towards H_2 whereas the composite of $AgInO_2$ responds to all the gases under study. Its performance in different humidity levels makes it very attractive for applications in harsh conditions.

CHAPTER 5

Thin films of $AgInO_2$: Optimization of deposition parameters, characterization and hydrogen sensing studies

---

This chapter is focused on the growth of thin films of $AgInO_2$ by pulsed laser deposition and its hydrogen sensing performance. Nanostructured thin films of rhombohedral $AgInO_2$ were successfully deposited at 200 ˚C under an unusual in-situ oxygen pressure of 0.7 mbar and characterized by GIXRD, FE-SEM and XPS. Stabilization of Ag^+ ion is the key issue which requires 0.7 mbar in-situ oxygen pressure for Ag particles free thin films of $AgInO_2$. Gas sensing studies revealed that these films were highly selective to hydrogen with a significant reduction in response and recovery times when compared to that of screen-printed thick films of $AgInO_2$. Hall studies showed n-type semiconducting behavior of thin films.

5.1. Introduction

Delafossite family of oxides (ABO_2; A = Cu, Ag, Pt, Pd; B = In, Al, Ga, Fe) are not amenable for the bulk synthesis despite their promise for applications in transparent electrodes, p-n junction, solar cells, flat panel displays, semiconductor lasers and light-emitting devices [78, 81, 84, 142-146]. Attempts have been made to deposit the compounds as thin films with the help of lattice matched substrate to realize the growth. After the recent success on synthesis of phase pure $AgInO_2$ without Ag or In_2O_3 under modified hydrothermal conditions [83], the focus shifted to stabilization of $AgInO_2$ as thin films for practical applications. Apart from the report of Otabe, et al. claiming the formation of relatively pure $AgInO_2$ film at in-situ pressure of 1.3×10^{-1} mbar at 400°C using RF sputtering in 1998 [156], no other report of confirmation by other laboratories across the globe till date is available which prompted us to re-investigate the thin film processing conditions. Indium oxide is stable over a wide range of temperature and pressure whereas Ag_2O is a meta-stable compound which decomposes to give Ag around 180°C. Unless the decomposition of Ag_2O is suppressed, the growth of thin films of $AgInO_2$ cannot be realized and hence, a literature review of growth conditions of pure Ag_2O was taken up. Deposition of thin films under 0.08 – 0.2 mbar oxygen partial pressure was reported to yield a mixture of Ag, Ag_2O and AgO [190]. The objective of the work is to identify the growth conditions for the formation of thin films of pure Ag_2O under different temperatures and in-situ oxygen pressures and then apply those conditions for the growth of phase pure $AgInO_2$ thin films. As higher in-situ pressures are handled by Pulsed Laser Deposition (PLD) with ease, this technique is chosen for growth of thin films.

This chapter deals with the optimization of thin film deposition parameters of $AgInO_2$ along with its hydrogen sensing characteristics for the first time. The influences of working temperature, H_2 gas concentration, selectivity and long term performance of the sensor were investigated. The mechanism of interaction of trace levels of H_2 with $AgInO_2$ thin film is probed by in-situ Hall carrier measurements and four-probe conductivity studies.

5.2. Experimental Details

5.2.1. Deposition of $AgInO_2$ thin films using Pulsed Laser Deposition (PLD)

$AgInO_2$ target for PLD is prepared by hydrothermal route. The detailed synthesis procedure was described in Chapter 3 [83]. The synthesized powder was compacted in the form of a pellet of 12.5 mm diameter and heated to 450 °C for 24 h. Thin films were deposited by pulsed KrF (λ = 248 nm) operating at 5 Hz at a fluence of 10 J/cm^2 on polycrystalline alumina, quartz and α-Al_2O_3 (001) substrates at 200 ˚C. The vacuum chamber was initially evacuated to a base pressure of $3x10^{-6}$ mbar during which the substrate was gradually heated to 200°C. The base pressure was gradually raised to 0.7 mbar by bleeding oxygen into the vacuum chamber at the rate of 20 mL/min. Pre-ablation was carried out for 3 min to remove any surface contaminated layers of the target. The deposition of thin film was carried out for 20 min under the in-situ oxygen pressure of 0.7 mbar. Soon after the deposition, the heater was turned off and the film was allowed to cool in the same pressure to 25 °C.

5.2.2. Characterization of $AgInO_2$ target and thin films

The phase purity of the PLD target was checked by X-ray diffraction using Cu K_α radiation (λ=1.5406 Å) with a step size of 0.02°. XRD patterns of thin films were recorded at a glancing angle (ω) of 3°. Surface morphology and elemental composition of the target and films were analyzed using FE-SEM/EDX. The surface roughness of films was obtained using AFM. X-ray photoelectron spectroscopy measurements (XPS) were carried out to determine the oxidation states of Ag, In and Oxygen. Films deposited on polycrystalline alumina substrate were used for investigation of structural, surface morphology and gas sensing properties. Bandgap measurements were carried out on thin films deposited on quartz substrates and the optical bandgap was deduced from the transmittance data obtained from UV-Visible spectrophotometer in the range of 200 to 800 nm.

5.2.3. Gas sensing studies

The thin film of $AgInO_2$ was mounted in an in-house designed and fabricated sensor chamber of 75 mL capacity with a provision for gas inlet and outlet as shown in Figure 2.16 (Chapter 2). The desired operating temperature of the sensor was maintained by adjusting the current through the Pt heater by a power source. The response to different analytes like H_2, NO_2, NH_3, CH_4, LPG and formaldehyde was measured at different operating temperatures starting from 200 ˚C to 400 ˚C at an interval of 40 ˚C. To find the optimum temperature of operation, a known concentration of the analyte gas (100 ppm) was injected into the test chamber through an injection port and the transient changes in resistance were recorded at different temperatures using a data logger. The chamber was then purged with air through gas inlet so that the resistance of the sample retraces back to the original value. Gas sensing response for a given concentration of gas defined as

$$\mathbf{Response} = \left(\frac{\mathbf{R_a}}{\mathbf{R_g}} \right) \tag{5.1}$$

where R_a and R_g are the resistances of the $AgInO_2$ in air and the presence of gaseous analyte respectively. After finding the suitable operating temperature, calibrations were carried out on thin films of $AgInO_2$ for hydrogen. The short and long term repeatability, baseline stability of the $AgInO_2$ thin films were evaluated for about 6 months.

5.2.4. In-situ Hall measurement

In-situ four-probe electrical conductivity and Hall measurements of $AgInO_2$ films were carried out using van der Pauw technique [137] to find the changes in charge carrier concentration in air and the presence of trace levels of H_2. The details of the Hall measurement test facility adopted for carrying out the measurements were described in Chapter 2. $AgInO_2$ thin film deposited on α-Al_2O_3 (001) was mounted on the sample stage and the measurements were carried out in air and in presence of 100 ppm of H_2 from 50 ˚C to 350 ˚C in steps of 40 ˚C using a magnetic flux of 3000 Gauss.

5.3. Results and Discussion

5.3.1. Structural and morphological studies of $AgInO_2$ pellet

The XRD pattern of $AgInO_2$ target used for the deposition of thin films is shown in Figure 5.1 (a). All the diffraction peaks are indexed in terms of rhombohedral ($R\bar{3}m$ (166); ICDD # 96-150-9398) system. Field emission scanning electron microscopy (FESEM) analysis shows that the target is composed of hexagonal grains with an average size of ~ 300 nm (Figure 5.1 (b)). EDX analysis performed on the target (hexagons and small particles) shows that the composition is close to the stoichiometric value as seen from the inset of Figure 5.1 (b).

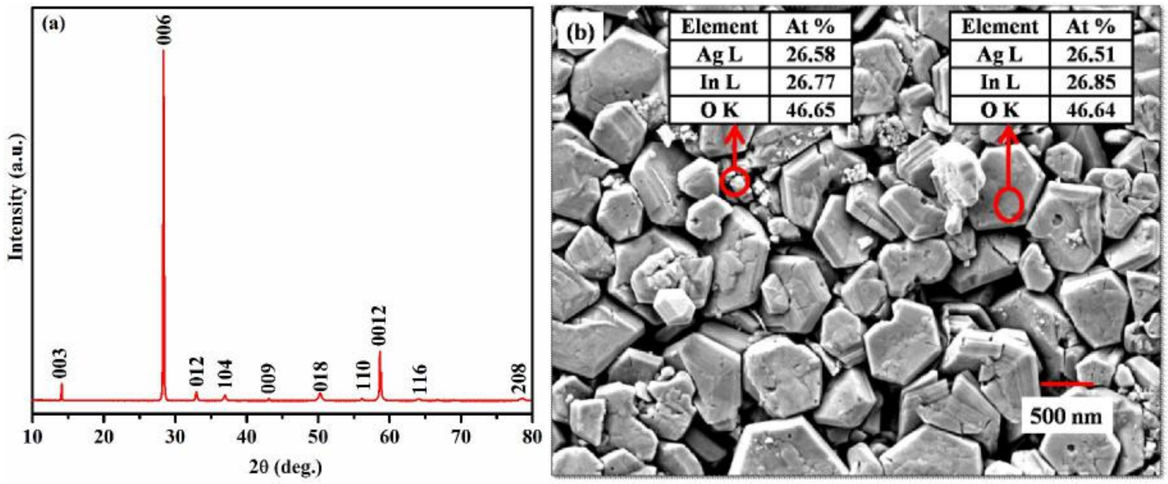

Element	At %
Ag L	26.58
In L	26.77
O K	46.65

Element	At %
Ag L	26.51
In L	26.85
O K	46.64

Figure 5.1. (a) XRD pattern and **(b)** FE-SEM image with EDX of $AgInO_2$ pellet

During the deposition of thin films of $AgInO_2$, two parameters viz. deposition temperature and in-situ oxygen pressure were varied. Depositions were performed at four different temperatures (100 ˚C, 200 ˚C, 300 ˚C & 400 ˚C) with the in-situ pressures of oxygen kept at 0.1 mbar and 0.7 mbar. Other parameters like deposition time (15 mins), fluence (10 J/cm^2), substrate-target distance (4 cm) and repetition rate (5 Hz) were kept constant. The deposition parameters are given in Table 5.1.

Table 5.1. Deposition conditions of thin films of $AgInO_2$ for PLD process

Experiment No.	Temperature (°C)	pO_2 (mbar)
1	100	0.1
2	200	0.1
3	300	0.1
4	400	0.1
5	100	0.7
6	**200**	**0.7**
7	300	0.7
8	400	0.7

The X-ray diffraction patterns of the films deposited at different conditions (Table 5.1) revealed that the conditions corresponding to experiment no. 6 alone yielded a phase pure product.

5.3.2. Structural, morphological and optical studies of optimized $AgInO_2$ thin film

Figure 5.2 shows the GI-XRD pattern of $AgInO_2$ thin film deposited on α-Al_2O_3 substrate at 200 ˚C and 0.7 mbar (experiment no. 6). All the diffraction peaks with significant intensity can be indexed on the basis of the rhombohedral system of $AgInO_2$ and the space group of $R\bar{3}m$ (166) (ICDD # 96-150-9398). The lattice parameters were deduced to be a = 3.2775 Å and c = 18.8834 Å. No evidence for the formation of trace levels of elemental Ag is seen up to the detection limit of XRD. Morphology of thin films showed uniform sized grains having an average size of about 20 nm (Figure 5.3 (a)). Cross-sectional SEM (Figure 5.3 (b)) shows that thin films exhibit a columnar growth pattern with a width of ~20 nm. The length of the strand extends up to the thickness of the film which is about 175 nm. AFM image of the optimized film is shown in Figure 5.3 (c) reveals films are highly granular without particulates having grains of uniform size. The roughness values of films range from 2.5 to 4.2 nm with a mean roughness of about 3.0 nm as shown in their inset.

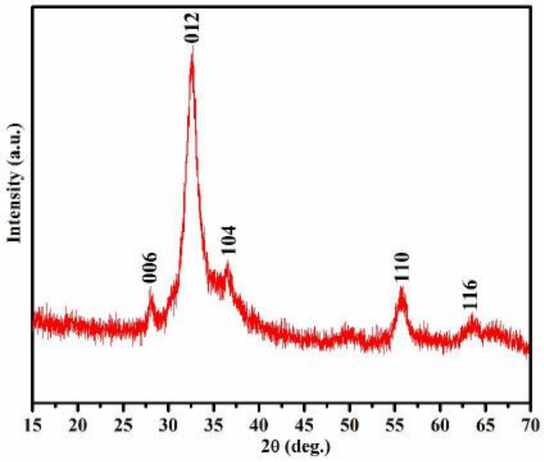

Figure 5.2. GI-XRD pattern of $AgInO_2$ thin film on α-Al_2O_3 substrate (experiment no. 6)

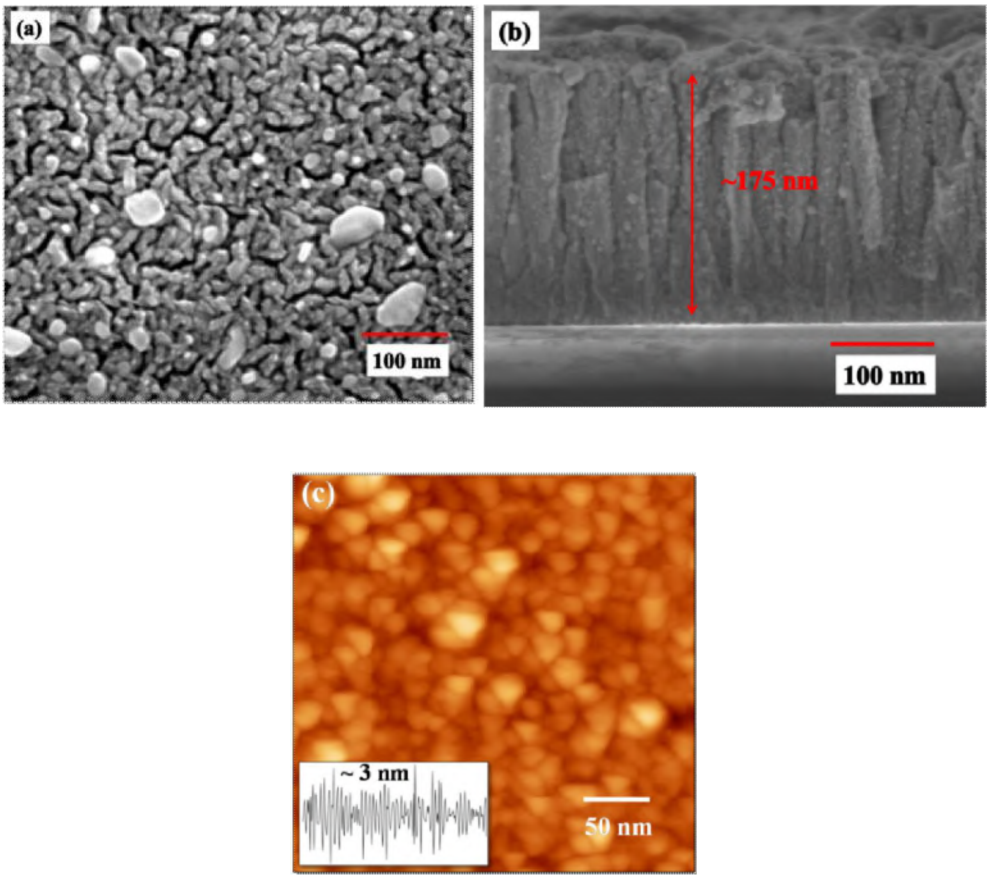

Figure 5.3. (a) FE-SEM image, **(b)** cross-sectional SEM and **(c)** AFM image with roughness profile of $AgInO_2$ thin film

XPS measurements were carried out to determine the oxidation states of the elements of Ag, In and O in the thin film. Curve fitting carried out on the Shirley background subtracted Ag 3d pattern shows that all the Ag ions are in single oxidation state as shown in Figure 5.4 (a). The binding energy position of the peak shows that Ag is in +1 oxidation state [83, 145, 153]. Similarly, curve fitting was carried out for Shirley background subtracted In 3d level. Analysis of In 3d pattern shows that all the indium ions in +3 oxidation state (Figure 5.4 (b)) [83, 145, 154]. On the other hand, O 1s pattern provides the finger prints for two different oxygen species with a peak at 529.6 eV corresponding to lattice oxygen (O^{2-}) and a minor peak at 531.7 eV generally assigned to adsorbed O_x^- species (Figure 5.4 (c)) [83, 145, 154].

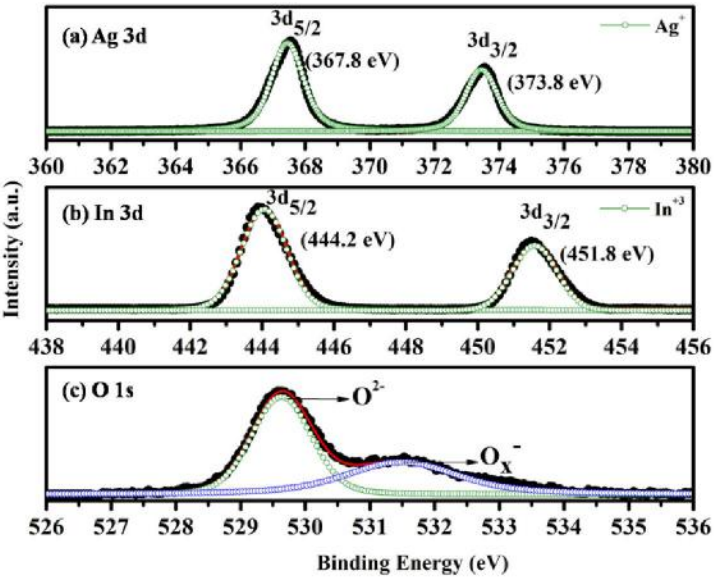

Figure 5.4. XPS spectra of $AgInO_2$ thin film

The optical absorbance spectra of $AgInO_2$ thin film deposited on quartz substrate recorded in the wavelength range 200 – 800 nm is shown in the inset of Figure 5.5. $AgInO_2$ thin films showed 62 % transparency in the visible region. The optical bandgap (E_g) extracted from the Tauc plot shown in the Figure 5.5 yields a band gap of about 3.65 eV which is in agreement with the literature data [156].

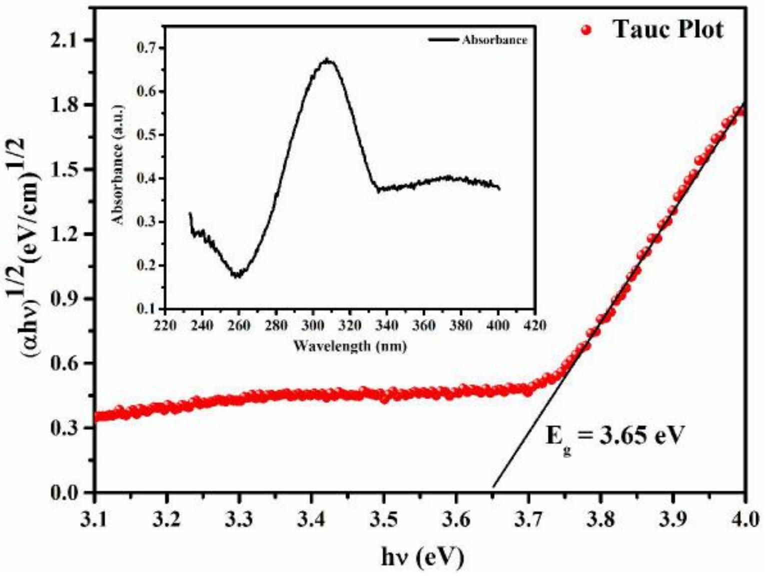

Figure 5.5. Tauc plot of $AgInO_2$ thin film; Inset: Absorbance spectra of $AgInO_2$ thin film

5.3.3. Mechanism of phase pure formation of $AgInO_2$

If the structural constraint is argued to be the primary reason for the use of extremely high pressures (> 500 bar) and temperatures (T ~ 500 °C) for stabilizing the $AgInO_2$ phase, then its formation at 200 °C at a hydrothermal pressure of 9 bar directly implies that it is not the only factor demanding high pressures. First of all, the availability of Ag and In-ions with respective oxidation states of +1 and +3 in precise relative abundance of must be ensured at the processing conditions to comply with the requirements of formal oxidation states of these ions in $AgInO_2$. While In_2O_3 is a stable trivalent oxide over a wide range of temperature and pressure, the relatively less stable mono-valent Ag_2O (decomposes at around ~200 °C in air) requires the use of high pressures to suppress its decomposition at 500 °C for solid state synthesis or 9 bar hydrothermal pressure at 180 °C along with a pH of 12.5 to suppress the decomposition of $Ag(OH)_x$. The first report on the formation of $AgInO_2$ employed a pressure of 500 bar at 500 °C used Ag_2O and In_2O_3 precursors. A closer look at the equilibrium of the following reaction at high temperatures

$$2Ag + 1/2O_2 \underset{500\ ^oC}{\overset{\Delta}{\rightleftharpoons}} Ag_2O \tag{5.2}$$

reveals that the forward reaction deals with the solubility of oxygen at high pressures in molten silver forming Ag_2O and the reverse reaction deals with the latter's decomposition and both of which have to be dealt with in order to understand the synthesis. Allen and co-workers tracked the forward reaction by investigating the suppression of melting point of Ag and proposed the following the empirical relation [191]:

$$T = 961 - 22.31\sqrt{p} \tag{5.3}$$

where p is measured in atm and T is the temperature (˚C). The pressure – temperature relation for the reverse reaction of Ag_2O dissociation was studied by Lewis who measured the pressure generated during the decomposition [191]. They have proposed an empirical relation for the dissociation pressure shown below,

$$\log(p) = -\frac{2859}{T} + 6.2853 \tag{5.4}$$

The intersection of the extrapolated melting point curve of molten silver in equilibrium with silver oxide for the forward reaction and the pressure-temperature curve for the dissociation of Ag_2O of the reverse reaction yields a temperature of 507 ˚C and a pressure of 414 atm, suggesting the eutectic between Ag and Ag_2O near this point (Figure 5.6) [191-193]. This shows a pressure of at least 415 atm is necessary at 507 ˚C to prevent the decomposition of Ag_2O [191-193]. Incidentally, the synthesis conditions employed by Shannon and co-workers through high pressure solid state route satisfied the requirements which resulted in the formation of $AgInO_2$ with minor impurities [88].

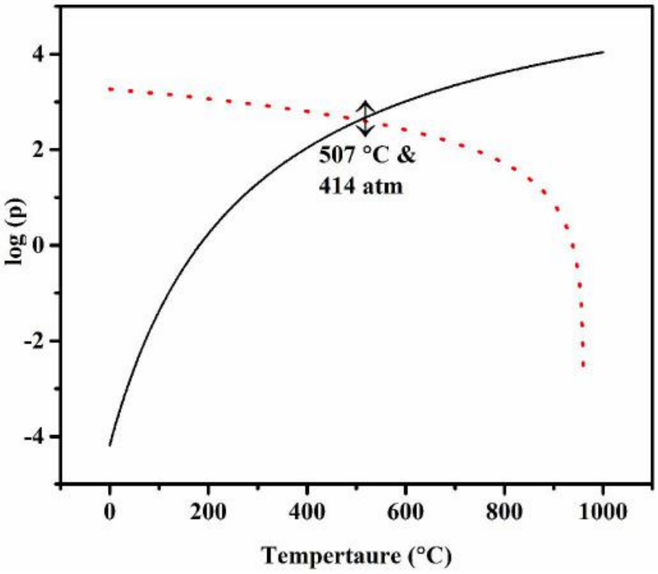

Figure 5.6. Equilibrium diagram for Ag-Ag_2O system [193].

On the other hand, hydrothermal synthesis of $AgInO_2$ reports a pressure of 9 bar at ~200 ˚C with a pH of 12.5 to prevent the decomposition of $Ag(OH)_x$ to Ag_2O/Ag through the large amount of common OH-ions present in the solution. The decomposition pressure of Ag_2O at 200 ˚C evaluated from Equation 5.4 is 1.9 atm whereas the hydrothermal pressure at this temperature is around 9 atm which suppresses the decomposition of Ag_2O to a large extent during hydrothermal synthesis [194].

Although the bulk synthesis of $AgInO_2$ was reported in 1971, the growth of thin films of $AgInO_2$ was reported only in 1998. Thin film of $AgInO_2$ was deposited on α-Al_2O_3 substrate using RF sputtering at a partial pressure of 0.13 mbar at 400˚C [156]. Subsequently, formation of Sn-doped $AgInO_2$ by pulsed laser deposition technique at an in-situ oxygen pressure of 0.13 mbar was reported by Ibuki, et al. in 2000 [147]. However, there was no other report thereafter to verify their claim which implies that the conditions are extremely sensitive and narrow, prompting us to investigate. The challenge here is to identify the appropriate in-situ growth conditions to retain Ag in +1 oxidation state (as in Ag_2O) to realize the formation of $AgInO_2$. As Ag_2O decomposes to metallic Ag at 200˚C at atmospheric pressure, its decomposition is accelerated at lower pressures during thin film processing making it impossible to realize the formation and hence it demands the evaluation of growth conditions of Ag_2O thin films before attempting $AgInO_2$.

Review of literature shows that an in-situ pressure $p < 10^{-2}$ mbar always yielded pure Ag films forcing us to investigate the formation of Ag_2O at higher in-situ pressures. Since the highest in-situ pressure achievable in reactive sputtering is approximately 0.2 mbar which is reported to yield a mixture of Ag and Ag_2O, thin film deposition technique which offers the film growth at higher in-situ pressure would be right choice. PLD, the only other technique with its source kept outside the processing chamber, offers film growth at higher in-situ pressures even up to 1 mbar and hence it was chosen for investigation [195]. Keeping in view the reported temperature window for formation of $AgInO_2$, growth conditions of Ag_2O are searched in the temperature interval of 200 ˚C to 400 ˚C beginning with the in-situ pressures of 0.13 mbar and above. Figure 5.7 shows the GI-XRD patterns of thin films of Ag_2O deposited at in-situ pressures of 0.1 mbar & 0.7 mbar from 200˚C to 400˚C at an interval of 100 °C. XRD results in Figure 5.7 (a) shows all the films yielded a mixture of Ag ($Fm\bar{3}m$ (225); ICDD # 89-3722) and Ag_2O ($Pn\bar{3}m$ (224); ICDD # 41-1104) with elemental Ag fraction gradually increasing with the rise in temperature. At 0.7 mbar phase pure Ag_2O is obtained at 200 ˚C (Figure 5.7 (b)). With the rise in temperature purely elemental Ag was formed implying higher temperatures are not favorable for the formation of Ag_2O. The use of 0.7 mbar during in-situ growth is rather unusual and is not reported hitherto as the short mean free path not only reduces the plume size but also the growth rate. Thin film growth at higher in-situ pressure of 0.7 mbar optimized for Ag_2O directly yielded high quality thin films of phase pure $AgInO_2$ at 200 ˚C (as reported in Figure 5.2) which otherwise would require > 500 bar pressure and temperature of 500 ˚C. Even the extremely challenging oxygen sensitive

$YBa_2Cu_3O_{7-\delta}$ thin films require an in-situ oxygen pressure of 0.17 mbar only to force $\delta < 0.1$ to get a superconducting transition temperature of 90 K.

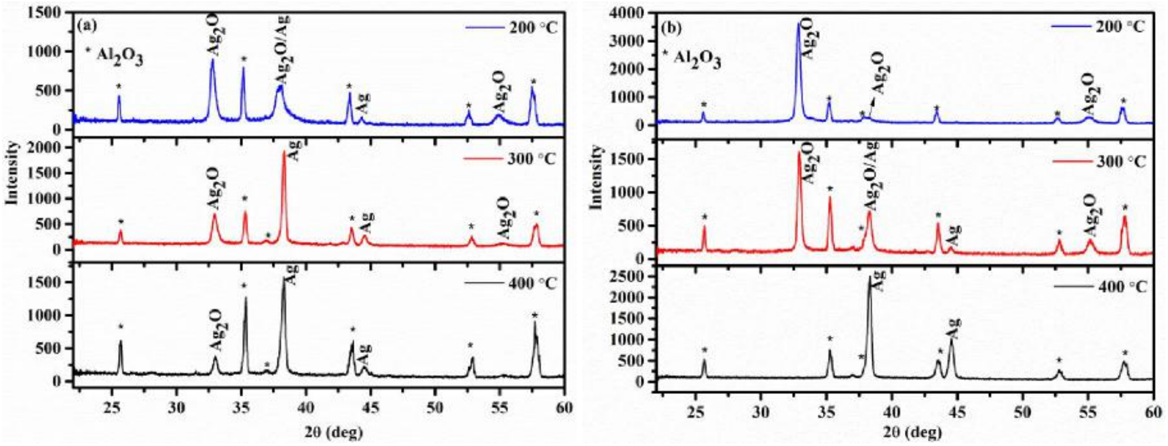

Figure 5.7. GI-XRD patterns of thin films of Ag_2O deposited on polycrystalline Al_2O_3 substrate at **(a)** 0.1 mbar & **(b)** 0.7 mbar at different temperatures

The density of singly charged Ag ions, n_i per cm^3 is calculated using Saha's equation for a gas at local thermal equilibrium which is given by [118],

$$\mathbf{n_i = \sqrt{2.4\times10^{15}T^3n}\left[\exp\left(-\frac{U_i}{2kT}\right)\right]} \qquad \mathbf{(5.5)}$$

where n is the density of neutral per cm^3 and U_i is the first ionization potential of Ag in eV. Taking the ionization potential of Ag to be 7.576 eV, the plot of singly charged ions versus the total number density is shown for different temperatures in Figure 5.8. A laser pulse of 30 ns produces a power density of 10^8 W/cm^2 generating an electric field of approximately 10^5 V/cm. This can cause dielectric break down in many materials paving the way for absorption of most of laser radiation. The temperature of the nascent plasma can rise up to 8000 K at which most of the Ag could be ionized. The absorption coefficient of laser radiation by the nascent plasma is proposed to take place through inverse Bremstralung method which occurs in the time scale of femtoseconds (fs) which quickly raises the temperature of the plasma to

10,000 K – 30,000 K in accordance with the following Equation proposed for 248 nm nanosecond pulse [118, 120, 195].

$$\alpha = 3.8\times10^{8}\left[\frac{Z^{3}n_{i}^{2}}{\upsilon^{3}\sqrt{T}}\right]\left[1-\exp\left(-\frac{h\upsilon}{kT}\right)\right] \qquad \textbf{(5.6)}$$

It is reported that at such high temperature of plasma, a high degree ionization close to unity is experimentally observed for nanosecond pulse of wavelength of 248 nm for most of the materials [118]. Besides enhancing the stability of Ag^+ species, the in-situ growth traps the Ag^+ ions in the lattice at higher oxygen partial pressure of 0.7 mbar and 200 ˚C allowing the growth of $AgInO_2$ phase. This investigation reveals two important aspects. First it opens up a new route to probe the physical properties of certain high pressure stabilized compounds of technological importance directly in thin films. Secondly, certain high pressure compounds can be grown as thin films if the issues related to their stability are suitably addressed. In the present thesis, the deposited films were used to study their performance as a gas sensor.

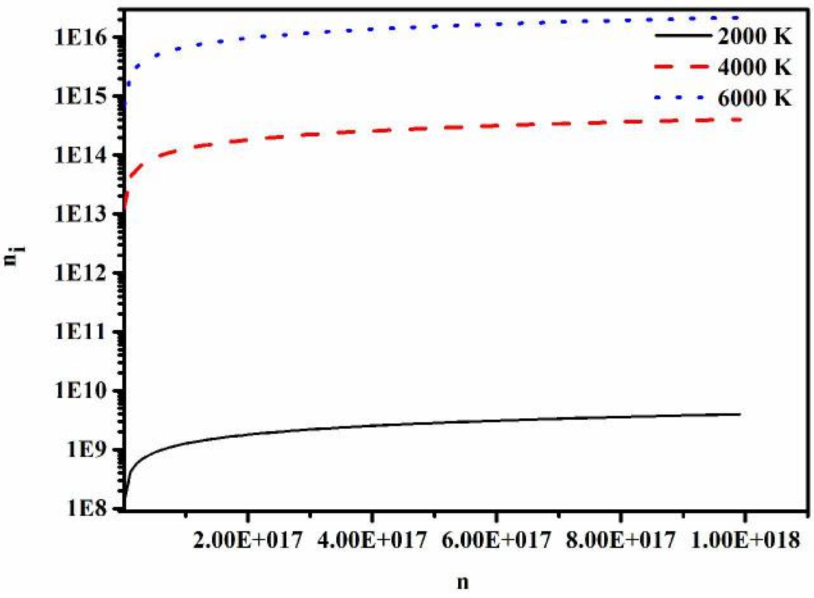

Figure 5.8. Plot of singly charged ions (n_i) versus the total number density (n) for different temperatures

5.3.4. Gas sensing studies

The gas sensing properties of thin film of $AgInO_2$ was investigated and the results were compared with those of thick films. The optimum temperature of sensing hydrogen was obtained by injecting 100 ppm of H_2at different working temperatures (200 ˚C to 400 ˚C) and the corresponding responses were calculated (Figure 5.9 (a)). As seen from Figure 5.9 (a), the highest response of 8.9 (R_a/R_g) was obtained at 360 ˚C towards 100 ppm of H_2 followed by a decrease in response with increase in operating temperature. This shows an operating temperature of 360 ˚C is found to be optimum for H_2 sensing. The response of thick film was also shown in Figure 5.9 (b). As sesn form Figure 5.9, the response of thin films were found to be superior for hydrogen (~1.5 times higher for 100 ppm) than that of thick films of $AgInO_2$.

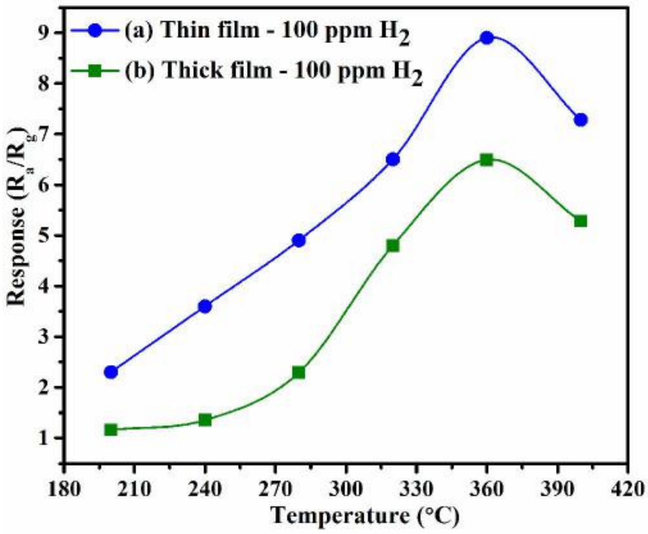

Figure 5.9. The responses for **(a)** thin and **(b)** thick films of $AgInO_2$ towards 100 ppm of H_2 at different temperatures

Figure 5.10 (a & b) shows a transient reponse patterns of thin and thick films of $AgInO_2$ towards 100 pmm H_2. At 360 ˚C, the response and recovery times for 100 ppm of H_2

was ~ 6 s and ~22s for thin films (Figure 5.10 (a)) which were quite faster than that of thick films for which the vales were ~30 s and ~120 s respectively (Figure 5.10 (b)).

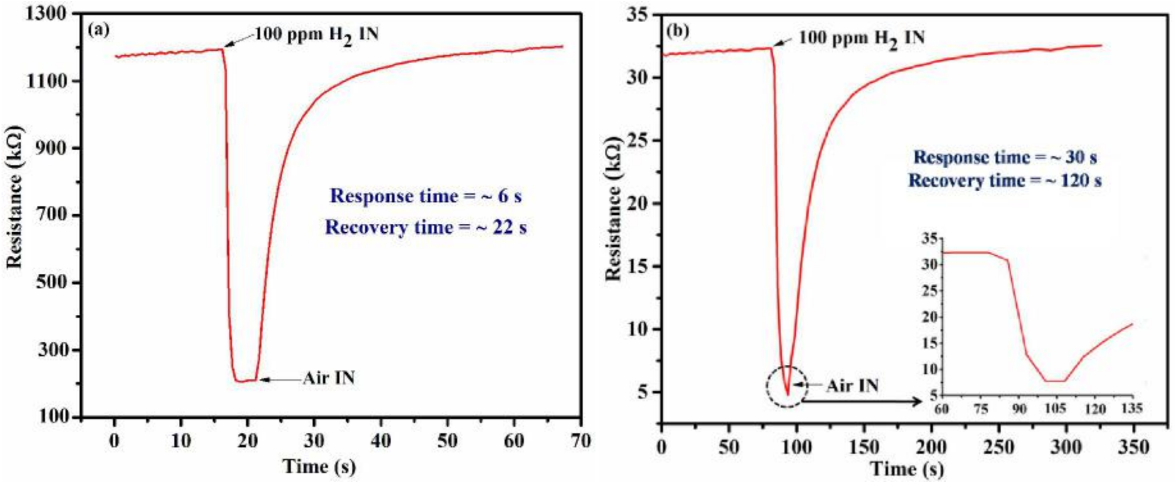

Figure 5.10. Transient response patterns of **(a)** thin and **(b)** thick films of $AgInO_2$ (inset shows the satuartion) towards 100 ppm of H_2

In order to assure the selectivity of the material towards H_2, the response of thin films were recorded for 100 ppm of analytes such as NO_x, LPG, HCHO, NH_3 and CH_4 at 360 ˚C (Figure 5.11). As seen from the Figure 5.11, thin films of $AgInO_2$ showed higher response to H_2, least response for LPG and NH_3 and no response for HCHO and CH_4 just as observed for thick films. The responses of H_2 over LPG & NH_3 were ~7 & ~7.5 times higher that indicate the selectivity of $AgInO_2$ towards H_2. The selectivity coefficients of 100 ppm of H_2 over other analytes for thin and thick films of $AgInO_2$ are presented in Table 5.2. This shows that thin films of $AgInO_2$ have relatively high response and selectivity towards H_2 at 360 °C compared to that of thick films.

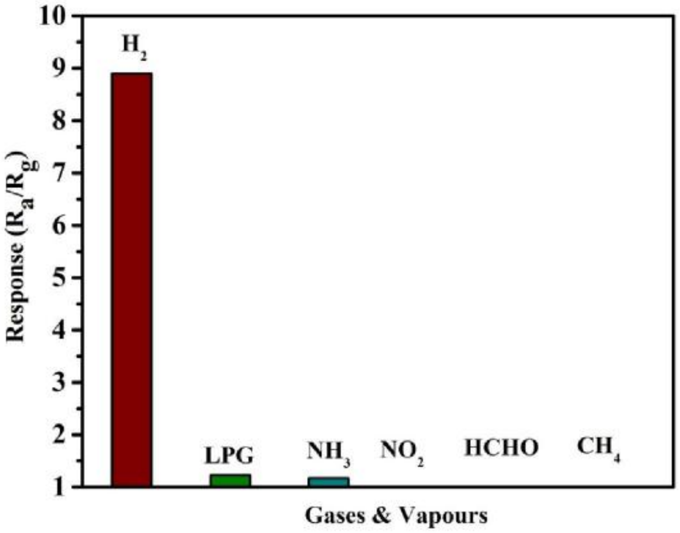

Figure 5.11. The responses for thin film of $AgInO_2$ towards 100 ppm of various gases/vapours at 360 °C

Table 5.2. Selectivity Coefficients of 100 ppm of H_2 over other analytes for thin and thick films of $AgInO_2$

	Selectivity Coefficients of H_2 over other analytes of $AgInO_2$	
Analyte	**Thin film**	**Thick film**
LPG	7.1	3.8
NH_3	7.6	6.5
NO_2	8.9	6.5
CH_4	8.9	6.5
HCHO	8.9	6.5

Thin film of $AgInO_2$ was tested for a wide range of H_2, from 1 ppm to 10000 ppm at 360°C and the results are presented in Figure 5.12. The calibration plot (Figure 5.12) shows that a systematic increase in response was observed with an increase in H_2 concentration and the response found to be linear from 1 ppm to 1000 ppm with an Adj. $R^2$of 0.9941 (inset of Figure 5.12), beyond which a non-linear response with marginal variation is noticed. It is noticed that the surface effects are more pronounced in nanostructured thin film of thickness of ~ 175 nm with adsorbed oxygen species playing a dominant role compared to that of lattice oxygen.

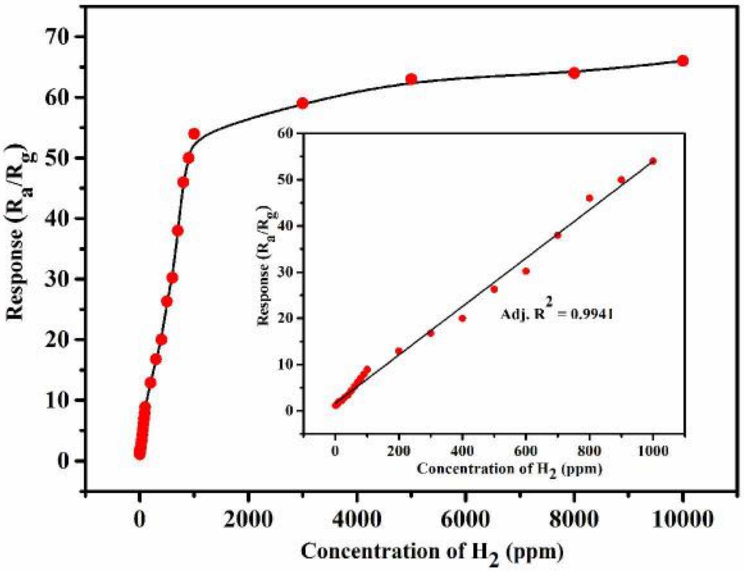

Figure 5.12. Calibration plot of thin films of $AgInO_2$ towards different concentrations of H_2 at 360°C (inset linear fit for 1 – 1000 ppm of H_2)

For practical use, consistency in repeatability and stability of the sensor are of major concern. To check the repeatability of thin films of $AgInO_2$, the responses for 10 ppm, 100 ppm and 10000 ppm covering the low and high ranges of H_2 were recorded (Figure 5.13). The short term repeatability was tested for 5 consecutive injections and the average responses (R_a/R_g) was calculated to be 1.9 ± 0.002, 8.95 ± 0.004 & 66 ± 0.005 for 10, 100 & 10000 ppm of H_2 respectively. The sensor's response was consistant. At these concentrations, the response and recovery times for thin films were calculated and the results are compared with that of thick films (Table 5.3). To be noticed, a significant reduction in response and recovery times than that of thick films of $AgInO_2$ is noteworthy of thin film configuration. The experiments were repeated three times for confirming the consistency in response and recovery times.

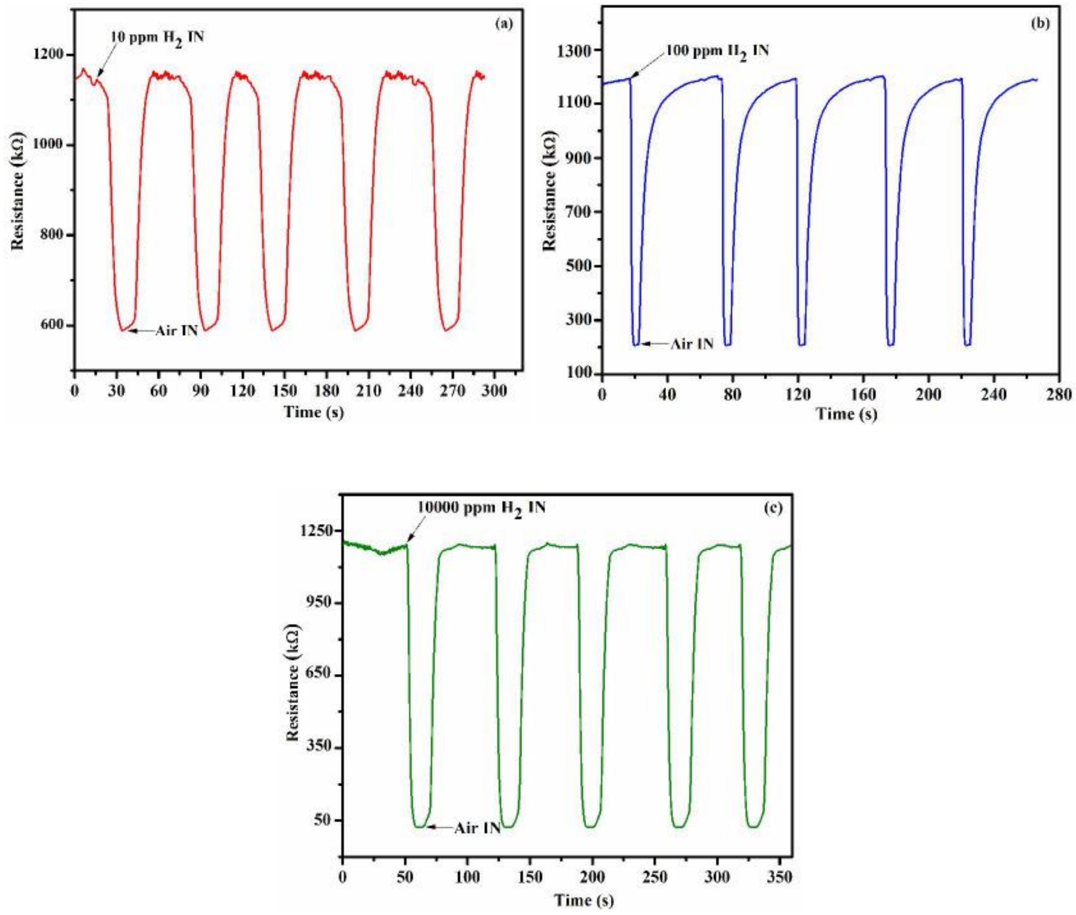

Figure 5.13. Repeatability test patterns of $AgInO_2$ towards **(a)** 10 ppm, **(b)** 100 ppm and **(c)** 5000 ppm of H_2 gas

Table 5.3. Response and recovery times for thick & thin films for different concentrations of hydrogen

Concentrations of H_2 gas (ppm)	Thick film		Thin film	
	Response time (s)	Recovery time (s)	Response time (s)	Recovery time (s)
1	8	9	5	8
10	12	36	7	10
100	28	120	6	22
1000	36	265	19	66
10000	62	562	22	94

The long-term repeatability tests were performed at 360 ˚C for a period of six months at an interval of 10 days for 100 ppm of H_2 and the results are displayed in Figure 5.14 (a). Thin film was tested for 20 times at regular intervals over a period of 180 days and the results showed a highly repeatable patterns with an average response of 8.95 ± 0.004. Figure 5.14 (b) shows the baseline data of $AgInO_2$ thin film monitored for six months averaged at a frequency of 10 days. The mean value of the baseline resistance of the sensor is found to be 1197 kΩ with a standard deviation of 10 kΩ which falls in the acceptable limit indicating a satisfactory baseline stability of the material. Overall thin films of $AgInO_2$ had showed higher response towards hydrogen with a significant reduction in the response and recovery times than that of thick films of $AgInO_2$.

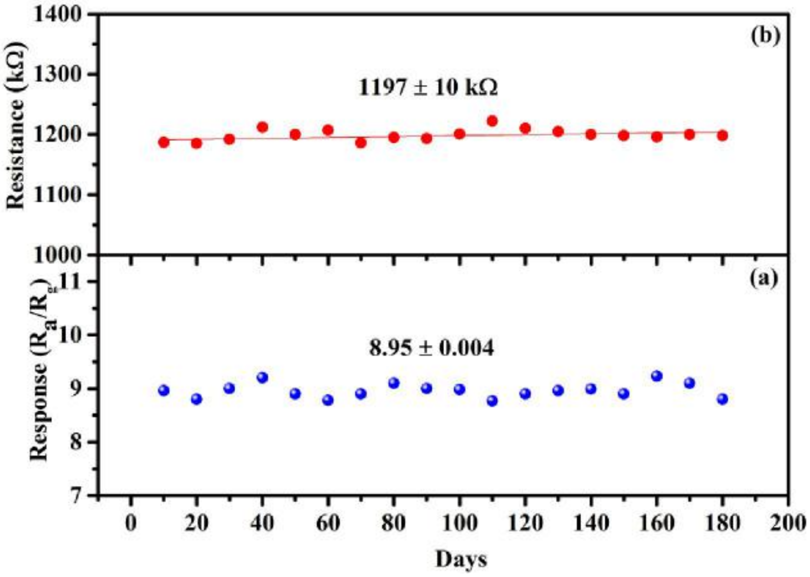

Figure 5.14. (a) Long term stability towards 100 ppm of H_2 and **(b)** baseline stability data of $AgInO_2$ thin films for six months at 360 ˚C

5.3.5. In-situ Hall measurement studies

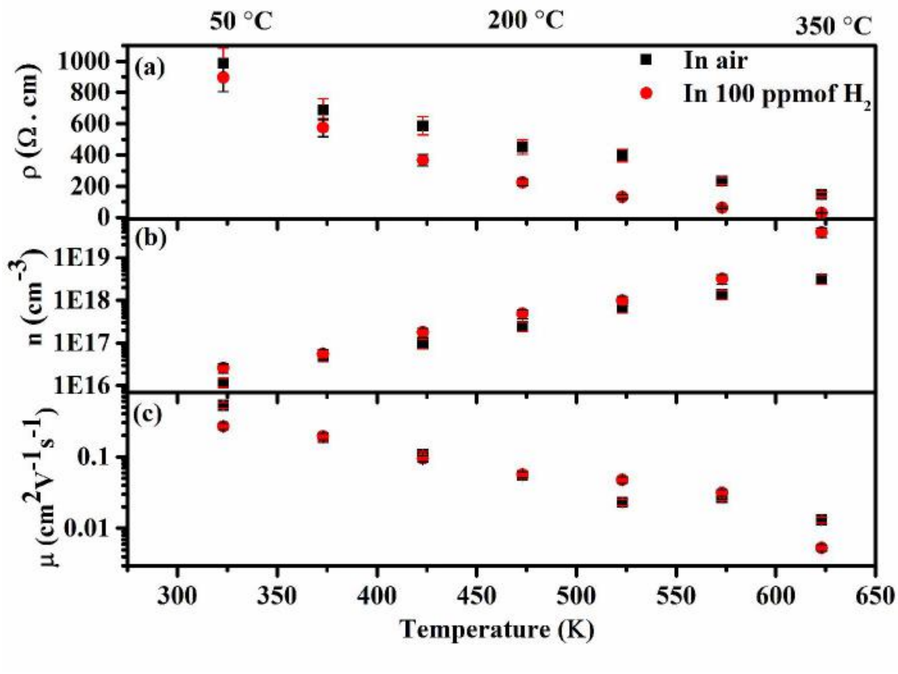

Figure 5.15. (a) Resistivity (ρ), **(b)** electron carrier concentration (n) and **(c)** mobility (μ) of $AgInO_2$ thin film in air and air containing 100 ppm of H_2 as a function of temperature

To understand the mechanism of interaction of hydrogen with $AgInO_2$, Hall coefficients of thin film were measured in air and air containing 100 ppm of H_2 for the temperature interval of 50 ˚C - 350 ˚C. The sign of Hall voltage indicates an n-type behavior. The changes in four probe-resistivity (ρ), charge (electron) carrier concentration (n) and mobility (μ) were evaluated at different temperatures.

Figure 5.15 (a) shows the plot of four probe resistivity of thin film as a function of temperature in air (■) and air containing 100 ppm of H_2 (●). As seen from the Figure, the resistivity in air decreases with increase in temperature typical of a semiconducting behavior. The room temperature resistivity of ~ 1000 ohm^{-1} cm^{-1} was observed which is in agreement with the literature [147, 156]. Three surface adsorbed oxygen species were reported to exist in the temperature interval of 50 °C - 600 °C. All the three adsorbed species control the surface resistivity of the semiconductor in different ways [25]. Depending upon the temperature, one or more of these adsorbed species will be in dynamic equilibrium with oxygen in air as given by the following Equation and controls the resistivity.

$$\mathbf{O_{2\,(gas)} \xrightleftharpoons{50^{o}C\text{ to }75^{o}C} O_{2\,(physisorbed)} \xrightleftharpoons{50^{o}C\text{ to }200^{o}C} O_2^{-}{}_{(chemisorbed)}}$$

$$\mathbf{O_2^{-}{}_{(chemisorbed)} \xrightleftharpoons{175^{o}C\text{ to }425^{o}C} O^{-}{}_{(chemisorbed)} \xrightleftharpoons{400^{o}C\text{ to }600^{o}C} O^{2-}{}_{(lattice)}} \qquad \mathbf{(5.7)}$$

It is evident that the resistivity of the film in air containing 100 ppm of H_2 was lower than that of air throughout the temperature range of investigation.

Further inference about the mechanism of conduction was deduced from Hall coefficient data. Figure 5.15 (b) shows the changes in electron carrier concentration as a function of temperature in air containing 100 ppm of H_2. For comparison, a variation in carrier concentration in air is also plotted in the same graph. The electron carrier concentration of $AgInO_2$ in air steadily increases from 10^{16} to 10^{18} cm^{-3} with rise in temperature. The carrier concentration estimated at room temperature is 1.1×10^{16} cm^{-3} which is not yet reported. In the presence of 100 ppm of H_2 in air, a significant gain in electron carrier concentration is observed throughout the temperature range of investigation. Incidentally the maximum change in carrier concentration (n) occurred at 350 ˚C justifies the choice of this operating temperature. This implies that H_2 reacts with O_x^- ions (O_2^-/O^-) during sensing in accordance with the Equation 5.8 and releases the trapped electrons back to the solid causing a decrease in resistivity as described in the Chapter 4 [187, 188].

$$\mathbf{O^{-}_{ad} + H_2 \xrightarrow{350^{\circ}C} H_2O + e^{-}(SMO)} \qquad \mathbf{(5.8)}$$

The temperature dependence of mobility curve of $AgInO_2$ in air for the same interval is shown in Figure 5.15 (c). The mobility of charge carriers (electrons) decreases with increase in temperature in air and air containing 100 ppm of H_2. It is evident that no appreciable difference in mobility was observed after exposure to hydrogen. To the best of author's knowledge, temperature dependent measurements of carrier concentration and mobility of $AgInO_2$ thin film were not reported so far.

5.4. Conclusions

Granular thin films of randomly oriented rhombohedral $AgInO_2$ were successfully deposited at 200 ˚C under the in-situ pressure of 0.7 mbar oxygen which otherwise stabilize at high pressures of about > 500 bar at 500 ˚C by high pressure synthesis or 9 bar and 200 ˚C by a single step hydrothermal synthesis. Thin films exhibited columnar growth with a column width of ~ 20 nm and thickness of ~175 nm. Decomposition of Ag_2O to elemental Ag is identified to be the key issue. Experimental conditions for stabilizing Ag^+ ions were worked out and applied for the successful growth of thin film of $AgInO_2$. Thin films were highly selective and sensitive to H_2 and responds from 1 ppm to 10000 ppm exhibiting superior performance with faster response and recovery times that of thick films. Hall measurements showed n-type behaviour with room temperature carrier concentration of 1.1×10^{16} cm^{-3}. In-situ Hall studies show that both resistivity and carrier concentration were strongly attenuated in the presence of even trace levels of hydrogen. This result opens up stabilization of other delafossite members directly in thin films which are not amenable for bulk chemical synthesis and provides opportunities to investigate the properties of certain high pressure stable materials.

CHAPTER 6

Highly selective PbS thin film based ammonia sensor for inert ambient: In-situ Hall and photoelectron studies

---

This chapter deals with the optimization of thin film deposition parameters of PbS by the pulsed laser deposition technique. Granular thin films of p-type semiconducting PbS (Cubic) with predominantly a-axis oriented grains having an average thickness of about 140 nm were realized at 553 K under the in-situ argon pressure of 1×10^{-1} mbar. Thin films were selective to ammonia at 473 K even in the presence of hydrogen and they operate in inert ambient with a typical response and recovery times of about 25 s and 120 s respectively. In-situ Hall measurements show an exponential decrease in hole carrier concentration with increasing NH_3 level. XPS analysis of Pb 4f and S 2p levels reveals that the valence state of Pb and Sulphur remain in +2 and −2 respectively after exposure to the reducing ammonia and the appearance of N 1s peak at 398.1 eV confirms dissociative chemisorption of ammonia on PbS surface.

6.1. Introduction

During the past few decades, semiconductor oxide-based sensors were developed for monitoring toxic and harmful gaseous species in the environment [13, 14, 196, 197]. These sensors require oxygen for sensing and regeneration. The widely accepted mechanism of sensing proposed for semiconductor oxides (n-type) like SnO_2 [198, 199], In_2O_3 [50], ZnO [200] etc., involves the transfer of carriers from the conduction band to the surface adsorbed oxygen species and their release during interaction with the analyte species. Measurements of changes in carrier concentration during sensing have been attempted to validate the proposed mechanism using well studied n-type semiconducting SnO_2, In_2O_3 oxide gas sensors [201-203]. Relatively less number of p-type semiconducting oxide sensors [204] such as Cr_2O_3 [205], CuO [206], NiO [207] are reported and their performance not comparable to that of n-type oxides.

As the kinetics of the analyte gas with the surface chemisorbed oxygen which controls the conductivity is exploited in both n-type and p-type semiconducting oxides and careful control of operating temperature is required to make it selective to a specific analyte gas among many analytes. Sensors for certain process control have to work in inert gas ambient and the semiconductor sensors whose conductivity varies with the changes in surface coverage of the chemisorbed oxygen species cannot be deployed. Semiconductors having a direct interaction of the analyte species without the mediation of chemisorbed oxygen are suitable for operations in inert ambient and PbS, a semiconducting chalcogenide used in IR detectors [208], solar cells [209], display devices [210], optical switches [211] is a promising candidate. Maximization of surface contribution to the overall conductivity can result in large changes in conductivity even for trace levels of analytes during interaction and hence thin films configuration is ideal for investigation. Among many thin film deposition methods, pulsed laser deposition (PLD) offers greater control over the grain size, thickness, composition, adhesion, and stoichiometry of the multi-component materials is used for in-situ growth of PbS thin films.

Room temperature NO_2 and NH_3 sensing properties of PbS in the air were first reported by Fu et al. [212] whereas NO_x sensing properties of thin films of PbS in the air were reported by Navale et al. and Kaci et al. [213, 214]. Liu et al. probed the feasibility of PbS quantum dots/TiO_2 nanotube arrays for ammonia detection in the air [215]. The objective is to develop an ammonia sensor based on PbS which has to operate in inert ambient in order to track the hydrolysis of uranium nitrides in low levels of moisture which releases ammonia [216]. This kind of sensors can be used in anaerobic environments also [217].

This chapter deals with the ammonia sensing characteristics of thin films of PbS in inert ambient is reported for the first time along with its sensing mechanism. The influences of working temperature, NH_3 gas concentration, cross-sensitivity in argon were investigated. The mechanism of trace levels of NH_3 with PbS thin film is probed under in-situ Hall carrier measurements, four-probe conductivity and the chemical intermediates through X-ray photoelectron spectroscopy.

6.2. Experimental Details

6.2.1. Deposition of PbS thin films using Pulsed Laser Deposition (PLD)

The PbS powder was prepared by the addition of 0.18 M thiourea solution to 0.13 M lead acetate solution under constant stirring at 343 K [218]. The resultant black precipitate was washed thoroughly with water, ethanol, and acetone successively and finally dried at 373 K in air for 2 h. The resultant powder was pressed into 12.5 mm diameter discs at a pressure of 20 MPa for 2 hours to be used as targets for PLD. A KrF excimer laser operating at a wavelength of 248 nm under the repetition rate of 5 Hz and a fluence of 6 J/cm^2 was used for deposition. To avoid the oxygen contamination, films were grown in a fixed argon background in-situ pressure of 3×10^{-1} mbar with substrate temperature varied from 353 - 673 K. Once the optimum growth temperature is identified, then the in-situ argon pressure was varied from 3×10^{-1} to 3×10^{-4} mbar. PbS thin films were deposited on polycrystalline alumina, quartz and single crystal $LaAlO_3$ (012) substrates.

6.2.2. Characterization of PbS thin films

The phase purity of the powder was checked by X-ray diffraction (XRD) using Cu K_α radiation (λ=1.5406 Å) with a step size of 0.02°. XRD patterns of thin films were recorded at a glancing angle (ω) of 3°. Surface morphology and elemental composition of the powder and films were analyzed using FE-SEM/EDX. The surface roughness of films was obtained using AFM. Bandgap measurements were carried out on thin films deposited on quartz substrates and the bandgap was deduced from the transmittance data obtained from UV-Visible spectrophotometer in the range of 200 to 800 nm.

6.2.3. Gas sensing studies

The thin films of PbS deposited on polycrystalline Al_2O_3 substrate integrated with necessary electrical gold pads were mounted inside a vacuum compatible stainless steel chamber of volume 8 mL which has been provided with gas inlet and outlet as shown in Figure 2.18 (Chapter 2). The desired analyte concentration in argon is obtained by adjusting the flow rates of the respective gases using mass flow controllers. The response towards NH_3 was measured at operating temperatures varied from 373 to 523 K in argon flowing at a rate of 100 mL/min. PbS thin films were tested for 20 – 500 ppm of NH_3 at the optimum temperature of sensing. The cross selectivity of PbS thin films towards H_2, a strong reducing gas, and NO_2, a strong oxidizing gas were also investigated at the same temperature. The transient changes in resistance of PbS thin films were recorded using Agilent Data Acquisition Switch Unit. Response (R) is defined as

$$\mathbf{Response} = \left(\frac{(\mathbf{R_g - R_a})}{\mathbf{R_a}} \right) \times \mathbf{100} \qquad \mathbf{(6.1)}$$

where ‘R_a’ is the resistance of the thin film in argon and ‘R_g’ is the resistance in the presence of an analyte. The response time is calculated based on the time is taken for 90% change from its initial value and the recovery time is calculated based on the time taken to retrace back to 90% of its initial value after the analyte is withdrawn from the environment.

6.2.4. In-situ Hall measurement and X-ray photoelectron spectroscopic studies

In-situ Hall measurements and four-probe electrical conductivity of PbS films were carried out using van der Pauw technique [137] to find the concentration of charge carriers in argon and argon containing trace levels of NH_3. The details of the Hall measurement test facility adopted for carrying out the measurements were described in Chapter 2. PbS thin film deposited on (012) $LaAlO_3$ was mounted on the sample stage and measurements were carried out in the argon and argon containing a specific concentration of NH_3 (100 ppm) flowing at a rate of 50 mL/min. The measurements were carried out in the temperature range of 373 to 523 K at a magnetic flux of 3000 Gauss. Hall measurements were also recorded with the concentration of NH_3 varied from 20 – 500 ppm at the optimum temperature of sensing. X-ray photoelectron spectroscopy (XPS) was used to record the survey and selected area scans. A special reaction chamber attached to the XPS system for heating the thin film using an IR lamp to the desired temperature (200 ˚C) in flowing argon/analyte. Photoelectron spectra of PbS thin film were recorded before exposure to ammonia at room temperature. Thin film was taken to the reaction chamber and was exposed to argon containing 500 ppm of NH_3 at 473 K for about 10 minutes. The thin film was cooled to room temperature under the same condition and the reaction chamber was evacuated. The thin film exposed to NH_3 in argon was transported back to the analysis chamber without exposure to air ambient. The recorded spectra were corrected with respect to the C 1s (284.8 eV). An instrumental shift of 0.7 eV was considered while deconvoluting the spectra. A Shirley background subtraction procedure was adopted before processing the XPS data.

6.3. Results and Discussion

6.3.1. Structural, optical and morphological studies

Figure 6.1 shows the powder XRD pattern of the as-prepared PbS. All the diffraction peaks were indexed in terms of the face-centered cubic structure of PbS with a space group of $Fm\bar{3}m$ (225) (JCPDS Card No. 77-0244) confirms the formation of PbS. The unit cell length (*a*) was calculated to be 5.9344 Å. To assess its thermochemical stability, its TG-DTA pattern was recorded in argon which shows a weight loss of about 0.1% only for the temperature interval of 573 – 673 K and this could be due to decomposition of leftover organic precursors or desorption of any adsorbed gases (Figure 6.2 (a)). No additional weight loss indicates that the compound is thermodynamically stable up to 873 K in argon. In contrast to its behavior in argon, a gradual weight gain observed in air beyond 500 K as shown in Figure 6.2 (b) indicates oxygen pick up by PbS probably to form sulphates or oxides [219]. This restricts the deposition temperature for thin film processing in air/oxygen to be under 500 K.

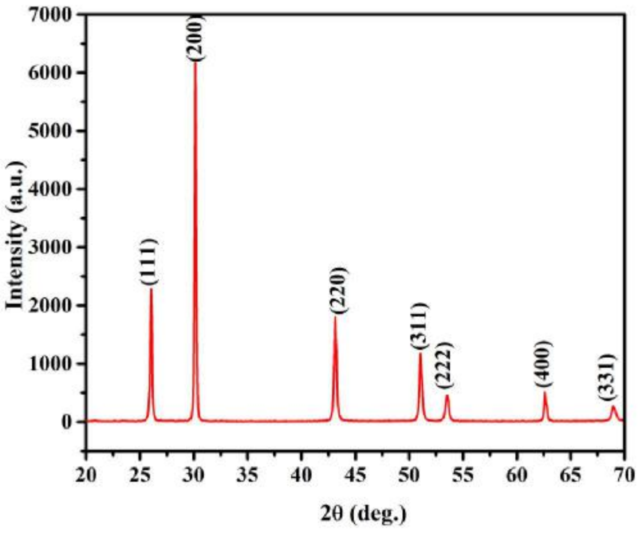

Figure 6.1. Powder XRD pattern of as-prepared PbS

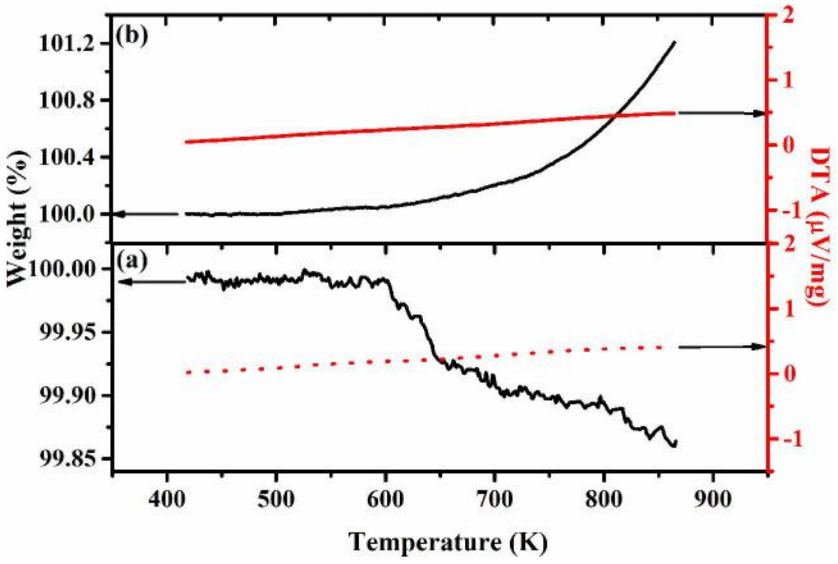

Figure 6.2. TG-DTA pattern of PbS powder in **(a)** argon and **(b)** air ambient

To avoid oxygen contamination in the growing PbS thin film, the collision of Pb and S ions/neutral species with the degassing oxygen in the background need to be minimized due to the formation of PbO or SO_x. This enforces that the mean free path of the ablated species should be greater than the flying distance of the ions. Taking, molecules collision diameter $(\delta_m)_{air} = 3.7\times10^{-8}$ cm, the mean free path (L) at a pressure of 5×10^{-6} mbar is calculated using

$$\mathbf{L = \frac{k\ \ T}{\sqrt{2}\ \ \pi\ \ \delta_m^2\ \ p} = 3.107 \times 10^{-20} \left(\frac{T}{\delta_m^2\, p_{(mbar)}} \right)} \quad \textbf{(6.2)}$$

which becomes 5.6×10^{3} cm at T = 298 K. here, ‘k’ stands for Boltzmann constant. The XRD pattern of films deposited at this vacuum is mostly in the form of Pb/PbO/PbO_2 as shown in Figure 6.3 despite the mean free path being in the range of 56 m. The reason for the formation of PbO is due to the collision of residual oxygen molecules degassing from the interior surfaces with the growing film throughout the film growth. That is, the number of oxygen molecules striking the film to oxidize the film depends on the pressure inside the chamber which needs to be lowered. The no of oxygen molecules per litre at 5×10^{-6} mbar during the film growth is given by

$$\mathbf{N\ (molecules/lit) = 7.24 \times 10^{21}\left(\frac{p_{(mbar)}}{T_{(K)}}\right) = 1.2\times10^{14}\ at\ 298K} \tag{6.3}$$

and the number collisions per unit area per second (φ) to be calculated from the kinetic theory of gases given by

$$\boldsymbol{\varphi} = \left(\frac{1}{4}\mathbf{n\,v_a}\right) = \left(\frac{1}{4}\right)\left(\frac{\mathbf{p}}{\mathbf{RT}}\right)\mathbf{N_a}\left(\sqrt{\frac{\mathbf{2RT}}{\mathbf{M}}}\right) = \mathbf{2.635\times10^{22}\ \frac{p_{mbar}}{\sqrt{TM}} = 1.5\times10^{15}} \tag{6.4}$$

for 5×10^{-6} mbar at 298 K. Here, R stands for the gas constant, N_a is Avogadro number and M stands for molar mass of oxygen. With the deposition rate typically around 0.6 Å for the 30 ns pulse of 248 nm (KrF), the total number of collisions during the growth time of 1200 s is calculated to be 1.8×10^{18}. The volume of 1000 Å thick PbS film over the substrate area of 1 cm × 1 cm is $1\times1\times10^{-5}$ cm^3. As the density of PbS is reported to be 7.6 g/cm^3, the weight of thin film of PbS is 7.6×10^{-5} g which corresponds to 1.9×10^{17} unit cells of PbS. Hence, depositing the film at higher vacuum leads to oxygen pick up and decomposition. The only alternative is to bring down the background partial pressure of oxygen thereby depositing the film under inert ambient which not only suppresses the outgassing rate of oxygen but also helps the film stability. With these inputs, the temperature and in-situ argon background pressure ranges are chosen and the films were deposited.

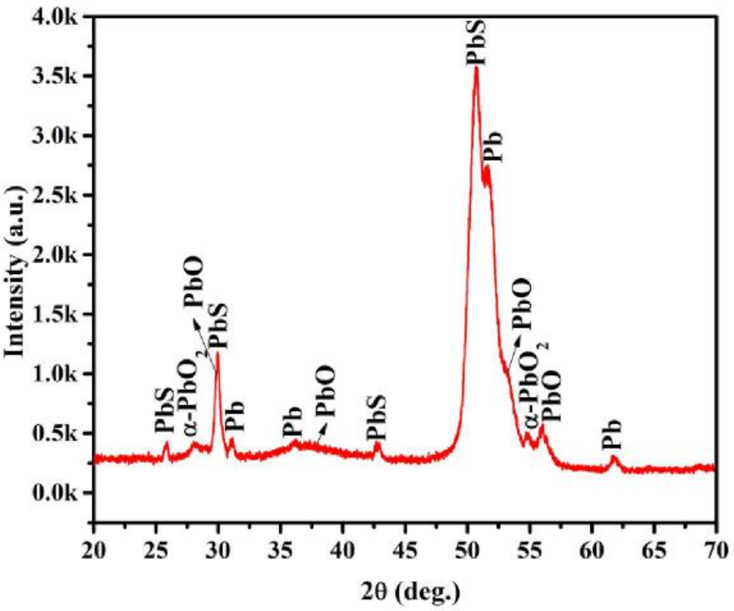

Figure 6.3. GI-XRD pattern of PbS thin film deposited on (012) $LaAlO_3$ at 10^{-5} mbar

Figure 6.4 (a) shows XRD pattern of the films deposited on (012) $LaAlO_3$ at 10^{-1} mbar pressure of argon. Films deposited at 453 K showed small reflections of diffraction peaks. However, films deposited at 553 K exhibited strong reflections at (111), (200), (220), (311) and (400) which were indexed in terms of the face-centered cubic structure of PbS (JCPDS Card No. 77-0244) and also textured along (200) plane. Films deposited at 673 K showed a randomly oriented polycrystalline pattern. Therefore, the optimized temperature for PbS deposition was found to be 553 K. Having fixed the deposition temperature at 553 K, the partial pressure of argon was varied from 10^{-1} mbar to 10^{-4} mbar. Figure 6.4 (b) shows the film deposited at 10^{-1} mbar exhibits a preferential orientation along (200) plane. Reducing the in-situ pressure favours texturing along (311) direction. Overall the optimized condition for deposition of PbS thin films were found to be 553 K and the in-situ argon pressure of 10^{-1} mbar.

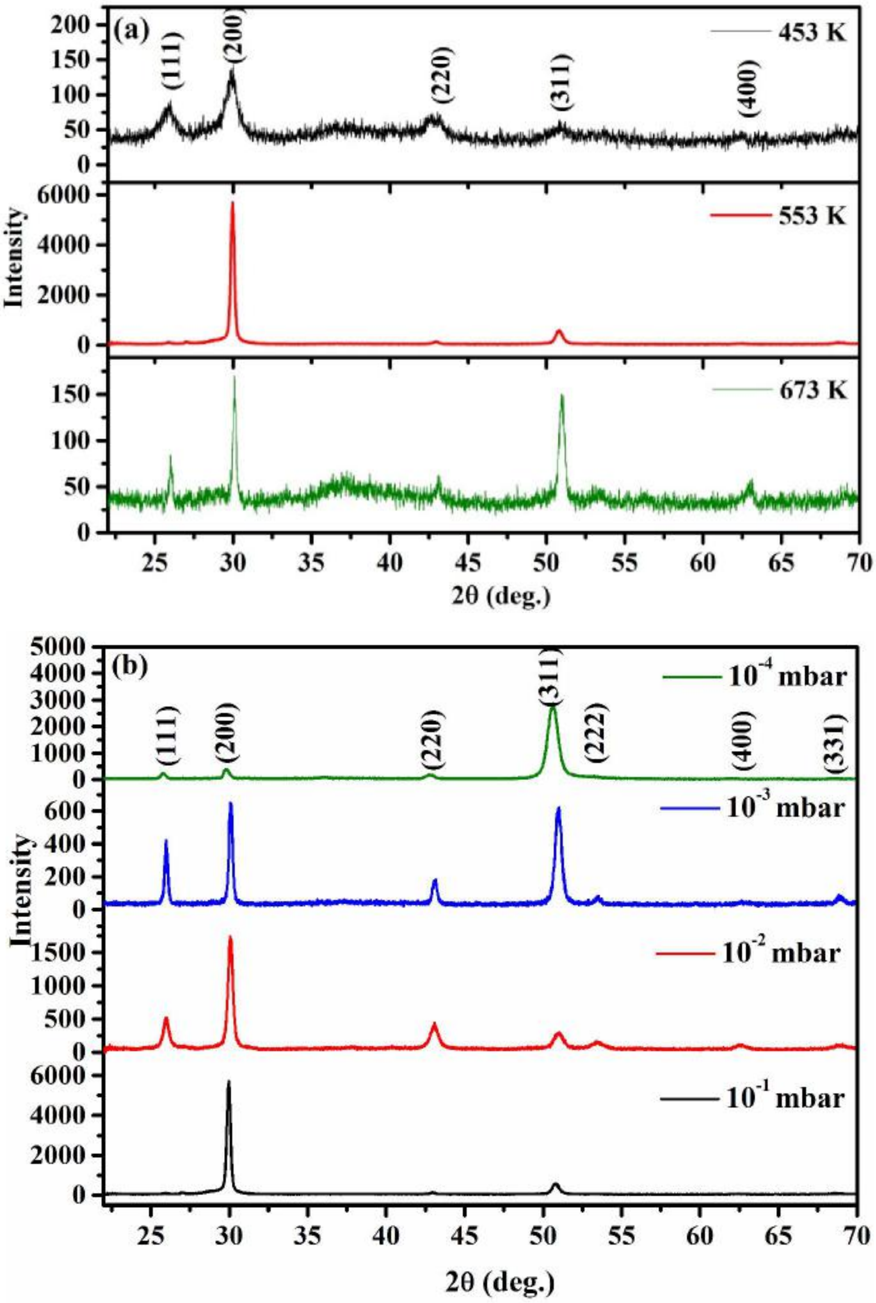

Figure 6.4. GI-XRD patterns of PbS deposited on (012) $LaAlO_3$ at different **(a)** temperatures and **(b)** partial pressures of argon

The optical transmittance spectra of PbS thin film deposited on a quartz substrate recorded in the wavelength range 200 – 800 nm is shown in Figure 6.5. The optical bandgap (E_g) was calculated using the Tauc relation given in Equation 6.5 [220, 221]:

$$\alpha = \frac{A\sqrt{h\upsilon - E_g}}{h\upsilon} \qquad (6.5)$$

where α is the absorption coefficient (cm^{-1}), hυ is the incident photon energy (eV), A is a constant. The plot of $(\alpha h\upsilon)^2$ versus photon energy (hυ) (inset of Figure 6.5) is found to be a straight line when extrapolated gives rise to a bandgap of 2.25 eV from the intercept with the hυ axis [221]. Large variations in bandgap from 1.5 – 3.2 eV have been reported in the literature [213, 221-223]. A possible reason for such variations in the bandgap of thin films is attributed to the quantum confinement effect [220].

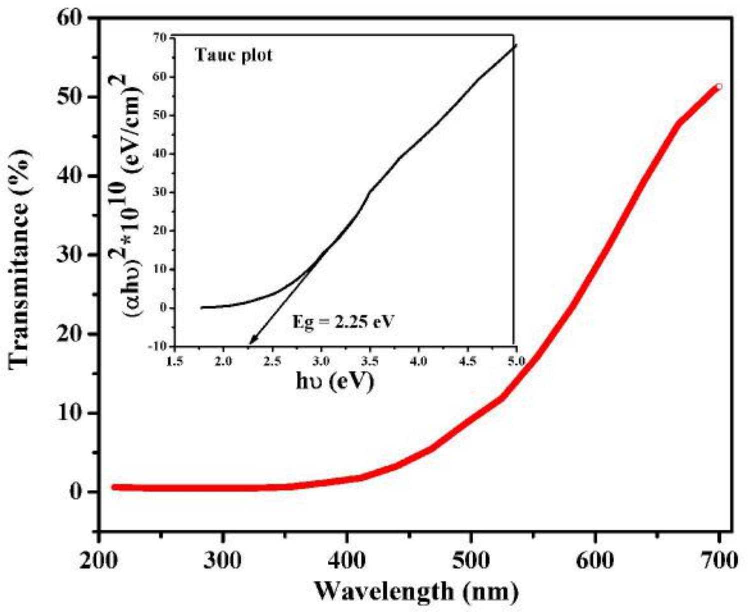

Figure 6.5. Transmittance spectra of PbS thin film; Inset: Plot of $(\alpha h\upsilon)^2$ vs hυ of PbS thin film

Figure 6.6 (a) displays the FE-SEM image of PbS thin film deposited on Al_2O_3 substrate. The morphology shows the film is highly granular with a uniform distribution of grains having an average grain size of about ~300 nm. The magnified portion of the grain (inset of Figure 6.6 (a)) reveals a flower-like morphology with blunt spikes. Energy-dispersive X-ray spectra (EDX) of PbS thin film shows the atomic ratio of Pb to S to be 0.98, close to the stoichiometric value (Figure 6.6 (b)). The traces of substrate peaks (Al & O) are also noticed in the background as the thickness of the PbS film under investigation is about

140 nm (Figure 6.6 (c)). AFM image of the optimized film reveals films were highly granular having grains of uniform size with a mean roughness of about 3.7 nm as shown in the inset of Figure 6.6 (d).

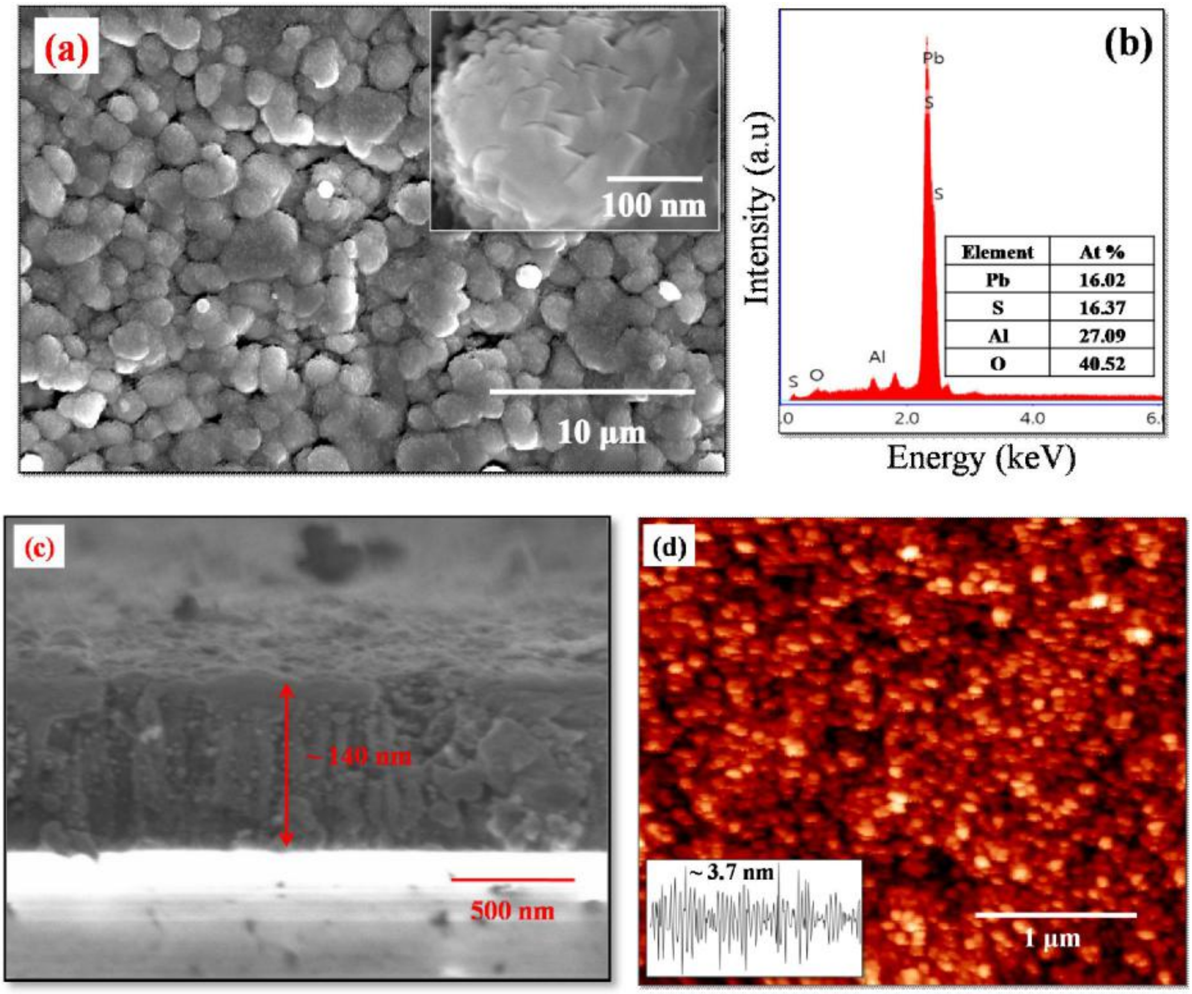

Element	At %
Pb	16.02
S	16.37
Al	27.09
O	40.52

Figure 6.6. (a) FE-SEM image of PbS thin film at low magnification and inset corresponding to a magnified portion of the grain, **(b)** corresponding EDX spectrum, **(c)** cross-sectional SEM image and **(d)** AFM image with roughness profile

6.3.2. Ammonia sensing studies

To find out the optimum temperature of sensing for ammonia, PbS thin film was initially exposed to a typical concentration of 500 ppm of NH_3 at different temperatures ranging from 373 – 523 K. Figure 6.7 (a) shows the plot of response (R) as a function of operating temperature. As shown in Figure 6.7 (a), the response for NH_3 increases with the operating temperature and reaches a maximum of 28 % around 473 K. The response and recovery times of the PbS thin film at different temperatures is evaluated and is shown in Figure 6.7 (b). From the Figure, it is evident that the thin films of PbS exhibit fast response and quick recovery times at 473 K. Therefore, further studies were carried out at an optimum operating temperature of 473 K.

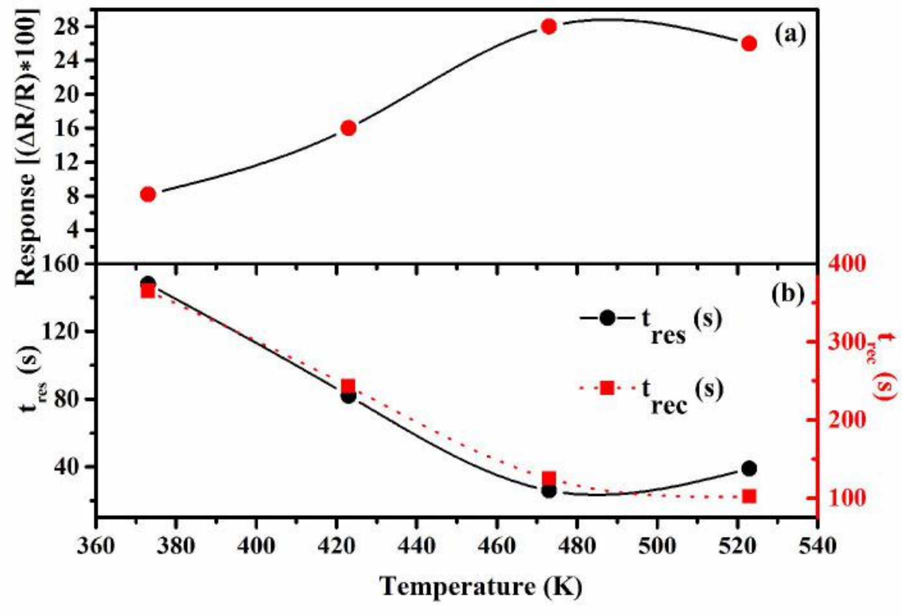

Figure 6.7. (a) Response vs temperature and **(b)** Response & recovery time vs temperature plot of PbS thin film towards 500 ppm of NH_3

The response patterns towards different concentrations of ammonia were recorded at 473 K thereby exposing PbS thin films to 20 – 500 ppm of NH_3 (Figure 6.8). The transient changes in resistance show that the response is systematic with the increase in NH_3 concentration up to 500 ppm. A sharp rise in resistance indicates a p-type behavior of PbS thin films. Generally, a reducing gas always causes a decrease in resistance for an n-type semiconductor as opposed to the p-type semiconductor. The sensor quickly retraces to the baseline value on withdrawal of NH_3. The inset of Figure 6.8 shows the calibration plot which yields a polynomial fit with the regression coefficient of 0.996.

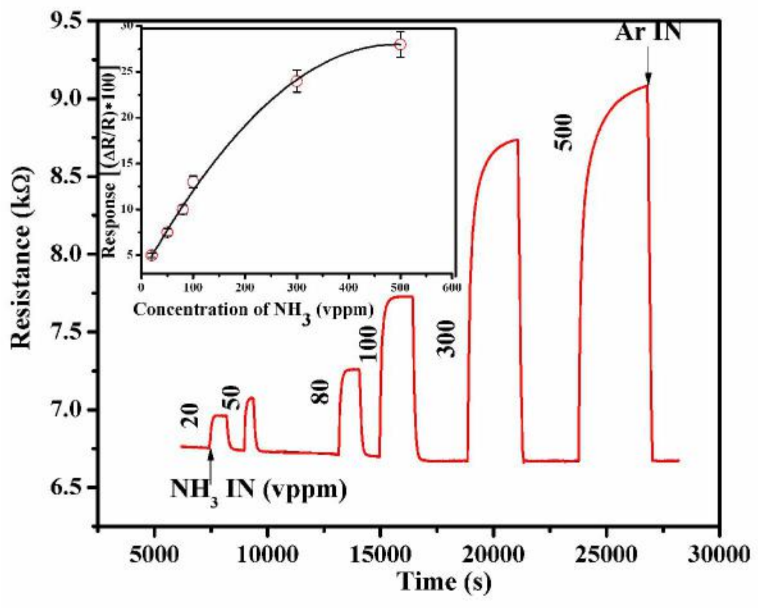

Figure 6.8. The typical response pattern of PbS thin film towards different concentrations of NH_3 at 473 K; Inset shows the corresponding calibration plot

To confirm the reproducibility, PbS thin film was repeatedly exposed to 50 ppm of NH_3 at 473 K and the response is shown in Figure 6.9. The average response is derived to be 8.4% with a standard deviation of 8×10^{-4} which indicates a high reproducibility of PbS thin films towards ammonia.

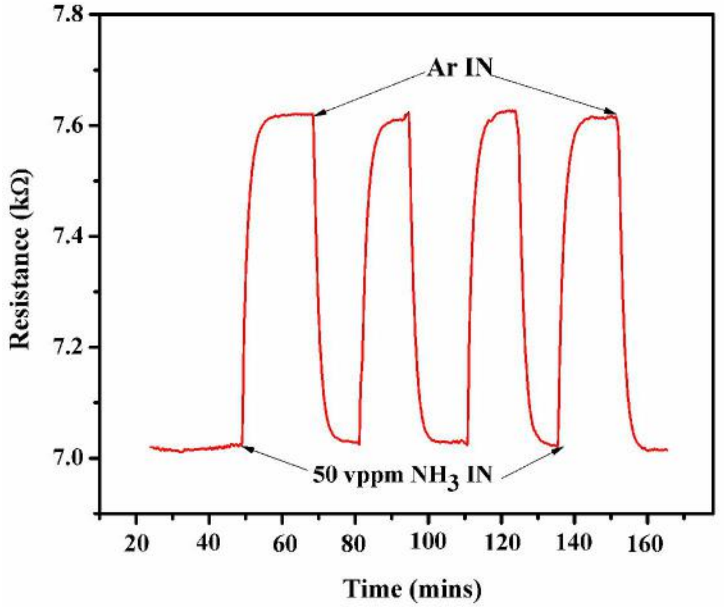

Figure 6.9. Reproducibility test pattern of PbS thin film towards 50 ppm of NH_3 at 473K

Besides ammonia, the PbS thin film was also tested individually for 500 ppm of NO_2, an oxidizing gas and H_2, a reducing gas to check for its cross-sensitivity at 473 K. PbS showed a decrease in resistance towards NO_2, characteristics of an oxidizing gas for the p-type semiconductor with about 8 % change, whereas, it exhibited an increase in resistance for H_2 similar to that for NH_3 with a response less than 0.5 %. The column plot indicates a high degree of selectivity offered by the PbS thin films for ammonia at 473 K (Figure 6.10).

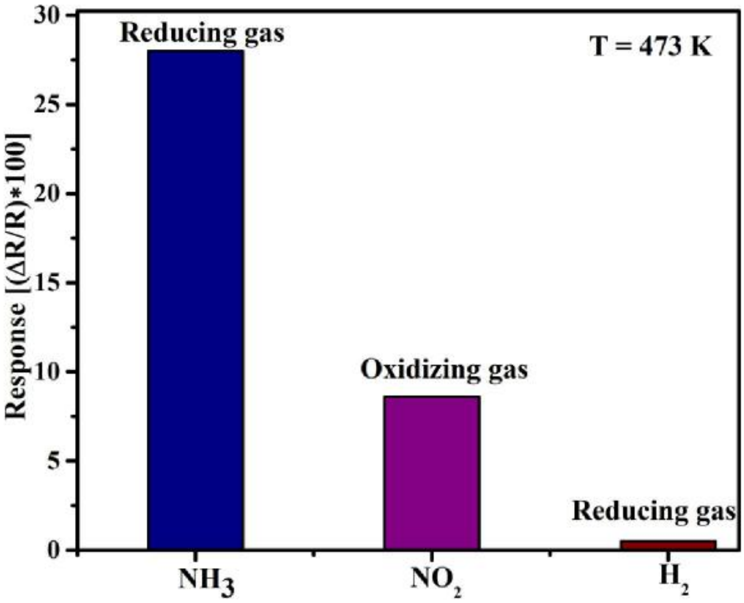

Figure 6.10. Responses of PbS thin film towards 500 ppm of three analytes at 473K

6.3.3. Hall measurement

In order to understand the mechanism of interaction of ammonia with the PbS, in-situ Hall coefficients of PbS thin film was measured in argon and argon containing a specified concentration of ammonia for the temperature range from 373 to 523 K. The positive Hall voltage indicates that the PbS thin film exhibiting a p-type behavior in this temperature range. The hole carrier concentration (p) and mobility (μ) are calculated from the Hall coefficient and four probe-conductivity measured at different temperatures.

The logarithmic conductivity (4-probe) versus inverse temperature plot of PbS thin film in argon (■) and argon containing 100 ppm of NH_3 (●) is shown in Figure 6.11 (a). The plot shows two distinct regions having different slopes observed for both argon and argon containing 100 ppm of ammonia. An activation energy of 0.18 (± 0.04) eV is obtained for the high-temperature region (448 – 523 K) and another with an activation energy of 0.03 eV for the low-temperature region (323 – 423 K) for PbS in argon. Similar values of activation energy were also observed for argon containing 100 ppm of NH_3. The cationic vacancies in PbS introduce acceptor level at 0.18 eV whereas the activation energy of 0.03 eV is due to acceptor level lying close to the valence band of PbS introduced by the adsorbed oxygen. Moreover, the conductivity of PbS thin film in argon containing 100 ppm of NH_3 is lower than that of argon throughout the temperature range of investigation irrespective of nature of conduction.

Figure 6.11 (b) shows the changes in hole carrier concentration of PbS thin film as a function of inverse temperature in argon containing 100 ppm of NH_3. For comparison, a variation in carrier concentration in argon is also plotted in the same graph. The hole carrier concentration of PbS in argon ambient increased from 10^{11} to 10^{13} cm^{-3} [224, 225] for the entire temperature range of 373 – 523 K. However, a significant reduction in hole carrier concentration is observed even for the presence of 100 ppm of NH_3 in argon. This reduction in carrier concentration is noticed throughout the temperature range of investigation. This implies that ammonia interacts with the PbS through its lone pair of electrons after getting adsorbed on the surface which in turn leads to the localization of holes near its vicinity.

Further, the mobility of charge carriers (holes) decreases with increase in temperature (Figure 6.11 (c)) in argon and argon containing 100 ppm of NH_3 [226]. Factors such as lattice vibration scattering (μ_l), impurity scattering (μ_i) and grain boundary scattering (μ_g) have been reported for the changes in mobility [227]. Being granular with an average grain size of about

300 nm, grain boundary scattering may also play a dominant role in these semiconductor thin films [228, 229]. Higher mobility in the presence of ammonia is not understood.

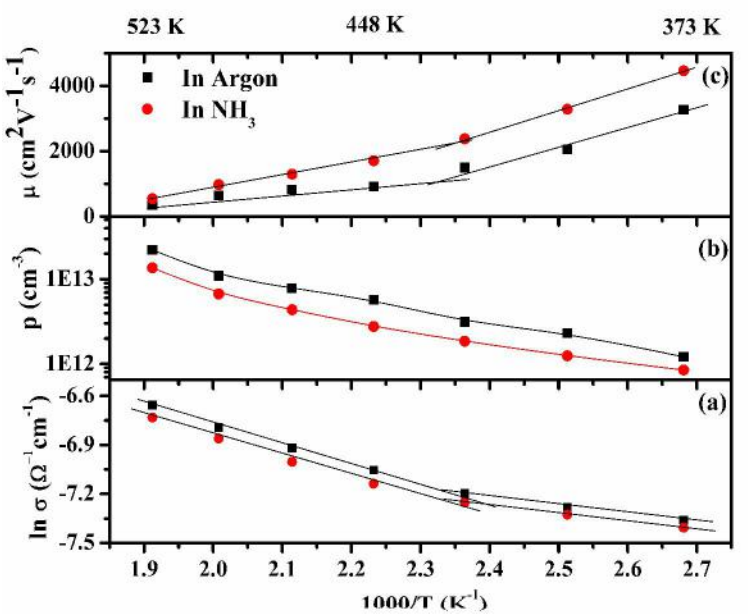

Figure 6.11. **(a)** Conductivity (σ), **(b)** Hole carrier concentration (p) and **(c)** Mobility (μ) of PbS thin film in argon and argon containing 100 ppm of NH_3 as a function of 1/T

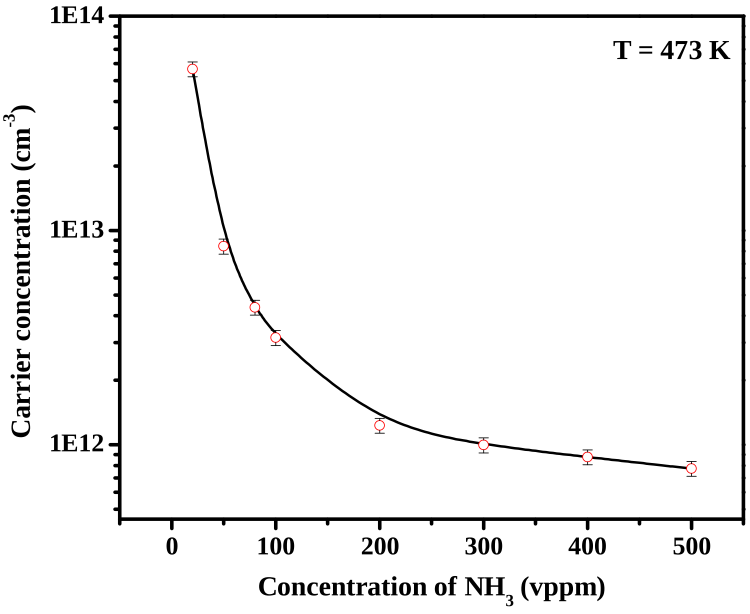

Figure 6.12. Changes in Carrier concentration of PbS thin film as a function of NH_3 concentration at 473 K

Figure 6.12 shows the plot of variations in hole carrier concentration as a function of ammonia concentration. An exponential decrease is observed with increase in ammonia concentration (20 – 500 ppm) when the sensor is operated at 473 K. It should be noted that the carrier concentration decreases by about two orders even for 200 ppm of ammonia. It is quite likely that the interaction of lone pair of electrons of adsorbed ammonia with the holes in the accumulation layer modulates the total conductivity of PbS thin films.

6.3.4. X-ray Photoelectron Spectroscopic studies

XPS analysis is performed to obtain detailed information on chemical states of the constituents of the as-deposited PbS thin film before and after exposure to ammonia. Summary of binding energies with FWHM (Full Width Half Maxima) are presented in Table 6.1.

The selected area high-resolution scan of Pb 4f and S 2p before and after exposure to 1000 ppm NH_3 is shown in Figure 6.13. The Pb 4f pattern was fitted with two components viz., $4f_{7/2}$ and $4f_{5/2}$ peaks at 137.9 eV and 142.8 eV with a spin-orbit coupling parameter (SOCP) of 4.8 eV with the intensity ratio of 4:3 (Figure 6.13 (a)). After exposure to NH_3, the Pb $4f_{7/2}$ and $4f_{5/2}$ peaks were appeared at 137.8 eV and 142.7 eV respectively (Figure 6.13 (b)). The peak position of $4f_{7/2}$ of Pb^{2+} is reported to be in the ranges of 137.3 – 138.9 eV [230-238]. This confirms that lead is in the divalent state before and after exposure to ammonia and no other oxidation states are noticed.

Similarly, the S 2p pattern is fitted with $2p_{3/2}$ and $2p_{1/2}$ components at 161.2 eV and 162.4 eV using a spin-orbit coupling constant of 1.2 eV and the relative intensity ratio of 2:1 as shown in Figure 6.13 (c). After exposure to ammonia, S $2p_{3/2}$ and $2p_{1/2}$ peaks are observed at 160.9 and 162.2 eV respectively (Figure 6.13 (d)). The reported literature for a $2p_{3/2}$ component of divalent sulphur (S^{2-}) lies in the range of 160.7 – 161.5 eV [53, 231-235, 239].

The measured values of S 2p are close to that of values reported in the literature and are indicative of its -2 oxidation state. The absence of any extra features in the spectrum shows that all sulphur ion is in a single oxidation state.

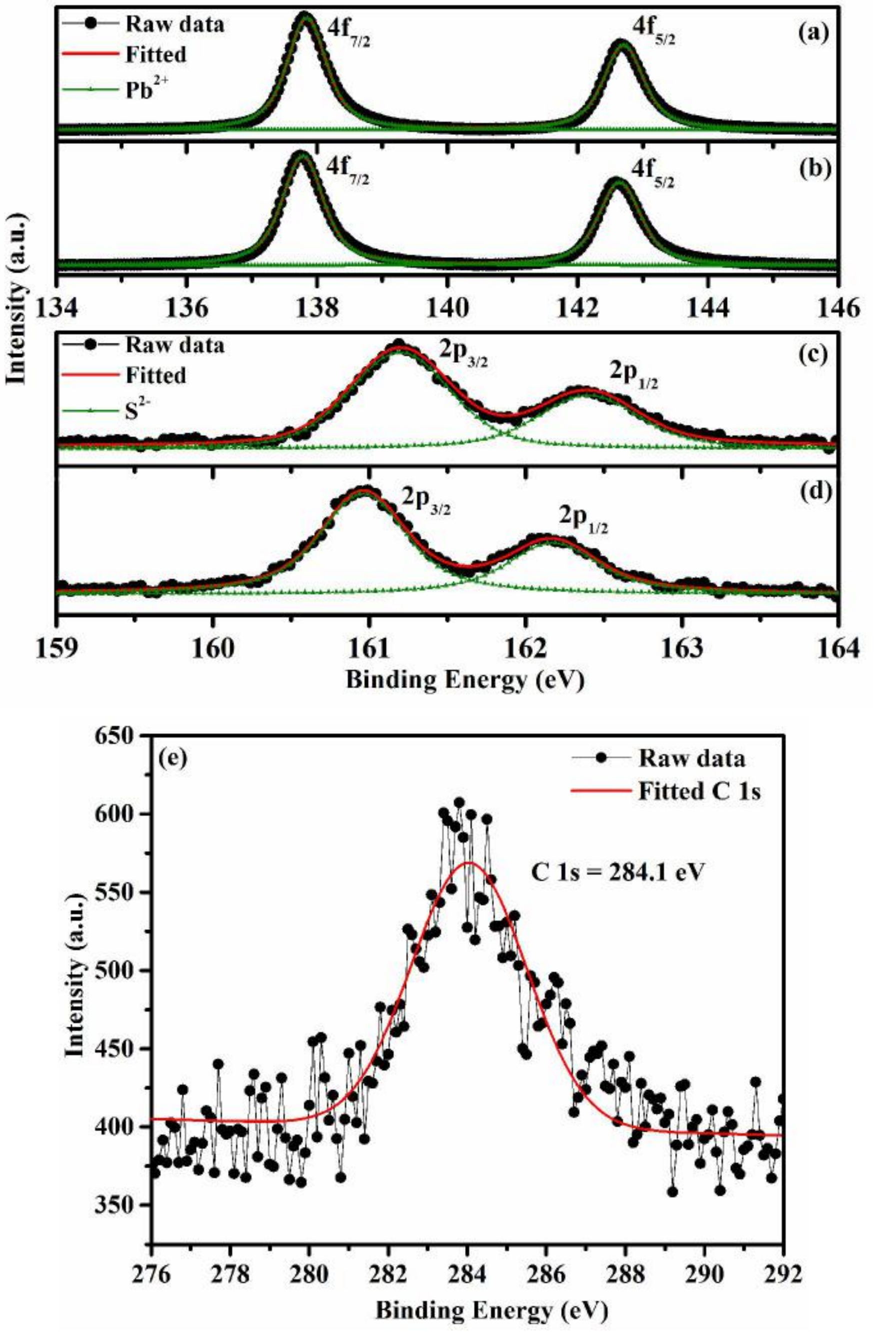

Figure 6.13. Pb 4f and S 2p pattern of PbS **(a) & (c)** before, **(b) & (d)** after exposure to ammonia and **(e)** C 1s pattern

Although the oxidations states of Pb and S remain +2 and -2 respectively even after exposure to ammonia, a shift of ~0.2 eV towards the lower binding energy was noticed for both Pb 4f and S 2p levels. In the absence of any extra feature for both Pb 4f and S 2p patterns, the observed shift of 0.2 eV is correlated to the changes in the chemical environment brought about by the adsorption of NH_3. A similar shift of about 0.19 eV for Pb 4f has been reported by Feng et al., who attributed the change to chemisorption of salicyl hydroxamic acid (SHA) when the chemical status of chemisorbed Pb^{2+} ions on cassiterite (SnO_2) surface was investigated [238]. This drives us to investigate N 1s state of the adsorbed ammonia.

Figure 6.14 shows the background corrected N 1s pattern of the adsorbed species after exposure to ammonia. This provides the spectroscopic evidence for adsorption of NH_3 on PbS surface. Being a nucleophile, NH_3 can donate its lone pair of electrons probably to the 6p level of lead (II) ions which contributes to the valence band of PbS wherein the holes are located [240, 241]. Earlier, Fu et al. have reported ammonia adsorption on the surface of PbS takes place through a weak coordinate bond formation between NH_3 and lead (II) ions in PbS [212]. Considering their observation and the XPS results along with Hall studies, it is proposed that ammonia adsorption can lead to a reduction in hole carrier concentration of PbS thin film thereby localization of holes near its adsorption vicinity and this can cause a rise in resistance of the p-type PbS. Moreover, analysis of N 1s level yields binding energy of 398.1 eV which is less than 400.1 eV reported for NH_3 [242]. The observed value indicates dissociative adsorption of ammonia involving NH_2 / NH species on PbS surface at 473 K. The binding energy value matches with that reported by Peden et al. [242]. In fact, the nitridation process carried out at 473 – 850 K using ammonia is reported to proceed through the dissociative adsorption of NH_3 [242].

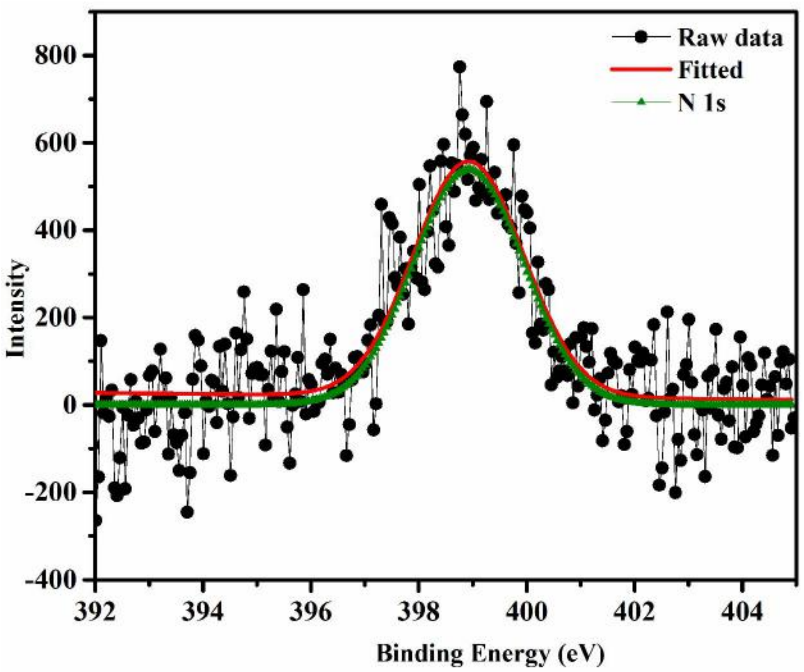

Figure 6.14. N 1s pattern of PbS thin film after exposure to ammonia

Table 6.1. Peak positions and FWHMs of PbS thin film derived from X-ray photoelectron spectra

	Before exposure to ammonia			**After exposure to ammonia**	
	BE(eV)	**FWHM**	**Component**	**BE(eV)**	**FWHM**
Pb^{2+}	137.9	0.8500	**$4f_{7/2}$**	137.8	0.8280
	142.8	0.8614	**$4f_{5/2}$**	142.7	0.8330
S^{2-}	161.2	0.7254	**$2p_{3/2}$**	160.9	0.6651
	162.4	0.7605	**$2p_{1/2}$**	162.2	0.6840
N	__	__	**1s**	398.1	2.3965

6.4. Conclusions

Laser deposited thin films of PbS were highly promising for sensing trace levels of NH_3 in the inert ambient (Ar) and potentially useful for monitoring NH_3 released during the hydrolysis of uranium nitrides stored in an inert atmosphere. Thin films of PbS were grown by pulsed laser deposition under inert ambient as the presence of trace levels of outgassing oxygen leads to its oxidation. Films were highly selective and sensitive to NH_3 with a typical response and recovery times of about 26 s and 125 s respectively for 500 ppm of NH_3 at 473 K. In-situ Hall studies show that both carrier concentration and mobility are altered significantly in the presence of trace levels of ammonia (100 ppm). Adsorption of NH_3 does not alter the oxidation states of Pb and S but causes a shift of 0.2 eV towards the lower binding energy side. A binding energy value of 398.1 eV for N 1s level shows dissociative adsorption of NH_3 involving $–NH_x$ species at 473 K.

APPENDIX 1

Alternate methods attempted to prepare $AgInO_2$

Following methods were attempted for the preparation of $AgInO_2$ based on the available literature.

1. Solid state reaction

Stoichiometric quantities of Ag_2O and In_2O_3 were mixed thoroughly using an agate mortar and pestle for about 2 h. The resultant mixture was compacted to 16 mm diameter and ~ 3 mm thick pellet by uniaxial pressing to about 20 MPa pressure. The pellets were heat treated at 500 ˚C for 24 h. The resulting product was ground, pelletized and again heated to 500 ˚C for another 24 h. This process was repeated three times in order to get a homogeneous product [156]. XRD analysis of the resultant product showed the presence of Ag and In_2O_3 (Figure A1 (a)). This infers, as the noble oxides have low free energies of formation and they decompose before the reaction can occur which results in the formation of Ag and In_2O_3 phases instead of $AgInO_2$.

2. Cation exchange reaction

In cation exchange reaction, first $NaInO_2$ was prepared by direct solid state reaction using Na_2CO_3 and In_2O_3. The precursors were thoroughly mixed and calcined at 850 ˚C for 12 h in O_2flow. $NaInO_2$ powder thus obtained was mixed with $AgNO_3$ and KNO_3 in the molar ratio 1:1.5:1.5 and heated at 200 ˚C for 48 h in air. Under the heat treatment, it is expected the exchange of Na with Ag in the melt and reorganization of crystal structure to delafossite type. The solidified mixture was washed by water to leach out the remaining nitrates. The resulting powder was ground, pelletized and again heated at 500 ˚C for 24 h in O_2 flow [89, 156]. XRD analysis of the resultant product showed the formation of $AgInO_2$phase along with large fractions of Ag and In_2O_3 (Figure A1 (b)). This shows that the crucial step affecting during the synthesis is the decomposition of Ag_2O forming Ag.

Solution/wet chemistry methods were tried to avoid high temperature treatments that resulted in decomposition of Ag_2O during the process.

3. Co-precipitation reaction

$AgNO_3$ and Indium were dissolved in 5 mL each of water and 16 M HNO_3 separately. To the silver nitrate solution, indium nitrate solution was added in drops under constant stirring at 150 ˚C. The above solution was stirred for 30 minutes by adding 4 M KOH. The resultant precipitate was washed several times with deionized water and acetone and then dried in air. XRD analysis of the resultant product showed the formation of only Ag and $In(OH)_3$ phases (Figure A1 (c)).

4. Combustion synthesis

Stoichiometric amounts of $AgNO_3$ was dissolved in water and Indium was dissolved in nitric acid. The stoichiometric amounts of respective solutions were mixed with the calculated amount of glycine to maintain the stoichiometric fuel to oxidizer ratio (i.e. F/O = 1). The reactant mixture was kept on a furnace preheated to 350 ˚C, where it boiled and ignited by leaving a voluminous mass within 5 min. This mass was characterized by XRD shows the presence of Ag and In_2O_3 as products (Figure A1 (d)).

5. Hydrothermal synthesis

An attempt was also made using the hydrothermal method using Ag_2O and In_2O_3 as starting precursors as reported in the literature [91, 145]. Stoichiometric quantities of Ag_2O and In_2O_3along with KOH were placed in a Teflon-lined stainless steel autoclave of 100 mL capacity filled with 50 ml of deionized water. The vessel was sealed and heated at 210 ˚C for 60 h. After the dwell time, the autoclave was cooled to room temperature naturally and the resultant was washed several times with deionized water and acetone and then dried in air. XRD analysis of the resultant product showed the formation of $AgInO_2$along with Ag and In_2O_3 impurity phases (Figure A1 (e)). From the XRD results, it is observed that the fraction of impurities were significantly reduced using this method compared with that of the above mentioned methods. By considering these inputs, in the present thesis, we had adopted a modified hydrothermal route for the preparation of $AgInO_2$ (Chapter 3).

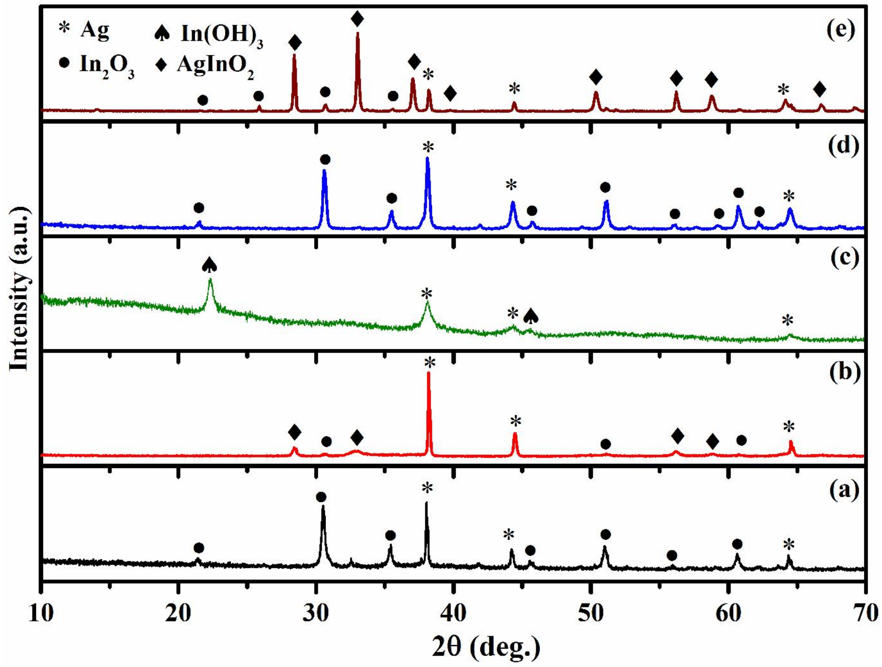

Figure A1. XRD patterns of $AgInO_2$ prepared by **(a)** Solid state reaction, **(b)** Cation exchange reaction, **(c)** Co-precipitation reaction, **(d)** Combustion synthesis and **(e)** Hydrothermal synthesis.

APPENDIX 2

Methodology of factorial analysis

Factorial design approach was adopted by many experimentalists for designing the experiments and infers the inter-dependence of either process parameters or intrinsic characteristics of the species involved. There are many reasons for the success of the process; out of which screening, optimization and saving time by performing minimum number of experiments are possibly the major motivations for experimental design. To perform a factorial design, we have to select a fixed number of “levels” (l) and number of “factors” (n) (parameters or variables) and then run experiments in all possible combinations (l^n) [243, 244].

As an example, in the present thesis, a factorial design approach was adopted for optimizing the synthesis conditions for the phase pure formation of $AgInO_2$. Keeping in view of the reported literature, temperature (150 ˚C – 210 ˚C), mineralizer (KOH) concentration (4 M – 6 M) and dwell time (24 h – 60 h) were chosen as most important factors for the successful formation of $AgInO_2$. One can perform innumerable number of experiments using these three factors within the limits mentioned in braces. With increase in number of choices, it is time consuming and not cost-effective that would result in tedious interpretation. Further, it is impractical to conduct all the experiments. When we use one-factor-at-a-time method of experimentation, the factors are varied one at a time with the remaining factors held constant. But this method only provides an estimate of the effect of a single factor at selected and fixed conditions of the other factors [243]. In contrast, factorial design approach helps to study the effect of each factor on the response variables, as well as the effects of interactions between factors on the response variable with more precision even by performing minimum number of experiments by choosing the appropriate levels and factors [243, 244].

The following is an example of two level and three factor factorial design.

- Purpose: Optimizing the synthesis conditions to obtain $AgInO_2$ in pure form
- Factors (n) chosen are three: 1. Temperature (A): 150 ˚C, 180 ˚C & 210 ˚C
  2. KOHconcentration (B): 4 M &6 M
  3. Dwell time (C): 24 h & 60 h
- No of levels (l) are two: 1. Low (coded as -1)
  2. High (coded as +1)
- Response (Y): Fractional intensities of the highly oriented peaks[1] of the phases $AgInO_2$, Ag and In_2O_3, calculated from the X-ray diffraction patterns of the respective samples.

By varying the possible combinations with above mentioned limits of variables, the optimum experimental condition to obtain $AgInO_2$ in pure form is attempted. The factorial analysis is performed by splitting the experimental runs into two blocks corresponding to two levels of each factor as given in Table A2.1. Coded values of actual experimental conditions considered for the two design matrices are given in Table A2.2. There are eight different ways of combining high and low levels of each factor. These eight runs are shown at the corners of the following diagram with the codes (Figure A2.1). Note that if we have “n” factors, each run at two levels, there will be “2^n” different combinations of the levels [243, 244]. In the present case, n = 3 and $2^3 = 8$ combinations. Therefore, total no. of experiments in each block is 8 + 8 = 16 and four of them are counted twice. Hence, overall experiments carried out were 12.

---

[1] $AgInO_2$ @ 2θ = 28.343, Ag @ 2θ = 38.121 and In_2O_3@ 2θ = 30.586

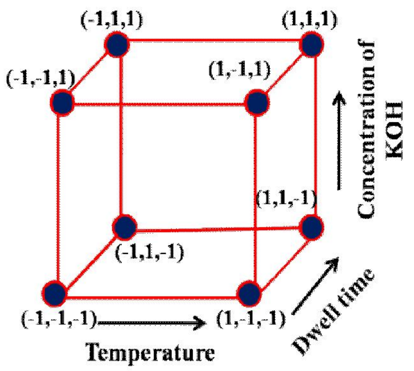

Figure A2.1. A two level factorial design with coded values

Table A2.1. Mixed level design for the synthesis of $AgInO_2$

S. No.	Experiments
1.	150 °C, 4 M, 24 h
2.	150 °C, 4 M, 60 h
3.	150 °C, 6 M, 24 h
4.	150 °C, 6 M, 60 h
5.	**180 °C, 4 M, 24 h**
6.	**180 °C, 4 M, 60 h**
7.	**180 °C, 6 M, 24 h**
8.	**180 °C, 6 M, 60 h**
9.	210 °C, 4 M, 24 h
10.	210 °C, 4 M, 60 h
11.	210 °C, 6 M, 24 h
12.	210 °C, 6 M, 60 h

Block I

Block II

Table A2.2. Coded values of actual experimental conditions considered for the two design matrices

	Block I		Block II	
Coded value	-1	+1	-1	+1
Temperature (˚C)	150	180	180	210
Concentration of KOH (M)	4	6	4	6
Dwell time (h)	24	60	24	60

Considering the block wise factorial analysis, all the main and interaction effects can be estimated. As an example, the design matrix and coefficients for the experiment is given in Table A2.3.

Table A2.3. Design matrix and coefficients for the experiment

Run No.	Intercept	Temperature (A) X_1	Concentration of KOH (B) X_2	Dwell time (C) X_3	A×B X_1X_2	B×C X_2X_3	C×A X_1X_3	A×B×C $X_1X_2X_3$	Response Y
1	1	-1	-1	-1	1	1	1	-1	91.11
2	1	-1	-1	1	1	-1	-1	1	97.07
3	1	-1	1	-1	-1	-1	1	1	96.99
4	1	-1	1	1	-1	1	-1	-1	98.01
5	1	1	-1	-1	-1	1	-1	1	100.00
6	1	1	-1	1	-1	-1	1	-1	100.00
7	1	1	1	-1	1	-1	-1	-1	97.48
8	1	1	1	1	1	1	1	1	97.82
	b_0	b_1	b_2	b_3	b_{12}	b_{23}	b_{13}	b_{123}	Y

There are three main effects, three two-factor interaction and a three factor interaction. The non-linear equation relating the response with individual and interaction effects is given as [244]:

$$\begin{array}{ll}
\mathbf{Y =} & \textbf{(response)} \\
\quad \mathbf{b_0 +} & \textbf{(an intercept or average)} \\
\quad \mathbf{b_1x_1 + b_2x_2 + b_2x_2 +} & \textbf{(linear terms depending on each of the three factors)} \\
\quad \mathbf{b_{11}x_1^{\,2} + b_{22}x_2^{\,2} + b_{33}x_3^{\,2} +} & \textbf{(quadratic terms depending on each of the three factors)} \\
\quad \mathbf{b_{12}x_1x_2 + b_{13}x_1x_3 + b_{23}x_2x_3} & \textbf{(interaction terms between the factors)}
\end{array} \qquad \textbf{(A2.1)}$$

The different coefficients in the above equation reveal differently as mentioned below.

- The intercept relates to the average experimental value
- The linear terms allow for a direct relationship between the response and a given factor.
- Quadratic terms helps to understand the optimum performance of the reaction
- Interaction terms arise due to the influence of two factors on the response

Calculation of main and interaction effects

Mathematically, the calculation of each effect is expressed as follows [243]:

$$\mathbf{Effect} = \frac{\sum \mathbf{Y_+}}{\mathbf{n_+}} - \frac{\sum \mathbf{Y_-}}{\mathbf{n_-}} \qquad \textbf{(A2.2)}$$

where the “n” refers to the number of repetitions or data points collected at each level. “Y” refers to the associated responses. ΣY_+ and ΣY_- are the average responses corresponding to the plus level and minus level of the factors respectively. Therefore using this formula one can estimate the values of main effects as well as the interaction effects. For example, thecalculated effects along with their standard errors for the design matrices are given in Table A2.4.

Table A2.4. Calculated effects and standard errors for the design matrices

	First block of experiments	**Second block of experiments**
Effect	**Estimate ± standard error**	**Estimate ± standard error**
Average	97.31 ± 2.77	90.31 ± 9.19
Main effects		
Temperature (A)	**3.03 ± 1.88**	**-17.04 ± 1.09**
Concentration of KOH (B)	0.53 ± 1.88	-0.63 ± 1.09
Dwell time (C)	1.83 ± 1.88	-0.27 ± 1.09
Two-factor interactions		
A×B	**-2.88 ± 1.32**	**1.73 ± 0.80**
B×C	-1.15 ±1.32	**0.97 ± 0.80**
C×A	-1.66 ±1.32	-0.44 ± 0.80
Three-factor interactions		
A×B×C	1.32	0.80

Estimation of standard errors

The standard error calculations for experiments with replicated runs are described as follows. From any individual difference "d" between duplicated runs an estimate of variance with one degree of freedom is $s^2 = d^2/2$. The average of these single degree of freedom estimate yields a pooled estimate s^2 with eight degree of freedom. Because each estimated effect is a difference between two averages of eight observations, the variance of an effect is given as

$$\mathbf{V\,(effect)} = \left(\frac{1}{8} + \frac{1}{8}\right)s^2 \qquad \textbf{(A2.3)}$$

and its square root is the standard error of an effect [243].

If the experiment doesn't contain the replicated runs, then the errors can be calculated by considering the higher order interactions which provides a reference set for the remaining effects. In the present example, the estimated interaction effects forming the reference set for calculating errors are AB, BC, CA and ABC. Employing these four estimates, the square of standard error (SE) effect is given by

$$\mathbf{(SE\ effect)^2 = \frac{1}{4}\left\{(Estimate\ of\ AB)^2 + (Estimate\ of\ BC)^2 + (Estimate\ of\ AC)^2 + (Estimate\ of\ ABC)^2\right\}} \quad \textbf{(A2.4)}$$

and its square root is the standard error for the main effects. Similar procedure is followed for calculating the errors for the two factor interaction by considering the three factor interactions as a reference set [243].

Interpretation of data

From Table A2.4. it is observed that, the estimate of dwell time shows least significance in the first block of experiments. Even though temperature raise looks like a favourable factor, its interaction with the concentration of KOH has opposite effect to the same extent. The combined effect of temperature and concentration of KOH value indicatesthat the temperature of 180 °C and 4 M KOH are the more suitable conditions for the formation of pure $AgInO_2$.

Calculated effects for the second block of experiments, where the temperature was raised from 180 °C to 210 °C by keeping other two factors at same levels as in the first block indicate that increase in temperature results in the composite mixture instead of pure phase. The high value of temperature effect dominates the positive contribution from interaction terms (A×B and B×C). Overall, the pure phase formation conditions derived from X-ray diffraction intensities suggest 180 °C and 4 M KOH as the best conditions with no dependence on dwell timefrom 24 h to 60 h.

REFERENCES

[1] N. Barsan, D. Koziej, U. Weimar, Metal oxide-based gas sensor research: How to?, Sensors and Actuators B: Chemical, 121 (2007) 18-35.

[2] G. Korotcenkov, Handbook of gas sensor materials, Volume 1: Conventional Approaches, (2013).

[3] R.A. Potyrailo, C. Surman, N. Nagraj, A. Burns, Materials and transducers toward selective wireless gas sensing, Chemical reviews, 111 (2011) 7315-7354.

[4] Global Industry Analysts, Inc. Gas Sensors Market - Analysis and Forecast to 2027, https://www.strategyr.com/market-report-gas-analyzer-sensor-and-detector-forecasts-global-industry-analysts-inc.asp, (2020).

[5] A.D. McNaught, A. Wilkinson, Compendium of chemical terminology, Blackwell Science Oxford, 1997.

[6] Occupational Safety and Health Standards-1915.11-Scope, application, and definitions applicable, https://www.osha.gov/laws-regs/regulations/standardnumber/1915/1915.11, (1994).

[7] Annual Reports of the Committees on on TLVs and BEIs, https://www.acgih.org/forms/store/ProductFormPublic/annual-reports-on-tlvs-beis-2019, (2019).

[8] U.S. Environmental Protection Agency Acute Exposure Guide- line Levels (AEGL), https://www.epa.gov/aegl/access-acute-exposure-guideline-levels-aegls-values, (2020).

[9] OSHA Occupational Chemical Database, https://www.osha.gov/chemicaldata/, (2020).

[10] A. Hulanicki, S. Glab, F. Ingman, Chemical sensors: definitions and classification, Pure and applied chemistry, 63 (1991) 1247-1250.

[11] N. Yamazoe, K. Shimanoe, Fundamentals of semiconductor gas sensors, in: Semiconductor Gas Sensors, Elsevier, 2020, pp. 3-38.

[12] X. Liu, S. Cheng, H. Liu, S. Hu, D. Zhang, H. Ning, A survey on gas sensing technology, Sensors, 12 (2012) 9635-9665.

[13] G. Korotcenkov, B. Cho, Metal oxide composites in conductometric gas sensors: Achievements and challenges, Sensors and Actuators B: Chemical, 244 (2017) 182-210.

[14] Y. Shimizu, M. Egashira, Basic aspects and challenges of semiconductor gas sensors, Mrs Bulletin, 24 (1999) 18-24.

[15] G. Korotcenkov, B. Cho, Instability of metal oxide-based conductometric gas sensors and approaches to stability improvement (short survey), Sensors and Actuators B: Chemical, 156 (2011) 527-538.

[16] S. Cui, P. Ling, H. Zhu, H.M. Keener, Plant pest detection using an artificial nose system: a review, Sensors, 18 (2018) 378.

[17] M.J. Madou, S.R. Morrison, Chemical sensing with solid state devices, Elsevier, 2012.

[18] A. D'Amico, C. Di Natale, A contribution on some basic definitions of sensors properties, IEEE Sensors Journal, 1 (2001) 183-190.

[19] P. Gründler, Chemical sensors: an introduction for scientists and engineers, Springer Science & Business Media, 2007.

[20] A. Shrivastava, V. Gupta, Methods for the determination of limit of detection and limit of quantitation of the analytical methods, Chronicles of young scientists, 2 (2011) 21-25.

[21] R. Murray, K.E. Holbert, Nuclear energy: an introduction to the concepts, systems, and applications of nuclear processes, Elsevier, 2014.

[22] A.M. Judd, Fast breeder reactors: an engineering introduction, Elsevier, 2013.

[23] B. Raj, P. Chellapandi, P.V. Rao, Sodium fast reactors with closed fuel cycle, CRC press, 2015.

[24] P. King, T.D. Veal, F. Fuchs, C.Y. Wang, D. Payne, A. Bourlange, H. Zhang, G.R. Bell, V. Cimalla, O. Ambacher, Band gap, electronic structure, and surface electron accumulation of cubic and rhombohedral In_2O_3, Physical Review B, 79 (2009) 205211.

[25] N. Barsan, U. Weimar, Conduction model of metal oxide gas sensors, Journal of electroceramics, 7 (2001) 143-167.

[26] T. Seiyama, A. Kato, K. Fujiishi, M. Nagatani, A new detector for gaseous components using semiconductive thin films, Analytical Chemistry, 34 (1962) 1502-1503.

[27] M.A. Carpenter, S. Mathur, A. Kolmakov, Metal oxide nanomaterials for chemical sensors, Springer Science & Business Media, 2012.

[28] A. Rothschild, Y. Komem, The effect of grain size on the sensitivity of nanocrystalline metal-oxide gas sensors, Journal of Applied Physics, 95 (2004) 6374-6380.

[29] G. Eranna, Metal oxide nanostructures as gas sensing devices, CRC press, 2011.

[30] G. Korotcenkov, V. Brinzari, A. Cerneavschi, M. Ivanov, A. Cornet, J. Morante, A. Cabot, J. Arbiol, In_2O_3 films deposited by spray pyrolysis: gas response to reducing (CO, H_2) gases, Sensors and Actuators B: Chemical, 98 (2004) 122-129.

[31] G. Sakai, N. Matsunaga, K. Shimanoe, N. Yamazoe, Theory of gas-diffusion controlled sensitivity for thin film semiconductor gas sensor, Sensors and Actuators B: Chemical, 80 (2001) 125-131.

[32] P. Sun, W. Zhao, Y. Cao, Y. Guan, Y. Sun, G. Lu, Porous SnO_2 hierarchical nanosheets: hydrothermal preparation, growth mechanism, and gas sensing properties, CrystEngComm, 13 (2011) 3718-3724.

[33] Y. Shimizu, T. Maekawa, Y. Nakamura, M. Egashira, Effects of gas diffusivity and reactivity on sensing properties of thick film SnO_2-based sensors, Sensors and Actuators B: Chemical, 46 (1998) 163-168.

[34] L. Li, N. Zhang, H. He, G. Zhang, L. Song, W. Qiu, Shape-controlled synthesis of Pd nanocrystals with exposed {110} facets and their catalytic applications, Catalysis Today, 327 (2019) 28-36.

[35] S. Rong, P. Zhang, F. Liu, Y. Yang, Engineering crystal facet of α-MnO_2 nanowire for highly efficient catalytic oxidation of carcinogenic airborne formaldehyde, ACS Catalysis, 8 (2018) 3435-3446.

[36] X. Wang, X. Han, S. Xie, Q. Kuang, Y. Jiang, S. Zhang, X. Mu, G. Chen, Z. Xie, L. Zheng, Controlled synthesis and enhanced catalytic and gas·sensing properties of tin dioxide nanoparticles with exposed high·energy facets, Chemistry–A European Journal, 18 (2012) 2283-2289.

[37] Z. Wang, G. Yang, Z. Zhang, M. Jin, Y. Yin, Selectivity on etching: Creation of high-energy facets on copper nanocrystals for CO_2 electrochemical reduction, ACS nano, 10 (2016) 4559-4564.

[38] K. Zhou, Y. Li, Catalysis based on nanocrystals with well·defined facets, Angewandte Chemie International Edition, 51 (2012) 602-613.

[39] X. Gao, T. Zhang, An overview: Facet-dependent metal oxide semiconductor gas sensors, Sensors and Actuators B: Chemical, 277 (2018) 604-633.

[40] X. Han, M. Jin, S. Xie, Q. Kuang, Z. Jiang, Y. Jiang, Z. Xie, L. Zheng, Synthesis of tin dioxide octahedral nanoparticles with exposed high·energy {221} facets and enhanced gas·sensing properties, Angewandte Chemie International Edition, 48 (2009) 9180-9183.

[41] Q. Kuang, X. Wang, Z. Jiang, Z. Xie, L. Zheng, High-energy-surface engineered metal oxide micro-and nanocrystallites and their applications, Accounts of chemical research, 47 (2014) 308-318.

[42] Z. Lin, M. Xu, P. Fu, Q. Deng, Crystal plane control of 3D iron molybdate and the facet effect on gas sensing performances, Sensors and Actuators B: Chemical, 254 (2018) 755-762.

[43] H. Wang, K. Dou, W.Y. Teoh, Y. Zhan, T.F. Hung, F. Zhang, J. Xu, R. Zhang, A.L. Rogach, Engineering of facets, band structure, and gas‐sensing properties of hierarchical Sn^{2+}‐doped SnO_2 nanostructures, Advanced Functional Materials, 23 (2013) 4847-4853.

[44] X. Zhou, Z. Wang, X. Xia, G. Shao, K. Homewood, Y. Gao, Synergistic cooperation of rutile TiO_2 {002},{101}, and {110} facets for hydrogen sensing, ACS applied materials & interfaces, 10 (2018) 28199-28209.

[45] M. Silberberg, Principles of general chemistry, McGraw-Hill Education, 2012.

[46] J.-M. Jeon, Y.-S. Shim, S.D. Han, Y.H. Kim, C.-Y. Kang, J.-S. Kim, M. Kim, H.W. Jang, Vertically ordered SnO_2 nanobamboos for substantially improved detection of volatile reducing gases, Journal of Materials Chemistry A, 3 (2015) 17939-17945.

[47] B. Liu, D. Cai, Y. Liu, D. Wang, L. Wang, Y. Wang, H. Li, Q. Li, T. Wang, Improved room-temperature hydrogen sensing performance of directly formed Pd/WO_3 nanocomposite, Sensors and Actuators B: Chemical, 193 (2014) 28-34.

[48] Y.-S. Shim, H.Y. Jeong, Y.H. Kim, S.H. Nahm, C.-Y. Kang, J.-S. Kim, W. Lee, H.W. Jang, Utilization of both-side metal decoration in close-packed SnO_2 nanodome arrays for ultrasensitive gas sensing, Sensors and Actuators B: Chemical, 213 (2015) 314-321.

[49] J.M. Suh, Y.-S. Shim, K.C. Kwon, J.-M. Jeon, T.H. Lee, M. Shokouhimehr, H.W. Jang, Pd-and Au-Decorated MoS_2 Gas Sensors for Enhanced Selectivity, Electronic Materials Letters, 15 (2019) 368-376.

[50] S. Wang, B. Xiao, T. Yang, P. Wang, C. Xiao, Z. Li, R. Zhao, M. Zhang, Enhanced HCHO gas sensing properties by Ag-loaded sunflower-like In_2O_3 hierarchical nanostructures, Journal of materials chemistry A, 2 (2014) 6598-6604.

[51] D. Xue, P. Wang, Z. Zhang, Y. Wang, Enhanced methane sensing property of flower-like SnO_2 doped by Pt nanoparticles: A combined experimental and first-principle study, Sensors and Actuators B: Chemical, 296 (2019) 126710.

[52] X. Yang, H. Fu, Y. Tian, Q. Xie, S. Xiong, D. Han, H. Zhang, X. An, Au decorated In2O3 hollow nanospheres: A novel sensing material toward amine, Sensors and Actuators B: Chemical, 296 (2019) 126696.

[53] R. Zhou, X. Lin, D. Xue, F. Zong, J. Zhang, X. Duan, Q. Li, T. Wang, Enhanced H2 gas sensing properties by Pd-loaded urchin-like $W_{18}O_{49}$ hierarchical nanostructures, Sensors and Actuators B: Chemical, 260 (2018) 900-907.

[54] K. Bunpang, A. Wisitsoraat, A. Tuantranont, S. Singkammo, S. Phanichphant, C. Liewhiran, Highly selective and sensitive CH_4 gas sensors based on flame-spray-made Cr-doped SnO_2 particulate films, Sensors and Actuators B: Chemical, 291 (2019) 177-191.

[55] H. Chen, J. Hu, G.-D. Li, Q. Gao, C. Wei, X. Zou, Porous Ga–In bimetallic oxide nanofibers with controllable structures for ultrasensitive and selective detection of formaldehyde, ACS applied materials & interfaces, 9 (2017) 4692-4700.

[56] W. Jiang, L. Meng, S. Zhang, X. Chuai, Z. Zhou, C. Hu, P. Sun, F. Liu, X. Yan, G. Lu, Design of highly sensitive and selective xylene gas sensor based on Ni-doped MoO_3 nano-pompon, Sensors and Actuators B: Chemical, 299 (2019) 126888.

[57] G.K. Mani, J.B.B. Rayappan, ZnO nanoarchitectures: ultrahigh sensitive room temperature acetaldehyde sensor, Sensors and Actuators B: Chemical, 223 (2016) 343-351.

[58] A.S.R. Murthy, D. Pathak, G. Sharma, K. Gnanasekar, V. Jayaraman, A. Umarji, T. Gnanasekaran, Application of principal component analysis to gas sensing characteristics of $Cr_{0.8}Fe_{0.2}NbO_4$ thick film array, Analytica chimica acta, 892 (2015) 175-182.

[59] C. Wang, X. Cui, J. Liu, X. Zhou, X. Cheng, P. Sun, X. Hu, X. Li, J. Zheng, G. Lu, Design of superior ethanol gas sensor based on Al-doped NiO nanorod-flowers, Acs Sensors, 1 (2016) 131-136.

[60] L. Zhu, Y. Wang, D. Zhang, C. Li, D. Sun, S. Wen, Y. Chen, S. Ruan, Gas Sensors Based on Metal Sulfide $Zn_{1-x}Cd_xS$ Nanowires with Excellent Performance, ACS applied materials & interfaces, 7 (2015) 20793-20800.

[61] J.M. Walker, S.A. Akbar, P.A. Morris, Synergistic effects in gas sensing semiconducting oxide nano-heterostructures: a review, Sensors and Actuators B: Chemical, 286 (2019) 624-640.

[62] Y. Cao, Y. He, X. Zou, G.-D. Li, Tungsten oxide clusters decorated ultrathin In_2O_3 nanosheets for selective detecting formaldehyde, Sensors and Actuators B: Chemical, 252 (2017) 232-238.

[63] J. Liu, M. Dai, T. Wang, P. Sun, X. Liang, G. Lu, K. Shimanoe, N. Yamazoe, Enhanced gas sensing properties of SnO_2 hollow spheres decorated with CeO_2 nanoparticles heterostructure composite materials, ACS applied materials & interfaces, 8 (2016) 6669-6677.

[64] B. Zhang, W. Fu, X. Meng, A. Ruan, P. Su, H. Yang, Synthesis of actinomorphic flower-like SnO_2 nanorods decorated with CuO nanoparticles and their improved isopropanol sensing properties, Applied Surface Science, 456 (2018) 586-593.

[65] G. Korotcenkov, B. Cho, Engineering approaches for the improvement of conductometric gas sensor parameters: Part 1. Improvement of sensor sensitivity and selectivity (short survey), Sensors and Actuators B: Chemical, 188 (2013) 709-728.

[66] W.J. Moon, J.H. Yu, G.M. Choi, The CO and H_2 gas selectivity of CuO-doped SnO_2–ZnO composite gas sensor, Sensors and Actuators B: Chemical, 87 (2002) 464-470.

[67] T. Jinkawa, G. Sakai, J. Tamaki, N. Miura, N. Yamazoe, Relationship between ethanol gas sensitivity and surface catalytic property of tin oxide sensors modified with acidic or basic oxides, Journal of Molecular Catalysis A: Chemical, 155 (2000) 193-200.

[68] K. Schierbaum, U. Weimar, W. Göpel, Comparison of ceramic, thick-film and thin-film chemical sensors based upon SnO_2, Sensors and Actuators B: Chemical, 7 (1992) 709-716.

[69] G. Korotcenkov, The role of morphology and crystallographic structure of metal oxides in response of conductometric-type gas sensors, Materials Science and Engineering: R: Reports, 61 (2008) 1-39.

[70] L.J. Edgar, Method and apparatus for controlling electric currents, in, Google Patents, 1930.

[71] D. Dowden, 56. Heterogeneous catalysis. Part I. Theoretical basis, Journal of the Chemical Society (Resumed), (1950) 242-265.

[72] P. Weisz, Effects of electronic charge transfer between adsorbate and solid on chemisorption and catalysis, The Journal of Chemical Physics, 21 (1953) 1531-1538.

[73] T. Wolkenstein, The electron theory of catalysis on semiconductors, in: Advances in Catalysis, Elsevier, 1960, pp. 189-264.

[74] W.H. Brattain, J. Bardeen, Surface properties of germanium, The Bell System Technical Journal, 32 (1953) 1-41.

[75] G. Heiland, Zum Einfluß von adsorbiertem Sauerstoff auf die elektrische Leitfähigkeit von Zinkoxydkristallen, Zeitschrift für Physik, 138 (1954) 459-464.

[76] P. Shaver, Activated tungsten oxide gas detectors, Applied Physics Letters, 11 (1967) 255-257.

[77] N. Taguchi, Gas detecting device, in, Google Patents, 1972.

[78] S.-H. Chuang, C.-S. Tsung, C.-H. Chen, S.-L. Ou, R.-H. Horng, C.-Y. Lin, D.-S. Wuu, Transparent conductive oxide films embedded with plasmonic nanostructure for light-emitting diode applications, ACS applied materials & interfaces, 7 (2015) 2546-2553.

[79] A. Facchetti, T. Marks, Transparent electronics: from synthesis to applications, John Wiley & Sons, 2010.

[80] N. Faraji, C. Ulrich, N. Wolff, L. Kienle, R. Adelung, Y.K. Mishra, J. Seidel, Visible‐light driven nanoscale photoconductivity of grain boundaries in self‐supported ZnO nano‐and microstructured platelets, Advanced Electronic Materials, 2 (2016) 1600138.

[81] H. Kawazoe, M. Yasukawa, H. Hyodo, M. Kurita, H. Yanagi, H. Hosono, P-type electrical conduction in transparent thin films of $CuAlO_2$, Nature, 389 (1997) 939.

[82] J.-J. Shyue, R.E. Cochran, N.P. Padture, Transparent-conducting, gas-sensing nanostructures (nanotubes, nanowires, and thin films) of titanium oxide synthesized at near-ambient conditions, Journal of materials research, 21 (2006) 2894-2903.

[83] T.V. Beatriceveena, A. Sree Rama Murthy, S. Murugesan, E. Prabhu, K.I. Gnanasekar, A Factorial Design Approach for Hydrothermal Synthesis of Phase‐Pure $AgInO_2$: A Parametric Optimization Study, Angewandte Chemie, 132 (2020) 2261-2265.

[84] M. Yasukawa, K. Ikeuchi, T. Kono, K. Ueda, H. Hosono, Thermoelectric properties of delafossite-type layered oxides $AgIn_{1-x}Sn_xO_2$, Journal of applied physics, 98 (2005) 013706.

[85] H. Kawazoe, H. Yanagi, K. Ueda, H. Hosono, Transparent p-type conducting oxides: design and fabrication of pn heterojunctions, MRS Bulletin, 25 (2000) 28-36.

[86] B. Köhler, M. Jansen, Synthesis and crystal structure of $AgInO_2$, Journal of Solid State Chemistry, 71 (1987) 566-569.

[87] W.C. Sheets, E. Mugnier, A. Barnabe, T.J. Marks, K.R. Poeppelmeier, Hydrothermal synthesis of delafossite-type oxides, Chemistry of materials, 18 (2006) 7-20.

[88] R.D. Shannon, D.B. Rogers, C.T. Prewitt, Chemistry of noble metal oxides. I. Syntheses and properties of ABO_2 delafossite compounds, Inorganic Chemistry, 10 (1971) 713-718.

[89] J.E. Clayton, D.P. Cann, N. Ashmore, Synthesis and processing of $AgInO_2$ delafossite compounds by cation exchange reactions, Thin Solid Films, 411 (2002) 140-146.

[90] D.Y. Shahriari, N. Erdman, U.T. Haug, M.C. Zarzyczny, L.D. Marks, K.R. Poeppelmeier, Direct synthesis of $AgInO_2$, Journal of Physics and Chemistry of Solids, 64 (2003) 1437-1441.

[91] L. Zwiener, T. Jones, E.H. Wolf, F. Girgsdies, M. Plodinec, A.Y. Klyushin, E. Willinger, F. Rosowski, R. Schlögl, E. Frei, Synthesis and Characterization of Ag‐Delafossites $AgBO_2$ (B: Al, Ga, In) from a Rapid Hydrothermal Process, European Journal of Inorganic Chemistry, 2019 (2019) 2333-2345.

[92] R.M. Dell, V. Wheeler, N. Bridger, Hydrolysis of uranium mononitride, Transactions of the Faraday Society, 63 (1967) 1286-1294.

[93] S. Acharya, D. Sarma, Y. Golan, S. Sengupta, K. Ariga, Shape-dependent confinement in ultrasmall zero-, one-, and two-dimensional PbS nanostructures, Journal of the American Chemical Society, 131 (2009) 11282-11283.

[94] A.H. Khan, Q. Ji, K. Ariga, U. Thupakula, S. Acharya, Size controlled ultranarrow PbS nanorods: spectroscopy and robust stability, Journal of Materials Chemistry, 21 (2011) 5671-5676.

[95] S. Acharya, B. Das, U. Thupakula, K. Ariga, D. Sarma, J. Israelachvili, Y. Golan, A bottom-up approach toward fabrication of ultrathin PbS sheets, Nano letters, 13 (2013) 409-415.

[96] H. Choi, J.-H. Ko, Y.-H. Kim, S. Jeong, Steric-hindrance-driven shape transition in PbS quantum dots: understanding size-dependent stability, Journal of the American Chemical Society, 135 (2013) 5278-5281.

[97] F.P.G. de Arquer, A. Armin, P. Meredith, E.H. Sargent, Solution-processed semiconductors for next-generation photodetectors, Nature Reviews Materials, 2 (2017) 16100.

[98] R. Saran, R.J. Curry, Lead sulphide nanocrystal photodetector technologies, Nature Photonics, 10 (2016) 81.

[99] W. Yoon, J.E. Boercker, M.P. Lumb, D. Placencia, E.E. Foos, J.G. Tischler, Enhanced open-circuit voltage of PbS nanocrystal quantum dot solar cells, Scientific reports, 3 (2013) 2225.

[100] A.H. Khan, U. Thupakula, A. Dalui, S. Maji, A. Debangshi, S. Acharya, Evolution of long range bandgap tunable lead sulfide nanocrystals with photovoltaic properties, The Journal of Physical Chemistry C, 117 (2013) 7934-7939.

[101] L. Sun, J.J. Choi, D. Stachnik, A.C. Bartnik, B.-R. Hyun, G.G. Malliaras, T. Hanrath, F.W. Wise, Bright infrared quantum-dot light-emitting diodes through inter-dot spacing control, Nature nanotechnology, 7 (2012) 369.

[102] Y. Liu, H. Wang, S. Yang, K. Chen, T. Yang, J. Wei, J. Tian, W. Chen, ppb level ammonia detection of 3-D PbS quantum dots/reduced graphene oxide nanococoons at room temperature and Schottky barrier modulated behavior, Sensors and Actuators B: Chemical, 255 (2018) 2979-2987.

[103] S.K. Kulkarni, Synthesis of nanomaterials—II (Chemical methods), in: Nanotechnology: Principles and Practices, Springer, 2015, pp. 77-109.

[104] C. Dhand, N. Dwivedi, X.J. Loh, A.N.J. Ying, N.K. Verma, R.W. Beuerman, R. Lakshminarayanan, S. Ramakrishna, Methods and strategies for the synthesis of diverse nanoparticles and their applications: a comprehensive overview, RSC Advances, 5 (2015) 105003-105037.

[105] K. Byrappa, N. Keerthiraj, S.M. Byrappa, Hydrothermal Growth of Crystals—Design and Processing, in: Handbook of Crystal Growth, Elsevier, 2015, pp. 535-575.

[106] K. Byrappa, M. Yoshimura, Handbook of hydrothermal technology, William Andrew, 2012.

[107] S.-H. Feng, G.-H. Li, Hydrothermal and solvothermal syntheses, in: Modern inorganic synthetic chemistry, Elsevier, 2017, pp. 73-104.

[108] A. Rabenau, The role of hydrothermal synthesis in preparative chemistry, Angewandte Chemie International Edition in English, 24 (1985) 1026-1040.

[109] A.R. West, Solid state chemistry and its applications, John Wiley & Sons, 2014.

[110] I. Kolthoff, Theory of coprecipitation. The formation and properties of crystalline precipitates, The Journal of Physical Chemistry, 36 (2002) 860-881.

[111] G. Xu, X. Zhang, W. He, H. Liu, H. Li, R.I. Boughton, Preparation of highly dispersed YAG nano-sized powder by co-precipitation method, Materials Letters, 60 (2006) 962-965.

[112] M.F. Zawrah, H. Hamaad, S. Meky, Synthesis and characterization of nano $MgAl_2O_4$ spinel by the co-precipitated method, Ceramics International, 33 (2007) 969-978.

[113] S. Kasap, P. Capper, Springer handbook of electronic and photonic materials, Springer, 2017.

[114] M. Prudenziati, Thick film sensors, Elsevier Amsterdam, 1994.

[115] M. Prudenziati, B. Morten, Thick-film sensors: an overview, Sensors and Actuators, 10 (1986) 65-82.

[116] N. White, J. Turner, Thick-film sensors: past, present and future, Measurement Science and Technology, 8 (1997) 1.

[117] A. Tricoli, M. Righettoni, A. Teleki, Semiconductor gas sensors: dry synthesis and application, Angewandte Chemie International Edition, 49 (2010) 7632-7659.

[118] P. Willmott, J. Huber, Pulsed laser vaporization and deposition, Reviews of Modern Physics, 72 (2000) 315.

[119] N.P. Ong, J.K. Moyle, J. Bajaj, J. Cheung, Quantized Hall effect and weak localization effects in two‐dimensional HgTe–CdTe superlattices, Journal of Vacuum Science & Technology A: Vacuum, Surfaces, and Films, 5 (1987) 3079-3084.

[120] J. Cheung, J. Horwitz, Pulsed laser deposition history and laser-target interactions, MRS bulletin, 17 (1992) 30-36.

[121] D. Geohegan, D. Chrisey, G. Hubler, Pulsed laser deposition of thin films, Chrisey and GK Hubler (eds), Wiely, New York, (1994) 59-69.

[122] M. Bouroushian, T. Kosanovic, Characterization of thin films by low incidence X-ray diffraction, Cryst. Struct. Theory Appl, 1 (2012) 35-39.

[123] B.D. Cullity, Elements of X-ray Diffraction, Addison-Wesley Publishing, 1956.

[124] J.P. Kenney, H. Veeramani, D.S. Alessi, Analytical Geomicrobiology, Cambridge University Press, 2019.

[125] B. Bhushan, H. Fuchs, Applied scanning probe methods II, Springer, 2006.

[126] B. Bhushan, H. Fuchs, S. Hosaka, Applied scanning probe methods I, Springer Science & Business Media, 2014.

[127] C.C. Chusuei, D.W. Goodman, X-ray photoelectron spectroscopy, (2013).

[128] D. Briggs, Practical surface analysis, Auger and X-Ray Photoelecton Spectroscory, 1 (1990) 151-152.

[129] J.F. Moulder, Handbook of X-ray photoelectron spectroscopy, Physical electronics, (1995) 230-232.

[130] M. Seah, Quantification of AES and XPS, Practical surface analysis, 1 (1990) 201.

[131] J.F. Watts, J. Wolstenholme, An introduction to surface analysis by XPS and AES, (2003).

[132] D.M. Hercules, S.H. Hercules, Analytical chemistry of surfaces. Part II. Electron spectroscopy, Journal of Chemical Education, 61 (1984) 483.

[133] P. Atkins, T. Overton, Shriver and Atkins' inorganic chemistry, Oxford University Press, USA, 2010.

[134] A.R. Barron, Physical methods in chemistry and nano science, (2015).

[135] P. O'Hare, H. Hoekstra, Thermochemistry of uranium compounds VI. Standard enthalpy of formation of cesium diuranate ($Cs_2U_2O_7$). Thermodynamics of formation of cesium and rubidium uranates at elevated temperatures, The Journal of Chemical Thermodynamics, 7 (1975) 831-838.

[136] D.K. Schroder, Semiconductor material and device characterization, John Wiley & Sons, 2015.

[137] O. Philips’Gloeilampenfabrieken, A method of measuring specific resistivity and Hall effect of discs of arbitrary shape, Philips Res. Rep, 13 (1958) 1-9.

[138] L.J. van der Pauw, A method of measuring the resistivity and Hall coefficient on lamellae of arbitrary shape, Philips technical review, 20 (1958) 220-224.

[139] C. Friedel, Sur une combinaison naturelle des oxydes de fer et de cuivre, et sur la reproduction de l’atacamite, Sciences Academy, 77 (1873) 211-214.

[140] A. Pabst, Notes on the structure of delafossite, American Mineralogist: Journal of Earth and Planetary Materials, 31 (1946) 539-546.

[141] R.D. Shannon, D.B. Rogers, C.T. Prewitt, J.L. Gillson, Chemistry of noble metal oxides. III. Electrical transport properties and crystal chemistry of ABO_2 compounds with the delafossite structure, Inorganic Chemistry, 10 (1971) 723-727.

[142] K. Ikeuchi, M. Yasukawa, T. Kono, K. Ueda, H. Hosono, Synthesis and thermoelectric properties of delafossite-type layered oxides $AgInO_2$-based solid solutions, in: Preprints of Annual Meeting of The Ceramic Society of Japan Preprints of Fall Meeting of The Ceramic Society of Japan Annual Meeting of The Ceramic Society of Japan, 2005, The Ceramic Society of Japan, 2005, pp. 264-264.

[143] M.R. Hoffmann, S.T. Martin, W. Choi, D.W. Bahnemann, Environmental applications of semiconductor photocatalysis, Chemical reviews, 95 (1995) 69-96.

[144] A. Mills, R.H. Davies, D. Worsley, Water purification by semiconductor photocatalysis, Chemical Society Reviews, 22 (1993) 417-425.

[145] H. Dong, Z. Li, X. Xu, Z. Ding, L. Wu, X. Wang, X. Fu, Visible light-induced photocatalytic activity of delafossite $AgMO_2$ (M= Al, Ga, In) prepared via a hydrothermal method, Applied Catalysis B: Environmental, 89 (2009) 551-556.

[146] S. Ouyang, N. Kikugawa, D. Chen, Z. Zou, J. Ye, A systematical study on photocatalytic properties of $AgMO_2$ (M= Al, Ga, In): effects of chemical compositions, crystal structures, and electronic structures, The Journal of Physical Chemistry C, 113 (2009) 1560-1566.

[147] S. Ibuki, H. Yanagi, K. Ueda, H. Kawazoe, H. Hosono, Preparation of n-type conductive transparent thin films of $AgInO_2$:Sn with delafossite-type structure by pulsed laser deposition, Journal of Applied Physics, 88 (2000) 3067-3069.

[148] H. Yanagi, K. Ueda, S. Ibuki, T. Hase, H. Hosono, H. Kawazoe, Transparent p-and n-type conductive oxides with delafossite structure, MRS Online Proceedings Library Archive, 623 (2000).

[149] W. Croft, N. Tombs, R. England, Crystallographic data for pure crystalline silver ferrite, Acta Crystallographica, 17 (1964) 313-313.

[150] H. Rietveld, A profile refinement method for nuclear and magnetic structures, Journal of applied Crystallography, 2 (1969) 65-71.

[151] A. Larson, R. Von Dreele, General Structure Analysis System. Lansce, MSH805, Los Alamos, in, New Mexico, 1994.

[152] B.H. Toby, EXPGUI, a graphical user interface for GSAS, Journal of applied crystallography, 34 (2001) 210-213.

[153] L. Tjeng, M. Meinders, J. Van Elp, J. Ghijsen, G. Sawatzky, R. Johnson, Electronic structure of Ag_2O, Physical Review B, 41 (1990) 3190.

[154] D. Briggs, Handbook of X·ray Photoelectron Spectroscopy CD Wanger, WM Riggs, LE Davis, JF Moulder and GE Muilenberg Perkin·Elmer Corp., Physical Electronics Division, Eden Prairie, Minnesota, USA, 1979. 190 pp. $195, Surface and Interface Analysis, 3 (1981) v-v.

[155] Y. Maruyama, H. Irie, K. Hashimoto, Visible light sensitive photocatalyst, delafossite structured α-$AgGaO_2$, The Journal of Physical Chemistry B, 110 (2006) 23274-23278.

[156] T. Otabe, K. Ueda, A. Kudoh, H. Hosono, H. Kawazoe, n-type electrical conduction in transparent thin films of delafossite-type $AgInO_2$, Applied physics letters, 72 (1998) 1036-1038.

[157] S. Xu, Z.L. Wang, One-dimensional ZnO nanostructures: solution growth and functional properties, Nano Research, 4 (2011) 1013-1098.

[158] B.G. Pound, D.D. Macdonald, J.W. Tomlinson, The electrochemistry of silver in KOH solutions at elevated temperatures—I. thermodynamics, Electrochimica Acta, 24 (1979) 929-937.

[159] N. Yamazoe, New approaches for improving semiconductor gas sensors, Sensors and Actuators B: Chemical, 5 (1991) 7-19.

[160] M.E. Franke, T.J. Koplin, U. Simon, Metal and metal oxide nanoparticles in chemiresistors: does the nanoscale matter?, Small, 2 (2006) 36-50.

[161] X. Zhou, S. Lee, Z. Xu, J. Yoon, Recent progress on the development of chemosensors for gases, Chemical reviews, 115 (2015) 7944-8000.

[162] B.-Y. Kim, J.H. Ahn, J.-W. Yoon, C.-S. Lee, Y.C. Kang, F. Abdel-Hady, A.A. Wazzan, J.-H. Lee, Highly selective xylene sensor based on $NiO/NiMoO_4$ nanocomposite hierarchical spheres for indoor air monitoring, ACS applied materials & interfaces, 8 (2016) 34603-34611.

[163] Y. Kim, Y.S. Choi, S.Y. Park, T. Kim, S.-P. Hong, T.H. Lee, C.W. Moon, J.-H. Lee, D. Lee, B.H. Hong, Au decoration of a graphene microchannel for self-activated chemoresistive flexible gas sensors with substantially enhanced response to hydrogen, Nanoscale, 11 (2019) 2966-2973.

[164] A. Kolmakov, D. Klenov, Y. Lilach, S. Stemmer, M. Moskovits, Enhanced gas sensing by individual SnO_2 nanowires and nanobelts functionalized with Pd catalyst particles, Nano letters, 5 (2005) 667-673.

[165] N. Yamazoe, Y. Kurokawa, T. Seiyama, Effects of additives on semiconductor gas sensors, Sensors and Actuators, 4 (1983) 283-289.

[166] B. Tong, Z. Deng, B. Xu, G. Meng, J. Shao, H. Liu, T. Dai, X. Shan, W. Dong, S. Wang, Oxygen Vacancy Defects Boosted High Performance p-Type Delafossite $CuCrO_2$ Gas Sensors, ACS applied materials & interfaces, 10 (2018) 34727-34734.

[167] S. Thirumalairajan, V.R. Mastelaro, C.A. Escanhoela Jr, In-depth understanding of the relation between $CuAlO_2$ particle size and morphology for ozone gas sensor detection at a nanoscale level, ACS applied materials & interfaces, 6 (2014) 21739-21749.

[168] X. Wang, Z. Shi, S. Yao, F. Liao, J. Ding, M. Shao, Gamma ray irradiated $AgFeO_2$ nanoparticles with enhanced gas sensor properties, Journal of solid state chemistry, 219 (2014) 228-231.

[169] Z. Deng, G. Meng, X. Fang, W. Dong, J. Shao, S. Wang, B. Tong, A novel ammonia gas sensors based on p-type delafossite $AgAlO_2$, Journal of Alloys and Compounds, 777 (2019) 52-58.

[170] Q.-q. Jia, H.-m. Ji, D.-h. Wang, X. Bai, X.-h. Sun, Z.-g. Jin, Exposed facets induced enhanced acetone selective sensing property of nanostructured tungsten oxide, Journal of Materials Chemistry A, 2 (2014) 13602-13611.

[171] T.V. Beatriceveena, A. Sree Rama Murthy, S. Murugesan, E. Prabhu, K.I. Gnanasekar, A Factorial Design Approach for Hydrothermal Synthesis of Phase-Pure $AgInO_2$: A Parametric Optimization Study, Angewandte Chemie (International ed. in English), (2019).

[172] Z. Wang, Z. Li, T. Jiang, X. Xu, C. Wang, Ultrasensitive hydrogen sensor based on Pd^0-loaded SnO_2 electrospun nanofibers at room temperature, ACS applied materials & interfaces, 5 (2013) 2013-2021.

[173] L. Liu, C. Guo, S. Li, L. Wang, Q. Dong, W. Li, Improved H_2 sensing properties of Co-doped SnO_2 nanofibers, Sensors and Actuators B: Chemical, 150 (2010) 806-810.

[174] P. Wadkar, D. Bauskar, P. Patil, High performance H_2 sensor based on $ZnSnO_3$ cubic crystallites synthesized by a hydrothermal method, Talanta, 105 (2013) 327-332.

[175] H.-T. Wang, B.S. Kang, F. Ren, L.-C. Tien, P. Sadik, D. Norton, S. Pearton, J. Lin, Hydrogen-selective sensing at room temperature with ZnO nanorods, Applied Physics Letters, 86 (2005) 243503.

[176] A. Soleimanpour, S.V. Khare, A.H. Jayatissa, Enhancement of hydrogen gas sensing of nanocrystalline nickel oxide by pulsed-laser irradiation, ACS applied materials & interfaces, 4 (2012) 4651-4657.

[177] M.M. Alsaif, S. Balendhran, M.R. Field, K. Latham, W. Wlodarski, J.Z. Ou, K. Kalantar-Zadeh, Two dimensional α-MoO_3 nanoflakes obtained using solvent-assisted grinding and sonication method: application for H_2 gas sensing, Sensors and Actuators B: Chemical, 192 (2014) 196-204.

[178] S. Roso, C. Bittencourt, P. Umek, O. González, F. Güell, A. Urakawa, E. Llobet, Synthesis of single crystalline In_2O_3 octahedra for the selective detection of NO_2 and H_2 at trace levels, Journal of Materials Chemistry C, 4 (2016) 9418-9427.

[179] A.S.R. Murthy, K. Gnanasekar, V. Jayaraman, A. Umarji, T. Gnanasekaran, Conductometric Sensing of H_2 by Chromium Niobate, IEEE Sensors Journal, 15 (2015) 7054-7060.

[180] O.E. Yilmaz, R. Erdem, Evaluating hydrogen detection performance of an electrospun $CuZnFe_2O_4$ nanofiber sensor, International Journal of Hydrogen Energy, (2020).

[181] S. Mao, H. Zhou, S. Wu, J. Yang, Z. Li, X. Wei, X. Wang, Z. Wang, J. Li, High performance hydrogen sensor based on Pd/TiO_2 composite film, International Journal of Hydrogen Energy, 43 (2018) 22727-22732.

[182] Z. Han, J. Ren, J. Zhou, S. Zhang, Z. Zhang, L. Yang, C. Yin, Multilayer porous Pd-WO_3 composite thin films prepared by sol-gel process for hydrogen sensing, International Journal of Hydrogen Energy, 45 (2020) 7223-7233.

[183] H. Huang, Y. Lee, O. Tan, W. Zhou, N. Peng, Q. Zhang, High sensitivity SnO_2 single-nanorod sensors for the detection of H_2 gas at low temperature, Nanotechnology, 20 (2009) 115501.

[184] S. Öztürk, N. Kılınç, I. Torun, A. Kösemen, Y. Şahin, Z.Z. Öztürk, Hydrogen sensing properties of ZnO nanorods: effects of annealing, temperature and electrode structure, International Journal of Hydrogen Energy, 39 (2014) 5194-5201.

[185] M. Zhao, C.W. Ong, Improved H_2-sensing performance of nanocluster-based highly porous tungsten oxide films operating at moderate temperature, Sensors and Actuators B: Chemical, 174 (2012) 65-73.

[186] H. Meixner, U. Lampe, Metal oxide sensors, Sensors and Actuators B: Chemical, 33 (1996) 198-202.

[187] T. Hübert, L. Boon-Brett, G. Black, U. Banach, Hydrogen sensors–a review, Sensors and Actuators B: Chemical, 157 (2011) 329-352.

[188] O. Lupan, V. Ursaki, G. Chai, L. Chow, G. Emelchenko, I. Tiginyanu, A. Gruzintsev, A. Redkin, Selective hydrogen gas nanosensor using individual ZnO nanowire with fast response at room temperature, Sensors and Actuators B: Chemical, 144 (2010) 56-66.

[189] L.-H. Tjeng, M.B. Meinders, J. van Elp, J. Ghijsen, G.A. Sawatzky, R.L. Johnson, Electronic structure of Ag_2O, Physical Review B, 41 (1990) 3190.

[190] N.R.C. Raju, K.J. Kumar, A. Subrahmanyam, Physical properties of silver oxide thin films by pulsed laser deposition: effect of oxygen pressure during growth, Journal of Physics D: Applied Physics, 42 (2009) 135411.

[191] N. Allen, The effect of pressure on the liberation of gases from metals (with special reference to silver and oxygen), J. Inst. Metals, 49 (1932) 317-346.

[192] A. Butts, C.D. Coxe, Silver--economics, Metallurgy, and Use, 1967, 488 P. D. VAN NOSTRAND COMPANY, INC., PRINCETON, NEW JERSEY, (1967).

[193] H. Vacher, Metals Handbook, (1948).

[194] T.V. Beatriceveena, A. Sree Rama Murthy, S. Murugesan, E. Prabhu, K.I. Gnanasekar, A Factorial Design Approach for Hydrothermal Synthesis of Phase-Pure $AgInO_2$: A Parametric Optimization Study, Angewandte Chemie (International ed. in English), 59 (2020) 2241.

[195] G.K.H. D B Chrisey, Pulsed Laser Deposition of Thin Films, Wiley–Blackwell, (1994) 1.

[196] D.E. Williams, Semiconducting oxides as gas-sensitive resistors, Sensors and Actuators B: Chemical, 57 (1999) 1-16.

[197] N. Yamazoe, K. Shimanoe, New perspectives of gas sensor technology, Sensors and Actuators B: Chemical, 138 (2009) 100-107.

[198] J. Rebholz, C. Dee, U. Weimar, N. Barsan, A self-doping surface effect and its influence on the sensor performance of undoped SnO_2 based gas sensors, Procedia engineering, 120 (2015) 83-87.

[199] Y. Liu, E. Koep, M. Liu, A highly sensitive and fast-responding SnO_2 sensor fabricated by combustion chemical vapor deposition, Chemistry of materials, 17 (2005) 3997-4000.

[200] J. Guo, J. Zhang, M. Zhu, D. Ju, H. Xu, B. Cao, High-performance gas sensor based on ZnO nanowires functionalized by Au nanoparticles, Sensors and Actuators B: Chemical, 199 (2014) 339-345.

[201] A. Oprea, A. Gurlo, N. Barsan, U. Weimar, Transport and gas sensing properties of In_2O_3 nanocrystalline thick films: A Hall effect based approach, Sensors and Actuators B: Chemical, 139 (2009) 322-328.

[202] A. Oprea, E. Moretton, N. Barsan, W. Becker, J. Wöllenstein, U. Weimar, Conduction model of SnO_2 thin films based on conductance and Hall effect measurements, Journal of applied physics, 100 (2006) 033716.

[203] E. Prabhu, K. Gnanasekar, T. Ravindran, V. Jayaraman, T. Gnanasekaran, Changes in carrier concentration and debye length: Experimental evidence from van der Pauw Hall measurements on NO_x sensing of In_2O_3, Journal of The Electrochemical Society, 161 (2014) B176-B182.

[204] H.-J. Kim, J.-H. Lee, Highly sensitive and selective gas sensors using p-type oxide semiconductors: Overview, Sensors and Actuators B: Chemical, 192 (2014) 607-627.

[205] T.-H. Kim, J.-W. Yoon, Y.C. Kang, F. Abdel-Hady, A. Wazzan, J.-H. Lee, A strategy for ultrasensitive and selective detection of methylamine using p-type Cr_2O_3: Morphological design of sensing materials, control of charge carrier concentrations, and configurational tuning of Au catalysts, Sensors and Actuators B: Chemical, 240 (2017) 1049-1057.

[206] J. Dhakshinamoorthy, B. Pullithadathil, New insights towards electron transport mechanism of highly efficient p-Type CuO (111) nanocuboids-based H_2S gas sensor, The Journal of Physical Chemistry C, 120 (2016) 4087-4096.

[207] H.-I. Chen, C.-Y. Hsiao, W.-C. Chen, C.-H. Chang, T.-C. Chou, I.-P. Liu, K.-W. Lin, W.-C. Liu, Characteristics of a Pt/NiO thin film-based ammonia gas sensor, Sensors and Actuators B: Chemical, 256 (2018) 962-967.

[208] X. Liu, M. Zhang, Studies on PbS and PbSe detectors for IR system, International journal of Infrared and Millimeter waves, 21 (2000) 1697-1701.

[209] S. Günes, K.P. Fritz, H. Neugebauer, N.S. Sariciftci, S. Kumar, G.D. Scholes, Hybrid solar cells using PbS nanoparticles, Solar Energy Materials and Solar Cells, 91 (2007) 420-423.

[210] P. Yang, C.F. Song, M.K. Lü, X. Yin, G.J. Zhou, D. Xu, D.R. Yuan, The luminescence of PbS nanoparticles embedded in sol–gel silica glass, Chemical physics letters, 345 (2001) 429-434.

[211] A. Martucci, J. Fick, J. Schell, G. Battaglin, M. Guglielmi, Microstructural and nonlinear optical properties of silica–titania sol-gel film doped with PbS quantum dots, Journal of applied physics, 86 (1999) 79-87.

[212] T. Fu, Research on gas-sensing properties of lead sulfide-based sensor for detection of NO2 and NH3 at room temperature, Sensors and Actuators B: Chemical, 140 (2009) 116-121.

[213] S. Kaci, A. Keffous, S. Hakoum, M. Trari, O. Mansri, H. Menari, Preparation of nanostructured PbS thin films as sensing element for NO_2 gas, Applied Surface Science, 305 (2014) 740-746.

[214] S. Navale, D. Bandgar, M. Chougule, V. Patil, Facile method of preparation of PbS films for NO_2 detection, RSC Advances, 5 (2015) 6518-6527.

[215] Y. Liu, L. Wang, H. Wang, M. Xiong, T. Yang, G.S. Zakharova, Highly sensitive and selective ammonia gas sensors based on PbS quantum dots/TiO_2 nanotube arrays at room temperature, Sensors and Actuators B: Chemical, 236 (2016) 529-536.

[216] R. Dell, V. Wheeler, N. Bridger, Hydrolysis of uranium mononitride, Transactions of the Faraday Society, 63 (1967) 1286-1294.

[217] O. Yenigün, B. Demirel, Ammonia inhibition in anaerobic digestion: a review, Process Biochemistry, 48 (2013) 901-911.

[218] L. Koao, F. Dejene, H. Swart, Synthesis of PbS nanostructures by chemical bath deposition method, Int. J. Electrochem. Sci, 9 (2014) 1747-1757.

[219] S. Sadovnikov, N. Kozhevnikova, A. Rempel, Oxidation of nanocrystalline lead sulfide in air, Russian Journal of Inorganic Chemistry, 56 (2011) 1864-1869.

[220] Z.Q. Mamiyev, N.O. Balayeva, Preparation and optical studies of PbS nanoparticles, Optical Materials, 46 (2015) 522-525.

[221] C. Rajashree, A. Balu, Tuning the physical properties of PbS thin films towards optoelectronic applications through Ni doping, Optik-International Journal for Light and Electron Optics, 127 (2016) 8892-8898.

[222] R.K. Joshi, A. Kanjilal, H. Sehgal, Solution grown PbS nanoparticle films, Applied Surface Science, 221 (2004) 43-47.

[223] R. Thielsch, T. Böhme, R. Reiche, D. Schläfer, H.-D. Bauer, H. Böttcher, Quantum-size effects of PbS nanocrystallites in evaporated composite films, Nanostructured materials, 10 (1998) 131-149.

[224] M.G. Faraj, Effect of Thickness on the Structural and Electrical Properties of Spray Pyrolysed Lead Sulfide Thin Films, American Journal of Condensed Matter Physics, 5 (2015) 51-55.

[225] F. Gode, O. Baglayan, E. Guneri, p-type nanostructure PbS thin films prepared by the silar method, Chalcogenide Letters, 12 (2015) 519-528.

[226] C.I. Pearce, R.A. Pattrick, D.J. Vaughan, Electrical and magnetic properties of sulfides, Reviews in Mineralogy and Geochemistry, 61 (2006) 127-180.

[227] K.H. Ri, Y. Wang, W.L. Zhou, J.X. Gao, X.J. Wang, J. Yu, The structural properties of Al doped ZnO films depending on the thickness and their effect on the electrical properties, Applied Surface Science, 258 (2011) 1283-1289.

[228] J.Y. Seto, The electrical properties of polycrystalline silicon films, Journal of Applied Physics, 46 (1975) 5247-5254.

[229] T. Miyata, T. Minami, Stability and sensing mechanism of high sensitivity chlorine gas sensors using transparent conducting oxide thin films, Thin Solid Films, 355 (1999) 35-40.

[230] D.J. Cant, K.L. Syres, P.J. Lunt, H. Radtke, J. Treacy, P.J. Thomas, E.A. Lewis, S.J. Haigh, P. O'Brien, K. Schulte, Surface properties of nanocrystalline PbS films deposited at the water–oil interface: a study of atmospheric aging, Langmuir, 31 (2015) 1445-1453.

[231] K. Laajalehto, I. Kartio, P. Nowak, XPS study of clean metal sulfide surfaces, Applied surface science, 81 (1994) 11-15.

[232] S.M. Lee, D.H. Yeon, S.S. Chon, Y.S. Cho, Effect of double substitutions of Cd and Cu on optical band gap and electrical properties of non-colloidal PbS thin films, Journal of Alloys and Compounds, 685 (2016) 129-134.

[233] A. Manocha, R.L. Park, Flotation related ESCA studies on PbS surfaces, Applications of Surface Science, 1 (1977) 129-141.

[234] R.B. Shalvoy, G. Fisher, P. Stiles, Bond ionicity and structural stability of some average-valence-five materials studied by x-ray photoemission, Physical Review B, 15 (1977) 1680.

[235] B. Touati, A. Gassoumi, I. Dobryden, M.M. Natile, A. Vomiero, N.K. Turki, Engineering of electronic and optical properties of PbS thin films via Cu doping, Superlattices and Microstructures, 97 (2016) 519-528.

[236] D. Zingg, D.M. Hercules, Electron spectroscopy for chemical analysis studies of lead sulfide oxidation, The Journal of Physical Chemistry, 82 (1978) 1992-1995.

[237] Q. Feng, S. Wen, W. Zhao, J. Deng, Y. Xian, Adsorption of sulfide ions on cerussite surfaces and implications for flotation, Applied Surface Science, 360 (2016) 365-372.

[238] Q. Feng, W. Zhao, S. Wen, Q. Cao, Activation mechanism of lead ions in cassiterite flotation with salicylhydroxamic acid as collector, Separation and Purification Technology, 178 (2017) 193-199.

[239] Q. Feng, S. Wen, J. Deng, W. Zhao, Combined DFT and XPS investigation of enhanced adsorption of sulfide species onto cerussite by surface modification with chloride, Applied Surface Science, 425 (2017) 8-15.

[240] A. Walsh, G.W. Watson, The origin of the stereochemically active Pb (II) lone pair: DFT calculations on PbO and PbS, Journal of Solid State Chemistry, 178 (2005) 1422-1428.

[241] T. Grandke, L. Ley, M. Cardona, Angle-resolved uv photoemission and electronic band structures of the lead chalcogenides, Physical Review B, 18 (1978) 3847.

[242] C. Peden, J. Rogers Jr, N. Shinn, K. Kidd, K. Tsang, Thermally grown Si 3 N 4 thin films on Si (100): Surface and interfacial composition, Physical Review B, 47 (1993) 15622.

[243] G.E. Box, W.H. Hunter, S. Hunter, Statistics for experimenters, John Wiley and sons New York, 1978.

[244] R.G. Brereton, Applied chemometrics for scientists, John Wiley & Sons, 2007.

Thesis Highlight

Name of the Student: T. V. Beatriceveena

Name of the CI/OCC: Indira Gandhi Centre for Atomic Research

Enrolment No.: CHEM02201504003

Thesis Title: Investigations on $AgInO_2$ and PbS: Preparation, Characterization and Gas Sensing Behavior of Thick and Thin Films

Discipline: Chemical Sciences **Sub-Area of Discipline:** Gas sensors, nanomaterials, thin films

Date of viva voce: 15.04.2021

Rapid growth of industrialization has driven the society to face the broad spectrum of gaseous pollutants having profound toxic effects. Although the development of robust, miniaturized, low-cost and low power devices for environmental monitoring is given the priority, their reliability to operate in harsh industrial ambients is also stressed. Semiconducting metal oxides (SMOs) based chemiresistive gas sensors are very attractive due to their ease of fabrication, simple operation, low power consumption and amenable for miniaturization. Some of the major concerns of the SMO gas sensors are their cross-sensitivity to other gases, effect of humidity on long term performance, baseline drifts and frequent calibrations still remain unresolved driving the search for advanced materials. This thesis outlines some of the issues specific to certain industrial processes requiring rugged and reliable sensors that operate under harsh ambient.

The first idea is the development of wide range hydrogen sensors that operate under harsh and humid industrial environments. $AgInO_2$, a semiconducting delafossite reported to stabilize at a hydrothermal pressure of about 10 bar at 210 ^{o}C is chosen. After addressing the issues related to its synthesis, a modified hydrothermal route is employed to stabilize the impurity-free phase pure nanoplates of $AgInO_2$ by adopting the factorial design approach (Figure 1). Thick films of $AgInO_2$ exhibit reasonable response towards hydrogen over a wide concentration range from 1 ppm to 10000 ppm with good repeatability and baseline stability which makes it a potentially wide range H_2 sensor. XPS results showed a decrease in the peak area of O_x^- after exposure to H_2 is a clear indication of the consumption of O_x^- ions due to H_2 interaction. Granular thin films of $AgInO_2$ were deposited at 200 ˚C under the in-situ pressure of 0.7 mbar oxygen using PLD. A significant reduction in response and recovery times than that of thick films of $AgInO_2$ is noteworthy of thin film configuration. The second idea is focused on the development of ammonia sensor for inert ambient to track the moisture leaks which generates ammonia due to hydrolysis of uranium nitrides stored in fuel storage facilities. Thin films of PbS were grown by PLD under inert ambient as the presence of trace levels of outgassing oxygen leads to its oxidation. Films were highly selective and sensitive to NH_3. Adsorption of NH_3 does not alter the oxidation states of Pb and S, but the binding energy value of 398.1 eV for N 1s level shows dissociative adsorption of NH_3 involving $–NH_x$ species at 473 K.

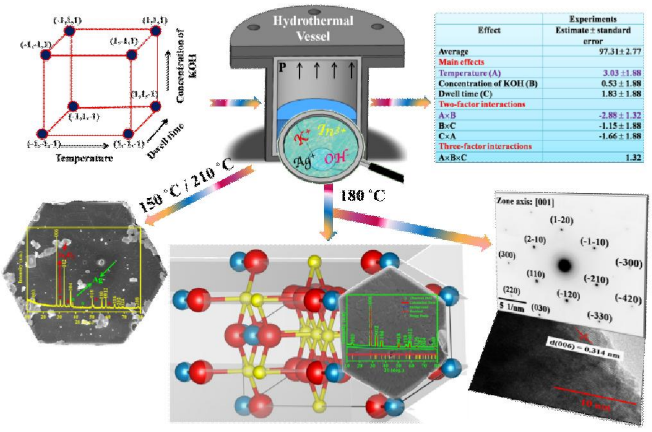

Figure 1. Factorial design approach was adopted for synthesizing phase pure $AgInO_2$ using hydrothermal route. Silver nitrate and indium nitrate with KOH as a mineralizer promote the formation of $AgInO_2$ in the form of hexagonal nanoplates. The optimum condition of 180 ˚C and 4 M KOH was the crucial combination to obtain the pure phase of $AgInO_2$